# Mechanical behavior of high-entropy alloys

Weidong Li <sup>1,1</sup> Di Xie <sup>1</sup>, Dongyue Li <sup>2</sup>, Yong Zhang <sup>2</sup>, Yanfei Gao <sup>1</sup>, Peter K. Liaw <sup>1,\*</sup>

<sup>1</sup> Department of Materials Science and Engineering, University of Tennessee, Knoxville, TN 37996, USA

<sup>2</sup> State Key Laboratory of Advanced Metals and Materials, University of Science and Technology

Beijing, Beijing, 10083, China

#### **Abstract**

Research in the field of high-entropy alloys has been surging since 2010s. As widely acknowledged, researchers' interest to this field is largely sparked by the enormous possibilities in compositions, microstructures, and properties. In the first decade of extensive investigations, while many avenues of research in this vibrant field are being continuously opened, a considerable portion of endeavors is in fact directed toward two very fundamentally important aspects. One is the exploration of the huge compositional space and microstructures with the aid of thermodynamics and kinetics, while the other is the characterization and comprehension of their mechanical behavior from fundamental and practical perspectives. Each of these two aspects contains numerous, scattered, sometimes confusing or conflicting data and findings in the literature. Thank to a number of excellent comprehensive reviews [1-3], the accomplishments and challenges in the first aspect are neatly presented to researchers in the field. Nonetheless, the second aspect, i.e., the mechanical behavior of high-entropy alloys, is still largely afloat in abundant literature. In consideration of this insufficiency, the present review intends to offer a comprehensive, critical review on the mechanical behavior of high-entropy alloys and some closely related topics. The content is organized in 10 independent chapters including Introduction and Concluding remarks. In each core chapter, the topics of common concern are thoroughly reviewed and discussed. Hopefully this work can serve as a useful guidebook for those who are interested in learning, understanding, and researching high-entropy alloys, particularly their mechanical behavior.

*Keywords*: Strength; Ductility; Creep; Fracture; Fatigue; Mechanical properties; Deformation mechanism; Strengthening mechanism; Application

<sup>1\*</sup> Corresponding authors: wli20@utk.edu; pliaw@utk.edu

# Table of Contents

- 1 6
  - 1.1 6
  - 1.2 7
  - 1.3 8
  - 1.4 9
  - 1.5 11
  - 1.6 11
  - 1.7 12
  - 1.8 12
- **2** 16
  - 2.1 16
    - 2.1.1 16
    - 2.1.2 17
    - 2.1.3 18
  - 2.2 19
    - 2.2.1 19
    - 2.2.2 19
    - 2.2.3 20
    - 2.2.4 22
    - 2.2.5 23

    - 2.2.6 23
    - 2.2.7 24
  - 2.3 24
    - 2.3.1 25
    - 2.3.2 26
    - 2.3.3 29
  - 2.4 29
    - 2.4.1 29
    - 2.4.2 30
    - 2.4.3 32
  - 2.5 32
    - 2.5.1 32
    - 2.5.2 33
    - 2.5.3 34
  - 2.6 35
    - 2.6.1 35
    - 2.6.2 35
  - 2.7 36

- **3** 43
  - 3.1 43
  - 3.2 46
  - 3.2.1 46
  - 3.2.2 52
  - 3.3 53
  - 3.4 56
  - 3.5 58
  - 3.6 62
  - 3.7 64
  - 3.8 66
- **4** 72
  - 4.1 73
  - 4.1.1 73
  - 4.1.2 73
  - 4.1.3 74
  - 4.1.4 74
  - 4.2 74
    - 4.2.1 75
  - 4.2.2 78
  - 4.2.3 79
  - 4.3 80
  - 4.3.1 80
  - 4.3.2 81
  - 4.3.3 81
  - 4.4 82
    - 4.4.1 83
    - 4.4.2 83
    - 4.4.3 83
    - 4.4.4 84
    - 4.4.5 85
    - 4.4.6 86
  - 4.4.7 87
  - 4.5 87
- **5** 91
  - 5.1 91
    - 5.1.1 92
    - 5.1.2 93
    - 5.1.3 96

- 5.1.4 97
- 5.2 98
- 5.3 100
- 5.3.1 100
- 5.3.2 102
- 5.3.3 102
- 5.3.4 103
- 5.3.5 104
- 5.3.6 104
- 5.4 105
- **6** 110
  - 6.1 111
  - 6.1.1 111
  - 6.1.2 111
  - 6.1.3 112
  - 6.1.4 114
  - 6.2 115
  - 6.2.1 115
  - 6.2.2 117
  - 6.2.3 117
  - 6.3 118
  - 6.3.1 118
  - 6.3.2 119
  - 6.3.3 119
  - 6.3.4 120
  - 6.4 120
  - 6.4.1 120
  - 6.4.2 121
  - 6.5 122
  - 6.5.1 122
  - 6.5.2 123
  - 6.5.3 123
  - 6.6 125
  - 6.7 126
  - 6.7.1 126
  - 6.7.2 127 6.8 128
- 7 135
- 7.1 135

- 7.1.1 136
- 7.1.2 137
- 7.1.3 138
- 7.1.4 140
- 7.1.5 140
- 7.1.6 142
- 7.2 143
- 7.2.1 143
- 7.2.2 144
- 7.2.3 146
- 7.2.4 147
- 7.3 148
- **8** 154
- 8.1 155
- 8.1.1 155
- 8.1.2 156
- 8.2 156
- 8.2.1 156
- 8.2.2 158
- 8.2.3 158
- 8.3 159
- **9** 162

#### 1 Introduction

## 1.1 How did high-entropy alloys come out?

The human exploration of metallic materials began with pure metals (e.g., Cu), gradually evolved to binary (e.g., Fe-C), ternary (e.g., Ni-Co-Al), quaternary (e.g., Ni-Co-Al-Cr), quinary (e.g., Ni-Fe-Cr-Ti-Al), and higher-order alloys to acquire desirable properties to meet increasingly demanding needs. In the whole history of alloy developments, the mainstream strategy is, to a large extent, constrained to a niche, i.e., pick one element as the solvent and add small amounts of alloying elements as solutes to tailor properties toward desired directions. Over past millennia, this approach has enabled the discovery of a huge number of alloys. Nonetheless, the number of alloys already found is still rather small in comparison to the total number of alloys available. One can easily appreciate this by thinking a triangle-shaped ternary phase diagram, in which the summed area of three corners, which represents the alloy compositions already or could be discovered by the traditional alloy design strategy, is only a small portion of the total area of the triangle, which represents all feasible alloy composition. This ratio becomes even smaller as we move to higher-order alloy systems. After thousands of years of exploitation, alloys that humans can uncover with the traditional approach are close to exhaustion, which is particularly true when considering our pursuit of improved alloy properties or performances.

New hope is lighted up at the birth of high-entropy alloys (HEAs) in 2004, following the publication of five journal articles by Yeh and co-workers [4-8] and a concurrent one by Cantor [9]. This family of alloys is designed with a completely new strategy, i.e., use five or more principal elements in equal or near-equal concentrations as alloying elements with no differentiation of solvent and solute atoms. The new alloy design strategy, on one hand, expands alloy composition space to the uncharted central region of phase diagrams. On the other hand, it produces alloys with much simpler structures (e.g., disordered face-centered cubic solid solution) than expected for multi-component alloys.

As a matter of fact, As a matter of fact, HEAs were not discovered overnight. The work along this line in Yeh's group can be traced back to six Master's theses spanning from 1996 to 2002 [6], while the work on Cantor's side started as early as in 1981 with an undergraduate thesis followed by another in 1995 [10]. Cantor is also the first to use this strategy to make amorphous alloys in 2002 [11]. After emergence, research in high-entropy alloys was slow-paced in 2000s but substantially accelerated in 2010s.

## 1.2 What are high-entropy alloys?

In a series of papers in 2004, this new family of alloys were referred to as high-entropy alloys, multi-principal element alloys, and multi-component alloys. High entropy alloys were first referred to by Yeh et al. and were compositionally defined as alloys with at least five major metallic elements, each of which has an atomic percentage varying from 5% to 35% [4, 12]. High entropy was coined into the name because it was believed that random solid solutions prevail over intermetallic compounds in these alloys primarily due to the high configurational entropy of mixing in comparison to traditional alloys. By assuming alloys as ideal solutions as done by Yeh et al., one can appreciate the rise of configurational entropy of mixing with the increase in the number of composing elements and their concentrations with

$$\Delta S_{mix,ideal} = -R \sum_{i=1}^{n} c_i ln c_i, \qquad (1.1)$$

where R is the gas constant,  $c_i$  is the molar fraction of the ith component, and n is the total number of the constituent elements. In equiatomic alloys, Equation (1.1) can be further simplified to

$$\Delta S_{mix,ideal} = -Rln(n), \tag{1.2}$$

with which,  $\Delta S_{mix,ideal}$  in equiatomic ternary, quinary, and senary alloys is calculated to be 1.39R, 1.61R, and 1.79R, respectively. The entropy idea later motived researchers to define HEAs in terms of configurational entropy of mixing. At the first attempt, Yeh divided all alloys into three groups based on their  $\Delta S_{mix,ideal}$  values, that is, (i) high-entropy alloys with  $\Delta S_{mix,ideal} \ge 1.61R$  for alloys with more than five principal elements, (ii) medium-entropy alloys with  $1.61R \ge \Delta S_{mix,ideal} \ge 0.69R$  for alloys with two to four principal elements, and (iii) low-entropy alloys with  $\Delta S_{mix,ideal} \le 0.69R$  for traditional alloys. Nevertheless, the entropy-based definition is inconsistent with the composition-based definition as the former obviously exclude all non-equiatomic quinary HEAs defined in the latter. To remedy this inconsistency, Miracle et al had suggested to change the bound of HEAs to  $\Delta S_{mix,ideal} \ge 1.5R$ , which in reality still excludes a fraction of quinary HEAs compositionally defined as the minimum  $\Delta S_{mix,ideal}$  for non-equiatomic quinary HEAs is 1.36R.

Considering the ambiguity in the definitions of HEAs, some people like to refer to these alloys in a more general sense, such as multi-principal element alloys, and multi-component alloys, concentrated solid solution alloys [13], and complex concentrated alloys [14]. These terms somewhat loosen the restrictions in both the composition- and entropy-based definitions, e.g.,

equiatomic quaternary alloys may also be classified into HEAs [15, 16]. But, for historic reasons, HEA is the prevalent name used, but now not necessarily restricted to its original definitions, for example, equiatomic ternary alloys are often also referred to as HEAs [17]. HEA is the name used throughout the present paper.

## 1.3 Why are we interested in high-entropy alloys?

Vastly expanded compositional space of alloys: As stated early, the amounts of alloys that can be located with the traditional alloy design strategy based on one (sometimes two) principal element is very limited. Over thousands of years of explorations, only around 30 alloy systems were discovered for common usages as documented in the ASM Metal Handbook. With the multiprincipal-element-based design approach, the compositional space of alloys can be considerably expanded by moving from the small area of corners and edges to the large central area in phase diagrams. According to Cantor's conservative estimate, the total number of possible alloys that may be mapped out of 60 feasible elements is in the order of  $10^{177}$  [10]. By the conventional method, roughly  $10^{11}$  alloys have been investigated [10], thereby leaving  $10^{177} - 10^{11} \approx 10^{177}$  alloy systems unexploited. HEAs and their derivatives (e.g., interstitial HEAs and medium-entropy alloys) surely are offering the route to cover a significant portion of unexploited alloys systems.

Enormous possibilities in microstructures properties and: Expectedly, the expansion of the compositional space alloys will undoubtedly bring about rich opportunities in achieving affluent, diverse microstructures as well as structural and functional properties unseen before. As a matter of fact, some compelling, previously unseen properties have already been reported. For instance, the FeMnCoCrNi HEA with a single fcc phase were reported to exhibit extremely high fracture toughness, particularly at cryogenic temperatures [18]. Besides, the strength and ductility in this alloy shows unusual temperature dependence, that is, both get improved as temperature drops [18]. This type of temperature dependence is barely seen in conventional alloys and can make this alloy very promising for cryogenic applications. Also, the long-standing strength-ductility trade-off is overcome in a dual-phase Fe<sub>50</sub>Mn<sub>30</sub>Co<sub>10</sub>Cr<sub>10</sub> HEA through a partial martensitic transformation from a FCC structure to a HCP structure upon cooling [19]. As we get into specific topics in the following chapters, more examples like these are to be seen.

Advancing metallurgical knowledge: The present physical metallurgy knowledge is established primarily on the basis of investigating numerous conventional, dilute alloys with one

or sometimes two principal elements. As research in the field of HEAs proceeds, inapplicability of existing physical metallurgy knowledge in certain aspects is continuously being revealed. A classic example is the applicability of the Gibbs phase rule in predicting the number of phases that could be present in an alloy. According to the Gibbs rule, the maximum number of phases in an alloy is [10]

$$N_{phase}^{max} = n + 1 \text{ at equilibrium},$$
 (1.3)

$$N_{phase}^{max} > n + 1 at$$
,  $non - equilibrium$ , (1.4)

where n is the number of constituent elements. This rule normally works well for conventional alloys. For instance, at room-temperature non-equilibrium conditions, binary alloys (n = 2) usually comprise three or four phases, and ternary alloys (n = 3) usually have four or five phases. Nevertheless, when it is applied to HEAs, the rule breaks down. The phases that could be present in many HEAs are far less that the maximum phase number allowed by the Gibbs phase rule. According to the Gibbs rule, the maximum phase number in a quinary HEA (e.g., FeMnCoCrNi) should be six under an equilibrium condition and over six under a non-equilibrium condition. Experiences in binary and ternary alloys further imply that the actual number of phases that may appear in this alloy should be close the maximum number. The fact, however, is contrasting – this alloy consists of a single FCC phase [9]. Another example that puzzle researchers is the solid solution strengthening mechanism in HEAs, which is obviously distinct from that in conventional dilute alloys. Thus, the studies of HEAs provide great opportunities to ameliorate, advance, and refine the physical metallurgy knowledge.

## 1.4 What differentiate high-entropy alloys from conventional alloys?

It is commonly acknowledged that there exist four core effects in HEAs that differentiate them from other alloys, which are high entropy, severe lattice distortion, sluggish diffusion, and cocktail effect [20].

High entropy: The high configurational entropy of mixing in HEAs can be easily recognized from Equations (1.1) and (1.2). The role of high entropy in promoting the formation of simple solid solutions in HEAs can be understood from the thermodynamics standpoint. Specifically, whether a reaction can win in competition with others is dictated by the Gibbs free energy of mixing it involves, which is calculated as [3, 21]

$$\Delta G_{mix} = \Delta H_{mix} - T \Delta S_{mix}, \tag{1.5}$$

where T is the temperature.  $\Delta H_{mix}$  is the enthalpy of mixing, which is a measure of energy change.  $\Delta S_{mix}$  is the entropy of mixing, which is a measure of randomness of a system at the molecule level. In the case of HEAs, consider the competition between a solid solution and intermetallic compounds. In ideal solutions assumed for HEAs,  $\Delta H_{mix,ideal}^{SS} = 0$ . On the other hand, if assuming intermetallic compounds are perfectly ordered,  $\Delta S_{mix,ideal}^{IM} = 0$ . As a result  $\Delta G_{mix,ideal}^{SS} = -T\Delta S_{mix,ideal}^{SS}$  for the solid solution, while  $\Delta G_{mix,ideal}^{IM} = \Delta H_{mix,ideal}^{IM}$  for the intermetallic compounds. High entropy makes  $-T\Delta S_{mix,ideal}^{SS} < \Delta H_{mix,ideal}^{IM}$  and  $\Delta G_{mix,ideal}^{SS} < \Delta G_{mix,ideal}^{IM}$ , thereby promoting the formation of solid solutions rather than complex intermetallic compounds in HEAs.

Severe lattice distortion: The level of lattice distortion in pure metals, conventional dilute alloys, and HEAs can be appreciated by viewing their respective hard-sphere model of lattice. As schematically illustrated in Figure 1.1, a pure metal has the same type of atoms occupying the lattice sites and thus causes no distortion to the lattice at all. In conventional dilute alloys, the invasion of a small amount of second atomic species causes slight distortion to the lattice. In HEAs, the high concentrations of multiple different-sized atoms force them to randomly co-exist in the lattice to create severe distortion. The severe lattice distortion in HEAs has been claimed to be detected by X-ray and neutron diffractions [22-25]. Macroscopically, the lattice distortion is believed to be responsible for strong strengthening as well as reduced thermal and electrical conductivity as a result of strong electron and phonon scattering [20, 26].

Sluggish diffusion: Sluggish diffusion was first conjectured based on the observed tendency of forming nano-size precipitates as well as nanocrystalline and amorphous phases in HEAs [4, 20]. Later investigations indeed provide proof on this by comparing the measured diffusion rates of Ni in HEAs and medium-entropy alloys [27-31], as summarized in Figure 1.2. Sluggish diffusion in HEAs is believed to originate from the need of cooperative diffusion of atoms of different kinds [12], and affect all diffusion-controlled process, such as solidification, grain growth, recovery and recrystallization, phase transformation, creep [20, 26].

Cocktail effect: Cocktail effect, a term originally used by Ranganathan for describing amorphous alloys, gum metals, and HEAs [32], has a meaning in physical metallurgy that bending many different element species could produce unexpectedly remarkable properties [1]. If one views a HEA as a composite at the atomic level, the cocktail effect roots in the composite effect – the interactions among all composing elements [20]. As a concrete example, the MoNbTaVW

possess a Vickers hardness of 5250 MPa, far greater than the value of 1596 MPa calculated by the rule of mixture [33].

Apart for the commonly recognized four core effects, there are also some other differences observed between HEAs and conventional alloys. These differences, which is not a complete list for sure, are tabulated in Table 1.1. Some of these are the derivatives of the four core effects.

## 1.5 Classification of high-entropy alloys

HEAs may be classified based on different considerations. Most classifications of HEAs in the literature is based upon the compositions and microstructures of the HEAs reported so far, with some being based on properties or a combination of microstructures and properties. These classifications are compiled in Table 1.2. Those with a given reference are from the literature, and one can refer to the respective work for the rationale behind each classification. Others simpler classifications without an associated reference, such as equimolar vs. non-equimolar HEAs and stable vs. metastable HEAs, are suggested by the authors in consideration of the prevalent usages of these names in the literature.

## 1.6 A glance of constituting elements

The periodic table encompass 118 confirmed elements, 72 out of which are not noble gases, halogens, or radioactive and may be used for alloying HEAs. Over 37 elements have been employed for making hundreds of HEAs [1]. Among these elements, the top 15 elements used for making HEAs are Fe, Ni, Cr, Co, Al, Cu, Ti, Mn, V, Zr, Mo, Nb, Si, Ta, and Sn. Fe, Ni, Cr, Co, Cu, and Mn have been extensively utilized for exploring HEAs with a single fcc phase, following the first reports of the FeNiCrCoCuAl<sub>x</sub> alloy system by Yeh [4], and the FeNiCrCoMn alloy by Cantor [9]. In the periodic table, these 6 elements are neighbouring 3d transition metals with comparable atomic sizes as seen from Figure 1.3. V, Zr, Mo, Nb, and Ta, refractory elements of relatively large atomic sizes as seen from Figure 1.3, are normally used for making bcc-structured refractory HEAs [34]. Al, Ti, Si, and Sn are commonly varied at a range of concentrations to alter the microstructures and/or properties of HEAs [35-41]. Mn is also an important element for tuning phase stability in the metastable engineering of HEAs [19]. Other less used elements include Li, Be, B, C, Mg, Sc, Zn, Ge, Y, Ru, Rh, Pd, Ag, Hf, W, Au, Nd, Gd, Tb, Dy, Tm, and Lu.

### 1.7 A glance of microstructures

HEAs evoked wide interests in the beginning largely due to the unanticipated formation of single-phase solid solutions. As research in this area continues to move on, interests has been expanded to HEAs with dual phases or multiple phases given that many extraordinary properties have been found in these alloys. The ultimate goal of any alloy research and development is to make practically usable materials. In consideration of this, the question of how to make single-phase HEAs becomes less important in comparison to the questions of what microstructures can give high-performance alloys and how to achieve these microstructures.

According to a recent statistical analysis [1], among all single-phase HEAs reported, the FCC structure appears most frequently followed closely by the BCC structure, while the reports of the HCP structure are much less. In multi-phase HEAs, the intermetallic compounds that have been observed include A5 (tI4, β-Sn), A9 (hP4, graphite), A12 (cI58, α-Mn), B2 (cP2, ClCs, AlNi), C14 (hP12, MgZn<sub>2</sub>, Fe<sub>2</sub>Ti, hexagonal Laves phase), C15 (cF24, Cu<sub>2</sub>Mg, cubic Laves phase), C16 (tI12, Al<sub>2</sub>Cu), D8<sub>b</sub> (tP30, σ-CrFe), D0<sub>2</sub> (cF16, BiF<sub>3</sub>, Li<sub>2</sub>MgSn), DO<sub>11</sub> (oP16, Ni3Si), D0<sub>22</sub> (tI8, Al<sub>3</sub>Ti), D0<sub>24</sub> (hP16, Ni<sub>3</sub>Ti), D2<sub>b</sub> (tI26, Mn<sub>12</sub>Th, AlFe<sub>3</sub>Zr), D8<sub>5</sub> (hR13, Fe<sub>7</sub>W<sub>6</sub>, Co-Mo and Fe-Mo), D8<sub>m</sub> (tI32, W<sub>5</sub>Si<sub>3</sub>, Mo<sub>5</sub>Si<sub>3</sub>), E9<sub>3</sub> (cF96, Fe<sub>3</sub>W<sub>3</sub>C, Fe-Ti); L1<sub>0</sub> (tP2, AuCu), L1<sub>2</sub> (cP4, AuCu<sub>3</sub>), and L2<sub>1</sub> (cF16, AlCu<sub>2</sub>Mn, Heusler). The listed compounds are noted with the Strukturbericht notation, with the first notation in the parentheses being the corresponding Pearson symbol, second being the prototype phase followed by the reported phases when different from the prototype, if any. The nicknames of compounds, if any, are given as the last in the parentheses. These intermetallic compounds may influence the properties of HEAs positively or negatively.

#### 1.8 Current status and trend

In 2010s, the research in this field of HEAs is substantially accelerated. Here, we use the search engine in Web of Science as a tool to explore the trend in HEA research in the past 15 years from 2004 to the end of 2019. For not losing generality, we limit our search to English journal and proceeding papers collected in two primary databases, i.e., Science Citation Index Expanded and Conference Proceedings Citation Index-Science. A number of naming conventions referring to HEAs are used for search, including high entropy (high-entropy) alloy, multiprincipal (multiprincipal) element alloy, concentrated solid solution alloy, multicomponent (multi-component) alloy, and complex concentrated alloy. We restrict the search of these keywords to the titles of

articles, allowing us to attain a conservative but rather precise representation of published articles in this field compared to searching these keywords otherwise. During searching, some of aforementioned terms cannot exclusively define HEAs, for example, multicomponent alloys may be ternary alloys [42] or metallic glasses and their derivatives [43, 44]. In such cases, we used further refinements to narrow down the search results only to HEA-related ones. With these five terms used, the searches returned a total of 2587 articles. Within these 2587 articles, high entropy (high-entropy) alloy is the term predominantly used accounting for 93.62%, followed by multicomponent (multi-component) alloy (2.09%), multiprincipal (multi-principal) element alloy (1.70%), concentrated solid solution alloy (1.58%), and complex concentrated alloy (1.01%), as graphed in Figure 1.4.

The growth of publications in the field of HEAs over years is bar-charted in Figure 1.5. One can easily see that after 2013 the number of published articles experiences an exponential growth. Overall, the trend on the number of publications against year approximately follows an exponential relationship of y = 3.05exp(0.33x). Alongside shown in Figure 1.5 is the cumulative citation over years. Till now, more than 50 thousands citations are generated for all 2587 papers.

We also sort out the top 12 universities and research institutes as well as top 13 journals that have greatest HEA publications in amount, as given in Figure 1.6. The University of Tennessee at Knoxville, University of Science and Technology Beijing, and Oak Ridge National Laboratory lead by publishing 237, 186, and 138 papers, respectively. It is worth emphasizing that when counting the number of papers published by different institutes, a single paper may go to multiple organizations due to their collaborative relations. The most HEA papers are published in Journal of Alloys and Compounds (280), followed by Materials Science and Engineering A (215), Intermetallics (154), followed by others.

# **Table Captions**

**Table 1.1** Differences between conventional dilute alloys and high-entropy alloys considered from different aspects.

 Table 1.2 Classification of high-entropy alloys based upon different features.

## **Figure Captions**

- Figure 1.1 Schematics of lattice distortion in body-centered cubic pure metals, conventional dilute alloys, and high-entropy alloys. A D represent different element species in general.
- Figure 1.2 Diffusion coefficients of Ni,  $D_{Ni}$ , in a series of fcc alloys including high-entropy alloys against the inverse homologous temperature,  $T_m/T$ , including NiCo [29], NiFe [29], NiCoFe [29], NiCoFeCr [29], NiCoFeCr [29], NiCoFeCrMn [29], and NiCoFeCrPd [45], CoCrFeMnNi [46], CoCrFeNi [46], and FeCoCrNiMn<sub>0.5</sub> [27, 30].  $T_m$  denotes melting temperature.
- Figure 1.3 Periodic table of elements by atomic size. Courtesy of Sciencenotes.org at http://sciencenotes.org/printable-periodic-table/.
- Figure 1.4 Percentages of different naming conventions for "high entropy alloys". The statistics is based on merely considering the usages of these terms in the titles of 2587 papers from 2004 to the end of 2019.
- Figure 1.5 Number of HEA publications by year, along with cumulative citations over years from 2004 to the end of 2019. The growth of HEA articles can be described by an exponential rise of y = 3.05exp(0.33x).
- Figure 1.6 (a) Top 12 universities and research institutes, and (b) top 13 journals in publishing HEA articles, sorted by the number of publications from year 2004 to the end of 2019.

#### 2 Deformation mechanisms

The deformation mechanism is always a hot topic since the occurrence of HEAs due to the demand and pursues of mechanical properties improvement. In order to design HEAs with enhanced mechanical properties, a detailed understanding of all active deformation mechanisms and their interaction is essential. In this session, we would like to provide a general picture of the deformation mechanisms on HEAs.

#### 2.1 Dislocation mediated deformation

## 2.1.1 Face centered cubit alloys

The mechanical properties of HEAs, similar to those in the conventional metals and alloys, strongly depend on the microstructure and, particularly, the structure of dislocations and dislocation interactions. Take the single FCC structure CoCrFeMnNi HEA as an example. Similar with traditional FCC metals, highly planar deformation involving dislocation arrays on {111} slip systems was firstly observed by Otto et al. in the initial stages of plasticity in a large range of temperatures (77–873 K), and the dissociation of some of the ½<110> {111} dislocations into partials was reported [47]. Figure 2.1 clearly shows that the typical planar slip of ½<110>-type dislocations along two {111} slip planes in the (CoCrNi)<sub>94</sub>Al<sub>3</sub>Ti<sub>3</sub> MEA after ~2% deformation [48]. The low stacking fault energy (SFE) in these FCC structured HEAs results in the widely dissociated dislocations and extensive dislocation reactions. Lomer-Cottrell locks are also observed, shown in Figure 2.2, in the deformed HEA by Xu et al. through investigating the facecentered cubic Al<sub>0.1</sub>CoCrFeNi HEA, due to the widely dissociated dislocation cores with two partials, responsible for the significant work hardening with a large hardening rate in the alloy [49]. Patriarca et al. [50] reported the critical resolved shear stress (CRSS) to initiate slip for the single crystal FeNiCoCrMn alloy was 70 MPa at room temperature while 175 MPa at 77 K. And similar founding is proposed by Abuzaid et al. that the CRSS for slip activation in FeNiCoCrMn alloy has a very strong temperature dependence increasing from ~ 55 MPa at room temperature to around 150 MPa at 77 K. Such temperature dependence, which is common in BCC alloys, is unusual for FCC alloys [51].

While owning to the concentration fluctuation in HEAs, there are unique dislocation structure characters compared with that in conventional FCC solid solution alloys. Figure 2.3(a) and (b) give the FCC crystal lattice of a dilute system and a high-alloy system containing an edge

dislocation, respectively [52]. According to the conventional dislocation theory in dilute alloys, the local potential energy for a dislocation segment in dilute alloys,  $\Delta E_{DA}$ , is the sum of the superposition of the local Peierls potential energy in the solvent pure metal,  $\Delta E_{PM}$ , and the energy contribution of lattice distortion caused by the solute atom,  $\Delta E_{LD}$  [Figure 2.3(c)] [52]. While in the high-alloy systems, the change of the local arrangement of elements can lead to the change in bonding energy and lattice strain energy [52]. Therefore, extra activation energy,  $\Delta E_{ee}$ , should be taken into consideration for dislocations to move in the crystal lattice in addition to  $\Delta E_{PM}$  and  $\Delta E_{LD}$ , as shown in Figure 2.3(d) [52]. Consequently, the average potential energy for a dislocation in high-alloy systems is larger than that in dilute alloys even having similar average lattice distortions to the high-alloy systems, resulting in an additional strengthening effect in high-alloy systems [Figure 2.3(e) and (f)] [52]. Wu et al. [53] suggested the dislocations are narrower in a family of CoCrFeMnNi alloy ( $\omega_0 = b$  at 0 K) than in pure FCC metals ( $\omega_0 = 1.5b$  at 0 K). Smith et al. [54] observed the large variability of dissociation distances as a consequence of complex solute configurations in CoCrFeMnNi alloy, indicating the variable value of dislocation dissociation in this alloy, and proposed the local varied SFE instead of a global variable in these concentrated solid solution alloys. Rao et al. [55] reported the core structure of a/2<110> screw and edge dislocations in an FCC multicomponent alloy, Co<sub>30</sub>Fe<sub>16.67</sub>Ni<sub>36.67</sub>Ti<sub>16.67</sub>, to be planar with significant variations in the Shockley partial splitting along the dislocation line (factor of ~3) due to concentration fluctuations through examining the behavior of a/2[110] screw and edge dislocations via molecular statics and molecular dynamics simulations. And the critical stress to move a/2<110> dislocations in the FCC multicomponent alloy at 0 K is found to be significantly higher as compared to pure Ni [55]. Also, local fluctuations in the concentration of solutes are proposed to have a strong effect on the effective cross-slip activation energy of screw dislocations in the random alloy [55].

#### 2.1.2 Body centered cubit alloys

Recently, Couzinié et al. [56] investigated the dislocation structures in a BCC  $Ti_{20}Zr_{20}Hf_{20}Nb_{20}Ta_{20}$  HEA after mechanical tests through TEM observations and observed that the motion of screw dislocation with b = a/2<111> Burgers vector aligned in <111> directions was dominated at the initial stage of plastic deformation. The screw character of dislocation in this alloy has been found to become stronger due to the reduced mobility of screw dislocations

compared to edge dislocations with the increase of strain [57]. Rao et al. [58] have examined the behavior of a/2[111] screw and edge dislocations in a model BCC multicomponent alloy, Co<sub>16.67</sub>Fe<sub>36.67</sub>Ni<sub>16.67</sub>Ti<sub>30</sub>, and found, similar to simple BCC metals, the core structure of a/2[111] screw dislocations was non-planar. Meanwhile, cross-slip of screw dislocations is observed in the BCC HEAs [59]. Consequently, the screw dislocation motion is proposed to be more importance in coordinating the plastic deformation in the BCC HEAs [59]. These observations allow the clarification of the dislocation-mediated deformation mechanism of the multi-component alloy.

However, different from simple BCC metals and a mean-field version of the same alloy composition, the multi-component random alloy has shown a much larger CRSS and activation energy, which leads to a weak temperature dependence of the strengthening via atomistic modeling the dislocation behavior in the BCC Co<sub>16.67</sub>Fe<sub>36.67</sub>Ni<sub>16.67</sub>Ti<sub>30</sub> alloy by molecular statics and molecular dynamics simulations [58]. And significant core structure variations along equilibrium a/2(111) screw dislocation are observed, presumably due to the local compositional fluctuations that change the local SFEs on different possible slip planes, which contribute to the frequent formation of super jogs [58].

## 2.1.3 Eutectic alloys

Recently, based on the eutectic-alloy concept, eutectic high-entropy alloys (EHEAs) are designed, which combine the advantages of both high-entropy alloys (HEAs) and conventional eutectic alloys, which usually show a fine dual phase lamellar microstructure [60-62]. Take the AlCoCrFeNi2.1 eutectic high-entropy alloy as an example, which combines the high ductility of the FCC (L1<sub>2</sub>) phase and the high strength of the BCC (B<sub>2</sub>) phase [61]. Gao et al. [61] reported the deformation mechanisms of FCC(L1<sub>2</sub>) and BCC(B<sub>2</sub>) phase with lamella structure were different from each other in the sense the dislocation glide in a manner of planar slip is in the former and precipitate-strengthening effect played an important role in the latter. And dislocations are rarely observed in the BCC phase as the phase boundaries act as a potent barrier to dislocation motion resulting in dense dislocation storage in FCC phases [60]. Based on the former investigation, Shi et al. [62] proposed an AlCoCrFeNi<sub>2.1</sub> alloy with an ultrafine-grained duplex FCC and B2 lamellar structure an excellent combination of high strength and high ductility. Upon tension, the soft FCC lamella matrix is more susceptible to starting plastic deformation [62]. Nevertheless, the soft FCC matrix cannot plastically deform freely, owning to the constraint by the still elastic B2 lamellae [62]. Figure 2.4 shows the dislocation evolution of this alloy during

tensile deformation [62]. In the early stage of deformation ( $\varepsilon$ =4%), there are more obvious dislocations in soft FCC grains than hard P2 (the intergranular B2 grains) and B2 grains near phase interfaces [62]. At medium strains ( $\varepsilon$ =13%), dislocations density significantly increases in FCC grains and P2. With further deformation to fracture ( $\varepsilon$ =21%), the dual-phase lamellae and P2 show apparent dislocations [62]. The modulated hard and soft eutectic lamellar structures of AlCoCrFeNi<sub>2.1</sub> EHEA are attributed to the excellent combination of high strength and high ductility [62].

## 2.2 Twining medicated deformation

#### 2.2.1 Microstructural process of twin formation

Mechanical twinning is another common deformation mechanism in metals and alloys, which also has observed in HEAs [63]. Table 2.1 compiles previous reported HEAs that exhibit twining medicated deformation. While, to our knowledge, the unusual plastic deformation mechanism, mechanical twinning, are encountered by FCC HEAs, the characteristic of mechanical twins in BCC and HCP HEAs are seldom reported. Same to the microstructural process of twin formation in FCC metals, the deformation of FCC-structured HEAs involves the glide of Shockley partial dislocations with a Burgers vector of a/6(112) on successive {111} planes [64] with twinning elements  $K_1 = (\underline{1}1\underline{1})$ ,  $\eta_1 = [\underline{1}12]$ ,  $K_2 = (\underline{1}11)$ ,  $\eta_1 = [\underline{1}12]$  and a shear  $s=1/\sqrt{2}$  [47] between the relative orientations of the parent crystal and the twins.

#### 2.2.2 Evolution of twins

Nanoscale deformation twins, observed after interrupted tests in HEA, are proposed to contribute to the excellent mechanism properties [53]. When focusing more on the deformation mechanisms of these HEAs with twinning-induced plasticity (TWIP), a clear transition is seen from prevalent dislocation slip at low strain to slip plus twinning at high strain [47, 53, 65]. There is a critical strain level for the formation of deformation twins [65]. An example of the evolution of twin density with strain in FeNiCoCrMn alloy at 77 K is shown in Figure 2.5 [65]. At the initial stage of plastic deformation (2.1%), dislocation glide is controlled mechanism without the observation of deformation twins [Figure 2.5(a)]; first, nanotwins are observed [Figure 2.5(b)]; at the strain increasing to  $\sim$  6%, and the volume fraction of twins increases systematically with the strain increase [Figure 2.5(b)-(e)];; several intersecting twins are presented within the grains at

~15% strain [Figure 2.5(e)] [65]. A similar deformation response is also reported by Wu et al. [53] on a series of single FCC equiatomic solid solution alloys.

## 2.2.3 Competition between twins and dislocations

### 2.2.3.1 Critical twining stress

Previous reports have suggested the exist of critical stress for twinning in HEAs [65]. The twinning behavior of HEAs is strongly dependent on the competition between the flow stress and critical twinning stress. Sun et al. found the twining capacity in FCC HEAs was weakened by the grain size refinement, due to the dramatically increased critical stress for twinning [66]. The critical shear stress for twinning can be expressed by the following equation [67],

$$\tau_{twin} = \frac{\gamma}{Fb_p} + \frac{k_T}{\sqrt{d'}},\tag{2.1}$$

where  $\tau_{twin}$  is the critical resolved shear stress (CRSS) required to separate a leading Shockley partial dislocation from the trailing partial and thus create a twin,  $\gamma$  is the SFE, F is a fitting parameter that was determined to be 2.0 by Narita and Takamura [68],  $b_p$  is the Burgers vector of a partial dislocation,  $k_T$  is the Hall-Patch constant for twinning and d is the grain size. The normal twin stress ( $\sigma_{twin}$ ) is obtained by multiplying  $\tau_{twin}$  by the average Taylor factor (M). Apparently, the value of critical stress for twinning is related with the SFE and grain size. The critical resolved shear stress for twinning in the CoCrFeMnNi alloy is determined to be ~ 235 MPa in the range of 77-293 K, which is roughly temperature independent [65].

#### 2.2.3.2 Compositional effect

Composition changing is an effective way to trigger a transition from dislocation glide dominated plasticity to a mixed deformation mode consisting of dislocation glide and twining in HEAs with FCC structure [63, 69-72]. According to Equation (2.1), it is plausible the critical twinning stress decreases with the decrease of SFE, which is related to the constitute composition [73, 74]. Hence, the transition of twinning behavior is supposed to be determined by the lowing SFE through varying composition. Deng et al. [74] found that SFE can be reduced by lowering Ni content in the CoCrFeMnNi alloy and developed a Fe<sub>40</sub>Mn<sub>40</sub>Cr<sub>10</sub>Co<sub>10</sub> alloy with mechanical twinning controlled deformation mechanism during the tensile test at room temperature. Liu et al. [73] reported the increased Co content decreased the SFE in an Fe<sub>20</sub>Co<sub>x</sub>Ni<sub>40-x</sub>Cr<sub>20</sub>Mn<sub>20</sub> (x =20-27 at.%) HEAs, resulting in the deformation mode change from dislocation glide to mechanical

twinning. Meanwhile, minor interstitial atoms addition, e.g. C, can promote the activation of primary and secondary twinning systems in these interstitial strengthened HEAs at room temperature [70, 71]. The strong substitutional or interstitial solid solution strengthening effect results in the critical stress for twinning to be easily achieved, even though the interstitial atoms may increase the SFE [69, 75].

#### 2.2.3.3 Grain size effect

Twinning activity in HEAs has been found strongly related to grain size [64, 66, 76]. Sun et al. [66] investigated the size effect on the deformation twinning behavior and observed the deformation twinning becomes popular with the increase of grain size and absent when the grain size falls in the ultrafine-grained (UFG) regime. Considering the grain size effect on the critical stress for twinning in HEAs, large grains in HEAs can reduce the critical stress for twinning, retarding the onset of strain localization [66], which indicates the twinning behavior of the HEAs is strongly dependent on the competition between the flow stress and critical twinning stress with grain refinement. The mechanical twinning is exhibited even at 500 °C because of the very large grain size (>1000 µm) in CoCrFeMnNi alloy [64]. Meanwhile, twinning spacing and twin thickness are also grain-size dependents [77]. Increased twinning spacing and decreased twin thickness in HEAs with small grain sizes will inhibit pronounced twinning activity [77].

#### 2.2.3.4 By thermo-mechanical processing

Controlling the heat treatment process can also affect the activation of twinning [47, 76]. Chen et al. [78] suggested the twinning occurred only in the FCC phase during the SPS process instead of the MA process in  $Al_{0.6}CoNiFeTi_{0.4}$ . Twinning in the FCC phase occurred during the deformation and densification to facilitate deformation and achieve full densification [78]. Fu et al. [79] reported the deformation twinning possibly occurred during mechanical alloying (MA) due to the severe plastic deformation or spark plasma sintering (SPS) simultaneously with phase evolution during the SPS process in the CoNiFeCrAl<sub>0.6</sub>Ti<sub>0.4</sub> alloy. Yu et al. [80] observed nanotwins in the AlCoCuFeNi alloy, produced by melt-spinning. The Cu-rich nanotwins have a face-centered-cubic (FCC) structure diffused in the ordered body-centered-cubic (B2) matrix, which decomposes from the matrix with the K-S crystallographic relationship:  $\{111\}_{FCC}\|$   $\{110\}_{B2}$  and  $\{110\}_{FCC}\|$   $\{111\}_{ECC}\|$   $\{1$ 

## 2.2.3.5 Temperature effect

The temperature-induced competition between slip and twinning in FCC HEAs is commonly observed [53, 64, 81]. The deformation twinning in CrMnFeCoNi alloy is difficult to observe when the deformation temperature increases from cryogenic temperature to room temperature [47]. In contrast to the planar-slip-deformation controlled mechanisms at 298 K, mechanical twinning is the dominated deformation mechanism at 77 K [81]. As the critical stress for twinning slightly increases with the increase of temperature [64] whereas the strength decreases with temperature increases, the critical stress for twinning is difficult to achieve to initiate twins at room temperature. Hence, in order to overcome the temperature effect, efforts have been made, i.e. introducing interstitial atoms and grain size effect, to induce deformation twinning at room and even higher temperatures [64, 66, 69-71].

#### 2.2.4 Interactions between twins and dislocations

A high density of twins is expected to have a significant strengthening effect due to the interactions between twins and dislocations. The formation of deformation twinning during plastic deformation continually introducing additional twin boundaries and decreasing mean free path of dislocation and thereby enhance strain hardening, usually referred to as the "dynamic Hall-Petch" effect [53]. And the twin boundaries also act as sites for dislocation nucleation and accumulation. Therefore, increasing the density of twin boundaries can effectively increase the strength of HEAs and, simultaneously, retain or improve their ductility. While Stepanov et al. [82] proposed the "dynamic Halle Petch" in CoCrFeMnNi alloys is overestimated due to demonstrated low efficiency of the high coherent twin boundaries ( $\sum_3$  type) as an obstacle for dislocation glide. For example, as shown in Figure 2.6, TEM investigations of the CrCoNi samples revealed that large numbers of deformation twinning events occurred in samples deformed in uniaxial tension and the twins typically had thicknesses ranging from ~100 nm to several micrometers [83]. Two types of twin boundaries are observed:  $\Sigma_3\{111\}$  coherent twin boundaries (CTBs) and  $\Sigma_3$ {112} incoherent twin boundaries (ITBs) [83]. Dislocations interact with these TBs in various ways. And dislocation pile-ups at CTBs are observed when they glide on a {111} plane that is not parallel to the CTB [83]. Meanwhile, Zhang et al. [83] reported the intersected twin boundary of different twins provides multiple pathways enabling the fast motion of dislocations and cross slip, resulting in homogeneous plastic deformation.

#### 2.2.5 Twin-twin interactions

When more than one twinning system operates, the twin-twin intersection can occur among twin bands on different planes. The twin-twin intersections are commonly observed in materials and usually give rise to high stress concentration in the intersected region. For example, the twintwin interactions resulted in severe lattice distortion and accumulation of high densities of dislocations in the interaction areas [84]. Figure 2.7 shows twin-twin interactions in a FeCoCrNi HEA introduced by high-pressure torsion (HPT) [84]. Three close twins (T2, T3, and T4) propagate along the same direction, interacted with the pre-existing twin T1, are shown in the HRTEM micrograph in Figure 2.7(a) [84]. The interactions result in the severe local stress concentration at one side of T1 and the stress is partly released from the other side of T1 through the twinning of T5 and T6 [84]. A high density of dislocations (marked with "T") and severe lattice distortion are observed near the interacted TBs in the Fourier filtered image obtained from the twin–twin interaction area marked by a white dashed square in Figure 2.7(a) [Figure 2.7(b)] [84]. And a Lomer-Cottrell (L-C) lock is observed in the area (Fig. 3b), which is formed by the reaction of two leading partials from two dissociated 60° lattice dislocations on two intercrossing slip planes [84]. High densities of dislocations accumulated in the twin-twin interaction areas result in local heavy lattice distortion. And the twin-twin intersected regions provide the sites for the nucleation for phase transformation and amorphous phase due to the accumulation of dislocations and SFs [85]. The intersected twinning boundaries can also lead to complex dislocation reactions and the formation of more mobile and immobile dislocations [86].

### 2.2.6 Effect of precipitates on deformation mechanisms

Zhao et al. [87] found the deformation mode transfered from mechanical twinning in CoCrNi alloy to stacking faults (SFs) controlled mechanism in (CoCrNi)<sub>94</sub>Al<sub>3</sub>Ti<sub>3</sub> with L1<sub>2</sub> phase strengthen. The appearance of mechanical twinning is not solely determined by the low stacking fault energy, but also dependent on the critical twinning stress. The increased critical twinning stress affected by the channel width of the matrix in the precipitation-strengthened with even lower SFE results in the absence of mechanical twinning observed in the single-phase CoCrNi MEA [87]. Tong et al. [88] developed a FeCoNiCrTi<sub>0.2</sub> alloy with coherent precipitates to investigate the effect of precipitate on the twinning behavior of low SFE HEAs at cryogenic temperature. Different from the single-phase FeCoNiCr HEA, twinning rarely happens in the γ'-strengthened

regions even when the aged FeCoNiCrTi<sub>0.2</sub> HEA is deformed at 77 K, suggesting that twin nucleation is impeded by the  $\gamma'$  nano-particles [88]. Microtwins, however, is observed in the regions strengthened by chemically disordered lamellar precipitates, suggesting that the chemical ordering of the  $\gamma'$  nano-particles dramatically increases the energy barrier for twin nucleation [88]. The fundamental understanding of the deformation micro-mechanism of the precipitation strengthened HEAs can provide useful guidance for the development of precipitation hardened concentrated multi-component alloys in the future.

## 2.2.7 Outcome of twinning

The mechanical properties, e.g. strength, ductility, and work hardening in HEAs, are significantly enhanced by the introduction of deformation twinning [47, 53, 64-66, 69-71]. Several factors related to the mechanical twinning in HEAs have been briefly discussed, which indicate the activation of twinning in HEA can be enhanced to obtain excellent mechanical properties, even comparable to those of advanced TWIP steels, through proper tuning these factors. The extensively understood on the twinning mechanism in FCC HEAs can shed light on the alloy design for future applications.

## 2.3 Deformation mediated by phase transformations

The "metastability-engineering" strategy, promoting plastic deformation via deformation-induced transformation, recently has been introduced into HEAs to pursue further improving the mechanical properties, which opens a new strategic path for designing high strength materials [89]. This section will review the unusual plastic deformation mechanisms, phase transformations, encountered in HEAs summarized in Table 2.2. Combining the strong solid solution strengthening effect and transformation-induced plasticity (TRIP) effect, the HEAs exhibit excellent mechanical properties without strength and ductility trade-off [19]. Besides the transformation-induced hardening effect, an additional phase interface, introduced by the deformation-induced phase transformation, further enhances the dislocation slip resistance [19]. Moreover, the ductility has also been improved by the increase of strain hardening capacity, which attribute to the dislocation hardening of the stable phase and transformation-induced hardening of the metastable phase [19].

## 2.3.1 Types of phase transformations

### 2.3.1.1 Phase transformation from face-centered-cubic structured HEAs

Through varying the content of Mn element of Fe<sub>80-x</sub>Mn<sub>x</sub>Co<sub>10</sub>Cr<sub>10</sub> (at%) system to tune phase stability and achieve the TRIP effect, the dual-phase (DP) Fe<sub>50</sub>Mn<sub>30</sub>Co<sub>10</sub>Cr<sub>10</sub> alloy, consisting 72% FCC matrix and 28% HCP phase laminate layers, has been achieved with significantly improved strength and ductility [19]. Figure 2.8 exhibits the EBSD phase maps of the quinary dual-phase Co<sub>20</sub>Cr<sub>20</sub>Fe<sub>34</sub>Mn<sub>20</sub>Ni<sub>6</sub> HEA with increasing tensile deformation at room temperature [90]. Upon tensile straining, the metastable FCC phase shows a martensitic transformation to the HCP martensite phase, and following monotonic deformation to a local engineering strain of about 60%, the fraction of martensite increases to about 61% [90]. Concomitantly, intense strain hardening is observed [19]. The HCP phase exhibits higher stability over the FCC phase at low temperature via thermodynamic calculations [91], contributing the plastic accommodation and hardening at later stages of deformation via multiple deformation mechanisms, including dislocation slip, twinning and the formation of SFs [19]. The SFs, formed by the glide of Shockley partials of 1/6<112> Burgers vector in the FCC matrix, provide the nuclei for the formation of the  $\varepsilon$  (HCP) martensite phase [92]. Meanwhile, metastability-promoted  $\gamma$  (FCC phase)  $\rightarrow \epsilon$  (HCP phase) phase transformation in HEAs has induced the excellent fatigue performance [93]. Besides monotonic deformation, these phase-transformation assisted HEAs also exhibit excellent fatigue properties [94, 95]. It was shown that unlike the negative effect of HCP-martensite in the fatigue crack growth rate of HEAs, the HCP-martensite in a metastable dual-phase HEA, Fe<sub>30</sub>Mn<sub>10</sub>Cr<sub>10</sub>Co<sub>10</sub> (FCC matrix and HCP second phase) possesses high plastic deformation and associated stress accommodation capacity due to the large orientation gradient and high density of dislocations in it [94]. The initial and the transformed HCP phase in the TRIP-DP-HEA are ductile and deform further via dislocation slip at the different strain rates [95].

#### 2.3.1.2 Phase transformation from Body-centered-cubic structured HEAs

Limited plasticity restricts the widespread use of body-centered cubic (BCC) HEAs. While recent studies indicate the "metastability-engineering" approach can successfully be applied in the

BCC HEAs to improve the limited ductility without the compromise of strength [89]. Through reducing the BCC stabilizer element Ta, Huang et al. [89] successfully introduced the TRIP effect in the BCC TaxHfZrTi HEA system with {110}bcc//{0001}hcp crystallographic orientation relationship between the BCC and HCP phase. The controlled deformation mechanism is determined by the competition between the dislocation slip and phase transformation mechanism [89]. Phase transformation during plastic deformation can introduce significant strain-hardening effect by dynamic strain/stress partitioning between the BCC and HCP phases and promote continuous plastic deformation in the BCC matrix [89]. In situ scanning electron microscope (SEM) observation of the lateral morphology evolution in alloy Ta<sub>0.5</sub>HfZrTi as a function of loading is shown in Figure 2.9 [89]. Lamellar hcp phase starts to form inside grains after the macroscopic yielding of this alloy (about 700 MPa) and then multiplies and coarsens with further loading [89]. Meanwhile, a TRIP assisted Ti<sub>35</sub>Zr<sub>27.5</sub>Hf<sub>27.5</sub>Nb<sub>5</sub>Ta<sub>5</sub> was developed by reducing the content of β-stabilizers (Nb and Ta) in the BCC Ti-Zr-Hf-Nb-Ta system using the 'd-electron alloy design' approach [96]. The architectural-type microstructures and a high volume fraction of internally twinned stress induced the forming of martensite a" during plastic deformation contribute the remarkable strain harden rate without the compromise of ductility, compared with the Ti<sub>20</sub>Zr<sub>20</sub>Hf<sub>20</sub>Nb<sub>20</sub>Ta<sub>20</sub> alloy [96]. While it is worth noting that the investigation on "metastability-engineering" in HEAs with the BCC phase is limited.

#### 2.3.2 Tuning phase stability

#### 2.3.2.1 By chemical compositions

HEAs with metastability of phases can be designed using element alloying strategy to tune the stress/strain accommodation by favoring transformation and/or twinning during deformation. One key approach is to reduce the amount of phase stabilizer element to tune the metastability of the matrix [19, 73, 89]. Recent results on TRIP assisted FCC structured HEAs indicate that the concurrence of Fe and Mn is needed for altering the (FCC)  $\gamma$  phase stability during deformation [19]. The "metastability-engineering" approach was successfully introduced to the Fe<sub>80-x</sub>Mn<sub>x</sub>Co<sub>10</sub>Cr<sub>10</sub> (at%) HEA system by reducing the Mn content [19]. And Li et al. [90] proposed the Ab initio simulations of thermodynamic phase stabilities enables to obtain the promising compositions showing the TRIP effect in HEAs, which extends the TRIP behavior exhibiting from quaternary FeMnCoCr system to quinary system of Co<sub>20</sub>Cr<sub>20</sub>Fe<sub>40-x</sub>Mn<sub>20</sub>Ni<sub>x</sub> (x = 0-20 at. %) HEAs

via changing the content of Ni. The deformation mode of the Fe<sub>20</sub>Co<sub>x</sub>Ni<sub>40-x</sub>Cr<sub>20</sub>Mn<sub>20</sub> HEAs changes from the dislocation slip of Fe<sub>20</sub>Co<sub>23</sub>Ni<sub>17</sub>Cr<sub>20</sub>Mn<sub>20</sub> to TWIP of Fe<sub>20</sub>Co<sub>27</sub>Ni<sub>13</sub>Cr<sub>20</sub>Mn<sub>20</sub>, then to TRIP of Fe<sub>20</sub>Co<sub>30</sub>Ni<sub>10</sub>Cr<sub>20</sub>Mn<sub>20</sub>, owning to the negative relationship between Co content and SFE [73]. Recent reports found the Ta level in the refractory TiZrHfTa<sub>x</sub> system can destabilize the body-centered cubic (BCC) phase and leads to the appearance of the hexagonal close-packed (HCP) phase embedded in the BCC matrix, according to both experimental result [89] and firstprinciple theory [97]. Figure 2.10 shows the phase constitution and structural evolution of the ascast TaxHfZrTi (x = 1, 0.6, 0.5, and 0.4) alloys, characterized by X-ray diffraction (XRD) and electron backscatter diffraction (EBSD) analysis [89]. A small amount of hcp phase is detected from the EBSD image when the Ta content is decreased from 25% to 16.7% and a dual-phase microstructure consisting of interwove hcp lamella plates embedded in the bcc matrix is observed with the further decrease of Ta content to 14.3% and 11.8% [89]. Besides adding transition elements, another method is to introduce minor elements. It is shown that light weight elements like Si, C, Al have a massive effect on the γ phase evolution in TRIP assisted HEAs [98-100]. Nene et al. [101] reported the addition of Si can alter the FCC phase stability, promote pronounced transformation induced plastic deformation in both as-cast and grain refined Fe<sub>42</sub>Mn<sub>28</sub>Co<sub>10</sub>Cr<sub>15</sub>Si<sub>5</sub> HEA, and result in very high strength (1.15 GPa) and work hardening (WH) ability due to the decrease of the stability of FCC  $(\gamma)$  matrix. And they also developed a new metastable transformation-induced plasticity dual-phase alloy, Fe<sub>39</sub>Mn<sub>20</sub>Co<sub>20</sub>Cr<sub>15</sub>Si<sub>5</sub>Al<sub>1</sub>, with excellent strength and ductility by adding Si and Al elements [100]. Al, C addition can attain more sustained work hardening in the material during deformation by tuning phase stability while enhancing the stability of the FCC matrix [71, 100]. Therefore, in order to retain the metastability of the matrix to obtain the TRIP effect, the content of Al and C element should be controlled to a small amount [71, 100].

### 2.3.2.2 By thermo-mechanical processing

Li et al. [19, 102] reported that the strength-ductility profile TRIP assisted HEAs depended not only on grain size but also on the fraction of the HCP phase and the density of stacking faults. In order to improve the TRIP effect, thermomechanical processing, like friction stir processing (FSP), has been applied in some TRIP assisted HEAs to tailor the microstructure of these alloy [100]. Take the Fe<sub>50</sub>Mn<sub>30</sub>Co<sub>10</sub>Cr<sub>10</sub> alloy as an example, which exhibits a significant tensile property enhancement by grain size refinement through FSP [99]. Compared with 32% HCP phase with the

grain size of 4.5  $\mu$ m after cold rolling and annealing treatment [19, 102], the friction of HCP phase is reduced to about 8% and 10% at similar grain sizes of  $\sim$  5.2 and  $\sim$  6.5  $\mu$ m after applying FSP, respectively [99]. Therefore, FSP is an effective way to obtain fine-grained TRIP HEAs with higher FCC-phase fraction, leading to a higher level of TRIP effect [99]. Enhanced strength and ductility are achieved in these TRIP-assisted dual-phase HEA, attributed by the TRIP effect, grain boundary strengthening, and effective strain partitioning between the two phases engineered via FSP [99]. Hence, FSP can result in a highly transient microstructure in HEAs, helping alter grain size, tune phase evolution, and retain chemical homogeneity of microstructure, which favors an optimal fraction between  $\gamma$  (FCC) phase and  $\varepsilon$  (HCP) phase [99, 100].

## 2.3.2.3 By grain sizes

Li et al. [102] systematically investigated the grain size effect on the strength and ductility of Fe<sub>50</sub>Mn<sub>30</sub>Co<sub>10</sub>Cr<sub>10</sub> alloy. Figure 2.11 shows the representative EBSD phase maps corresponding to various local strain levels in this alloy with different fine grains [102]. The transformation from FCC to the HCP phase, obviously, is the primary deformation mechanism in all of these grainrefined alloys [102]. However, the values observed for the retained FCC phase fraction at a certain local strain level in different alloys differ, suggesting deviations in FCC phase stability among these alloys [102]. Due to the dual effects of FCC grain boundary on HCP phase: providing the prime nucleating sites and suppressing the growth of HCP phase due to the blocking effect of grain boundaries and back-stresses, the variation phase friction of HCP phase is not linear with the reduction of the FCC grain size, indicating FCC grain size on the martensitic transformation during quenching depends on a variety of mechanisms [102]. Niendorf et al. [103] reported, during the fatigue testing, phase fractions change more significantly in the same TRIP-Fe<sub>50</sub>Mn<sub>30</sub>Co<sub>10</sub>Cr<sub>10</sub> HEA with fine grained (~ 5 μm) than coarse grained (~ 10 μm). Meanwhile, the grain size reduction can enhance the stability of the FCC phase grains against deformation-driven transformation, resulting in a more uniform distribution of the  $\gamma$  (FCC)  $\rightarrow \epsilon$  (HCP) transformation zones [19]. Meanwhile, considering the situation of variable grain size with similar HCP phase friction in Fe<sub>50</sub>Mn<sub>30</sub>Co<sub>10</sub>Cr<sub>10</sub> before load, the tensile properties, including yield strength, ultimate tensile strength, and elongation, increase with the decrease of average grain size, because of the Hall-Petch effect [102].

## 2.3.3 Outcome of phase transformation

Deformation-induced phase transformation in the high-entropy alloy (HEA) has been reported to overcome the strength-ductility balance [19, 89]. Phase transformation introduces significant strain-hardening effect by effective strain/stress partitioning and the interface between matrix and HCP phases and promotes continuous plastic deformation in the matrix. In particular, the dislocation motion is inhibited at the interface between matrix and HCP phases, which realizes high work hardening capacity and, accordingly, superior uniform elongation [19]. The high fraction of the metastable phase in the matrix results in a significant TRIP effect [99]. Some factors, like chemical composition, grain size, and thermal process, are associated with affecting the metastability of the matrix phase [19, 73, 89, 102]. Indicating proper changing in the parameters, new deformation-induced transformation HEAs with excellent mechanical properties can be achieved.

## 2.4 Deformation mediated jointly by twining and phase transformation

#### 2.4.1 Deformation mechanism

Among the aforementioned deformation mechanisms, the activation of mechanical twinning and phase transformation has been reported to effectively enhance strain hardening of HEAs without strength-ductility trade-off. Consequently, new HEAs with jointly twinning and phase transformation, giving rise to an excellent combination of strength and ductility, are developed, bringing a great challenge to deep understand the work-hardening mechanism [104]. Table 2.3 summarizes the HEAs with jointly twinning and phase transformation. When focusing on the deformation mechanism on both phases in TRIP-DP-Fe<sub>50</sub>Mn<sub>30</sub>Co<sub>10</sub>Cr<sub>10</sub> alloy, in terms of the FCC phase in this dual-phase alloy, the deformation-stimulated martensitic transformation is the dominate deformation mechanism [Figure 2.12(a)], while the deformation-induced twinning is dominated in HCP phase [Figure 2.12(b)][19]. Wang et al. [105] unraveled the mechanisms of phase transformation and mechanical twinning in a model interstitial high-entropy alloys (iHEAs) with a nominal composition of Fe-30Mn-10Co-10Cr-0.5C (at. %) and their effects on strain hardening through analyzing interrupted in-situ and full in-situ tensile tests in a scanning electron microscope (SEM) combining electron channeling contrast imaging (ECCI) and electron backscatter diffraction (EBSD) techniques. A schematic sketch of microstructure evolution with straining in the iHEA is provided in Figure 2.13, including the deformation-driven phase

transformation and mechanical twinning, where black arrows point in the direction of increasing strain [105]. The FCC  $\gamma$  grains and a small portion of thermally-induced HCP  $\epsilon$  phase (~0.2%) [Figure 2.13(a)] are observed in the undeformed state. Upon straining, SFs form along {111}//TA planes in the metastable FCC  $\gamma$  grains [Figure 2.13(b)], which expand and multiple inside localized microbands with the increase of strain, leading to a continuous decrease in the spacing among them [Figure 2.13(c)] [105]. After 10%–14% strain, the intrinsic HCP ε nucleation due to the overlap of SFs inside the microbanded regions reaches a critical density [Figure 2.13(d)], which are then formed within each individual microband [Figure 2.13(e)] [105]. The deformation-induced ε phase grows into the adjacent deformed  $\gamma$  grains and simultaneous formation of new  $\varepsilon$  lamellae along the microbands takes place with further strain. Besides phase transformation, mechanical twinning is also active during the deformation process [Figure 2.13(d)] [105]. Recently, Fu et al. [104] have uncovered the tensile deformation mechanism evolution in the FCC-to-HCP transformationinduced plasticity high entropy alloy (TRIP-HEA) utilizing the real-time in situ neutron diffraction. The state-of-art neutron diffraction technique offer the great opportunity to obtain the FCC phase fraction evolution during the plastic deformation, shown in Figure 2.14, which can provide direct evident for the FCC-to-HCP transformation. Four deformation stages, corresponding to elastic, TRIP + Slip, TRIP + Slip + single twin, and TRIP + Slip + multiple twin, are TRIP + Slip + single twin, are determined by stress redistribution at the aforementioned critical mechanism transition load points [104]. The combination of easily triggered persisting TRIP with the work-hardening potential of the HCP through twinning and dislocation slip contributes the continuous work-hardening of HEAs, compared with single phase HEAs [104].

### 2.4.2 Simultaneous triggering of twinning and phase transformation

#### 2.4.2.1 Compositional tailoring

We have a brief picture of the chemical compositions on the TRIP and TWIP effect in HEAs. Along a similar line, a novel strategy for designing a joint activation of twinning- and transformation-induced plasticity by incorporating additional interstitial elements to tune the stacking fault energy in a TRIP-assisted HEA was reported [102, 105]. For example, Li et al. [102] have designed a new HEA incorporating the additional interstitial element, C, by tuning the matrix phase's instability in a metastable TRIP-assisted dual-phase Fe<sub>50</sub>Mn<sub>30</sub>Co<sub>10</sub>Cr<sub>10</sub>HEA. Although the addition of C actually increases the stacking fault energy in the Fe<sub>49.5</sub>Mn<sub>30</sub>Co<sub>10</sub>Cr<sub>10</sub>Co<sub>.5</sub> (at%) alloy

and result in the reduce of metastability driven TRIP effect, resulting in the FCC phase has higher stability that in the Fe<sub>50</sub>Mn<sub>30</sub>Co<sub>10</sub>Cr<sub>10</sub> (at%) alloy [102], this new interstitial TWIP-TRIP-HEA exhibits a twice tensile strength and identical ductility compared to a single-phase HEA with similar composition incorporating, TWIP effect, TRIP effect, substitutional and interstitial solid solution strengthening, and grain boundary and interface strengthening [102].

### 2.4.2.2 Thermo-mechanical processing

The sequence or respectively overlap in the activation of TRIP and TWIP effect, concurrent with dislocation slip, depends not only on the loading process but also on the microstructures. Su et al. [106] demonstrated a novel approach of utilizing a hierarchical microstructure design to improve the mechanical properties of an interstitial carbon doped high-entropy alloy (iHEA) by cold rolling and subsequent tempering and annealing. Two different microstructures are obtained in Fe<sub>49.5</sub>Mn<sub>30</sub>Co<sub>10</sub>Cr<sub>10</sub>C<sub>0.5</sub>, as shown in Figure 2.15 [106]. After tempered treatment, the samples contain bimodal microstructures consisting of nano-grains (~ 50 nm) near the shear bands and the recovered parent grain (10-35 µm) with pre-existing nano-twins, yielding a superior yield strength of 1.3 GPa, owing to the presence of nano-sized grains and nano-twins [106]. And trimodal microstructure is obtained by partial recrystallization (annealing), characterized by small recrystallized grains (<1 μm) associated with shear bands, medium-sized grains (1-6 μm) recrystallized through subgrain rotation or coalescence of parent grains, and retained large unrecrystallized grains [106]. The ductility in trimodal is significantly improved to 4.3 times that in bimodal owning to a multi-stage work hardening behavior related to the sequential activation of TRIP and TWIP effect combined with the grain size effect on the phase stability [106]. Consequently, the above instance gives proof that microstructure tuning through thermoprocessing can give rise to a wide range of mechanical properties for HEAs.

#### 2.4.2.3 Grain size effect

According to the aforementioned discussion, both deformation mechanisms are grain-size dependent [66, 102]. The smaller FCC grain size increases the mechanical stability against deformation-induced phase transformation [19] and weakens the activation of deformation twinning [77]. Su et al. [106] observed the large grain size hierarchy in 49.5Fe-30Mn-10Co-10Cr-0.5C can lead to a wide variation in phase stability, giving rise to the sequential activation of TRIP and TWIP effect, contribute the strain hardening sequence in with the trimodal structure. Owing

to the individual grain size dependence of the activation of the TRIP and TWIP effect in HEAs, strain hardening concurrent with excellent combinations of strength and ductility can be tuned and adjusted over the entire deformation range by appropriate microstructure design.

#### 2.4.3 Outcome

The new design approach introducing jointly mechanical twining and phase transformation has open a broader window for achieving excellent mechanical properties for HEAs. Tuning compositional variations, microstructure, and phase stability can tailor the sequence or respectively overlap in the activation of TRIP and TWIP effect, leading to the significant strength hardening and excellent combination of strength and ductility [102, 106]. A new interstitial TWIP-TRIP-HEAs associated with multiple deformation mechanisms has successfully developed [105, 106], which provides promising guidance for the future HEAs design.

## 2.5 Deformation mediated by stacking faults

### 2.5.1 Staking fault-controlled deformation

Stacking faults (SFs) are considered as an important crystal defect impacting on mechanical behavior. Similar to grain size refinement, the spacing between SFs can be regarded as the mean free path for dislocation movement, improving the strength of alloys, due to the development of intersecting stacking fault bands [107]. And the SFs can prevent the planar dislocation glide, resulting in the cross slip of dislocation and high work hardening rate. Huo et al. [107] proposed the dominant deformation mechanism in CoCrFeNi alloy shifted from the dislocation motion at the lower strain rates to stacking faults at the higher strain rates. Tong et al. [88] reported in the precipitation-strengthened FeCoNiCrTi<sub>0.2</sub> alloy, the dominated deformation mechanism is SFs controlled mode at 77 K. Figure 2.16 shows the evolution of deformation defects in the by TEM after interrupted tensile tests at 77 K. The appearance of SFs [Figure 2.16(a)] at the early deformation stage and at 77 K prevents the planar dislocation glide, resulting in the cross slip of dislocations and high work hardening rate at cryogenic temperatures. With the increase of strain, the intersecting SFs are formed [Figure 2.16(b)], which further confines the direction of the dislocation motion and makes an extra contribution to the work hardening, followed by the forming of a defect network by intersecting multiple-layered SFs (i.e., SF bundles) and hierarchical SFs at different length scales [Figure 2.16(c) and (d)]. Meanwhile, some hierarchical structure of SFs are

observed [Figure 2.16(d)] with the primary SFs running from the top left to the bottom right corner and the secondary SFs oriented at an angle of  $\sim 70^{\circ}$  with respect to the primary SFs [88].

## 2.5.2 Stacking faults mediated TWIP and TRIP effect

It should be pointed out SFs, usually occurs with concurrent dislocation slip, phase transformation, and twinning in the constituent phase. The deformation mode in HEAs is mainly determined by the value of the SFE which depends not only on the number of elements but also on the chemical compositions in multi-element alloys. The planar slip is favored the decreasing SFE, which promotes the formation of partial dislocation associated with the cross slip activation barrier [108]. The intrinsic stacking fault energy (ISFE) is one of the essential parameters in determining the competition between the gliding of dislocations and twinning [73]. At higher stacking fault energies, deformation is controlled by dislocation glide whereas at very low stacking fault energies deformation twinning is favored [73]. The SFEs of some previous reported HEAs are listed in Table 2.4. Miao et al. [109] found the deformation twinning can occur in CoCrNi ternary alloy with the increasing strain at both room temperature and cryogenic temperature, due to the low stacking fault energy of CrCoNi alloy (22  $\pm$  4 mJ/m<sup>2</sup> [110]). The appearance of deformation twins at room temperature deformation in twinning-induced non-equiatomic Fe<sub>40</sub>Mn<sub>40</sub>Co<sub>10</sub>Cr<sub>10</sub> high entropy alloy indicates a lower SFE compared to the FeMnNiCoCr alloy  $(30 \pm 5 \text{ mJ/m}^2 \text{ [111]})$  where no deformation twins were observed at room temperature [47]. Meanwhile, SFE relates to phase transformation, as the low ISFE favors the phase transformation from the FCC phase to the HCP phase [112]. The overlap of SFs along {111} planes within microbands leads the embryo of the HCP phase in the TRIP assisted HEAs. Meanwhile, the interaction between the SF and the twin boundary leads the formation of HCP stacking along the twin boundary which may provide sites for the growth of the HCP phase [109]. Figure 2.17 presents results obtained from the direct coupling of deformation and phase transformation from FCC γ to HCP ε observed at different strain levels in the Fe<sub>49.5</sub>Mn<sub>30</sub>Co<sub>10</sub>Cr<sub>10</sub>Co<sub>.5</sub> alloy by interrupted *in-situ* testing [105]. Upon tension, the density of SFs increases [Figure 2.17(b<sub>1</sub>)-(b<sub>3</sub>)] and the HCP ε phase forms in the deformed structure [Figure 2.17(a<sub>3</sub>)] at 14% strain [105]. The SFs form along {111} planes (black lines) and are accompanied by {111} slip traces (red lines) [105]. Huang et al. [113] proposed that the SFE in FeCrCoNiMn HEA should be less than ~ 21 mJ/m<sup>2</sup> for the activation of the TWIP effect, while the TWIP-TRIP boundary somewhere close to  $8 \text{ mJ/m}^2$ .

## 2.5.3 Tuning stacking fault energies

A great number of theoretical studies have been focused on the investigation of realizing low SFEs in HEAs. Zaddach et al. [114] investigated the SFEs for a series of equiatomic and nonequiatomic alloys ranging from pure Ni to CoCrFeMnNi based on the combination of ab initio calculations of elastic moduli and experimental data, some of which show even better than conventional low SFE alloy, revealing the tunability of SFEs through proper alloy composition. And Bhattacharjee et al. [115] proposed that Suzuki mechanism doesn't work in HEAs due to the whole-solutes matrix and no segregation of solutes. The low SFEs value in HEAs originates from the combined effect of the high energy level of the distorted matrix and the in situ decreased strain energy by adjustment of solute atoms in the stacking faults. While Patriarca et al. [50] studied the role of solute segregation effects, which emphasized the Suzuki mechanism, on the SFE by firstprinciples calculations and claimed that the presence of Co atoms gathered near the stacking fault reduced the SFE by almost 55% (from 38 mJ/m<sup>2</sup> to 17 mJ/m<sup>2</sup>), compared to the presence of Co atoms away from stacking faults. Through employing first-principles calculations, Zhang et al. [116] claimed that the negative SFEs of FCC CrNiCo and FeCrNiCo alloys came from the thermodynamic metastablility of FCC stacking sequence and heavily influenced by the local atomic environment. The negative values of stacking fault energies, predicted by simulations of FCC HEAs, explain the twinning deformation mode in metastable alloy [116]. Rao et al. [55] and Zeng et al. [117] also found the fluctuation of SFE depends on the local composition of alloys. Figure 2.18(a) gives a picture of the variation of the stacking fault width along the dislocation line [117]. The extended edge dislocation tends to remain in lower SFE regions with applied stress, which means these zones serve as obstacles to hinder the dislocation motion and increase the critical stress [117]. The relationship between critical stress increment,  $\Delta \tau_c$  the minimum applied stress for extended dislocations glide, and the stacking fault region size for  $\gamma = 35.0 \, mJ/$  $m^2$ , 84.7  $mJ/m^2$ , and 127.1  $mJ/m^2$  with  $\sigma_{\gamma} = 12 \, mJ/m^2$  is exhibited in Figure 2.18(b) [117]. The maximum region of  $\Delta \tau_c$  for each SFs region size indicates the strengthening has a maximum when the particle size is closed to the stacking fault width inside the particles [117].

## 2.6 Effect of short-range fluctuation

## 2.6.1 Short-range ordering

It should be pointed out multiple principle elements in HEAs have introduced short-range, medium-range, and long-range stress fields. Wu et al. [118] illustrated that the short-range effects contribute to this process for the alloy with very low activation volumes, due to the short-range lattice distortion may lead to local fluctuations on the long-range lowing. Li et al. [119] have proposed that lattice friction to dislocation motion has a significant relationship with short-range ordering (SRO) in CoCrNi alloy. Ding et al. [120] also point out the SRO can be tuned through proper design high-entropy alloy system and processing conditions, affecting the stacking-fault energy. Zhang et al. [121] firstly observed the SRO in CoCrNi alloy using high resolution and energy-filtered transmission electron microscopy and quantify the relationship between the degree of SRO and mechanical properties in this alloy. Figure 2.19 shows energy-filtered diffraction patterns and dark-field (DF) images in CoCoNi alloy after aging treatment at 1000 °C for 120 hours. The dark field imaging, in Figure 2.19(a), taken with the objective aperture positioned in the center of the streaked region directly image the SRO domains [121]. It is known that the formation of SRO has a significant impact on dislocation plasticity, where an increasing degree of SRO tends to promote planar slip [47]. Instead of Shockley partial dissociation of perfect dislocation cores leading to planar slip in FCC materials, the SRO is proposed to be the origin of localized planar slip and dislocation pairs. Recently, Zhang et al. [121] observed SRO in CoCrNi alloy using energy-filtered transmission electron microscopy, and reported the increasing degree of SRO tends to increase the planarity of dislocation slip and promote the planar dislocation arrays. Compared with a random distribution of dislocations in the water-quenched CoCrNi alloy without SRO, a marked trend of localized planar configuration of dislocations was present in the 1,000 °C aged CoCrNi alloy with SRO (Figure 2.20). Meanwhile, SRO is reported not only to affect the plastic deformation but also the elastic performance due to the local bonding environment [121].

#### 2.6.2 Concentration waves

Recently, Ding et al. [122] reported the element distributions in the CrFeCoNiPd alloy exhibit strong inhomogeneous fluctuations with local aggregations in the form of concentration waves. Due to the largest electronegativity of Pd, the introducing Pd promotes aggregations all five elements, resulting in pronounced chemical inhomogeneities in this alloy, hence leading to

the non-uniform distribution of lattice strain due to mismatch of atomic sizes. The concentration waves are characterized as wavelength as small as 1–3 nm in the CrFeCoNiPd alloy, developing through the competing action of lattice strains and concentration gradients on the system energy [123]. The inhomogeneous element distribution has an importance effect on the microscopic deformation mechanisms. Full dislocations  $\frac{1}{2}$ <110>{111} are dominated in the CrFeCoNiPd alloy at room temperature deformation, in contrast with the combine of full dislocation  $\frac{1}{2}$ <110>{111} and partial dislocation  $\frac{1}{6}$ <112>{111} in CoCrFeMnNi alloy. In addition, pronounced concentration fluctuations in the CrFeCoNiPd alloy lead to considerable pinning effect on dislocation motion and modify the local value of stacking fault energy in the dislocation core, therefore, resulting in frequent cross-slip in the pile-up owing to the high resistance to the motion of dislocations on the primary slip plane. Hence, the formation of concentration waves and associated deformation mechanisms introduce an excellent combination of strength, strain hardening, and ductility in the CrFeCoNiPd alloy.

## 2.7 Summary and outlook

This chapter provides a rough picture of the deformation mechanisms in HEAs. The dislocation motion in HEAs is quite similar to typical metals and alloys [47, 49]. However, the nature of multicomponent in HEAs has introduced some unique features, i.e. the short-range concentration fluctuation, leading to quite different characters [51, 53, 58]. The low stacking fault energy (SFE) in these FCC structured HEAs results in the widely dissociated dislocations and extensive dislocation reactions [54, 55], while the motion of screw dislocation is dominated in plastic deformation in the BCC structured HEAs [57, 58]. Meanwhile, the activation of TRIP and TWIP effect, concurrent with dislocation slip, depends not only on the loading process but also on the microstructures, i.e. chemical composition, grain size, which overcome the strength-ductility balance and introduce significant strain-hardening effect in the high-entropy alloy (HEA) [19, 47, 53, 64-66, 69-71, 73, 89, 102]. Alloy strategy focusing phase metastability instead of phase stabilization and single phase in HEAs is significant importance in developing new alloys with excellent strength-ductility combination. In addition, incorporating short-range fluctuation, e.g. SRO and concentration waves, by tuning compositions can produce new deformation mechanisms and mechanical properties in HEAs. Figure 2.21 shows the exceptional strength-ductility combination of these TRIP/TWIP-TRIP-HEAs [102]. The materials exhibit excellent strength, dutility, and damage tolerance, characterized in terms of total elongation multiplied by ultimate tensile strength, exceeding that of most metallic materials [102].

In order to design new HEAs with excellent mechanical properties, several efforts still need to be done. First, compared with the extensive study TWIP effect on HEAs, the TRIP effect in HEAs has not been systematically studied. And the investigation on mechanical twinning in HEAs is focused on the Co-Cr-Fe-Mn system with FCC structure. Further systematic investigation in the HEAs with BCC structure and other FCC alloy systems should carefully proceed. Second, advanced characterization methods and modeling, e.g. in-situ neutron and synchrotron diffraction, high-resolution transmission-electron microscopy (HRTEM), atomic-scale mapping of chemical distribution and associated correlation analysis, density functional theory (DFT) and molecular-dynamic (MD) calculations, are needed to reveal the deformation mechanisms of HEAs at the micro- and atomic- level and optimize alloy design. Third, alloy strategy, making the utmost of affecting factors associated with affecting the TRIP and TWIP effect in HEAs, including chemical composition, grain size, and thermal process, should be well extensively investigated and developed, which can shed light on the alloy design for future application.

# **Table Captions**

- **Table 2.1** High-entropy alloys reported with twining-mediated deformation.
- Table 2.2 High-entropy alloys reported with phase-transformation assisted deformation.
- **Table 2.3** High-entropy alloys reported with both twinning and phase transformation.
- Table 2.4 Stacking fault energy (SFE) of the high-entropy alloys obtained by various techniques.

## **Figure Captions**

- Figure 2.1 TEM image of the deformed (CoCrNi)<sub>94</sub>Al<sub>3</sub>Ti<sub>3</sub> medium-entropy alloy, indicating planar slip of dislocations along with intersecting slip lines in two different {111} planes [48].
- Figure 2.2 Lomer-Cottrell (LC) junctions (e.g., the one marked by an arrow) formed on two {111} slip plane intersections in the Al<sub>0.1</sub>CoCrFeNi high-entropy alloy [49].
- Figure 2.3 Schematics showing the changes in the arrangement of neighboring atoms caused by an edge dislocation slip in the face-centered-cubic crystal lattices of (a) a dilute solid solution and (b) a high-alloy system, respectively. Local Peierls potential energy profiles around a dislocation segment are schematically illustrated for the (c) dilute system and (d) high-alloy system [52]. Distributions of the average potential energies in the (e) dilute system and (f) high-alloy system, which were obtained by averaging the local potential energies shown in (c) and (d) along the dislocation line [52].
- Figure 2.4 Deformation micro-mechanisms in the hierarchical AlCoCrFeNi<sub>2.1</sub> high-entropy alloy with the increasing tensile strain [62].
- Figure 2.5 TEM micrographs showing the evolution of twins with true tensile strain at 77 K in the FeNiCoCrMn alloy [65]. (a) Both figures are bright-field images. (b-e) Figures on the left are bright-field images while those on the right are dark-field images. The dashed rectangles in the left column delineate areas that are magnified in right column.
- Figure 2.6 Bright-field TEM image showing the hierarchical twinning architecture in a grain of the CrCoNi alloy [83]. A grain boundary (GB) is marked by the yellow line near the top-left corner.
- Figure 2.7 Twin-twin interactions in the FeCoCrNi alloy introduced by high-pressure torsion (HPT) [84]. (a) HRTEM image showing three incident twins (T2, T3, and T4) in the same direction interacting with one barrier twin (T1) and triggering the formation of T5 and T6 twins (twin boundaries highlighted by white lines). (b)

Fourier filtered image of the framed part in (a), showing plenty of dislocations (marked with white "T") and an Lomer-Cottrell (LC) lock (indicated by five red spots). [84]

- Figure 2.8 EBSD phase maps of the dual-phase  $Co_{20}Cr_{20}Fe_{34}Mn_{20}Ni_6$  alloy deformed at room temperature [90], reflecting the deformation-induced martensitic transformation as a function of deformation. The local strain,  $\varepsilon_{loc}$ , of (a) 20%, (b) 40%, (c) 60% and (d) 90% correspond to the early, medium and late uniform deformation and postnecking stages, respectively.
- Figure 2.9 In-situ SEM observation reveals the martensitic phase transformation process in the Ta<sub>0.5</sub>HfZrTi alloy during continuous loading [89].
- Figure 2.10 XRD patterns and EBSD images of the as-cast Ta<sub>x</sub>HfZrTi (x = 1, 0.6, 0.5, and 0.4) alloys [89]. The Ta concentration significantly influences the phase constitution of this alloy system, rendering either single (bcc) or dual-phase (bcc + hcp) structure [89]. The decrease of the Ta content destabilizes the bcc matrix and promotes the formation of the hcp phase.
- Figure 2.11 Representative EBSD phase maps showing the microstructural evolution with the increasing local strain,  $\varepsilon_{loc}$ , of the dual-phase Fe<sub>50</sub>Mn<sub>30</sub>Co<sub>10</sub>Cr<sub>10</sub> alloy with different fcc grain sizes and initially available hcp phase fractions: (a<sub>1-4</sub>) 4.5  $\mu$ m/32%; (b<sub>1-4</sub>) 6  $\mu$ m/14% and (c<sub>1-4</sub>) 15  $\mu$ m/31% [102].
- Figure 2.12 The deformation in the Fe<sub>50</sub>Mn<sub>30</sub>Co<sub>10</sub>Cr<sub>10</sub> alloy accommodated by phase transformation and twining [19]. (a) EBSD phase maps revealing the deformation-induced martensitic transformation as a function of deformation, with  $\varepsilon_{loc}$  and TD denoting the local strain and tensile direction, respectively. (b) ECCI analyses showing the evolution of defect substructures in the fcc and hcp phases, where the deformation-induced twinning is dominated in the hcp phase. g is the diffraction vector,  $\gamma$  is the fcc phase, and  $\varepsilon$  is the hcp phase.
- Figure 2.13 Schematic sketch of microstructural evolution with straining in an interstitial highentropy alloys [105]. Black arrows point in the direction of increasing strain values.

- Figure 2.14 The dynamic evolution of the fcc phase fraction under tension in the TRIP-HEA Fe<sub>50</sub>Mn<sub>30</sub>Co<sub>10</sub>Cr<sub>10</sub> [104].
- Figure 2.15 Schematic showing the thermomechanical processes for producing the bimodal and trimodal microstructures in the Fe<sub>49.5</sub>Mn<sub>30</sub>Co<sub>10</sub>Cr<sub>10</sub>C<sub>0.5</sub> alloy [106].
- Figure 2.16 Bright-field TEM images of dislocation structures and stacking faults (SFs) in the precipitation-strengthened FeCoNiCrTi<sub>0.2</sub> alloy after deformed to a true strain of ~2.5% (a), ~10% (b) and ~36% (c) at 77 K [88]. The inset in (c) is a SAED pattern of the region in the red circle. (d) HRTEM image of the blue region in (c). (a) is taken under the two-beam condition to see dislocations, and (c–d) are taken along the zone axis of [011] to observe intersecting stacking faults.
- Figure 2.17 Interrupted in-situ EBSD and ECCI observations of deformation and phase transformation at varying strain levels in the interstitial Fe<sub>49.5</sub>Mn<sub>30</sub>Co<sub>10</sub>Cr<sub>10</sub>Cc<sub>0.5</sub> high-entropy alloy [105]. (a) Overlay of phase map with image quality map. (b) ECC images.
- Figure 2.18 (a) Schockley partials revealed by theoretical calculations [117]. Left: the relaxed dislocation configuration at zero stress. Right: the dislocation configuration at an applied stress of 195 MPa. (b) The critical stress increment,  $\Delta \tau_c$ , as a function of the stacking fault region size d [117]. The stacking fault energies are chosen randomly from uniform distributions.
- Figure 2.19 Short-range ordering observed in the CoCrNi alloy [121]. (a) Energy-filtered diffraction pattern taken from the sample aged at 1000 °C. The line plot shows the periodic intensity of the "diffuse superlattice" streaks. (b) Energy-filtered dark-filed image taken from the 1000 °C aged sample. (c) Typical high-resolution TEM image and the associated FFT image of the 1000 °C aged sample, where superlattices are marked by the white circles and the associated streaking along the {111} direction is marked by the white arrows in the FFT image.

- Figure 2.20 Dislocations in the water-quenched and 1,000 °C aged CoCrNi samples [121]. (a) Two-beam bright-field image, showing the representative wavy configuration of dislocations in the water-quenched sample. (b) Two-beam bright-field image, showing the representative planar configuration of dislocations in the 1,000 °C aged sample, with the leading dislocation pair indicated by the white arrow.
- Figure 2.21 Strength-ductility profiles of various classes of metallic materials including highentropy alloys [102].

#### 3 Strengthening mechanisms

Like other polycrystalline metals and alloys, HEAs derives their basic strengths from the intrinsic lattice resistance to dislocation motion (i.e., lattice friction), and additional strengths from various incremental strengthening mechanisms. The yield strength ( $\sigma_y$ ) of a HEA is then the summation of the lattice friction stress ( $\sigma_{fr}$ ) and the contributions from all other strengthening mechanisms, including solid solution strengthening ( $\Delta\sigma_{ss}$ ), dislocation strengthening deduced from pre-existing dislocations ( $\Delta\sigma_{\rho i}$ ), grain boundary strengthening ( $\Delta\sigma_{gb}$ ), precipitation strengthening ( $\Delta\sigma_{ppt}$ ), twin boundary strengthening ( $\Delta\sigma_{tb}$ ), and phase-transformation induced strengthening ( $\Delta\sigma_{pht}$ ). Thus, the overall yield strength of an alloy is written in an additive form as follows

$$\sigma_{y} = \sigma_{fr} + \Delta \sigma_{ss} + \Delta \sigma_{\rho i} + \Delta \sigma_{gb} + \Delta \sigma_{ppt} + \Delta \sigma_{tb} + \Delta \sigma_{pht}, \tag{3.1}$$

Among these strength contributions,  $\sigma_{fr}$ ,  $\Delta\sigma_{ss}$ ,  $\Delta\sigma_{\rho i}$ , and  $\Delta\sigma_{gb}$  are normally present in all polycrystalline alloys, whereas  $\Delta\sigma_{ppt}$ ,  $\Delta\sigma_{tb}$ , and  $\Delta\sigma_{pht}$  can only arise in certain carefully tailored alloys.  $\Delta\sigma_{ss}$  can be further subdivided into substitutional solid solution strengthening,  $\Delta\sigma_{sss}$ , and interstitial solid solution strengthening,  $\Delta\sigma_{iss}$ .  $\Delta\sigma_{sss}$  in HEAs is oftentimes smeared into  $\sigma_{fr}$  due to indistinguishable solvents and solutes in certain alloys.

These strengthening mechanisms may not necessarily all exist in a single HEA. Depending on the alloy design strategy adopted, a certain combination of strengthening mechanisms may collectively contribute to the yield strength of a HEA in addition to the friction stress,  $\sigma_{fr}$ . For instance, the strength of the (FeCoNiCr)<sub>94</sub>Ti<sub>2</sub>Al<sub>4</sub> HEA is a combined effect of  $\sigma_{fr}$ ,  $\Delta\sigma_{ss}$ ,  $\Delta\sigma_{\rho i}$ ,  $\Delta\sigma_{gb}$ , and  $\Delta\sigma_{ppt}$  [124].  $\sigma_{fr}$ ,  $\Delta\sigma_{ss}$ ,  $\Delta\sigma_{\rho i}$ ,  $\Delta\sigma_{gb}$ , and  $\Delta\sigma_{tb}$  all contribute to the strength of the nanocrystalline fcc AlCoCrCuFeNi alloy [125]. In what follows, the lattice friction and each of the major strengthening mechanisms that have been reported in HEAs will be discussed in detail.

#### 3.1 Lattice resistance

A clear distinction between the solvent lattice and solute atoms exists in dilute alloys. Due to the low concentration of solute atoms, the lattice resistance to dislocation motion in these alloys is exclusively from the solvent lattice. Solute atoms, on the other hand, contribute to solid solution strengthening by interacting with moving dislocations. The lattice resistance landscape, however, becomes different when coming to concentrated HEAs due to the nonexistence of an unambiguous

division between the solvent and solute atoms. In concentrated HEAs, all alloying elements are intermixed and distribute randomly over all lattice sites. Because of element size mismatch, the random distribution of these alloying elements naturally creates a significant lattice distortion – one of the four "core effects" in HEAs [20]. It is expected that the lattice distortion increases with the increasing number of constituent elements [24]. Thus, the lattice resistance in concentrated HEAs originates from the distorted lattice, which essentially is the summation of the resistance from the base lattice composed of a single element specie and the lattice distortion after substituting the base element for other element species. Since the random distribution of substitutional elements creates a nearly uniform lattice distortion across the full material domain, the lattice resistance in concentrated HEAs can be viewed as the average resistance from all constituent elements incorporating the "substitutional solid solution strengthening" [53].

It is, therefore, anticipated that the lattice resistance of a concentrated HEA is correlated with the lattice distortion it encompasses. It is indeed justified that a linear relationship between the lattice distortion ( $\delta^*$ ) and the lattice friction stress ( $\sigma_{fr}$ ) or lattice distortion stress ( $\Delta\sigma_{fr}$ ) exists in a series of fcc-structured and bcc-structured equiatomic solid solution alloys [126, 127], as illustrated by  $\Delta\sigma_{fr}/E$  versus  $\delta^*$  in Figure 3.1, where E is the Young's modulus. Here, the lattice distortion is characterized as

$$\delta^* = (a - a_0)/a_0, \tag{3.2}$$

where a is the lattice constant of the equiatomic alloys,  $a_0$  is the lattice constant of the base pure metal based on which the equiatomic alloys are constructed, i.e., Ni for the fcc alloys and Nb for the bcc alloys. The lattice distortion stress is calculated from

$$\Delta \sigma_{fr} = \sigma_{fr} - \sigma_{fr,0},\tag{3.3}$$

where  $\sigma_{fr}$  is the friction stress of the equiatomic alloys, and  $\sigma_{fr,0}$  is the friction stress of the base pure metal, i.e., Ni for the fcc alloys and Nb for the bcc alloys.  $\sigma_{fr}$  and  $\sigma_{fr,0}$  are all calculated from

$$\sigma_{fr} = \sigma_y - \Delta \sigma_{\rho i} - \Delta \sigma_{gb}, \tag{3.4}$$

where  $\sigma_y$  is the yield strength of the alloy,  $\Delta \sigma_{\rho i}$  and  $\Delta \sigma_{gb}$  are the strength increments from dislocation strengthening and grain boundary strengthening, respectively.  $\sigma_{fr}$  may also be obtained from the rule of mixtures of constituent elements [125, 128] or Hall-Petch analyses which will be discussed shortly in Section 3.4.

Overall, the linear relation for the bcc equiatomic alloys in Figure 3.1 exhibits a larger slope than that in the fcc counterparts, indicating that the former possesses a greater lattice distortion and lattice friction than the latter. As in many other alloys, the lattice friction in concentrated HEAs may still be described by the Peierls-Nabarro stress given below [53, 126, 129]

$$\tau_{fr} = \frac{2G}{1-\nu} exp\left(\frac{-2\pi w_d}{b}\right),\tag{3.5}$$

where G is the shear modulus,  $\nu$  is the Poisson's ratio,  $w_d$  is the dislocation core width, b is the magnitude of the Burgors vector, and  $\tau_{fr}$  is the friction shear stress. The friction normal stress is then given as

$$\sigma_{fr} = M\tau_{fr},\tag{3.6}$$

where M = 3.06 is the Taylor factor converting the shear stress to the normal stress.

From Equation (3.5), it is clear that the dislocation width is one of the major factors that affect the lattice friction of alloys. The normalized dislocation widths of both the fcc and bcc alloys in Figure 3.1 are calculated reversely from Equations (3.5) and (3.6), i.e.,  $\frac{w_d}{b} = \frac{1}{2\pi} ln \left[ \frac{2MG}{\sigma_{fr}(1-\nu)} \right]$ , and their values are graphed in Figure 3.2. For both the fcc and bcc alloys, it is seen that the dislocation widths stabilize to an almost constant value after the number of principal elements exceeds three, specifically,  $\frac{w_d}{b} = 0.95 \pm 0.03$  for the bcc alloys and  $\frac{w_d}{b} = 1.33 \pm 0.04$ . For either fcc alloys or bcc alloys, the smaller dislocation widths in the tertiary or higher-order equiatomic alloys are indicative of higher lattice friction and more difficult dislocation glide in these alloys than those in the corresponding pure metal or binary alloys. Comparing the fcc with bcc alloys, the normalized dislocation widths of the latter is overall below those of the former. This is a clear indication that the lattice friction in the bcc alloys is greater than that in the fcc alloys, essentially consistent with the trend shown in Figure 3.1.

The dislocation width is also suggested to be temperature-dependent. Its dependence on temperature may be described by [53, 130]

$$\frac{w_d}{b} = \frac{w_{d,0}}{b_0} exp\left(\frac{T}{3T_m}\right),\tag{3.7}$$

where  $w_{d,0}$  and  $b_0$  are, respectively, the dislocation width and magnitude of the Burgers vector at 0 K, T is the temperature, and  $T_m$  is the melting temperature. The temperature dependence of the dislocation widths in a series of fcc equiatomic solid-solution alloys was analyzed by Wu et al. [53]

## 3.2 Solid solution strengthening

## 3.2.1 Substitutional strengthening

## 3.2.1.1 Experimental evaluation

Without resorting to any predictive models, substitutional solid solution strengthening may be evaluated by subtracting the strength of a substitutional alloy from its base alloy, after equating or removing all other strengthening effects in both alloys [87, 88]. For example, after approximately equating the Hall-Petch strengthening (by extrapolating to the identical grain size) and dislocation strengthening, the strength difference between the (CoCrNi)<sub>94</sub>Al<sub>3</sub>Ti<sub>3</sub> alloy at the solid-solution state and the CoCrNi is the solid solution strengthening effect caused by the substitutional Al and Ti solutes [87].

#### 3.2.1.2 Fleischer model

The Fleischer model, one of the very first models on substitutional solid solution strengthening in metallic alloys, built up on the assumption of low solute concentrations in alloys, in which one solute specie is considered to be in isolation from other solutes [131, 132]. It presumes strong pinning of isolated solute atoms to gliding dislocations as the source of solid solution strengthening as illustrated in Figure 3.3(a), and is applicable to dilute solution alloys. As HEAs fall into the category of concentrated solution alloys, the Fleischer model is not applicable in principle. This assertion is flawless when referring to equiatomic HEAs. Nonetheless, with approximate treatments certain non-equiatomic HEAs may be viewed as pseudo dilute alloys so that the Fleischer model become pertinent. For instance, the FeCoNiCr as a whole can be treated as the matrix in the (FeCoNiCr)<sub>94</sub>Ti<sub>2</sub>Al<sub>4</sub> [133] and FeCoNiCrT<sub>0.2</sub> [88] HEAs whereas other low-concentration elements are thought of as solutes. Also, the HfMo<sub>x</sub>NbTaTiZr HEAs may be viewed as a pseudo binary alloy with HfNbTaTiZr the matrix and Mo solutes [134].

The Fleischer model predicts the solid solution strengthening in dilute alloys as follow [88, 133, 135]

$$\Delta \sigma_{SSS} = \frac{MG\varepsilon_s^{3/2}c^{1/2}}{700},\tag{3.8}$$

where M=3.06 is the Taylor factor, G is the shear modulus of the matrix, C is the solute concentration in the molar fraction,  $\varepsilon_S$  is the solvent-solute interaction parameter considering the elastic modulus misfit,  $\eta_{em}$ , and atomic size misfit,  $\eta_{am}$ , defined as

$$\varepsilon_s = \left| \frac{\eta_{em}}{1 + 0.5\eta} - 3\eta_{am} \right|,\tag{3.9}$$

with  $\eta_{em} = \frac{dG}{dc} \frac{1}{G}$  and  $\eta_{am} = \frac{da}{dc} \frac{1}{a}$ , where a is the lattice constant of the matrix.

The Fleischer model has been loaned from dilute alloys to predict solid solution strengthening in certain non-equiatomic HEAs [88, 133, 135]. Nevertheless, the validity of the  $\Delta\sigma_{sss}\sim c^{1/2}$  relation was challenged in some other HEAs such as the HfMo<sub>x</sub>NbTaTiZr [134], MoxNbTiVZr [136], and Al<sub>x</sub>HfNbTaTiZr [137], where an approximately linear dependence of the yield strength increase,  $\Delta\sigma_y$ , on the solute concentration was suggested, as demonstrated in Figure 3.4 [134].

## 3.2.1.3 Labusch-type models

The Labusch model [138], a step forward to the Fleischer model, considers solute strengthening in alloys with a medium concentration of solute atoms (0 - 20 at.% mostly [139]). Due to the relatively high solute content, solute atoms no longer act isolatedly as pinning sites to gliding dislocations as in the Fleischer model. Instead, a forest of solute atoms constantly interact with and exert a friction effect on moving dislocations [131], causing a weak pinning effect as illustrated in Figure 3.3(b) [118]. The Labusch model for binary alloys takes the following form

$$\Delta \sigma_{sss} = Bc^{2/3},\tag{3.10}$$

where c is the solute concentration, and B is the hardening parameter depending on the alloy's shear modulus, G, the mismatch parameter,  $\epsilon_{mis}$ , and a constant, Z. B has a specific form of

$$B = 3ZG\epsilon_{mis}^{4/3},\tag{3.11}$$

where  $\epsilon_{mis}$  embodies the elastic misfit parameter,  $\eta'$ , and the atomic size misfit,  $\eta_{am}$ , and is expressed as

$$\epsilon_{mis} = (\eta'^2 + \alpha_{mis}^2 \eta_{am}^2)^{1/2},\tag{3.12}$$

where  $\alpha_{mis}$  is a constant and was suggested to take  $3 < \alpha_{mis} < 16$  for screw dislocations and  $\alpha_{mis} > 16$  for edge dislocations [140].  $\eta'$  is calculated as

$$\eta' = \frac{\eta_{em}}{1 + 0.5 |\eta_{em}|}.\tag{3.13}$$

To extend the Labusch model from binary alloys to multicomponent alloys, Toda-Caraballo et al. [131] adopted the following model proposed by Gypen and Deruyttere [141]

$$\Delta \sigma_{sss} = \left(\sum_{j}^{M} B_{j}^{3/2} c_{j}\right)^{2/3}, \tag{3.14}$$

where *M* is the total number of solutes in consideration. The application of the model in Equation (3.14) needs to construct a pseudo solvent, and then considers the additive strengthening effect of each solute species. For instance, FeNbV can be considered as the pseudo solvent while Cr as the solute in the (FeNbV)<sub>1-x</sub>Cr<sub>x</sub> HEAs [131]. Also, Ni may be considered as the solvent while Co and Cr as the solutes in the NiCoCr HEA [118]. Obviously, in such an additive strengthening model, the extensive solute-solute interaction in HEAs, as evidenced from the severe lattice distortion [2], is not taken into account. The failure of incorporating the lattice distortion in this strengthening model indeed caused large degrees of deviation of the predicted strengths from the experimental values in certain HEAs [131].

The consideration of the solute-solute interaction in solid solution strengthening may still start with the simplest case – binary alloys. In a highly concentrated binary alloys, the effect of the solvent i on the solute j can be as large as the effect of the solute j on the solvent i. To account for the interplay of the solvent and the solute in highly concentrated binary alloys, Toda-Caraballo modified the Labusch model into the following, conveniently adopting a matrix form [139]

$$\Delta \sigma_{sss}^{m} = 2Bc_{i}c_{j} = (c_{i}, c_{j})(0 B B 0)(c_{i} c_{j}),$$
(3.15)

where  $c_i$  and  $c_j$  are the solvent and solute concentrations, respectively.

Extending Equation (3.15) for binary alloys to highly concentrated multicomponent alloys such as HEAs gives

$$\Delta \sigma_{sss}^{m} = (c_{1}, ..., c_{n})(B_{11} \cdots B_{1n} : : : B_{n1} \cdots B_{nn})(c_{1} : c_{n}),$$
(3.16)

where n is the total elemental components contained in the alloy. In such a model, the solute-solute interaction (or lattice distortion) is embedded in the components of the matrix B. One can certainly calculate each component in B using the full set of equations, i.e., Equations (3.11) and (3.12). Nonetheless, given that  $\alpha_{mis}$  is normally taken a large value of 16 to accounts for a mixture of

edge and screw dislocations,  $\alpha_{mis}^2 \eta_{am}^2$  is much greater than  $\eta'^2$  in Equation (3.12). For this reason, Equation (3.12) may be simplified to

$$\epsilon = \xi \alpha_{mis} |\eta_{am}|, \tag{3.17}$$

Here an extra constant  $\xi$  is added to account for the difference in the activated slip systems in different crystal structures, taking 1 for fcc systems and 2 for bcc systems [139]. Combing Equations (3.11) and (3.17), the matrix B is written as [139]

$$B = (B_{11} \cdots B_{1n} : \because : B_{n1} \cdots B_{nn}) =$$

$$YG \left(\frac{\xi\beta}{a}\right)^{\frac{4}{3}} \left(0 \left|\frac{da}{c_1^2}\right|^{4/3} \dots \left|\frac{da}{c_n^2}\right|^{4/3} \left|\frac{da}{c_2^1}\right|^{4/3} 0 \dots \left|\frac{da}{c_2^n}\right|^{4/3} : \dots \because :$$

$$\left|\frac{da}{c_n^1}\right|^{4/3} \left|\frac{da}{c_n^2}\right|^{4/3} \dots 0\right),$$
(3.18)

where Y is a constant. Now the non-zero item in the matrix,  $\frac{da}{c_i^J}$ , reflects the change of the unit cell parameter by substituting an atom of type j for an atom of type i, namely, the lattice distortion.  $c_i^J$  is the new alloy composition after substituting an atom of type j for an atom of type i. For example,  $c_1^2 \equiv (c_1 - \eta_{am}c, c_2 + \eta_{am}c, ..., c_n)$  denotes the alloy composition after substituting an atom of type 2 for an atom of type 1, with  $\delta c$  being an infinitesimal amount of concentration variation. The calculations of both  $\frac{da}{c_i^J}$  and a requires the use of the interatomic spacing matrix  $S = \{s_{ij}\}$ , as detailed in [139].

The application of the model in Equation (3.16) to predicting the yield strengths of the single crystals of some HEAs and their subsystems is given in Figure 3.5. The prediction for the polycrystalline HEAs is given in Figure 3.6. In both cases, the predicted strengths align satisfactorily with the measured ones [139]. The relatively large deviation of some alloys from the diagonal line in Figure 3.6 is, in part, attributed to the Hall-Petch strengthening effect, which was not subtracted from the experimental strengths.

#### 3.2.1.4 First principles based models

Varvenne et al. [142] recently extended a solid solution strengthening model derived from first principles for dilute random alloys [143-146] to concentrated random alloys with an effective medium approximation, and applied it to predict the yield stress of single-phase HEAs [142, 146-

150]. Considering a *N*-component random fcc HEA with a concentration  $c_n$  for the  $n^{th}$  element  $(\sum_{n=1}^{N} c_n = 1)$ , an effective medium with average properties (e.g., elastic and lattice constants) of the true alloys is defined as the "matrix", and each elemental atom in the alloy is viewed as a "solute" embedded in it. This effective medium treatment is schematically illustrated in Figure 3.7(a) where an actual 3-component random HEA is given, and Figure 3.7(b) where the average "matrix" is formed with an embedded "solute" A at position  $(x_i, y_j, z_k)$ . Strengthening in an effective alloy as in Figure 3.7(b) arises from the interaction energies between the solutes and individual edge dislocations in the matrix, for example,  $U^A(x_i, y_j, z_k)$  for the interaction energy between the "solute" A and a dissociated edge dislocation. Since solutes are randomly distributed in the effective "matrix", spatial fluctuations in the solute concentration inevitably arise, a direct result of which is that dislocations are attracted to energetically favorable fluctuations but repelled by energetically unfavorable fluctuations. As a result, the initially straight dislocation is forced into a wavy configuration with a characteristic wavelength  $2\zeta_c$  and amplitude  $w_c$  to minimize the total energy of the entire alloy system. The wavy dislocation configuration is illustrated in Figure 3.8.

The full general model thus established is complex and has difficulty in measuring or computing necessary input quantities such as full dislocation/solute interaction energies. To facilitate its usages without sacrificing the predictive accuracy appreciably [147], the model was reduced to an analytic form by only considering the elastic contribution to the solute/dislocation interaction energy. The elastic interaction is due to the interplay of the pressure field of the dislocation and the solute n misfit volume  $\Delta V_n$  at the given solute site, i.e.,  $U_{el}^n(x_i, y_j, z_k) = -p(x_i, y_j)\Delta V_n(x_i, y_j, z_k)$ . In the reduced elasticity theory, two fundamental quantities, the zero-temperature yield stress,  $\tau_{y0}$ , and the zero-stress energy barrier,  $\Delta E_b$ , are first computed. For single-phase fcc HEAs, they are given as

$$\tau_{y0}^{fcc}(T) = 0.051 \alpha_{EM}^{-\frac{1}{3}} \alpha^{-\frac{1}{3}} b^{-4} \underline{G} \left( \frac{1+\underline{\nu}}{1-\underline{\nu}} \right)^{\frac{4}{3}} f_{\tau}^{fcc}(w_c) \left[ \sum_{n=1}^{N} c_n \Delta V_n^2 \right]^{\frac{2}{3}}, \tag{3.19}$$

$$\Delta E_b^{fcc}(T) = 0.274 \alpha_{EM}^{\frac{1}{3}} b \underline{G} \left( \frac{1+\underline{\nu}}{1-\underline{\nu}} \right)^{\frac{2}{3}} f_{\Delta E}^{fcc}(w_c) \left[ \sum_{n=1}^{N} c_n \Delta V_n^2 \right]^{\frac{1}{3}}, \tag{3.20}$$

where b is the magnitude of the Burgers vector of the N-component random alloy.  $\alpha_{EM} = 0.123$  is a dimensionless number.  $\underline{G}(T)$  and  $\underline{v}(T)$  are the temperature-dependent shear modulus and

Poisson's ratio, respectively, which may be obtained from measurements [142], empirical relations [146], first-principle calculations [149], or a rule of mixtures base on the elemental elastic constants  $E_n$ ,  $G_n$ , and  $v_n$  (i.e.,  $\underline{E} = \sum_{n=1}^N c_n E_n$ ,  $\underline{G} = \sum_{n=1}^N c_n G_n$ , and  $\underline{v} = \frac{\underline{E}}{2\underline{G}} - 1$ ) [148].  $f_{\tau}^{fcc}$  and  $f_{\Delta E}^{fcc}$  are numerical coefficients associated with the detailed dislocation core structures, and their values are  $f_{\tau}^{fcc} = 0.35$  and  $f_{\Delta E}^{fcc} = 5.7$  for dislocation cores with stacking fault separations greater than 10b [142, 146]. The elemental misfit volume can be acquired from first-principle calculations [149] or using the Vegard's law according to  $\Delta V_n = V_n - \underline{V} = V_n - \sum_{n=1}^N c_n V = \frac{a_n^3}{4} - \sum_{n=1}^N c_n V$ , where  $a_n$  and  $V_n$  are the lattice constant and volume of the solute n [142, 148].

Then, in the framework of the thermal activation theory, the yield stress at finite temperatures and strain rates is given as

$$\tau_{y}(T,\dot{\varepsilon}) = \tau_{y0}(T) \left[ 1 - \left( \frac{k_{B}T}{\Delta E_{b}(T)} ln \frac{\dot{\varepsilon}_{0}}{\dot{\varepsilon}} \right)^{\frac{2}{3}} \right], \tag{3.21}$$

where  $k_B$  is the Boltzmann constant, and  $\dot{\varepsilon}_0$  is the reference strain rate.

The success of the elasticity theory in predicting the yield stress has been demonstrated in the fcc Ni-Co-Fe-Cr-Mn alloys [142, 150], the fcc CoCrFeNiAl<sub>x</sub> and CoCrFeNiMnAl<sub>x</sub> HEAs with dilute Al doping [with necessary modifications to the functional forms of Equations (3.19) and (3.20)] [146], the fcc Pd-Pt-Rh-Ir-Au-Ag-Cu-Ni noble metal HEA systems [148, 149]. Examples are illustrated in Figure 3.9 for the Fe-Ni-Co-Cr-Mn alloys [142].

The same framework was also extended to some single-phase bcc HEAs such as the MoNbTaW and MoNbTaVW, where the strengthening of edge dislocations overwhelms that of screw dislocations [147]. In single-phase bcc HEAs, the zero-temperature yield stress and the zero-stress energy barrier are computed as

$$\tau_{y0}^{bcc}(T) = 0.051 \alpha_{EM}^{-\frac{1}{3}} b^{-4} \underline{G} \left( \frac{1+\underline{\nu}}{1-\nu} \right)^{\frac{4}{3}} f_{\tau}^{bcc}(w_c) \left[ \sum_{n=1}^{N} c_n \Delta V_n^2 \right]^{\frac{2}{3}}, \tag{3.22}$$

$$\Delta E_b^{bcc}(T) = 0.274 \alpha_{EM}^{\frac{1}{3}} b \underline{G} \left( \frac{1+\nu}{1-\nu} \right)^{\frac{2}{3}} f_{\Delta E}^{bcc}(w_c) \left[ \sum_{n=1}^{N} c_n \Delta V_n^2 \right]^{\frac{1}{3}}, \tag{3.23}$$

where  $f_{\tau}^{bcc} = 0.78$  and  $f_{\Delta E}^{bcc} = 7.3$ . Comparing with Equations (3.19) and (3.20), it is seen that the bcc model differs the fcc model only by the numerical coefficients and  $f_{\tau}$  and  $f_{\Delta E}$ , which

originates from the distinct atomic spacing along the edge dislocation and the slight difference in analysis [142, 147].

## 3.2.2 Interstitial strengthening

Interstitial solid solutions form by squeezing small solute atoms into interstitial sites between the solvent atoms. The invasion of the interstitial atoms deforms the alloy's lattice, leading to a local stress field that impedes dislocation motion to strengthen the alloy. Elements commonly used for interstitial strengthening include carbon, boron, oxygen, nitrogen, hydrogen, lithium, and sodium.

Cabon is the element most commonly used in HEAs for interstitial strengthening. Alloying a low content of carbon into FeNiCoCrMn [70, 71, 151], Fe<sub>40</sub>Mn<sub>40</sub>Co<sub>10</sub>Cr<sub>10</sub> [69, 152], Fe<sub>40.4</sub>Ni<sub>11.3</sub>Mn<sub>34.8</sub>Al<sub>7.5</sub>Cr<sub>6</sub> [153], and Fe<sub>50</sub>Mn<sub>30</sub>Co<sub>10</sub>Cr<sub>10</sub> [102] HEAs can improve their strengths while maintaining the original phase constitution, and increasing or decreasing ductility. The increase in the strengths is scribed to the interstitial carbon atoms suppressing dislocation motion and facilitating the formation of deformation twins [69-71]. An overdose of carbon can still maintain the interstitial strengthening effect but will deteriorate ductility significantly, partly because of the precipitation of carbides such as M<sub>7</sub>C<sub>3</sub> and M<sub>23</sub>C<sub>6</sub> at grain boundaries and/or in grain interiors [69, 71, 154, 155].

Besides, boron, oxygen, and nitrogen have also been used for interstitial strengthening in certain HEAs such as doping boron into the fcc Fe<sub>40.4</sub>Ni<sub>11.3</sub>Mn<sub>34.8</sub>Al<sub>7.5</sub>Cr<sub>6</sub> [153], oxygen into the bcc ZrTiHfNb<sub>0.5</sub>Ta<sub>0.5</sub> [156], and oxygen and nitrogen into the bcc TiZrHfNb HEA [157].

Like substitutional solid solution strengthening, interstitial solid solution strengthening also arises from the local stress fields caused by the atomic size mismatch between interstitial solutes and the solvent. Nonetheless, interstitial solutes normally cause a tetragonal distortion to the lattice, producing a shear field that strongly interacts with edge, screw, and mixed dislocations [158]. The strengthening effect induced from such a shear stress field in interstitial solid solutions is generally stronger than that from a spherically symmetric stress field without shear stress components in substitutional solid solutions [158]. Fleischer estimated the yield strength increase by interstitial strengthening as [155, 157-159]

$$\Delta\sigma_{iss} = \frac{MG\Delta\varepsilon c^{1/2}}{3},\tag{3.24}$$

where M = 3.06 is the Taylor factor, G is the shear modulus, c is the concentration of the interstitial solute,  $\Delta \varepsilon$  is the difference between the longitudinal and transverse trains of the tetragonal distortion source.

### 3.3 Dislocation strengthening

All crystalline metals contain pre-existing dislocations to a varying extent, and their movements carry the plastic flow. When in motion, dislocations from various slip planes interact with each other in different fashions. As a result, one group of dislocations oftentimes is the obstacle or pinning points of another group. The mutual hindrance of dislocations to their motion essentially requires a higher applied stress to keep the plastic flow continue compared to an ideal crystal without dislocations or a well annealed material with a very low density of dislocations. This dislocation interaction mechanism essentially constitutes the core of dislocation strengthening. The larger the amount of dislocations in a material, the higher the strength increase from the dislocation strengthening.

The dislocation strengthening is commonly described by the Taylor hardening model [125, 133, 135] as follows

$$\Delta \sigma_{\rho i} = M \Delta \tau_{\rho i} = M \alpha_T G b \rho_{dis}^{1/2}, \tag{3.25}$$

where M = 3.06 is the Taylor factor, G is the shear modulus, b is the magnitude of the Burgers vector, and  $\rho_{dis}$  is the dislocation density. To use Equation (3.25) to assess the strengthening effect from dislocation interactions, the values of all parameters need to be determined.

With known Young's modulus, E, and Poisson's ratio,  $\nu$ , G can be calculated from  $G = E/2(1+\nu)$  if the material under examination is elastically isotropic. For fcc and bcc lattices, b is calculated as  $||b|| = \frac{a}{2}\sqrt{h^2 + k^2 + l^2}$ , where  $b = \frac{a}{2}\langle hkl \rangle$  is the Burgers vector, with a being the lattice constant, and h, k, l being the components of the slip direction. If more than one phases coexist in an alloy, an average lattice constant may be used for calculating b [125].

The value of  $\alpha_T$  may be determined in different ways. Frequently,  $\alpha_T$  is approximated as 0.2 [133, 135] or 1 [125]. For those alloys that only have strain hardening in presence during plastic deformation,  $\alpha_T$  can be determined by carrying out a linear fitting to the  $\frac{\Delta \sigma_{max}}{MG} - b\rho_{dis}^{1/2}$  data pairs, where  $\Delta \sigma_{max}$  can be treated as the difference between the ultimate tensile strength and the yield

strength. With this method,  $\alpha_T$  in the fcc CrMnFeCoNi HEA was determined to be 0.4±0.1 [65], as demonstrated in Figure 3.10(a).

One of the most widely used methods for determining the dislocation density,  $\rho_{dis}$ , use the following relation [125, 133, 160, 161]

$$\rho_{dis} = \frac{2\sqrt{3}\varepsilon_M}{db},\tag{3.26}$$

where d is the average crystallite size (i.e., grain size), and  $\varepsilon_M$  is the micro strain (or lattice strain) present in materials. The average grain size, d, can be determined with any feasible methods (e.g., [125]).  $\varepsilon_M$  may be determined with the Stokes-Wilson method [125, 162]. A more commonly used technique to simultaneously determine d and  $\varepsilon_M$  is the Williamson-Hall method [163, 164]. The method is based on the theory that the line broadening of X-ray diffraction peaks,  $\beta$ , is a superposition of three distinct broadening effects, i.e., the instrument broadening,  $\beta_0$ , the crystallite broadening,  $\beta_G$ , and the strain broadening,  $\beta_S$ . One of their relations assumes a linear summation and is expressed as

$$\beta = \beta_G + \beta_S + \beta_0, \tag{3.27}$$

$$\beta_G = \frac{\kappa \lambda_{WV}}{d\cos\theta},\tag{3.28}$$

$$\beta_{S} = \frac{4\varepsilon_{M}}{\tan\theta'},\tag{3.29}$$

where K is a constant and usually approximated to be 0.9,  $\lambda_{WV}$  is the wavelength and equals 0.15405 nm for the Cu Ka radiation [133], and  $\theta$  is the Bragg angle of diffraction peaks,. The line broadening of diffraction peaks is usually quantified as the full width at half maximum intensity of the peak (FWHM).

Deducting the instrument broadening,  $\beta_0$ , from Equation (3.27), substituting Equations (3.28) and (3.29) into Equation (3.27) and performing a rearrangement, one can reach

$$\beta \cos\theta = \frac{\kappa \lambda_{WV}}{d} + 4\sin\theta \cdot \varepsilon_{M},\tag{3.30}$$

After extracting the values of  $\theta$  and  $\beta$  of a couple of diffraction peaks, Equation (3.30) can be used for a linear regression of  $\beta cos\theta$  against  $4sin\theta$ , through which  $\varepsilon_M$  is exactly the slope and d can be

calculated from the intercept. The dislocation densities in the (FeCoNiCr)<sub>94</sub>Ti<sub>2</sub>Al<sub>4</sub> HEAs processed by two different routes were determined with this approach [133]. As shown in Figure 3.10(b), the alloy by the Process 1 (P1) treatment (i.e., initial cold rolling of 30%  $\rightarrow$  annealing at 1273 K for 2 h  $\rightarrow$  aging at 1073 K for 18 h  $\rightarrow$  water quenching) results in  $\varepsilon_M^{P1} = 0$  and  $\rho_{dis}^{P1} = 0$ , primarily because the alloy is well annealed to achieve a minimization of dislocations [133]. On the other hand, the same alloy by the Process 2 (P2) treatment (i.e., initial cold rolling of 70%  $\rightarrow$  aging at 923 K for 4 h  $\rightarrow$  water quenching) has  $\varepsilon_M^{P2} = 0.102$  and  $\rho_{dis}^{P2} = 5.02 \times 10^{14} m^2$  because of the large density of dislocations induced by the heavy cold rolling [133].

In some other materials, the following quadratic relationship among different line broadening sources is used [165],

$$\beta^2 = \beta_G^2 + \beta_S^2 + \beta_0^2, \tag{3.31}$$

If using Equation (3.31), a nonlinear regression is required to determine d and  $\varepsilon_M$ .

The dislocation density may also be determined from the TEM images of samples using the Ham's method [65, 166]. In this method, a set of grid lines with a total length L is marked on a given area of the TEM image, and the number of intersections that dislocations with the grid lines is measured as N. Then, the dislocation density is estimated as

$$\rho_{dis} = 2N/Lt, \tag{3.32}$$

where t is the thickness of the TEM foil. This method was used to measure the dislocation density of the fcc CrMnFeCoNi HEA [65].

Some authors claimed to use the Kubin and Mortensen method to retrieve the density of the geometrically necessary dislocations (GND) for  $\rho$  [106, 135, 167-170], i.e.,

$$\rho_{dis} = \frac{2\theta_{mis}}{lb},\tag{3.33}$$

where  $\theta_{mis}$  is the misorientation angle that can be determined from the kernel average misorientation (KAM) plots [106, 135, 171, 172], l is the unit length and is taken as  $10^{-5}$  m in some case [106]. With this method,  $\rho_{dis}$  in the interstitial Fe<sub>49.5</sub>Mn<sub>30</sub>Co<sub>10</sub>Cr<sub>10</sub>C<sub>0.5</sub> HEA and Al<sub>10.5</sub>Cr<sub>21.1</sub>Fe<sub>21.1</sub>Co<sub>21.1</sub>Ni<sub>21.1</sub>Mo<sub>2.5</sub>C<sub>2.5</sub> HEA were estimated to be  $1 \times 10^{14} m^{-2}$  [106] and  $5.42 \times 10^{14} m^{-2}$  [135], respectively.

The strength increments resulted from the dislocation strengthening (i.e.,  $\Delta \sigma_{\rho i}$ ) as well as the values of the parameters (i.e.,  $\alpha_T$ , G, b, and  $\rho_{dis}$ ) used for evaluating  $\Delta \sigma_{\rho i}$  for a number of HEAs are compiled in Table 3.1. Alongside shown is the information on the alloy processing condition, phase constitution, and associated references.

#### 3.4 Grain-boundary strengthening

As in other polycrystalline metals, the grain boundary strengthening in HEAs arises from the impediment of grain boundaries to dislocation motion, which is further attributed to two microstructural reasons, i.e., the necessity of changing the moving direction for dislocations at grain boundaries due to the differing orientation of grains, and the discontinuity of the slip plane from one grain to another [173]. The grain boundary strengthening effect in a material does not remain constant but depends on the average grain size. Prior to reaching a critically small size below which the inverse Hall-Petch relation sets in, grain refinement can result in the increase in the yield strength of materials. This is because the stress required to move a dislocation from one grain to another depends on the grain size. When the grain size is large, each grain contains a large number of dislocations, a direct result of which is that many dislocations successively pile up at grain boundaries [173]. Since a dislocation induces a repulsive stress field, each successive dislocation will add an extra repulsive force to the dislocations piled up at the grain boundary. The repulsive forces from all pile-up dislocations collectively reduce the energetic barrier for them to move across the grain boundary [173]. Therefore, only a small applied force is needed to move the dislocation across the grain boundary. In this case, the grain boundary strengthening is weak. In contrast, fewer dislocations are contained in small grains and piles up at the grain boundary. As a consequence, the magnitude of repulsive forces available to reduce the energetic barrier of the grain boundary is diminished, and the amount of the applied stress to move a dislocation across the grain boundary increases [173].

The increase of the yield strength with the decreasing grain size,  $\Delta \sigma_{gb}$ , can be described by the Hall-Petch strengthening

$$\Delta \sigma_{gb} = k_S d^{-1/2},\tag{3.34}$$

where  $k_S$  the Hall-Petch strengthening coefficient and d is the average grain diameter. To evaluate the grain boundary strengthening effect, the value of  $k_S$  must be known.

To a first approximate, the  $k_S$  value may be estimated using the rule of mixture of alloy constituents [128]. Besides, using the  $k_S$  value of a compositionally close alloy for approximation (e.g., the  $k_S$  value of the Fe<sub>40.4</sub>Ni<sub>11.3</sub>Mn<sub>34.8</sub>Al<sub>7.5</sub>Cr<sub>6</sub> for the Al<sub>10.5</sub>Cr<sub>21.1</sub>Fe<sub>21.1</sub>Co<sub>21.1</sub>Ni<sub>21.1</sub>Mo<sub>2.5</sub>C<sub>2.5</sub>) is also an alternative [135].

Nevertheless, a rigorous method for evaluating  $k_S$  involves a curve fitting procedure using the full Hall-Petch relation, i.e.,

$$\sigma_y = \sigma_0 + k_S d^{-1/2}, (3.35)$$

where  $\sigma_y$  is the overall yield strength;  $\sigma_0$  is the friction stress considering the contributions from the lattice resistance to dislocation motion and solid solution strengthening, and may be viewed approximately as the yield stress of a very coarse-grained polycrystal.

The values of  $\sigma_0$  and  $k_S$  can be rigorously obtained by fitting Equation (3.35) to the experimental data of the yield strength,  $\sigma_y$ , as a function of  $d^{-1/2}$ . Different grain size – yield strength data points are acquirable by varying the control on materials preparation or processing (e.g., heat treatments). For the accurate determination of both  $\sigma_0$  and  $k_S$  using Equation (3.35), the grain size in different samples should be the only variable. The presence of some other strengthening mechanisms, such as precipitation strengthening, and the TWIP and TRIP effects, may invalidate this premise as they are hard to be made identical in different samples.

The grain boundary strengthening of HEAs and their subsets was investigated by utilizing Equation (3.35). The values of  $\sigma_0$  and  $k_S$  obtained for various HEAs and their subsets are tabulated in Table 3.2 along with other associated information. What is worth noting is that the same alloy (e.g., CoCrFeMnNi, HfNbTaZrTi, and CoCrFeNi) investigated in different works manifest slightly different  $\sigma_0$  and  $k_S$  values. The first source of the discrepancy might be from the difference in the alloy treatments, as found in Table 3.2. Additionally, the range of grain size and availability of the data points used for curve fitting may affect the quality of the fitting. For example, when the grain size goes beyond a certain threshold value, extra-hardening could add in some alloys to make the  $\sigma_y - d^{-1/2}$  data deviate from the linearity. In this scenario, the selection of the data range for curve fitting is critical to obtain reliable  $\sigma_0$  and  $k_S$  values. This situation is demonstrated by the CoCrNi MEA and the Ni-40Co alloy in Figure 3.11, in which the curve fitting (solid lines) was conducted by excluding the data in the extra-hardening region (dashed lines) [174].

 $\sigma_0$  and  $k_S$  of the HEAs and their subsets with a single fcc or bcc phase in Table 3.2 are plotted in Figure 3.12. Alongside plotted are the fcc pure metals Ni, Al, and Cu as well as bcc pure metals Cr, Fe, Nb, Ta, Mo, V, and W for comparison [175]. Comparing the HEAs with the pure metals of the same phase, i.e., fcc HEAs versus fcc pure metals and bcc HEAs versus bcc pure metals, it is seen that the HEAs possess both higher  $\sigma_0$  and  $k_S$  values than their pure metal counterparts. The higher  $\sigma_0$  value in HEAs is originated from their enhanced solid solution strengthening compared to pure metals, attained by the severe size and modulus mismatch of different atomic species [45, 174, 176]. The higher  $k_s$  value in the HEAs is an implication of harder slip transfer between grains and more significant grain boundary strengthening, which is caused by the fact that dislocation lines twisted by the severe lattice distortion in HEAs slip more difficultly than the straight ones in pure metals [177]. Comparing the bcc HEAs with fcc HEAs, it is clear that the  $\sigma_0$  and  $k_S$  values in the bcc HEAs are generally greater than those in the fcc HEAs, a trend consistent with bcc pure metals against fcc pure metals in Figure 3.12 and in the literature [175, 178, 179]. It was inferred that the higher  $k_S$  in bcc metals is because the greater resolved shear stress is required in bcc metals than in fcc metals to transmit plastic flow across grain boundaries, also because higher activation energies are required for the nucleation of full dislocations in bcc metals than for nucleating partial dislocations in fcc metals [179].

It was suggested that in HEAs the  $k_S$  value was primarily affected by the stacking fault energy (SFE) and shear modulus of alloys [180], analogous to the correlation in other alloy systems [53, 179, 180]. As pointed out by Fischmeister and Karlsson [181], the  $k_S$  value decreases with the increase in SFE because a high SFE promotes the formation of cell structures, whose boundaries can limit the slip lengths of dislocations [53, 181, 182]. Meanwhile, an alloy with a large shear modulus usually requires a greater shear stress to glide dislocations through the lattice and across grain boundaries, thereby leading to a high  $k_S$  value [180].

In the end, the values of the Hall-Peth coefficient for the hardness data,  $k_H$ , along with other relevant information for a number of HEAs are also compiled in Table 3.3 for reference.

#### 3.5 Precipitation strengthening

Precipitation strengthening makes use of the declining second-phase solubility in the matrix alloy with decreasing temperature to strength an alloy. Specifically, a two-step heat treatment process is indispensable, that is, the alloy needs to be first solution treated at an elevated

temperature, followed by aging at a lower temperature to precipitate out second-phase particles. The strengthening effect of precipitates essentially stems from their blockages to dislocation motion. The way that precipitates interact with and thus retard moving dislocations determines how a material is strengthened. Depending on the size and the lattice coherency with the matrix material, precipitates may impede dislocation motions in two broadly distinct ways. For precipitates that are small in size and coherent with the matrix, they resist dislocation motions by forcing dislocations to cut through them [183]. This process is normally referred to as the particle shearing mechanism, and may be affected by the coherency strain, stacking-fault energy, ordered structure, modulus effect, interfacial energy and morphology, and lattice friction stress [183]. As precipitation particles grow, they gradually become incoherent with the matrix to make the shearing mechanism infeasible. In this case, another particle-dislocation interaction mechanism called Orowan by-pass mechanism sets in, through which a dislocation loop is left around each particle following the bowing and passing of the dislocation line between the two adjacent particles, which exerts a back stress to strength the material [183].

Many attempts of using precipitation hardening as a means to enhance the strengths of HEAs have also been made. Examples include the fcc  $Al_{0.3}CoCrFeNiC_{0.1}$  [184], fcc  $CoCrFeNiMo_x$  (x=0, 0.1, and 0.2) [185], fcc  $Al_{0.3}CoCrFeNi$  [186, 187], fcc  $Cr_{15}Fe_{20}Co_{35}Ni_{20}Mo_{10}$  [188], fcc  $Cr_{15}Fe_{20}Co_{15}Nin_{10.5}$  [191], fcc+bcc  $Cr_{15}Fe_{1.5}MnNi_{0.5}$  [191], fcc+bcc  $Cr_{15}Fe_{20}Co_{15}Nin_{10.5}$  [193], eutectic  $CoCrFeNiNb_{0.25}$  [194], duplex  $Cr_{15}Pe_{12.5}V_{0.2}$  [195], duplex  $Cr_{15}Pe_{15}Ni_{10}Al_{8-x}Ti_{x}$  [196], and triplex  $CoCrFeNiMo_{0.85}$  [197]. Among these trials, prevailing applications of precipitation hardening is found in fcc HEAs in consideration of their low strengths.

One of the most widely investigated precipitation-hardened HEA is the (FeCoNiCr)<sub>94</sub>Ti<sub>2</sub>Al<sub>4</sub>, which results in a fcc FeCoNiCr matrix with nanosized, coherent L1<sub>2</sub>-Ni<sub>3</sub>(Ti, Al) precipitates upon aging and water quenching [133]. The nano-size and coherency with the matrix of the precipitates in this alloy makes the shearing mechanism prevail over the Orowan bypass mechanism. Prior to dislocations shearing through the particles, the particle-matrix coherency and modulus mismatch are the mechanisms to rule, causing the respective strength increment of [133, 198]

$$\Delta \sigma_{cs} = M \alpha_{\varepsilon} (G \varepsilon_{\alpha})^{\frac{3}{2}} \left(\frac{r f_{P}}{0.5 G b}\right)^{1/2}, \tag{3.36}$$

and

$$\Delta \sigma_{ms} = 0.0055 M \Delta G^{\frac{3}{2}} \left(\frac{2f_P}{G}\right)^{1/2} \left(\frac{r}{b}\right)^{\frac{3m}{2}-1},\tag{3.37}$$

where M=3.06 is the Taylor factor;  $\alpha_{\varepsilon}=2.6$  for a fcc structure; G is the shear modulus of the matrix;  $\varepsilon_a=\frac{2}{3}\left(\frac{\Delta a}{a}\right)$  is the constrained lattice parameter mismatch with  $\Delta a$  being the lattice parameter difference between the precipitates and the matrix and a being the lattice parameter of the matrix; r is the average particle radius;  $f_P$  is the volume fraction of the precipitates; b is the magnitude of the Burgers vector;  $\Delta G$  is the shear modulus mismatch between the precipitates and the matrix; m is a constant taken to be 0.85 [133].

In the process of dislocations cutting through particles, the strength increment is primarily dictated by atomic ordering, given by [133, 198]

$$\Delta\sigma_{os} = M0.81 \frac{\gamma_{APB}}{2b} \left(\frac{3\pi f_P}{8}\right)^{1/2},\tag{3.38}$$

where  $\gamma_{APB}$  is the anti-phase boundary energy of the precipitates.

For the simplest scenario in which a single type of particle morphology is identified, for example, the (FeCoNiCr)<sub>94</sub>Ti<sub>2</sub>Al<sub>4</sub> HEA by the Process 2 (P2) treatment in Ref. [133] (i.e., initial cold rolling of 70%  $\rightarrow$  aging at 923 K for 4 h  $\rightarrow$  water quenching), the strength gained from the shearing mechanism is simply the largest between  $\Delta \sigma_{cs} + \Delta \sigma_{ms}$  and  $\Delta \sigma_{os}$ , two sequential strengthening processes. The strength gains from each individual mechanism are calculated according to Equations (3.36) – (3.38). The values of  $\Delta \sigma_{cs}$ ,  $\Delta \sigma_{ms}$ , and  $\Delta \sigma_{os}$ , together with the ultimate strengthening from the shearing mechanism,  $\Delta \sigma_{sh}$ , are compiled in Table 3.4.

A little more complicated scenario is that the heat treated alloy contains more than one type of particle morphology, for example, the (FeCoNiCr) $_{94}$ Ti $_{2}$ Al $_{4}$  HEA by the Process 1 (P1) treatment in Ref. [133] (i.e., initial cold rolling of 30%  $\rightarrow$  annealing at 1273 K for 2 h  $\rightarrow$  aging at 1073 K for 18 h  $\rightarrow$  water quenching) was identified with two regions of distinct particle morphologies. In this case, owing to the difference in the particle size, spacing, and distribution, the strength gained from each micro-process in each individual region of an alike particle morphology needs to be computed separately. Then, the overall strengthening can be derived from a simple composite model [133]

$$\Delta \sigma_{ppt} = f_I \Delta \sigma_{ppt}^I + f_{II} \Delta \sigma_{ptp}^{II}, \tag{3.39}$$

where  $\Delta \sigma_p^I$  and  $\Delta \sigma_p^{II}$  are the precipitation strengthening resulting from the type I and II particle morphologies,  $f_I$  and  $f_{II}$  are the volume fractions of the regions containing the type I and II particles, respectively.  $\Delta \sigma_{cs}$ ,  $\Delta \sigma_{ms}$ ,  $\Delta \sigma_{os}$  for each particle morphology in the P1-treated alloy in Ref. [133], as well as the resulting  $\Delta \sigma_{ppt}^I$ ,  $\Delta \sigma_{ppt}^{II}$ , and  $\Delta \sigma_{ppt}$  are calculated this way and complied in Table 3.4 as well.

Some other compositions, for example, (FeCoNiCr)95Ti1Al4, (FeCoNiCr)91Ti3Al6, and (FeCoNiCr)88Ti3Al9, may precipitate larger L21-(Ni, Co)2TiAl Heusler particles (radius from 150 to 350 nm) in addition to the nano-sized, coherent (radius from 4 to 20 nm) L12-Ni3(Ti, Al) particles [189]. For the nano-sized, coherent L12-Ni3(Ti, Al) particles, the shearing mechanism remains dominant. However, for the larger L21-(Ni, Co)2TiAl Heusler particles, the occurrence of Orowan bowing also becomes likely. As it is changeling to precisely identify a critical particle size delimiting the shearing mechanism and the Orowan bowing, a workaround is to estimate the contributions from both mechanisms and pick the greatest one as the final precipitation hardening contribution [189]. The strength gain from the shearing mechanism,  $\Delta \sigma_{sh}$ , is likewise computed as the greatest between  $\Delta \sigma_{cs} + \Delta \sigma_{ms}$  and  $\Delta \sigma_{os}$  from Equations (3.36) – (3.38), while the contribution from the Orowan bowing is calculated from [189, 199, 200]

$$\Delta\sigma_{or} = 0.4MGb \frac{1}{\pi\sqrt{1-\nu}} \frac{\ln\left(\frac{2r}{b}\right)}{\lambda},\tag{3.40}$$

where  $\nu$  is the Poisson's ratio,  $\underline{r} = \sqrt{2/3} \cdot r$  is the mean particle radius on the slip planes with r being the average radius of particles,  $\lambda_P = 2\underline{r} \left( \sqrt{\frac{\pi}{4f_P}} - 1 \right)$  is the mean inter-particle spacing with  $f_P$  the volume fraction of precipitates.  $\Delta \sigma_{sh}$  for the fine L1<sub>2</sub>-Ni<sub>3</sub>(Ti, Al) particles and  $\Delta \sigma_{or}$  for the coarse L2<sub>1</sub>-(Ni, Co)<sub>2</sub>TiAl Heusler particles are calculated respectively for three compositions and given in Table 3.4 [189]. For each alloy composition, the greatest between  $\Delta \sigma_{sh}$  and  $\Delta \sigma_{or}$  is considered to be the ultimate precipitating strengthening result [189].

As precipitates grow with the prolonged aging time, the resultant strengthening effect varies. Figure 3.13(a) displays the nanoindentation hardness variation of the precipitation-hardened (FeCoNiCr)<sub>94</sub>Ti<sub>2</sub>Al<sub>4</sub> HEA with the aging time at three different aging temperatures [31]. It is seen that a peak hardness, preceded by the ascending hardness and followed by a decrease in hardness due to overaging, features all temperatures. It is of interest to mechanistically capture this increasing-decreasing strengthening trend. To begin, the focus is restricted to the particle-shearing

mechanism, in consideration of the nano-sized, coherent precipitates in the alloy. As outlined early, the shearing mechanism involves the strengthening from the particle-matrix coherency and modulus mismatch ( $\Delta\sigma_{cs} + \Delta\sigma_{ms}$ ) taking place prior to particle shearing as well as the order strengthening ( $\Delta\sigma_{os}$ ) activated during shearing. Based on the previous calculations, it will not cause appreciable errors to approximate the order strengthening as the sole contribution to the shearing mechanism. Nevertheless, the order strengthening mechanism described in Equation (3.38) lacks a precipitate size term to catch the increasing-decreasing strengthening trend in Figure 3.13(a). As a consequence, piece-wise, improved order strengthening models have to be employed. Specifically, as dislocation pairs cut through small precipitates, they tend to be weakly coupled and the resulting stress increment is given by [31, 201]

$$\Delta \sigma_{os}^{W} = M \frac{\gamma_{APB}}{2b} \left[ \left( \frac{4r f_{P} \gamma_{APB}}{\pi \Gamma} \right)^{1/2} - f_{P} \right], \tag{3.41}$$

where  $\Gamma = \frac{Gb^2}{2}$  is the estimated dislocation tension [202]. Equation (3.41) essentially describes a  $\Delta \sigma_{os} \propto r^{1/2}$  relation. On the other hand, when precipitates grows beyond a threshold size, the coupling of dislocation pairs becomes strong and the resulting stress increment turns to be a  $\Delta \sigma_{os} \propto r^{-1/2}$  type relation, as detailed by [31, 203]

$$\Delta \sigma_{os}^{s} = M \frac{0.18Gbw_{ER}f_{P}^{1/2}}{r} \left(\frac{2\pi r \gamma_{APB}}{w_{ER}Gb^{2}} - 1\right)^{1/2},$$
(3.42)

where  $w_{ER}$  is a constant describing the elastic repulsion between the strongly coupled dislocation pairs, and can be approximated as 1 [31]. After converting the normal stress to the hardness with  $\Delta H = 3\Delta\sigma$ , Equations (3.41) and (3.42) can nicely capture the increasing-decreasing hardness increment with the changing precipitate size in Figure 3.13(b), a trend analogous to that in Figure 3.13(a). From Figure 3.13(b), a critical precipitate radius that marks the transition of the shearing mechanism from weakly coupled dislocation pairs to strongly coupled dislocation pairs is identified to be about 11-12.5 nm [31].

#### 3.6 Twin-boundary strengthening

It is recognized that the appearance of deformation twins can increase both the strength and strain hardening of alloys, which is attributable to the blockage of twin boundaries to dislocation motion [204-208]. More specifically, twins generated during deformation gradually introduces new interfaces to reduce the dislocation mean free path and thus contribute to

strengthening [206-208]. The increased strain hardening, on the other hand, is caused by the impediment of dislocation glide by deformation twins containing a high density of sessile dislocations [65, 209-212].

The enhancement of the strength and strain hardening by nano-twins is also reported in multiple HEA systems, for example, the fcc CrMnFeCoNi [18] and AlCoCrCuFeNi with fcc and B2 phases [125]. In the interstitial TRIP-TWIP HEA, Fe<sub>49.5</sub>Mn<sub>30</sub>Co<sub>10</sub>Cr<sub>10</sub>Co<sub>.5</sub> with a fcc phase and a hcp martensite, the strengthening from twin boundaries makes a primary contribution to the improvement of the yield strength of the tempered and some annealed alloys, even greater than the contribution from the grain refinement in some cases [106]. When containing a high density of stacking faults, these nano-twins can further reinforce the strengthening effect, as revealed in the fcc CoCrFeMnNi HEA [213].

As the strengthening effect of twins is primarily from the blockage of twin boundaries to dislocation motion, it is not difficult to envision that the twin boundary strengthening in the first place depends on the twin spacing. Thus, the strengthening effect from twins is usually described by a Hall-Petch-type equation [106, 205, 214-216], given as

$$\Delta \sigma_{tb} = f_t k_{tb} \lambda_t^{-1/2},\tag{3.43}$$

where  $f_t$  is the volume fraction of the grains with twins,  $k_{tb}$  is the twin boundary strengthening coefficient,  $\lambda_t$  is the average twin spacing (i.e., the average twin thickness). Equation (3.43) is often referred to as the dynamic Hall-Petch relation [208, 213, 217].

To evaluate the strength gain from twins, the values of  $V_f$ ,  $k_{TB}$ , and  $\lambda$  are necessary to know.  $f_t$  and  $\lambda_t$  may be retrieved from the statistical analysis of a series of micrographs (e.g., SEM or TEM images) containing twins [77, 214]. The more micrographs used for the statistical analysis, the more accurate the obtained  $f_t$  and  $\lambda_t$  values. It is worth noting that the analysis of two-dimensional micrographs can only give the area fraction of the grains with twins, which may be assumed to be  $f_t$  to a first approximation [125, 214] or can be converted to  $f_t$  by certain geometric relationships (e.g., [218]). When a statistical analysis of twins is inconvenient because of, for example, the limited availability in micrographs or the amount of twins is small,  $f_t$  and  $\lambda_t$  may be crudely taken as the average of the a few discrete measurements [125]. A reliable way of determining the  $k_{tb}$  value is to conduct a linear curve fitting of

$$\sigma_{y} = \sigma_{I} + f_{t}k_{tb}\lambda_{t}^{-1/2}, \tag{3.44}$$

to the measured  $\sigma_y - \lambda_t^{-1/2}$  data pairs, from which the slope is literally  $k_{tb}$ . The intercept,  $\sigma_I$ , represents strength contributions from all mechanisms other than twins. To obtain a series of  $\sigma_y - \lambda_t^{-1/2}$  data pairs, the alloy preparation or processing route needs to be parametrically controlled to introduce samples with varying twin densities or spacing [205]. An example of using the curve fitting method to obtain the  $k_{tb}$  value is illustrated in an interstitial carbon doped HEAs (i.e., Fe<sub>50</sub>Mn<sub>30</sub>Co<sub>10</sub>Cr<sub>10</sub>Co<sub>.5</sub>, at.%, with a fcc phase and a hcp martensite) in Figure 3.14 [106]. In this case, HEAs with varied twin spacing,  $\lambda_t$ , are acquired by varying the annealing temperature and time, as representatively given in Figure 3.14(a) – (c) [106]. By plotting the yield strength,  $\sigma_y$ , of these alloys against the twin spacing quantity,  $\lambda_t^{-1/2}$ , in Figure 3.14(d) and carrying out a linear fitting with Equation (3.44),  $k_{tb}$  is determined to be 195 MPa· $\mu$ m<sup>0.5</sup> [106].

When the curve fitting approach is difficult or impractical to use for obtaining the  $k_{tb}$  value, approximate methods may be utilized. One of the methods is to approximate  $k_{tb}$  with the classical Hall-Petch coefficient,  $k_S$ , in the nanocrystalline regime, considering that the grain size in this regime is comparable to the size of nano-twins (i.e., both on the nanoscale). This method was used in evaluating the twin boundary strengthening in the AlCoCrCuFeNi and  $Co_{25}Ni_{25}Fe_{25}Al_{7.5}Cu_{17.5}HEAs$  [125, 214].

The values of  $k_{tb}$ ,  $f_t$ , and  $\lambda_t$  determined from both the curve fitting method and the approximate method in different HEAs, along with the estimated strength increase from the twin boundary strengthening,  $\Delta \sigma_{tb}$ , and other relevant information, are given in Table 3.5.

#### 3.7 Phase-transformation strengthening

The concept of the transformation-induced plasticity (TRIP) found in certain high strength steels [219-221] have been loaned to HEAs to improve both their strengths and ductility [19, 90, 98, 222, 223]. The TRIP effect in HEAs is induced by reducing the thermal and/or mechanical stability of the parent phase, i.e., making the parent phase metastable [19, 222, 224]. The metastable nature of the parent phase will enable it to partially transform into a martensitic phase upon the action of thermal processing [19] or more commonly mechanical loading [19, 98, 222]. An alloy may be made metastable by cautiously tuning its stacking fault energy (SFE) [90], practically through modifying the chemical composition or changing the deformation temperature

[105]. An example of devising the parent-phase metastability through tuning SFEs is found in the dual phase  $Co_{20}Cr_{20}Fe_{34}Mn_{20}Ni_6$  HEA exhibiting a fcc  $\rightarrow$  hcp transformation [90]. The parent fcc phase in the  $Fe_{80-x}Mn_xCo_{10}Cr_{10}$  and the  $Fe_{42}Mn_{28}Co_{10}Cr_{15}Si_5$  HEAs was made metastable through, respectively, reducing the Mn content [19] and adding Si [101].

The HEAs and MEAs in which the TRIP effect have been observed are summarized in Table 2.2. In general, two types of mechanically induced phase transformations have been reported in HEAs and MEAs. One type commonly seen is the fcc  $\rightarrow$  hpc transformation, as seen, for example, in the Fe<sub>50</sub>Mn<sub>30</sub>Co<sub>10</sub>Cr<sub>10</sub> [19, 98] and Co<sub>20</sub>Cr<sub>20</sub>Fe<sub>34</sub>Mn<sub>20</sub>Ni<sub>6</sub> HEAs [90]. Another type is the fcc  $\rightarrow$  bcc transformation, as reported in the Fe<sub>60</sub>Co<sub>15</sub>Ni<sub>15</sub>Cr<sub>10</sub> MEA at cryogenic temperatures [222]. The initial phase constitution of a metastable HEA could be either a single parent phase (e.g., fcc in the Fe<sub>60</sub>Co<sub>15</sub>Ni<sub>15</sub>Cr<sub>10</sub> MEA [222]) or dual phases with one being the parent phase and another being the martensitic phase (e.g., the fcc parent phase and hcp martensite in the Fe<sub>50</sub>Mn<sub>30</sub>Co<sub>10</sub>Cr<sub>10</sub> HEA [19, 98]).

In the sequential operation of the deformation-induced martensitic phase transformation, the improved strengths in TRIP HEAs is primarily attributed to the dynamically changing volume fraction of each phase during deformation, whereas the ductility enhancement is mainly caused by the boosted strain hardening [19, 90, 98] which sometimes exhibits multi-stage characteristics [101, 222]. The strengthening effect from the TRIP effect may be expressed as the combined strengths of two phases, i.e.,

$$\Delta\sigma_{pht} = \sigma_{par} \times f_{par} + \sigma_{mar} \times f_{mar}, \tag{3.45}$$

where  $\sigma_{par}$ , and  $\sigma_{mar}$  are the strengths of the parent and martensitic phases, respectively.  $f_{par}$  and  $f_{mar}$  are the volume fraction of the parent phase and the martensitic phase, respectively. Equation (3.45) may be used for calculating the strengths of metastable alloys at any applied strains as along as the volume fraction and strength of each phase can be satisfactorily quantified. Note that  $\sigma_{par}$  and  $\sigma_{mar}$  are the strengths manifested in the two phases after considering all other strengthening mechanism, e.g., solid solution strengthening, dislocation strengthening, and grain boundary strengthening.

The strength of each phase,  $\sigma_{par}$  or  $\sigma_{mar}$ , may be determined by conducting measurements on the alloy with a single parent or martensitic phase. Their volume fractions,  $f_{par}$  and  $f_{mar}$ , can be determined from X-ray, neutron diffractions [89, 98, 222], and EBSD phase maps [19, 90]. As

 $f_{par}$  and  $f_{mar}$  keep on changing with the increasing applied strain (or stress), they need to be quantified at different strain levels, as demonstrated in Figure 3.15. For the convenience of using Equation (3.45), a better treatment is to represent the evolution of the volume fraction of the martensite with the strain as a function in the form of  $f_{mar} = f(\varepsilon)$ . Then,  $f_{par} = 1 - f_{mar}$ . One may carry out nonlinear regressions to the  $f_{mar} - \varepsilon$  data similar to Figure 3.15 to obtain such a function. In the cases where the nucleation and growth of the martensitic phase is promoted by deformation-induced shear bands at their interactions [222], the volumetric evolution of the martensitic phase is expressed as [222, 225, 226]

$$f_{mar} = 1 - exp(-\beta_M f_{sb}^n), \tag{3.46}$$

$$f_{sb} = 1 - exp(\alpha_{SB}\varepsilon), \tag{3.47}$$

where  $f_{sb}$  is the volume fraction of shear bands in the parent phase;  $\varepsilon$  is the strain quantity;  $\alpha_{SB}$  is a parameter depending on strain rates and represents the formation rate of shear bands [226].  $\beta_M$  is the probability of the martensite nucleating at shear-band interactions, and it strongly depends on the SFE which may be estimated from the alloy thermodynamics [227]. The exponent n standards for the probability of shear-band interactions and was suggested to be 4.5 by Olson and Cohen [226].

#### 3.8 Summary and outlook

In terms of strengthening mechanisms, concentrated HEAs differs from conventional dilute alloys primarily in the lattice resistance to dislocation motion and solid solution strengthening. The severe lattice distortion in HEAs render them more resistant to dislocation motion than the dilute counterparts, partly contributing to their outstanding strengths. Multi-components and the indistinguishable solvent and solutes complicate the solid solution strengthening in HEAs. Although the Fleischer model may be used for approximate the strengthening effect in certain HEAs with dilute elements (e.g., FeCoNiCrT<sub>0.2</sub> [88]), the Labusch-type model has to be adapted with significant efforts to understand or predict the solid solution strengthening in HEAs, particularly for those of equiatomic or near equiatomic compositions. All other strengthening mechanisms found in HEAs behave rather similarly to those in pure metals and dilute alloys. Therefore, the classical models used in pure metals and dilute alloys for these strengthening

mechanisms can still be applied to HEAs for predicting strength gains. In addition to the widely encountered strengthening mechanisms covered in this chapter, some other less common strengthening mechanisms, such as ordering strengthening [157], have also be reported in HEAs.

Improving the understanding of lattice friction and solid solution strengthening in HEAs remains a pressing topic in the near future. Although a linear correlation between the lattice distortion and lattice friction has been demonstrated [126, 127], a physical connection between them is still unclear. Further efforts are worthwhile to reveal the underlying physics. Both the Labusch-type and the effective medium models adapted for predicting the substitutional solid solution strengthening in equiatomic or near equiatomic HEAs require enormous endeavors to obtain the model inputs, which largely restricts their widespread applications. It would be practically more useful if the present solid solution strengthening models could be further simplified or any other simpler model could be developed. In quantifying all other strengthening mechanisms, the methods adopted vary from work to work, with some using rigorous procedures while others use approximations. The varied methods lead to large uncertainties in the evaluated values of key strengthening parameters, such as the Hall-Petch slope and the twin boundary strengthening coefficient. Therefore, researchers are encouraged to employ rigorous methods and reliable data to quantify various strengthening mechanisms, whenever possible, so as to minimize the uncertainties. Furthermore, it is recommended that details for each step of strengthening analyses are specified.

## **Table Captions**

**Table 3.1** The values of the parameters used in the Taylor dislocation strengthening model for high entropy alloys. Alongside given is the information on the alloy processing condition, phase constitution, and estimated strength increment from the dislocation strengthening  $\Delta \sigma_{\rho i}$ , and associated references.

**Table 3.2** Hall-Petch intercepts and slopes, i.e.,  $\sigma_0$  and k in  $\sigma_y = \sigma_0 + k_S d^{-1/2}$ , of high entropy alloys and their subsets. Alongside given is the information on the alloy processing condition, phase constitution, grain size, testing temperature and associated references.

**Table 3.3** Hall-Petch intercepts and slopes based on the hardness, i.e.,  $H_0$  and  $k_H$  in  $H = H_0 + k_H d^{-1/2}$ , of high entropy alloys and their subsets. Alongside given is the information on the alloy processing conditions, phase constitution, grain sizes, testing temperatures and associated references.

**Table 3.4** Theoretically estimated precipitation hardening in high entropy alloys.  $\Delta \sigma_{cs}$ ,  $\Delta \sigma_{ms}$ ,  $\Delta \sigma_{os}$ ,  $\Delta \sigma_{sh}$ ,  $\Delta \sigma_{or}$ , and  $\Delta \sigma_{ppt}$  represent strengthening contributions from the particle-matrix coherency, modulus mismatch, order strengthening, particle shearing mechanism, Orowan bypass mechanism, and the ultimate precipitation strengthening, respectively.

**Table 3.5** The values of  $f_t$ ,  $k_{tb}$ , and  $\lambda_t$  used in the twin strengthening model  $\Delta \sigma_{tb} = f_t k_{tb} \lambda_t^{-1/2}$  for a number of high entropy alloys. Alongside given is the information on the alloy processing conditions, phase constitution, method to obtain  $k_{tb}$ , estimated strength increase  $\Delta \sigma_{tb}$ , and associated references.

## **Figure Captions**

- Figure 3.1 The linear correlations between the normalized lattice distortion stress,  $\Delta \sigma_{fr}/E$ , and the lattice distortion,  $\delta^*$ , for both the Ni-based fcc and Nb-based bcc equiatomic alloys [126].
- Figure 3.2 The normalized dislocation core width,  $w_d/b$ , for both the Ni-based fcc and Nb-based bcc equiatomic alloys [126].
- Figure 3.3 Schematics of the (a) Fleischer model and (b) Labusch model [118].
- Figure 3.4 The linear scaling between the yield strength increase,  $\Delta \sigma_y$ , and the solute concentration in the HfMo<sub>x</sub>NbTaTiZr [134], MoxNbTiVZr [136], and Al<sub>x</sub>HfNbTaTiZr [137] HEAs.
- Figure 3.5 Experimental yield strength,  $\sigma_y$ , versus the predicted solid solution strengthening effect,  $\Delta \sigma_{sss}^m$ , for the single crystals of HEAs and their subsystems [139].
- Figure 3.6 Experimental yield strength,  $\sigma_y$ , versus the predicted solid solution strengthening effect,  $\Delta \sigma_{sss}^m$ , for the polycrystalline HEAs [139]. Note that experimental  $\sigma_y$  in this case does not exclude the grain size effect.
- Figure 3.7 Schematics showing (a) the atom distribution in an actual 3-component HEA with a dissociated edge dislocation and (b) the effective matrix of the same alloy with "solute" A embedded at the position  $(x_i, y_j, z_k)$ , with an interaction energy  $U^A(x_i, y_j, z_k)$  with the dislocation [142].
- Figure 3.8 Schematic of the low-energy wavy dislocation configuration formed by moving a L long straight dislocation through the solute field with spatial fluctuations of concentrations. The total dislocation energy is minimized when  $\zeta$  and w reaches their characteristic values,  $\zeta_c$  and  $w_c$  [142].
- Figure 3.9 (a) Experimental vs. predicted yield strengths of the fcc FeNiCoCrMn HEA at varying temperatures [142]. (b) Experimental vs. predicted yield strengths of the

fcc HEA in the Fe-Ni-Co-Cr-Mn family at 293 K [142]. Note that the Hall-Petch contribution to the strengths are subtracted.

- Figure 3.10 (a)  $\frac{\sigma_{max} \sigma_y}{MG}$  plotted against  $b\sqrt{\rho_{dis}}$  for the fcc CrMnFeCoNi HEA, from which the value of  $\alpha$  in the Taylor hardening model can be determined from the slope of the linear fitting line [65]. (b) The line broadening parameter of X-ray diffraction peaks,  $\beta cos\theta$ , plotted against the diffraction angle parameter,  $4sin\theta$ , for the (FeCoNiCr)<sub>94</sub>Ti<sub>2</sub>Al<sub>4</sub> HEA processed by two different processing routes, i.e., Process 1 and Process 2 (refer to the text for the specifics of each process). A linear fitting to the  $\beta cos\theta 4sin\theta$  data pairs leads to the evaluation of the micro strain,  $\varepsilon_M$ , from the slope [133].
- Figure 3.11 The Hall-Petch relation of the CoCrNi and Ni-40Co alloys, with the dashed lines indicating extra hardening at small grain sizes. The solid lines are the linear fitting for the values of  $\sigma_0$  and  $k_S$ , with the data in the extra-hardening region excluded for use [174].
- Figure 3.12 The friction stress,  $\sigma_0$ , versus the Hall-Petch coefficient,  $k_S$ , of the alloys listed in Table 3.2. Alongside plotted are the fcc pure metals Ni, Al, and Cu as well as bcc pure metals Cr, Fe, Nb, Ta, Mo, V, and W for comparison [175]
- Figure 3.13 Precipitation hardening of the (FeCoNiCr)<sub>94</sub>Ti<sub>2</sub>Al<sub>4</sub> HEA at 750 °C, 775 °C, and 800 °C for varying aging durations [31]. (a) Variation of the nanoindentation hardness with the aging time at three temperatures, with the solid lines delineating the trends. (b) Hardness increment against the average precipitate radius at three temperatures, where the symbols represent measurement data whereas lines are theoretical predictions from Equations. (3.41) and (3.42).
- Figure 3.14 Electron channeling contrast (ECC) images of the nano-twins with varying spacing in the interstitial TRIP-TWIP Fe<sub>49.5</sub>Mn<sub>30</sub>Co<sub>10</sub>Cr<sub>10</sub>C<sub>0.5</sub> HEA (with fcc and hcp phases) annealed at (a) 650 °C for 3 min, (b) 650 °C for 10 min, and (c) 750 °C for 3 min. (d) The yield strength, σ<sub>ν</sub>, as a function of the twining spacing quantity,

 $\lambda_t^{-1/2}$ , on which a liner curving fitting is performed to retrieve the twin boundary strengthening coefficient,  $k_{tb}$  [106].

Figure 3.15 The volume fractions of the fcc parent phase and hcp martensitic phase in the  $Fe_{50}Mn_{30}Co_{10}Cr_{10}$  HEA at different local strain levels [98], which are quantified by both the X-ray diffractions and EBSD map.

#### 4 Creep

Creep property, as one fundamental high temperature property, serves as an important standard to evaluate service life and safety reliability of engineering components. Despite the excellent properties of HEAs at room and cryogenic temperature [1, 228, 229], the creep behavior of HEAs has not been studied systematically by far, which is of crucial importance for further practice application.

Previous investigations have focused on the effect of temperature on the mechanical properties of HEAs, which suggest that HEAs possess good high-temperature mechanical strength, hardness, and thermal resistance [47, 230, 231]. The deformation mechanism of CrMnFeCoNi alloy at elevated temperature has been investigated by Woo et al. [232] through in-situ neutron diffraction, which suggests that deformation occurred by the dislocation glide at 800K transforms to the diffusion-controlled dislocation at 1000K with a strain rate of  $6.7 \times 10^{-6}$  s<sup>-1</sup>. Meanwhile, superplasticity by grain boundary sliding can be another possible deformation mechanism of a fine-grained CrMnFeCoNi alloy at high temperature, which results in the good ductility of this alloy [233, 234]. Alloy design has provided a vast potential possibility for practical application. Although HEAs is a new emerging class of novel materials, these investigations have shown that the deformation mechanisms of HEAs are similar to those of common alloys [235], which provides a clear direction for future work for alloy design.

It is worth noting that the long-term phase stability in HEAs at elevated temperatures and the related mechanical performance has not been investigated in detail. Chang et al. [236] have shown that  $Al_xCo_{1.5}CrFeNi_{1.5}Ti_y$  (x + y = 0.5) high entropy alloys possessed excellent hardness from 773 K to 1273 K, comparable, even better than Inconel 718 with improving the thermal stability of  $\gamma'$  phase in the  $\gamma$  matrix due to increasing Al content. The  $Al_{02}Ti_{03}$  and  $Al_{03}Ti_{02}$  can still present good hardness at 1000 °C, although the  $\gamma'$  solvus temperature of  $Al_{02}Ti_{03}$  and  $Al_{03}Ti_{02}$  are 1010 °C and 970 °C, respectively, mainly because of limited testing time for fully dissolve of  $\gamma'$  phase [236]. And decomposition is a common phenomenon in HEAs [237-239], which may have a significant influence on creep performance in HEAs. Even though the equiatomic CrMnFeCoNi alloy is one of the well investigated HEAs, which was thought to be a single FCC structure at all temperatures below its melting point [47]. Recent studies have shown that second phase precipitates will be formed in the FCC matrix through severe plastic deformation (SPD) prior to annealing [240] or long-time annealing treatment [241]. Plastic deformation may stimulate

precipitation in HEAs at high temperatures [242]. Consequently, the creep characteristics in HEAs are very essential to enrich our knowledge of structure-property correlation in HEAs. This review chapter will aim at discussing the potentials in creep performance in HEAs and clarify the effect of precipitates on the creep behavior of HEAs, which are expected to shed light on future high-temperature HEAs design.

## 4.1 Creep characterizations

## 4.1.1 Uniaxial tension/compression

Uniaxial tensile/compressive creep test is the most widely used method to investigate the creep behavior of metals and alloys. Recently, the creep behavior of some HEAs under uniaxial tensile/compressive mode has been investigated [243, 244]. Cao et al. [245] investigated the uniaxial tensile creep behavior of the CoCrFeNiMn alloy with a grain size of ~25 µm at intermediate-temperature of 500, 550, and 600 °C under applied stresses of 140–400 MPa. Flat dog-boned specimens with a dimension of 25 mm in gauge length and 5.6 mm × 1.5 mm in cross-section were used in the creep tests. Dobeš et al. [246] reported the effect of yttrium-rich nanosized oxide particles on the creep behavior of CoCrFeMnNi HEA at a temperature range from 973 K to 1073 K under uniaxial compression mode. Dog-boned specimens with a gauge length of 12mm and a diameter of 5 mm were used in this study. Compared with other creep methods, the results from uniaxial tensile/compressive creep tests are the most reliable.

#### 4.1.2 Stress relaxation test

Stress relaxation test is another widely employed uniaxial creep test. During the creep test, the total strain  $\varepsilon_t$  is kept constant, which can be described as the sum of elastic deformation  $\varepsilon_e$  and creep deformation  $\varepsilon_c$ . The creep behavior of Al<sub>0.15</sub>CoCrFeNi and Al<sub>0.6</sub>CoCrFeNi have been investigated by Cao et al. employing the stress relaxation test (SRT) at 580–700 °C [247]. These samples, with a diameter of 5 mm and a gauge length of 25 mm, were loaded up to a strain of 0.2% at a loading rate of  $8 \times 10^{-5}$  s<sup>-1</sup>, followed by a holding period of 4 h for stress relaxation [247]. And the stress relaxation tests have also been conducted on the CoCrFeMnNi alloy at 873 K, 973 K and 1073 K [248]. The relaxation tests were conducted by holding the samples for 4 min at 5 different engineering strains amplitudes (0.04, 0.06, 0.08, 0.1 and 0.12) along with the plastic deformation [248].

## 4.1.3 Strain-rate-jump tests

The high-temperature steady state flow of the FeCoNiCrMn alloy and (FeCoNiCr)<sub>94</sub>Ti<sub>2</sub>Al<sub>4</sub> alloy was successfully investigated using strain-rate-jump test [249, 250]. High-temperature strain-rate-jump tests were conducted through successively changing the strain rate during uniaxial tension. For example, at a given temperature in the range of 1023–1173 K, a special strain-rate-jump test was applied in a single sample with a wide range of strain rates from 1.282×10<sup>-6</sup>, 6.410×10<sup>-6</sup>, 3.205×10<sup>-5</sup>, 1.603×10<sup>-4</sup>, 8.013×10<sup>-4</sup> to 3.205×10<sup>-3</sup> in the (FeCoNiCr)<sub>94</sub>Ti<sub>2</sub>Al<sub>4</sub> alloy [250]. Consequently, the correlation between stress and strain rate at a given temperature was obtained. However, from a scientific view, the strain-rate-jump test is inadequate using a single specimen at different temperatures due to the variation of microstructure during high temperature deformation [245].

## 4.1.4 Nanoindention creep

Nanoindentation is another widely used method to investigate creep performance of metals and alloys, without the limitation of standard sample size and long-time cost in uniaxial creep test, which has been applied in HEAs [251-254]. Lee et al. [255] have applied spherical nanoindentation to investigate the grain size effect in the creep behavior of the single phase CoCrFeMnNi HEA at room temperature. Ma et al. [256] systematically investigated the structure effect on the creep response of two typical HEA films namely CoCrFeNiCu (Al-0) with a face-centered cubic (FCC) structure and CoCrFeNiCuAl<sub>2.5</sub> (Al-2.5) with a body-centered cubic (BCC) structure by nanoindentation with a Berkovich indenter. Tsai et al. [257] evaluated the grain orientation effect and solid solution effect on the creep behavior in FeCoNiCrMn alloy and dual-phase Fe<sub>18</sub>Co<sub>18</sub>Ni<sub>20</sub>Cr<sub>18</sub>Mn<sub>18</sub>Al<sub>8</sub> high-entropy alloys using a nanoindentation method over temperatures range of 300–600 °C. In this study, the hardest <111> and softest <100> orientations were selected. However, it worth mentioning the reliability of the nanoindentation creep mechanism using a Berkovich indenter remains unclear [258], as overly large stress exponent was reported in several studies [253, 259].

## 4.2 Key deformation quantities

Same with conventional alloys, to reveal the operating mechanisms of plastic deformation in HEAs, the stress exponent (n), activation energy (Q), activation volume (V) are usually

measured. These parameters for some HEAs are summarized in Table 4.1. It is important to recognize that only a limited number of the above mechanisms may operate in a given material depending on the chemical composition, grain size, stress and temperature involved in the experiments.

#### 4.2.1 Stress exponent

#### 4.2.1.1 Uniaxial creep test

The stress exponent is the most widely used parameter to analyze the stress creep response. Meanwhile, the strain rate sensitivity (m), which is equal to reciprocal of n, sometimes also used to determine the deformation mechanism. Generally, the well-known power-law equation can be used to analyze the creep data [260],

$$\dot{\varepsilon} = \frac{AD_0Gb}{kT} \left(\frac{b}{d}\right)^p \left(\frac{\sigma}{G}\right)^n exp\left(-\frac{Q}{RT}\right),\tag{4.1}$$

where n is the stress exponent, Q is the activation energy, b is the Burger's vector length, d is the grain size, P is the inverse grain size exponent, G is the shear modulus, and  $D_0$  is the diffusion coefficient. In uniaxial creep tests, the correlation between strain and time is obtained at a given temperature and fixed stress amplitude. According to Equation (4.1), the value of n is calculated by assuming the stress exponent n is independent of the temperature. Based on the stress exponent of  $\sim 6.3$ , Dobeš et al. [246] proposed the possible dislocation motion as the controlled deformation mechanism in the CoCrFeMnNi alloy at a temperature range from 973 K to 1073 K. They also reported the introduction of nano-oxides into the single-phase CoCrFeMnNi alloy microstructure can significantly improve the creep resistance of this alloy, i.e., three orders lower for 30 MPa stress level, compared with the non-ODS HEA at 800 °C in Figure 4.1(a) [246]. Obviously, the creep curve for oxide disperse strengthened (ODS) HEAs can be divided into two regions, low stress level region ( $n \sim 1.8$ ) and high stress level ( $n \sim 13.2$ ). To characterize the creep mechanism for HEA-ODS alloy, by considering particle strengthening, the Equation (4.1) can be rewritten as

$$\dot{\varepsilon} = \frac{ADGb}{kT} \left(\frac{b}{d}\right)^p \left(\frac{\sigma - \sigma_{th}}{G}\right)^n,\tag{4.2}$$

where,  $\sigma_{th}$  is the threshold stress. Analysis of the creep mechanism of ODS HEA reveals that the lattice-diffusion controlled creep at low stress changes into the power-law breakdown creep characterized by the presence of threshold stress invoked by oxide particles at high stress region

[246]. The interaction between oxide particles and high angle grain boundary (GB, location A), a low-angle dislocation boundary (LADB, location B) and individual dislocations (location C), in Figure 4.1(b), are attributed to the high value of stress exponent.

A stress-dependent transition is observed in the CoCrFeMnNi alloy with an average grain size of 25 µm at an intermediate temperature ranging from 773 K to 873 K [245]. In the low-stress region (subsequently denoted as LSR-region), the stress exponent values vary in the range of 5 to 6. Stress-assisted dislocation climb controlled by lattice diffusion is suggested as a possible ratedominating mechanism at low stresses. While, in the high-stress region (denoted as HSR-region), the stress exponents are in the range of  $8.9 \sim 14$  with an average value of 380 kJ mol<sup>-1</sup>. The applied stress at which the transition occurred increased from 200 to 350 MPa with the temperature decreasing from 873 K to 773 K. Contrary to LSR, nano-sized M<sub>23</sub>C<sub>6</sub> carbides and the Cr-rich tetragonal phase have found precipitated along grain boundary, which indicates decomposition occurs during high-temperature deformation of initial single phase CoCrFeMnNi alloy. In this regard, dynamic recrystallization, precipitation, and lattice-diffusion controlled dislocation climb are proposed as the deformation mechanisms for HSR, which have attributed the high stress exponent. However, it is difficult to precisely estimate the values of boundary obstacle stress and the decrease in the stress exponent, due to the ambiguous interaction between dynamic precipitation and recrystallization. He et al. [249] investigated the high-temperature deformation mechanism of a FeCoCrMnNi and a precipitate-hardened (FeCoNiCr)94Ti2Al4 alloy applying strain rate jump test methods. Based on the observations, it is proposed that the deformation mechanism in the FeCoCrMnNi alloy has changed from dislocation glide ( $n \le 3$ ) at low strain rate to dislocation climb (n = 5) at high strain rates [249, 250]. And the precipitate-hardened alloy also exhibits two distinct deformation regimes depending upon the temperature [250]. Under a relatively low temperature range of 1023-1123 K, the *n* value is greater than 5 (6-9), corresponding to the power-law breakdown mechanism [250]. In this regime, coherent  $\gamma'$ precipitates effectively block the dislocation motion, resulting in a threshold stress effect [250]. When the temperature is between 1148 K to 1173 K, the stress exponent n is about 4.5 with the apparent activation energy of 350–450 kJ/mol [250]. Therefore, the dislocation climb mechanism is proposed for this region because of the dissolution of  $\gamma$  particles above 1123 K [250].

## 4.2.1.2 Nanoindentation creep test

The determine of stress exponent in the nanoindentation test is a little bit more complicated compared with the uniaxial creep test, based on the displacement-time creep curve. The indentation strain rate as a function of the creep time period can be depicted as [257]

$$\dot{\varepsilon} = \frac{1}{h} \frac{dh}{dt}, H \propto \frac{P}{h^2},\tag{4.3}$$

where t denotes the holding time, h refers to the indentation displacement, and P and H are the indentation load and hardness, respectively. The displacement rate,  $\frac{dh}{dt}$ , could be measured by fitting the displacement-holding time (h-t) on the basis of the empirical formula [261]:

$$h(t) = h_0 + a(t - t_0)^p + kt, (4.4)$$

where  $h_0$  refers to the displacement at the beginning stage of creep, and a,  $t_0$ , p, and k are fitting parameters. The relationship between the strain rate and the hardness could be written as

$$\dot{\varepsilon} = -\beta \frac{1}{H} \frac{dH}{dt}, H = c\sigma, \tag{4.5}$$

where  $\beta$  and c are the parameters corresponding to the indenter as well as the material. Substituting Equation (4.5) into Equation (4.1) and integrating the two sides of time, the relationship between the hardness of creep and the holding time can be described as follows [261]:

$$ln(H^{-n} - H_0^{-n}) = ln\left(\frac{An}{\beta c^n}\right) - \frac{Q}{RT} + ln(t - t_0), \tag{4.6}$$

where  $\frac{An}{\beta c^n}$  is a structure-dependent constant. At a fixed temperature and under the usual assumption of  $H^n << H_0^n$ , resulting in the linear relationship between lnH and  $ln(t-t_0)$ . Therefore, the stress exponent, n, can be measured through the slope of lnH vs lnt (t is the holding time,  $t_0 = 0$  seconds). According to the value of n, Coble creep mechanism has been proposed for nanocrystalline (nc) CoCrFeMnNi HEAs (with grain size  $\sim 49$  nm,  $\sim 33$  nm) at room temperature applying spherical nanoindentation [255]. Tsai et al. [257] found, over the temperature range of 400-600 °C, the creep stress exponent of  $\{111\}$  and  $\{100\}$  grains in single Fe<sub>20</sub>Co<sub>20</sub>Ni<sub>20</sub>Cr<sub>20</sub>Mn<sub>20</sub> and the dual-phase Fe<sub>18</sub>Co<sub>18</sub>Ni<sub>20</sub>Cr<sub>18</sub>Mn<sub>18</sub>Al<sub>8</sub> alloy is both about 3.8-5.0, suggesting the possible dislocation climb mechanism.

However, it should be noted that the mechanism determined solely by the value of n, sometimes, is misleading. Other analysis, for example, microstructure characterization, should be taken into consideration accompanying with the value of n to determine the deformation

mechanism. Shahmir et al. [262] reported CrCrFeMnNi alloy with an average grain size of 10 nm exhibited excellent elongation (> 600%) at the temperature of 973 K with strain rate sensitivity of  $m \approx 0.31$ . Superplasticity has been put forward as the deformation mechanism for this alloy, although the strain rate sensitivity is lower than the usual value of 0.5 (n = 2). They proposed that the low value of strain rate sensitivity was directly attributed to the occurrence of grain growth from  $\sim 10$  nm to  $\sim 1$  um during the tensile testing. Meanwhile, the activation energy Q has been measured to be 113 kJ/mole, which perfectly coincides with the activation energy for grain boundary diffusion in pure Ni ( $\sim 115$  kJ/mole) [262]. Similar results were obtained in Ref [263] that the CoCrFeNiMn alloy with an addition of 2 at.% Ti ( $\sim 30$  nm) exhibited excellent ductility with a maximum elongation of 830% at a temperature of 973 K with stress strain rate sensitivity of  $m \approx 0.3$ . Compared with the conventional CoCrFeNiMn alloy, the addition of a minor amount of Ti can result in smaller grain size, a higher volume fraction of precipitates and a significant improvement in the superplastic properties.

## 4.2.2 Activation energy

According to Equation (4.1), the value of activation energy, Q, can be obtained by estimating the dependence of the steady-state strain rate  $\varepsilon$  of on the reciprocal of the absolute temperatures (1/T) at a stress level on a semi-logarithmic scale. Cao et al. [245] reported the average activation energy Q in CoCrFeMnNi alloy takes a value of 268 kJ/mol in the low-stress region, which is quite close to the range of activation energies for lattice diffusion of the constituent elements in the alloy (288–317 kJ/mol [30]) and the reported activation energy value for the steady-state flow behavior of the same alloy at higher temperatures and lower stress levels [249]. Therefore, a dislocation climb mechanism is proposed for this alloy in the low-stress region. While the high value of activation energy of 380 kJ/mol in the high-stress region is attributed to the combinative effects of dynamic recrystallization and precipitation [245].

However, it is difficult to identify the creep mechanism based upon activation energy value alone. In the study of CoCrFeMnNi alloy at the stress range from 10–100 MPa, the activation energy is about 246 kJ/mol at temperatures between 973 K and 1023 K, and 704 kJ/mol at temperatures between 1023 K and 1073 K [246]. The quite different Q values, however, are related to the same dislocation motion mechanism for this alloy [246]. Because the measured activation energy of creep represents an apparent value, as a real value can be obtained only if the phase

composition is the same over the whole considered temperature range [246]. Meanwhile, due to the severe lattice distortion in HEAs, the diffusion process is more complicated, involving in the cooperative motion of several atoms in order to main compositional portioning [257]. Consequently, under the dislocation climb mechanism, it is hard to determine which single elemental constituent would control the creep deformation [257].

#### 4.2.3 Activation volume

Further insight into the mechanism of creep is obtained by estimating the value of the activation volume,  $V^*$ . Thermally activated mechanisms contributing to plastic deformation processes in metals and alloys are often quantitatively interpreted by examining the activation volume,  $V^*$ . The activation volume is broadly defined as the rate of decrease of activation enthalpy with respect to flow stress at a fixed temperature and which influences the rate-controlling mechanisms in the plastic deformation of engineering metals and alloys [264]. It has been well established that the activation volume varies by order of magnitude for different mechanisms, for example, point defect migration  $0.02 \sim 0.1 \ b^3$ , diffusional creep about  $\sim b^3$ , kink pairs in gliding screw dislocation in BCC metals  $1 \sim 5 \ b^3$ , dislocation-twin interactions  $1 \sim 100 \ b^3$ , and forest dislocation cutting  $\sim 10^3 \ b^3$ . The activation volumes for some typical HEAs calculated from different test methods are summarized in Table 4.1.

During the creep test, the strain is recorded as a function of time. For a strain-time curve of a monotonic creep test, the slope of the curve yields the plastic strain-rate,  $\dot{\varepsilon}$ . The activation volume was estimated by the following equation:

$$V^* = \sqrt{3}kT \left(\frac{\partial ln\varepsilon_{ss}}{\partial \sigma}\right),\tag{4.7}$$

where  $\dot{\varepsilon}_{SS}$  is steady-state creep rate, and k is Boltzmann's constant. Dobeš et al. [246] have calculated the activation volumes of CoCrFeMnNi alloy under the compressive creep test in the temperature range from 973 K to 1073 K. In order to obtain the activation volume, the steady-state creep rate and stress curve can be drawn in semilogarithmic coordinates, and the slope of the curve multiplied with the coefficient will give the value of activation volume at a certain temperature. In this study, the values of  $V^*$  has been estimated to be ranging from  $\sim 300 \ b^3$  to  $\sim 800 \ b^3$ , which are typical for a dislocation motion [246].

Similar to stress exponent, n, and activation energy, Q, the value of activation volume also needs to be carefully treated. Lee et al. [255] also employed this equation to estimate the activation

volume of the CoCrFeMnNi alloy in the nanoindentation test. The activation volume of  $\sim 0.8~b^3$  is obtained in nc HEAs, indicating the diffusion mechanism, consistent with the mechanism based on the value of stress exponent ( $n \sim 1$ ) [255]. Whereas the value of activation volume ( $\sim 4.6~b^3$ ) for this alloy with coarse grains is smaller than that for the dislocation mediated mechanism according to the stress exponent ( $n \sim 3$ ) [255]. The possible reason for the reduced value of  $V^*$  for coarse-grain HEA is the existent of interfacial diffusion between the indenter tip and sample surface [255]. Meanwhile, a relatively large activation volume of about 140 ų is obtained for dislocation-climb controlled mechanism in single-phase  $Fe_{20}Co_{20}Ni_{20}Cr_{20}Mn_{20}$  and dual-phase  $Fe_{18}Co_{18}Ni_{20}Cr_{18}Mn_{18}Al_8$ alloys at 873 K [257]. Different from the simple one-to-one atom-vacancy exchange during the vacancy diffusion in traditional metals and alloys, vacancy diffusion (for dislocation climb) in HEAs involves a series of cooperative motion of several atoms in order to maintain compositional partitioning, which can result in the enlargement in the activation volume in HEAs [257].

## 4.3 Creep mechanism in CoCrFeMnNi alloy

## 4.3.1 Based on stress exponents

Among all these creep parameters, stress exponent is still the most reliable one to determine the deformation mechanisms. In order to eliminate the effect of temperature on the determination of the stress exponent, the uniaxial creep data of CoCrFeMnNi alloy from Ref. [243, 245, 246, 249] are recalculated in terms of normalized creep rates versus the normalized applied stresses  $\sigma/G$ , where G is the shear modulus. The diffusivity of the slowest diffusing species, Ni  $(D_{Ni})$ , is used to normalize the strain rate by separating the temperature effect and clarify the role of stress [249]. The normalized plot is shown in Figure 4.2 in which  $D_{Ni} = 0.002 \times exp(-317500/RT)$  m<sup>2</sup>/s [249], G = 85 - 16/[exp(448/T) - 1] GPa [265]. Obviously, almost all data at different temperatures collapse into one single line in each study. The slopes of these curves yield the stress exponent, corresponding to different deformation mechanisms. According to Figure 4.2, the dislocation glide-controlled mechanism, dislocation climb-controlled mechanism, and power-law breakdown-controlled mechanism are all observed in the same CoCrFeMnNi alloy with various fine grain sizes during high-temperature deformation under different stress/temperature conditions. With the increase of normalized stress, the transitions of different mechanisms are observed. And the dislocation creep is the most popular deformation mechanism in this alloy. And

the power-law breakdown mechanism at high strength region mainly due to the occurrence of decomposition phenomenon in this this alloy [245].

## 4.3.2 Deformation map

Deformation mechanism maps are often used to determine the dominate deformation mechanisms under a set of external parameters such as temperature and applied stress. As the creep equation has three major variables of applied stress  $(\sigma)$ , temperature (T) and grain size (d), it is possible to plot maps of d/b vs  $\sigma/G$  for a constant temperature (T) or  $\sigma/G$  vs  $T/T_m$  at constant grain size (d). Chokshi [235] has developed a deformation mechanism map for CoCrFeMnNi alloy at a fixed temperature of 1023 K with appropriate constitutive relations of four deformation mechanisms, shown in Figure 4.3(a). This map works well for the data in Reddy [233] lying in the superplasticity regime, and part of the data from He et al. [249] lying in the superplaticity region and part lies in the power-law breakdown region, which maybe because of the Cr-rich precipitates observed along grain boundaries. However, recent data from Dobeš et al. [246], which are related to the dislocation motion mechanism, are located in the Coble creep region in this map. Although CoCrFeMnNi alloy is one of the most well studied HEAs, the grain sizes (d), testing temperatures (T), and methods are quite different in previous investigations. Therefore, more data is required to improve the deformation mechanism map. Figure 4.3(b) summarizes the deformation mechanisms of CoCrFeMnNi alloy according to the data compiled from reference [233, 243, 245, 246, 249, 255, 266]. The value of Burgers vector associated with dislocation in this alloy is 0.26 nm.

Despite the previous data cannot provide a detail mechanism map of this alloy with the relationship between  $\sigma/G$  vs  $T/T_m$ , some specific information can still be obtained. In Figure 4.3(b), five different deformation mechanisms of this alloy have been illustrated, including Coble, superplasticity, dislocation glide, dislocation climb, and power-law breakdown. And limited investigations focus on the mechanism during warm temperature (< 0.5  $T_m$ ). In order to fully understand the creep deformation behavior of HEAs, extensive investigations are critical importance.

## 4.3.3 Grain size effect on deformation mechanism

Generally speaking, coarse-grain materials favor the application at high temperatures. The grain boundaries are high energy regions, which become weaker at high temperatures. The cracks tend to propagate along these weaker grain boundaries under loading at high temperatures. And

larger grain size can also result in smaller steady-state creep rate in diffusion-controlled and grain boundary sliding creep. Therefore, coarse grain materials are usually used at high temperatures, while the nanocrystalline (nc) alloys have never been used at elevated temperatures because of their poor high-temperature strength and stability. However, recently, the creep behavior of nc HEAs has attracted a lot of interest [256], which may open the opportunity for developing thermally stable nanocrystalline systems that can retain high strengths over a wide temperature range from both scientific and engineering application aspects. It seems the deformation mechanisms in these nc HAEs are different from that in the HEAs with fine grain sizes under similar stress and temperature range. Lee et al. [255] reported plastic deformation in nc and coarsegrained FeCoNiCrMn alloy through nanoindentation creep analysis with a constant loading rate of 0.5 mN<sup>-1</sup>, 1000 s holding time at maximum loads and fully unloaded at room temperature. Through high-pressure torsion (HPT) processing, the grain size was reduced from ~46 μm to ~33 nm and ~ 49 nm [255]. Different grain sizes result in different deformation mechanisms in the sense that the creep stress exponent, n, extracted from the nanoindentation creep test is ~3 for coarse grains, corresponding to dislocation glide deformation, while n is ~1 for nc HEA, related to the Coble creep [255]. And the nc HEA exhibits much higher creep resistance as compared to conventional FCC nc metals mainly due to sluggish diffusion [255]. Recent experimental results on a CoCrFeMnNi HEA are shown in Figure 4.4 in terms of the variation in the strain rate with stress at T = 873 K for samples with initial grain sizes of 10 nm [266], and 25  $\mu$ m [245] under similar stress range. The fine-grained material exhibits a transition from a stress exponent of  $\sim 5.6$  to  $\sim 8.9$ with an increase in stress, whereas the nc HEA exhibits  $n \sim 3$ . Dislocation climb and power-law breakdown are proposed in the two stress regions in the fine grained HEA [245]. Superplasticity, however, is proposed to be the dominated mechanism for this nc HEA. Shahmir et al. [266] suggested that grain growth led to the apparent high stress exponent.

## 4.4 Factors affecting creep of HEAs

There are several unique effects in HEAs, which is relatively uncommon in conventional alloys. These effects can attribute to the outstanding properties of HEAs, such as phase stability, heat resistant, and high strength and ductility, which grant HEAs promising vast potentials for high temperature application. In this section, how these unique effects of HEAs affect the creep property is discussed.

## 4.4.1 High entropy effect

From a thermodynamic point of view, the large configurational entropy of mixing can lead to the decrease of Gibbs free energy, stabilizing and forming disordered solid solution phase over competing for intermetallic phases. Moreover, as  $T\Delta S_{mix}$  term dominates at high temperatures, it is expected that solid solution phases will be relatively stable at high temperature without the precipitation of harmful intermetallic, which indicate the possibility for better creep property. However, the definition of HEAs has increasingly been argued that high entropy is not sufficient alone to explain the formation of a single phase in HEAs [267]. Nevertheless, we cannot deny the role of  $\Delta S_{mix}$  in the formation of HEAs. HEAs with appropriate compositions have the potential to show superior high-temperature resistance over traditional alloys.

#### 4.4.2 Severe lattice distortion effect

The lattices of HEAs are perceived to be severely distorted because of the large difference of atom sizes [2], which is considered to an effective factor contributing to high strength and slower kinetics in HEAs [268]. Meanwhile, the local lattice distortion in HEAs can be an order of magnitude larger than the average, resulting in large energy barrier against dislocation movement, significant solid-solution strengthening, sluggish atom diffusion [269]. Komarasamy et al. [270] suggested the intrinsic lattice distortion is likely to be responsible for the observed high rate sensitivity of the flow stress and low activation volume of dislocations in CoCrFeMnNi alloy. The origin of local lattice distortion varies from size mismatch effect in FeCoNiCrMn alloy to chemical short-range order in NiCoCr alloy [271]. These lattice distortion can result in large energy barriers against dislocation movement, significant solid-solution strengthening, sluggish atom diffusion [269], thereby promoting high-temperature performance in HEAs.

## 4.4.3 Sluggish diffusion

As the mobility of atoms increases rapidly with temperature, the diffusion-controlled process is greatly important for creep deformation at high temperature, as the dominant plastic deformation mechanism, including the diffusional creep, dislocation creep and grain boundary sliding. Therefore, the diffusion rate is a key factor to affect the creep resistance of HEAs. Each diffusional creep mechanism can be described by Equation (4.1) with specific values of diffusion coefficient (D), inverse grain size exponent (P) and stress exponent (n). Therefore, the lower diffusion coefficient in multicomponent HEAs can result in better creep resistance, which should

be carefully discussed. The hypothesis retarded atomic diffusion has been considered crucial especially to the high-temperature behavior of HEAs. Zhao et al. [31] found the coarsening of L12 precipitates in the (NiCoFeCr)<sub>94</sub>Ti<sub>2</sub>Al<sub>4</sub> alloy was much slower than that in the conventional Nibased alloys because of sluggish diffusion, which indicated the remarkable thermal stability of the L12 precipitates. Figure 1.2 depicts the diffusion coefficients as a function of the inverse homologous temperature  $(T_m/T)$ , where  $T_m$  is the melting temperature), aiming to compensate for the different melting temperatures between some FCC HEAs from Ref [29, 30, 46]. The alloys with higher compositional complexity exhibit in general lower diffusion coefficients against homologous temperature, however, an exception is found that diffusion in the NiCoFeCrPd alloy, which is faster than that in the NiCoFeCr and NiCoCr alloys. Clearly, the controversial in the 'sluggish diffusion' behavior of HEAs are existing [46, 272, 273]. Lee et al. [255] reported a relatively larger  $Q_{GB}$  (~ 84 KJ/mol) for nc CoCrFeMnNi alloy with GB diffusion creep deformation at room temperature. Actually, the large activation energy turns out to be the sum of  $Q_{GB}$  for Ni (~ 67 kJ/mol for SPD processed ultrafine-grained Ni [274]) and  $\Delta Q_{GB}$  by the sluggish diffusion effect [255]. Therefore, sluggish diffusion is proposed to be the main reason for much higher creep resistance in nc HEA as compared to conventional fcc nc metal [255]. Furthermore, due to multiple principle elements with the equimolar or near-equimolar ratios in HEAs, the vacancy diffusion in HEAs is complicated compared with traditional alloys [257]. It is unclear which elemental constituent would make the first switch with the vacancy since the vacancy is surrounded by various constituent elements, involving the cooperative motion of chemical constitute atoms to keep the chemical homogeneity [257].

## 4.4.4 Stacking fault energy

Stacking fault energy (SFE) is another important factor affecting creep resistance, especially for the solid solution strengthened alloys with the dislocation climb mechanism. In these alloys, due to the strong interaction between stacking fault and solute atoms, the solid solution strengthening is achieved by the reduction of SFE which is associated with the content of alloy composition. The constitutive equation for climb-controlled dislocation creep rate with the stacking fault energy effect can be described as [275]:.

$$\dot{\varepsilon} = A' \left(\frac{\gamma_{SF}}{Gb}\right)^3 \left(\frac{\sigma}{G}\right)^5 exp\left(\frac{-Q}{RT}\right),\tag{4.8}$$

where A' is a constant,  $\gamma_{SF}$  is the stacking fault energy, G is the shear modulus, b is the Burgers vector, Q is the activation energy of creep and  $\sigma$  is the applied stress. Obviously, low SFE favors a high creep resistance. The SFE of the equiatomic NiFeCrCo and NiFeCrCoMn alloys measured by XRD is approximately 20 mJ/m² to 25 mJ/m², much lower than that of pure Ni and NiFe [114]. As alloy design has brought great opportunities for HEAs, through proper component design, the SFE of HEAs can be tailored to a wide range of values, comparable to or even lower than conventional low SFE alloys [120]. Recently, CoCrNi alloy has been reported to exhibit an excellent creep resistance, much better than CoCrFeMnNi alloy, with dislocation climb-controlled mechanism, and some commercial steels in the temperature range of 973-1023 K and stress range of 20-140 MPa in Figure 4.5(a) [276]. Meanwhile, comparing the creep lifetime of these alloys at 973 K in Figure 4.5(b), the creep lifetime of CrCoNi alloy is comparable to, or even better than, some commercial precipitate-strengthened ferritic alloys under the same stress level [276]. The lower stacking fault energy is proposed to be responsible for the much higher creep resistance in this alloy [276].

## 4.4.5 Precipitation/particle effect

In previous studies, simple phase HEAs have attracted great attention [214, 277, 278]. However, most of these single-phase HEAs usually have some limited mechanical properties, such as low strength for FCC structure HEAs [53] and low ductility for BCC structure [279, 280]. Thus, precipitation/particle hardening has been taken into consideration to improve the properties of HEAs [281]. Precipitation-strengthened alloys usually show superior mechanical properties at high temperatures, particularly when the two phases have a high degree of coherence [70, 238, 282, 283]. The interactions between particles and dislocation can be divided into two categories: Orowan bowing and particle shearing [264]. Usually, the size, morphology, coherency, and distribution of precipitations are responsible for the dislocation mechanism [264, 284]. Wang et al. [285] investigated an Al<sub>0.7</sub>CoCrFe<sub>2</sub>Ni with cuboidal B2 nanoprecipitates coherently embedded in the BCC matrix, which showed prominent tensile properties at both room temperature (ultimate tensile strength is 1223 MPa and elongation to fracture is 7.9%) and elevated temperatures. Based on the FeCoNiCr alloy, a coherent nano-size precipitate, *i.e.*, L1<sub>2</sub>-Ni<sub>3</sub>(Ti, Al) hardened HEA (FeCoNiCr)<sub>94</sub>Ti<sub>2</sub>Al<sub>4</sub>) with outstanding tensile properties by adding 2 at.% Ti and 4 at.% Al has been investigated [286]. In contrast with the single-phase FeCoNiCrMn alloy, this precipitate-

hardened alloy, (FeCoNiCr)94Ti<sub>2</sub>Al<sub>4</sub> not only shows significant tensile strength but also exhibits a large reduction of the steady-state strain rate (by ~2 orders of magnitude) at a temperature range of 1023-1073K, indicating significant improvement in high-temperature properties [250]. Meanwhile, the introduction of oxides is found to be an effect way to improve the elevated performance in alloys. Recently, Dobeš et al. [287] found the introduction of yttrium-rich nanosized oxide particles in CoCrFeMnNi alloy can lead to the enlargement of the effective grain boundary (50% grain size reduction to the size under 400 nm) and the dislocation pinning effects with ultimate tensile strength and the yield strength increase of 30% at room temperature and of about 70% at 800 °C. And the creep resistance of this alloy is significantly improved by the presence of oxide particles at the temperature range from 973 to 1073 K [246]. At high stresses, the creep behavior is characterized by the presence of threshold stress invoked by oxide particles [246].

#### 4.4.6 Solute addition effect

Recently, Kim et al. [288] developed a high-temperature deformation mechanism and processing maps of cast Al<sub>0.5</sub>CoCrFeMnNi that comprises face centered cubic (FCC) and body centered cubic (BCC) phases (where BCC phase is a minor phase) at the temperature range of 1023-1323 K and at strain rates in the range of 10<sup>-3</sup> to 10<sup>1</sup> s<sup>-1</sup>. At relatively low strain rates and high temperatures, solute drag creep is proposed to be the rate-controlling deformation mechanism due to the presence of Al solutes with a large atomic size in the FCC matrix phase [288]. Figure 4.6(a) shows the transition of creep mechanism from the climb-controlled creep (< 40 MPa) to viscous glide creep (> 40 MPa) in CoCrFeMnNi alloy at intermediate temperatures (535-650°C) [243]. In order to identify which element is the most responsible for the transition of creep mechanism from the dislocation climb to dislocation glide, the comparison of the calculated transition stress using the tracer diffusion coefficient of each element as Dg of glide-controlled creep with experimental transition stress exhibits in [288]. Figure 4.6(b) and (c). The experimental transition points of CoCrFeMnNi alloy at 600 °C and 650 °C marked on the Cr horizontal lines locate well on the theoretical transition points in the sloped lines, suggesting the Cr is the most influential element to the dislocation glide behavior at intermediate temperature associated with the large atomic size misfit to relieve the dislocation line energy and the appropriate diffusivity comparable to the dislocation velocity [243]. However, the comparable creep resistance in the <111> orientation of FeCoNiCrMn alloy and 8 at.% Al-modified FeCoNiCrMn alloy over

temperatures range of 300-600 °C suggest that the solid-solution effect (only ~4 at.% Al remaining in the FCC grains) plays an insignificant role for the FCC {111} grains with the possible climb-controlled dislocation creep [257].

#### 4.4.7 Structure effect

Ma et al. [256] have studied the strain-rate sensitivity, m, and activation volume,  $V^*$ , of an nc CoCrFeNiCu (Al-0) HEA thin film with an FCC structure and nc CoCrFeNiCuAl<sub>2.5</sub> (Al-2.5) HEA thin film with a BCC structure at room temperature by nanoindentation technique, where the BCC Al-2.5 exhibited a better creep resistance than the FCC Al-0. The creep characteristics of HEA films could be related to the different lattice structures, which apparently affect the kinetics of plastic deformation. The strain rate sensitivity and activation volume for the dislocation nucleation have been determined, which are 0.048 and 0.51 nm<sup>3</sup> in BCC Al-2.5 alloy and 0.035 and 0.08 nm<sup>3</sup> in the FCC Al-0 alloy, respectively [256]. The large discrepancy in the activation volumes for the dislocation nucleation may result in the different creep performances of these two HEA films [256]. However, the physical understanding of the distinction of the activation volumes between nanocrystalline FCC and BCC HEAs is still unclear [256]. Cao et al. [247] reported the Al<sub>0.15</sub>CoCrFeNi alloy with a single FCC structure exhibits a stronger creep resistance than the Al<sub>0.60</sub>CoCrFeNi alloy contained FCC+BCC duplex crystal structure. A rate limiting mechanism of cross-slip is proposed for both alloys [247]. They suggested the creep resistant is closely related to the stacking fault energy and the increased Al element tends to reduce the creep resistant property of the Al<sub>x</sub>CoCrFeNi alloys by increasing the stacking fault energy [247].

#### 4.5 Summary and future work

A rough picture of the creep behavior of HEAs can be imagined from these dedicated investigations. To date, dislocation climb, dislocation glide, grain boundary sliding (superplasticity), power-law breakdown, and Coble diffusion creep mechanism have been reported for HEAs. Despite the high-temperature deformation mechanisms of HEAs are similar with that of common alloys, microstructures (i.e., distorted lattices and sluggish diffusion) may impose important impacts on diffusion and dislocation glide in HEAs, making them fundamentally different from conventional alloys.

Nevertheless, the uniaxial creep behavior of HEAs has not quite been extensively studied and many questions are still left obscure. First, from previous analysis, most of the previous studies

are focused on the CoCrNi-based HEAs. Few studies are focused on the creep behavior of the refractory HEAs which are designed for high-temperature applications. Second, creep resistance is attributed to several parameters based on the deformation mechanism, i.e., difficusion, SFE. A systematic investigation needs to proceed to develop the deformation maps for a practical guide. Third, it is worth noting that HEAs are different from conventional metals by incorporating much more principle elemental species into a single lattice. The correlation between creep behavior and the unique feather of HEAs is still unclear. All these things deserve further in-depth investigations. As alloy design can bring great potential for HEAs by changing constitute elements and incorporating more minor elements, it is reasonable to deduce that HEAs have great potentials for further high-temperature applications.

# **Table Captions**

**Table 4.1** Key deformation parameters, including the stress exponent (n), activation energy (Q), activation volume (V), strain rate sensitivity (m), and the inferred deformation mechanisms of high-entropy alloys.

## **Figure Captions**

- Figure 4.1 (a) Dependence of the creep rates of the HEA-SP and HEA-ODS alloys on the applied stress [246]. (b) STEM HAADF image of the microstructure formed during creep at 1073 K and 67 MPa, for an accumulated strain of 9% [246]. The arrows highlight three locations in which oxide particles interact with a grain boundary (location A), a low-angle dislocation boundary (location B) and an individual dislocation (location C).
- Figure 4.2 Dependence of the normalized creep rates by the diffusion coefficient on the normalized applied stresses for the CoCrFeMnNi alloy [243, 245, 246, 249].
- Figure 4.3 (a) Deformation mechanisms for the CoCrFeMnNi alloy [233, 235, 246, 249]. (b) Deformation mechanism map for the CoCrFeMnNi alloy at a fixed temperature of 1023 K [233, 243, 245, 246, 249, 255, 266]. The shaded areas correspond to four different deformation mechanisms in this alloy.
- Figure 4.4 Variation of the strain rate with the stress in the CoCrFeMnNi HEA with initial grain sizes of 10 nm and 25 μm, tested at 873 K [245, 266].
- Figure 4.5 Comparison of creep behaviors. (a) Steady-state creep rate versus the applied stress for 304 stainless steel, commercial ferritic steels (P92, P122, and FBB8), CoCrFeMnNi alloy (with/without ODS), and CoCrNi alloy at 973 K [276]. (b) Applied stress versus time to rupture for commercial ferritic steels (P92, P122, T91, and FBB8), and CoCrNi alloy at 973 K [276].
- Figure 4.6 (a) The dependence of creep rates on the applied stress in the CoCrFeMnNi alloy.  $(\frac{kT}{ec^{0.5}Gb^3})^2$  versus  $(\frac{\gamma}{Gb})^3 \frac{D_C}{D_g} (\frac{\tau}{G})^2$  on a logarithmic scale at (b) 873 K (c) and 923 K for the CoCrFeMnNi alloy [243].

#### 5 Fracture

Fracture is closely pertinent to the structural integrity of a material or components made of it in practical applications. Prior to any concrete applications particularly in a structural sense, the fracture characteristics of materials usually need to be thoroughly understood. One on hand, the fracture resistance is required to be evaluated in order to decide if a given material or a class of materials could retain desired structural integrity under conditions consisting of a combination of loads, temperature, environment, etc. On the other hand, it is desirable to attain an in-depth understanding about the fracture mechanisms associated with material failures so that the composition or microstructure of materials may be further tuned in a favorable fashion so as to improve their fracture resistance.

For the same reason, the fracture behaviors of HEAs were investigated since 2010s. As HEAs cover broad compositional space and phase constitutions, their fracture properties expectedly vary to a large degree. For instance, some HEAs posses fracture toughness of less than  $5 MPa\sqrt{m}$  (e.g., the bcc Nb<sub>25</sub>Mo<sub>25</sub>Ta<sub>25</sub>W<sub>25</sub>[289]) while others can reach above  $200 MPa\sqrt{m}$  (e.g., the fcc CrMnFeCoNi [18]). Besides, fracture mechanisms also vary from alloy to alloy, particularly depending on their phase constitutions. Considering the variance, the key learnings so far gained in the fracture of HEAs are to be summarized in the present chapter. The fracture resistance of HEAs will be discussed in the background of different fracture toughness quantities, such as the impact toughness and critical stress intensity factor  $K_{IC}$ . The comparison of the fracture resistance of HEAs with that of many other metallic and non-metallic materials will give us an idea about how well certain HEAs could perform in resisting failures in anticipated applications. Furthermore, fracture mechanisms in HEAs with different phase structures are to be revealed to our best knowledge to mechanistically justify their respective fracture resistance.

#### 5.1 Fracture resistance

A structural component in service may fracture in three basic modes, i.e., Mode I – opening, Mode II – in-plane shear, and Mode III – out-of-plane shear, and their combinations. Among all possible fracture modes, Mode I is encountered most frequently and thus of a priority concern. As of the paper writing, fracture-characterization in HEAs is simply focused on Mode I failure. Two primary groups of characterization techniques, pendulum impact testing for measuring impact energy and fracture mechanics testing for deriving the fracture toughness,  $K_{IC}$ , or conditional

fracture toughness,  $K_Q$ , were employed. The majority of characterizations were conducted at room temperature, with a few at cryogenic and elevated temperatures.

#### 5.1.1 Impact toughness

The impact toughness of a number of HEAs was measured with pendulum-impact tests, and their resulting impact energies are compiled in Table 5.1. With such a pendulum system, Chen et al. [290] determined that the impact-toughness density (per unit cross-sectional area) in the  $Al_{18}Cr_{21}Fe_{20}Co_{20}Ni_{21}$ , Al<sub>15.5</sub>Cr<sub>22.25</sub>Fe<sub>20</sub>Co<sub>20</sub>Ni<sub>22.25</sub>, Al<sub>13</sub>Cr<sub>23.5</sub>Fe<sub>20</sub>Co<sub>20</sub>Ni<sub>23.5</sub>, and  $Al_{10.5}Cr_{24.75}Fe_{20}Co_{20}Ni_{24.75}$  HEAs are 12, 15, 106, 477 kJ/m<sup>2</sup>, respectively. Since they used  $6 \times 6$ × 55 mm<sup>3</sup> samples with a 2 mm U-notch, the cross-sectional area is calculated to be 24 mm<sup>2</sup>, and the total impact toughness of the four alloys are thus 0.29, 0.36, 2.54, and 11.45 J, respectively. Utilizing the Charpy-impact tests standardized in ASTM E-23 [291], Li et al. [292] measured the impact toughness values of the fcc Al<sub>0.1</sub>CoCrFeNi and Al<sub>0.3</sub>CoCrFeNi HEAs hot forged at 1323 K. The measurements were made on  $10 \times 10 \times 55$  mm<sup>3</sup> samples with a 2 mm deep V-notch in the middle, and the impact toughness values of the Al<sub>0.1</sub>CoCrFeNi at 77, 200, and 298 K were reported to be 292, 318, and 419 J, respectively. The Al<sub>0.3</sub>CoCrFeNi has the impact toughness values of 329, 409, and 415 J at 77, 200, and 298 K, respectively. Also using the  $10 \times 10 \times 55$  mm<sup>3</sup> samples with a 2 mm deep V-notch in the middle and Charpy-impact tests, Xia et al. [293] measured the impact toughness of the fcc CoCrFeNi, fcc Al<sub>0.1</sub>CoCrFeNi, Al<sub>0.75</sub>CoCrFeNi with fcc and B2 phases, and Al<sub>1.5</sub>CoCrFeNi with bcc and B2 phases at 77-298 K, and their corresponding values are listed in Table 5.1. What is worth noting is that the impact toughness of the as-cast fcc Al<sub>0.1</sub>CoCrFeNi HEAs measured by Xia et al. [293] (371, 327, and 294 J for the respective testing temperature of 77, 200, and 298 K) are different than the values reported by Li et al. [292] By comparing their samples and testing conditions, it is inferred that one possible source of the difference is their distinct processing histories, namely, the as-cast alloys by Li et al. [292] underwent hot forging at 1323 K whereas the same processing was not applied to the as-cast alloys by Xia et al. [293]

In regard to the change of the impact toughness with temperatures in HEAs, two opposing trends were reported. For the CoCrFeNi [293] and Al<sub>0.1</sub>CoCrFeNi by Xia et al. [293], their impact toughness increases with the descending temperature. On the contrary, reducing the testing temperature in the Al<sub>0.75</sub>CoCrFeNi [293], Al<sub>1.5</sub>CoCrFeNi [293], and Al<sub>0.1</sub>CoCrFeNi by Li et al.

[292] leads to a gradual decrease in their impact toughness values. Both trends are evident from the data in Table 5.1. What is of particular interest here is that in two separate works by Xia et al. [293] and Li et al. [292], temperature affects the impact toughness of the Al<sub>0.1</sub>CoCrFeNi HEAs in completely opposite directions. The difference, again, might be due to that their alloys have undergone different processing histories. However, further investigations are required to testify this inference or reveal other causes.

## 5.1.2 Fracture toughness

Fracture toughness, derived from fracture mechanics, provides a more rigorous means to assess the ability of a material to resist fracture. Depending on the extent of plasticity at the crack tip, the fracture toughness of materials may be characterized by  $K_{IC}$ , K-R curve,  $J_{IC}$ , or J-R curve [294-299]. The fracture toughness characterizations in HEAs use predominantly  $K_{IC}$ , either obtained from direct measurements or derived from other measures, e.g.,  $J_{IC}$  and J-R curve [18, 289, 290, 300-306]. The values of  $K_{IC}$  or conditional fracture toughness,  $K_Q$ , for a variety of HEAs are compiled in Table 5.2.

 $K_{IC}$  is defined, on the basis of linear elastic fracture mechanics (LEFM), as the critical stress intensity factor above which crack growth begins [294]. The use of  $K_{IC}$  is restricted by the requirements that testing specimens deform in a linear elastic manner and exhibit the minimal plasticity at the crack tip prior to failure. To this end, samples need to be dimensioned so that a plane strain condition at the crack tip prevails. The procedure of measuring  $K_{IC}$  by failing precracked specimens has been well documented in ASTM E399 [307]. Briefly speaking, a conditional fracture toughness,  $K_O$ , is firstly determined from

$$K_Q = \frac{P_Q S}{BW^{1.5}} f\left(\frac{a}{W}\right),\tag{5.1}$$

where B, W, and S are the sample thickness, width, and span, respectively. a is the average crack length.  $P_Q$  is the critical load determined from the recorded load-displacement curve [307].  $f\left(\frac{a}{W}\right)$  is a geometry-dependent polynomial function that can be looked up from the standard [307]. Then, the validity of  $K_Q$  as  $K_{IC}$  is checked against a number of criteria, primarily including

$$0.45 \le \frac{a}{W} \le 0.5,\tag{5.2}$$

$$B, a \ge 2.5 \left(\frac{\kappa_Q}{\sigma_y}\right)^2,\tag{5.3}$$

$$P_{max} \le 1.1 P_Q,\tag{5.4}$$

where  $\sigma_y$  is the yield strength, and  $P_{max}$  is the maximum load on the load-displacement curve.

The single edge-notched bend (SENB) specimen is one of sample geometries specified in ASTM E399 [307] for determining  $K_{IC}$ . With SENB specimens, the average  $K_{IC}$  of the as-cast Al<sub>23</sub>Co<sub>15</sub>Cr<sub>23</sub>Cu<sub>8</sub>Fe<sub>15</sub>Ni<sub>15</sub> HEAs with a bcc structure was determined to be 5.8  $MPa\sqrt{m}$  [302]. Following ASTM E1304, a verification measurement with a chevron-notched rectangular bar (CVNRB) specimens of the same HEA revealed a marginally small but overall consistent  $K_{IC}$  of 5.4  $MPa\sqrt{m}$  [302]. The marginal difference between the two measured  $K_{IC}$  values was ascribed to the fact that the SENB specimens were not fatigue pre-cracked. Again with the SENB specimens, Chen et al. [290] measured the fracture toughness of three as-cast HEAs, i.e., the Al<sub>18</sub>Cr<sub>21</sub>Fe<sub>20</sub>Co<sub>20</sub>Ni<sub>21</sub> with a bcc structure, Al<sub>15.5</sub>Cr<sub>22.25</sub>Fe<sub>20</sub>Co<sub>20</sub>Ni<sub>22.25</sub> with bcc and fcc phases, and  $Al_{13}Cr_{23.5}Fe_{20}Co_{20}Ni_{23.5}$  with a fcc structure, and reported 9, 11, and 53  $MPa\sqrt{m}$ , respectively. Given that validity checks were not performed in the original work, here we attempt to check if the measured  $K_Q$  values for the three alloys are actually  $K_{IC}$ . Firstly, we note that all samples used have W = 6 mm, B = 3 mm and  $a \approx 3$  mm. These dimensions lead to  $\frac{a}{W} = 0.5$ , meeting the requirement posted in Equation (5.2). Then, we substitute  $K_Q$  and  $\sigma_y$  listed in Table 5.2 into Equation (5.3), and the calculations suggest that B and  $\alpha$  for the Al<sub>18</sub>Cr<sub>21</sub>Fe<sub>20</sub>Co<sub>20</sub>Ni<sub>21</sub>,  $Al_{15.5}Cr_{22.25}Fe_{20}Co_{20}Ni_{22.25}$ , and  $Al_{13}Cr_{23.5}Fe_{20}Co_{20}Ni_{23.5}$  HEAs need to be greater than 0.58, 2.21, and 12.16 mm, respectively. From these checks, it is clear that 9 and 11  $MPa\sqrt{m}$  for the first two alloys are valid  $K_{IC}$  values whereas 53  $MPa\sqrt{m}$  for the last alloy should be regarded as  $K_0$ . Seifi et al. [303] utilized the same method to determine  $K_Q$  of the as-cast Al<sub>0.2</sub>CrFeNiTi<sub>0.2</sub> to be 32 – 35  $MPa\sqrt{m}$ , and  $K_0$  of the as-cast AlCrFeNi<sub>2</sub>Cu HEAs at room temperature and 473 K to be 40 –  $45 MPa\sqrt{m}$  and  $46 - 47 MPa\sqrt{m}$ , respectively. Following the same validity check procedure outlined above,  $32 - 35 MPa\sqrt{m}$  for the first alloy is decided to be a valid  $K_{IC}$  whilst the values reported for the second alloy at both temperatures are not. Zhang et al. [305] and Mohanty et al. [301] both measured the fracture toughness of the equiatomic AlCoCrFeNi alloy, but reported vastly different values. Zhang et al. [305] synthesized the alloy using spark plasma sintering (SPS) at 1473 K; the alloy consists of a disordered fcc phase and a duplex bcc phase comprising spinodally-decomposed ordered and disordered bcc structures. The fracture toughness measurements adopted SENB samples according to ASTM E399 [307], and  $K_{IC} = 25.2 \ MPa\sqrt{m}$ 

was reported. On the other hand, the same alloy was made by Mohanty et al. [301] also with SPS but at sintering temperatures of 973-1273 K. The alloy consist of a disordered fcc phase, an Al-Ni rich L1<sub>2</sub> phase, and a tetragonal Cr-Fe-Co based  $\sigma$  phase. The fracture toughness measurements utilized single-edge-V-notched beam (SEVNB) samples based on the EN 843-1 standard [301], and a minimum fracture toughness of 1  $MPa\sqrt{m}$  and a maximum value of 3.9  $MPa\sqrt{m}$  were reported for the alloys sintered at 1273 K and 973 K, respectively. From the above comparison, we can reason that the significant discrepancy in the fracture toughness of the AlCoCrFeNi alloys from the two separate works [301, 305] is primary originated from their dissimilar phase constitutions inherited from their distinct SPS parameters. The difference in the testing standards on which their fracture toughness measurements were based may also have some contribution but should be minimal if both groups strictly followed their respective standard.

The fracture toughness,  $K_{IC}$ , may also be determined with micro-sized samples. The fracture toughness determination of the refractory Nb<sub>25</sub>Mo<sub>25</sub>Ta<sub>25</sub>W<sub>25</sub> HEA with a bcc phase falls in this kind. The alloys were made into cantilever samples with a length of ~ 6-8 µm and a thickness and width of 1.5 - 2 µm. The fracture tests were conducted through the *in situ* TEM bending of the micro-cantilever samples, also according to ASTM E399 but with a modified  $f\left(\frac{a}{W}\right)$  function, as found in Ref. [289]. With this approach,  $K_{IC}$  of the single-crystal samples and the bi-crystal samples with a grain boundary were measured to be 1.6 and 0.2  $MPa\sqrt{m}$ , respectively. Both samples are brittle, but the presence of the grain boundary can induce further embrittlement.

For materials that are unavailable in bulk sizes, their fracture toughness values may also be determined from nanoindentation tests. In the widely used Vickers indentation, the fracture toughness is determined by [308]

$$K_{IC} = \alpha \left(\frac{E}{H}\right)^{0.5} \frac{P}{\alpha^{1.5'}} \tag{5.5}$$

where E is the Young's modulus, H is the hardness, P is the indentation load, and  $\alpha$  is the radial crack length from the indentation center to the crack tip.  $\alpha$  is a proportionality constant depending on the indenter geometry. Equation (5.5) can be adopted as well in nanoindentation tests except that a sharp cube-corner indenter with a center-to-face angle of 35.3° should be used to facilitate radial cracking in tested materials [308]. With the nanoindentation approach, the room-temperature fracture toughness values of two 1.5 mm thick, laser-solidified HEA coatings, i.e., the

FeCoNiCrAl<sub>3</sub> with a bcc phase and FeCoNiCrCuTiMoAlSiBe<sub>0.5</sub> with a mixture of a bcc phase and lath-like martensite, were measured as 7.6 and 50.9  $MPa\sqrt{m}$ , respectively.

If a material exhibits the appreciable plasticity during deformation, the direct measurement of  $K_{IC}$  according to ASTM E399 [307] becomes inconvenient or impractical. This is because very large sample sizes may be required in order to secure a plane strain condition at the crack tip and ultimately valid  $K_{IC}$  values. As a result, using the *J*-integral or *J*-integral resistance curve on the basis of the elastic-plastic fracture mechanics (EPFM) to determine the fracture toughness of these materials becomes a favorable alternative. The detailed procedure of using this approach is documented in ASTM E1820 [309]. Briefly, one firstly needs to determine a *J*-integral resistance curve (i.e., the *J*-integral against the crack extension), from which the critical *J*-integral near the onset of the ductile crack extension,  $J_{IC}$ , is determined by intersecting the resistance curve with the 0.2 mm offset line. One can certainly use  $J_{IC}$  to denote the fracture resistance of a material. However, for an easy comparison with other materials,  $J_{IC}$  can be converted to  $K_{IC}$  through  $K_{IC}$  $\sqrt{\frac{EJ_{IC}}{1-\nu^2}}$ , where E and  $\nu$  are the Young's modulus and Poisson's ratio, respectively. With SENB specimens, Chung et al. [300] used this approach to measure the room-temperature  $K_{IC}$  of the ascast CoCrFeNiNb<sub>0.5</sub> HEA with an eutectic structure, concluding with 11.4-14.8  $MPa\sqrt{m}$ . The fcc CrMnFeCoNi HEAs exhibit extensive plasticity (the tensile fracture elongation  $\varepsilon_f > 0.55$ ) after undergoing casting, homogenization, cold forging, cross rolling, and annealing for recrystallization [18], and are also suited for the *J*-integral method. By applying this method to the compact-tension (CT) samples, Gludovatz et al. [18] determined that  $K_{IC}$  for the CrMnFeCoNi HEAs at 77 K, 200 K, and 293 K were 219, 221, and 217  $MPa\sqrt{m}$ , respectively. It is evident that the  $K_{IC}$  of this alloy is insensitive to temperature reduction, opposed to many conventional metal alloys suffering from the ductile-to-brittle transition (DBT) upon cold-temperature exposures. This characteristic enables this HEA to stand out as an excellent candidate material for applications under extreme cold conditions.

#### 5.1.3 Other measures

The crack-tip-opening angle (CTOA), defined as the angle made by two cracking flanks, is another measure characterizing the resistance of materials to plastic fracture. It is primary applicable to thin-sheet structures subjected to a plane-stress condition. The rationale behind using

CTOA as a fracture-resistance criterion is that the attainment of a steady-state CTOA normally implies that the stable crack growth prevails in materials. Usually, a high steady-state CTOA value is indicative of the great crack propagation resistance and vice versa.

To determine the steady-state CTOA in a CoCrFeNiMn<sub>0.2</sub> HEA made by the powder metallurgy and composed of a fcc matrix and Cr-rich precipitates, Li et al. [310] conducted in situ SEM fracture tests on single-edge-notched-tension (SENT) samples ( $40 \times 10 \times 1 \text{ mm}^3$  with a 1 mm long notch), and measured CTOA from the interrupted SEM images as a function of crack extension,  $\Delta a$ . Ultimately, the steady-state CTOA was determined to be 18°. This value was believed by the authors to be a relatively high value, indicating the alloy under investigation possess high fracture resistance. Nevertheless, as this criterion is not used as frequently as others introduced before, its comparison with other criteria to rank the fracture resistance of different HEAs turns out to be unlikely.

## 5.1.4 Comparison with other materials

The Ashby plot of the fracture toughness against the yield strength is a useful tool to evaluate the overall damage tolerance of materials. With the valid  $K_{IC}$  data ( $K_Q$  values excluded) and corresponding  $\sigma_y$  in Table 5.2, in Figure 5.1 we outline the damage tolerance space for HEAs alongside many traditional metals and alloys and other material classes. The damage tolerance of HEAs covers a wide space, with the yield strength running from 294 MPa to over 5.7 GPa and the fracture toughness from 0.2 to 232  $MPa\sqrt{m}$ . Note that some unrealistically high strengths (e.g., 3770 MPa for FeCoNiCrCuTiMoAlSiBe<sub>0.5</sub> [306]) estimated from the hardness data with  $\sigma_y = \frac{H}{2}$ are excluded from plotting considering the crudeness of this relation. Overall, the HEA domain manifests a slight backward tilting, with fcc HEAs (e.g., CrMnFeCoNi [18]) having high fracture toughness (217 – 232  $MPa\sqrt{m}$ ) but low strengths (294 – 760 MPa), bcc HEAs (e.g.,  $Al_{18}Cr_{21}Fe_{20}Co_{20}Ni_{21}$  [290]) having low fracture toughness  $(0.2 - 9 MPa\sqrt{m})$  but high strengths (1020 – 5700 MPa), and those with multiple phases located in-between. According to the phase constitution, the entire HEA damage-tolerance domain can be roughly subdivided into three subdomains, that is, the single-fcc-phase, single-bcc-phase, and multi-phase subdomains, which are located at the top, bottom, and middle of the HEA domain, as demonstrated in Figure 5.1. In this subdivision, one exception is the spark-plasma-sintered AlCoCrFeNi HEA with fcc, L1<sub>2</sub>, and tetragonal Cr-Fe-Co based σ phases, which comprises multiple phases but its damage tolerance

falls in the bcc subdomain [301]. This is probably because the spark plasma sintering itself introduced certain fluctuations in the phase constitution and mechanical properties of the alloys compared to those made from traditional casting. But, the splitting of the damage-tolerance domain by the phase constitution is in general in line with the classical physical metallurgy wisdom that fcc phases are soft yet ductile, while the bcc phase are hard yet brittle.

In comparison with other materials, a large portion of HEAs are located at the top-right corner of the Ashby plot, a direction that material scientists have strived to search for extraordinary damage-tolerant materials. HEAs with a single fcc phase is usually limited by their low strength, while those having a single bcc phase oftentimes are brittle. With proper compositional and microstructural designs, HEAs with multiple phases, however, are likely to overcome both the strength and ductility constraints, standing out as remarkable fracture-resistant materials.

Likewise, with the data at 77 – 298 K in Table 5.1, an impact energy – yield strength plot is generated for HEAs whose fracture resistances are quantified by impact toughness. Such a plot is given in Figure 5.2, together with some selected conventional metals and alloys. Based on the phase constitution, HEAs in Figure 5.2 are separated into two groups. The first group is located at the top left of the plot with high impact toughness (177 - 420 J) but low strength (155 - 610 MPa), corresponding to those HEAs with a single fcc phase, such as the CoCrFeNi [293], CoCrFeMnNi [64], Al<sub>0.1</sub>CoCrFeNi [292, 293], and Al<sub>0.3</sub>CoCrFeNi [292, 293]. The second group sinks down at the bottom of the plot with the very low impact energy (< 12 J) but a wide span of strengths. The majority of HEAs falling in this group comprise either a single bcc phase or combined phases, with one exception being the Al<sub>13</sub>Cr<sub>23.5</sub>Fe<sub>20</sub>Co<sub>20</sub>Ni<sub>23.5</sub>, which has a single fcc phase [290]. This trend, again, is roughly aligned with the long-established understanding about the mechanical behaviors of fcc and bcc metals. Compared with other metal and alloys, the fcc CoCrFeNi, Al<sub>0.1</sub>CoCrFeNi, and Al<sub>0.3</sub>CoCrFeNi alloys indeed show superior impact toughness, but their strengths are relatively low, disqualifying them as materials of high damage tolerance. All other HEAs located on the bottom, on the other hand, possess extremely low impact toughness (0.29 – 11.45 J), and are not suitable for high damage-tolerance applications. Like the Ashby plot in Figure 5.1, the top-left corner in Figure 5.2 is a desirable direction for HEAs to be more damage-tolerant.

## 5.2 Fracture toughness – fractography correlation

A common method of fractographic analyses is to perform post-mortem on failed samples, mostly by virtue of SEM. Cleavage or quasi-cleavage, a mechanism of brittle transgranular

fracture, is commonly observed on the fracture surfaces of HEAs with low fracture/impact toughness, the majority of which are bcc alloys and some of which are those with mixed phases. For example, the bcc Al<sub>23</sub>Co<sub>15</sub>Cr<sub>23</sub>Cu<sub>8</sub>Fe<sub>15</sub>Ni<sub>15</sub> HEA with  $K_{IC} = 5.4 - 5.8 \, MPa\sqrt{m}$  manifests isolated facets and river lines on its fracture surfaces [302]. The fracture surfaces of the bcc Al<sub>18</sub>Cr<sub>21</sub>Fe<sub>20</sub>Co<sub>20</sub>Ni<sub>21</sub> with  $K_{IC} = 9 \, MPa\sqrt{m}$  and impact toughness of 0.29 J show fan-like fracture features, which are in fact facets separated by river lines [290]. River lines and facets are also noticed on the fracture surfaces of the bcc (TiZrNbTa)<sub>80</sub>Mo<sub>20</sub> HEA [304], the fcc + bcc Al<sub>15.5</sub>Cr<sub>22.25</sub>Fe<sub>20</sub>Co<sub>20</sub>Ni<sub>22.25</sub> with  $K_{IC} = 11 \, MPa\sqrt{m}$  and an impact toughness of 0.36 J [290], as well as the fcc + B2 Al<sub>1.5</sub>CoCrFeNi with an impact toughness of 0.64-1.28 J [293]. The cleavage fracture morphology is representatively shown in Figure 5.3 with the Al<sub>1.5</sub>CoCrFeNi HEA [293].

Additionally, some HEAs with low fracture toughness may also be failed by intergranular fracture along grain boundaries, such as the bcc Nb<sub>25</sub>Mo<sub>25</sub>Ta<sub>25</sub>W<sub>25</sub> bi-crystal with  $K_{IC} = 1.6 \, MPa\sqrt{m}$  [289] and the bcc TiZrNbTa [304]. The bcc (TiZrNbTa)<sub>90</sub>Mo<sub>10</sub> HEA even finds a mix of intergranular fracture and transgranular cleavage on its fracture surfaces [304]. The granular fracture morphology is another sign of brittle transgranular or intergranular failures, as observed in the AlCoCrFeNi HEA, which comprise fcc, L1<sub>2</sub>, and tetragonal  $\sigma$  phases and has  $K_{IC} = 1 - 3.9 \, MPa\sqrt{m}$  [301]. The SEM image of the fracture TiZrNbTa HEA in Figure 5.4 represents a intergranular fracture morphology [304].

HEAs with high fracture resistance, on the other hand, usually see dimples on their fracture surfaces, which are known to be formed through the nucleation, growth, and coalescence of microvoids. For instance, prevailing dimples are observed on the fracture surfaces of the fcc CrMnFeCoNi HEA with  $K_{IC} = 217 - 221 \, MPa\sqrt{m}$  [18], the fcc Fe<sub>45</sub>Co<sub>20</sub>Cr<sub>10</sub>Ni<sub>15</sub>V<sub>10</sub> with  $K_{IC} = 219 - 232 \, MPa\sqrt{m}$  [311], as well as the fcc CoCrFeNi, fcc Al<sub>0.1</sub>CoCrFeNi, and fcc Al<sub>0.3</sub>CoCrFeNi HEAs with impact toughness of 287-398 J, 292-491 J, and 329-415 J [293], respectively. An example SEM-imaged fracture morphology of this type is shown in Figure 5.5 on the Fe<sub>45</sub>Co<sub>20</sub>Cr<sub>10</sub>Ni<sub>15</sub>V<sub>10</sub> HEA [311].

For those HEAs with intermediate fracture resistance, a mix of cleavage fracture and dimples is usually seen upon their failures. A roughly half-and-half blend of river patterns (in the bcc phase) and dimples (in the fcc phase) was found for the AlCoCrFeNi HEA as shown in Figure 5.6, which consists of a fcc phase and a duplex bcc phase and has  $K_{IC} = 25.2 \, MPa\sqrt{m}$  [305]. The

fcc + bcc Al<sub>0.2</sub>CrFeNiTi<sub>0.2</sub> HEA with  $K_{IC} = 32 - 35 \, MPa\sqrt{m}$  exhibits apparent faceted zones with small-scale dimples on its fracture surfaces [303]. Likewise, the fcc + bcc Al<sub>10.5</sub>Cr<sub>24.75</sub>Fe<sub>20</sub>Co<sub>20</sub>Ni<sub>24.75</sub> with impact toughness of 11.45 J presents on its fracture surfaces a mixture of dimples and tear ridges [290]. Note that the formation of tear ridges is due to the blend of cleavage facets with areas of dimple ruptures.

To sum up, HEAs with low fracture toughness (e.g.,  $\sim \le 10~MPa\sqrt{m}$ ) or impact toughness (e.g.,  $\sim \le 10~J$ ) normally fail by either transgranular cleavage characteristic of river patterns and faceted zones or intergranular fracture featuring grained morphologies. The granular fracture morphology also falls into this category but can be incurred by either transgranular or intergranular failures. HEAs with high fracture toughness (e.g.,  $\sim \le 100~MPa\sqrt{m}$ ) or impact toughness (e.g.,  $\sim \le 100~J$ ) typically exhibit dimples formed from microvoid coalescence. Those HEAs having their fracture/impact toughness in between, as one can imagine, display a blend of cleavage morphology and dimples, sometimes a fused feature – tear ridges. Representative fractographs for commonly observed fracture modes in HEAs, including transgranular cleavage, intergranular fracture, dimpled fracture, and hybrid fracture blending dimples and cleavage, is given in Figure 5.3. Overall, these morphologies have no difference with those found in conventional metals and alloys with similar phase constitutions.

#### 5.3 Fracture mechanisms

For a good understanding about why some HEAs possess superior fracture resistance (e.g., fcc CrMnFeCoNi [18]) while others suffer from brittle failures (e.g., bcc Al<sub>18</sub>Cr<sub>21</sub>Fe<sub>20</sub>Co<sub>20</sub>Ni<sub>21</sub> [290]), examining their respective fracture mechanisms, from both macro and micro perspectives, is imperative. Besides, revealing their fracture mechanisms is also instructive to designing future fracture-resistant HEAs with deliberate compositional, microstructural, and/or processing controls. We herein summarize the fracture mechanisms in a number of HEA systems and group them by phase constitutions. In general, the portrayal of fracture mechanisms involves the initiation and propagation of cracks and their interactions with such microstructural features as phases, dislocations, twins, precipitates, etc.

#### 5.3.1 In face-centered-cubic alloys

The fracture mechanisms in the fcc CrMnFeCoNi HEA are mostly studied in consideration of its top-ranked fracture toughness among structural materials ever known. It is disclosed in

several investigations that the extraordinary fracture resistance in this alloy at both room and cryogenic temperatures is a consequence of the integrated intrinsic toughening and extrinsic toughening mechanisms [308, 312, 313].

The intrinsic toughening involves accomplishing a reconciled competition between ductilization and strengthening, two contradictory processes in many conventional materials. Microscopically, the balance between the ductility and stain hardening is achieved through unusual dislocation and twining activities in the vicinity of the crack tip, as revealed by in situ TEM observations. In the first place, the good ductility is made possible in the alloy by (1) extensive dislocation motions near the crack tip via glide of both perfect  $\frac{1}{2}\langle 110\rangle$  dislocations [18] and  $\frac{1}{6}\langle 112\rangle$ type Shockley partials [312]; (2) the activation of numerous deformation twins [18, 312, 313]; (3) the unceasing emission of partial dislocations from deformation twin boundaries with the aid of the stress field ahead of the crack tip [312, 313]. In the second place, strain hardening is attained by (1) the blockage of dislocation motions by stacking fault parallelepipeds [e.g., Figure 5.7(a)) formed from interacting stacking faults [312]; (2) the blockage of fast-moving partial dislocations by planar slip bands of perfect dislocations, as shown in Figure 5.7(b) [312]; (3) the blockage of moving dislocations at twin boundaries [83, 313]; (4) the trapping of sessile dislocations in deformation twins, as demonstrated by the almost immobile dislocation arrays contained in Twin 1 and Twin 2 in Figure 5.7(c) [313]; (5) the deflection and/or blockage of propagating cracks at deformation twin boundaries, as depicted in Figure 5.7(d) [313]; (6) the retardation of crack propagation by plastic relaxation through twining and detwining inside the crack-tip plastic zone [313]. One last note about twining is that reduced temperatures and increased loading rates [18, 293], in addition to the low stacking fault energy (SFE), can facilitate the formation of abundant nano twins. This is why the fcc CrMnFeCoNi [18], fcc CoCrFeNi [293], and fcc Al<sub>0.1</sub>CoCrFeNi [292, 293] HEAs can retain or even gain improved fracture/impact toughness at cryogenic temperatures.

Additionally, crack bridging, as an extrinsic toughening mechanism, acts behind the crack tip to resist crack opening, further toughening the alloy. Via *in-situ* TEM observations, it is demonstrated that the nano bridges binding crack faces together are formed through extensive shear along the (111) plane [313] or the interaction of two {111} slip planes [312], as given in Figure 5.7(e). Crack bridging is perceived to take place at the later stage of deformation to impede the extension of long cracks. What accompanies the crack bridging in Figure 5.7(e) is the formation

of microvoids, besides which some nanotwins are visible. In fact, in the later investigations of the fcc Fe<sub>40</sub>Mn<sub>40</sub>Co<sub>10</sub>Cr<sub>10</sub> [314] and fcc CoCrFeNiMo [315], it was suggested also with *in-situ* TEM straining experiments that deformation twins promote the nucleation and coalescence of microvoids, which eventually can evolve into microcracks propagating along twin boundaries. A typical TEM image of crack propagation along the twin boundary is given in Figure 5.7(e) [314].

## 5.3.2 In body-centered-cubic alloys

From Section 5.2, it is known that bcc HEAs fail by either transgranular cleavage or intergranular separation. Since both processes involve very limited plasticity, the associated fracture mechanisms in bcc HEAs is not expected to be as complex as in fcc HEAs. Like all other materials, cleavage in bcc HEAs also results from the breakage of weaker bonds between atoms on certain crystallographic planes. On the other hand, the intergranular fracture may be caused by the segregation of impurities at grain boundaries. In the case of the bcc Nb25Mo25Ta25W25 HEA, the impurities segregated at grain boundaries are N, C, O and induced oxides (e.g., TaO and NbO) and nitrides (e.g., TaN and NbN) [289]. N and O were inferred to be introduced during the sample preparation and annealing processes, while C was believed to be inherent to the raw materials. The segregation of these impurity elements at grain boundaries, particularly after their reactions with alloying elements to form brittle oxides and/or nitrides, is detrimental to the fracture resistance of HEAs.

#### 5.3.3 In alloys with face- and body-centered-cubic phases

The AlCoCrFeNi HEA constitutes a fcc phase and two distinct bcc phases accounting for approximately 17.2% and 82.8% volume fractions, respectively [305]. The two bcc phases are enclosed by the net-like fcc phase, as illustrated in Figure 5.8(a) [305]. The duplex bcc phase is further composed of a spinodally-decomposed ordered matrix rich in Al and Ni and disordered precipitates rich in Fe and Cr, as shown in the magnified microstructure in Figure 5.8(b). The crack in this alloy is found to propagate inside the fcc phase or along the fcc-bcc interfaces. Given that the fcc phase has a net-like distribution in the alloy, the crack propagation is forced to be curvy, which retains a greater amount of the surface energy than the straight one. In addition, cracks could be blunted and arrested by the ductile fcc phase, bridged by the fcc-phase or bcc-phase fragments, and deflected by the fcc-bcc interfaces. All these mechanisms seen in Figure 5.8(c) work

synergistically to toughen the AlCoCrFeNi HEA, leading it to an intermediate fracture toughness of 25.2  $MPa\sqrt{m}$  [305].

## 5.3.4 In eutectic alloys

Some carefully-tailored eutectic microstructures may benefit the fracture resistance of alloys by positively affecting crack propagation. Such a demonstration is found in the CoCrFeNiNb<sub>0.5</sub> HEA with a hierarchical, lamellar eutectic structure comprising Laves and fcc phases in approximately equal volume fractions [300]. The hierarchical eutectic microstructure overall has an appearance of grain-like colonial network, as shown by the optical microscopy (OM) image in Figure 5.9(a). Each colony is further composed of fine lamella structures and coarse lamella structures, as revealed by the top and bottom insets respectively in the SEM image in Figure 5.9(b), respectively. This particular hierarchical, lamellar eutectic structure intrinsically toughens the alloy. In the coarse lamellar structure (spacing  $\approx 250$  nm), cracks tend to initiate and propagate inside the brittle Laves phase, but arrested and blunted by the ductile fcc phase, as exemplified by the crack path rectangled in Figure 5.9(c). As cracks advance into the fine lamellar structure (spacing  $\approx 70$  nm), the roles of the Laves and fcc phases are reversed. Specifically, the crack propagation takes place within the embrittled fcc phase but is detoured by the ductilized Laves phase, as representatively illustrated by the rectangle region in Figure 5.9(d). Cleavage fracture favors the fcc phase in this structure because the crack-tip plasticity is suppressed in ductile lamellas whose thicknesses are smaller than two times the crack-tip plastic zone [300]. On the other hand, the nano-sized Laves phase in the fine lamellar structure experiences a size controlled brittle-to-ductile (BTD) transition, becoming ductile [300].

Furthermore, as cracks prefer to grow in the direction parallel to the local lamella, randomly oriented lamellas in both the coarse and fine lamellar structures continuously alter crack growth paths. Simply put, the lamellar structure causes crack deflection and detouring, as seen in Figure 5.9(e). Also, due to the vast difference in toughness of the Laves and fcc phases, the crack propagation can easily become discontinuous, forming intermittent ligaments bridging crack faces, as shown in Figure 5.9(e) [300]. With SEM imaging, the bridging ligaments are found to form in the fcc phase in the coarse lamellar structure but in the Laves phase in the fine lamellar structure [300]. The crack deflection and bridging triggered by the nature of the lamellar structure serve as extrinsic toughening mechanisms, additionally improving the fracture resistance of the alloy.

#### 5.3.5 In precipitation-hardened alloys

In the precipitation-hardened HEAs, for example, the CoCrFeNiMo<sub>0.2</sub> alloy with a fcc phase and Cr-rich intermetallic particles of 1-3  $\mu$ m in diameter [310], the high fracture resistance, as indicated by a 18° CTOA value [310], is suggested to be fulfilled by (1) excellent ductility and work hardening of the fcc matrix; (2) the nucleation of microvoids by the debonding of intermetallic particles from the fcc matrix [Figure 5.10(a)], followed by their growth and coalescence; (3) remarkable crack-tip blunting through massive plastic deformation in the fcc matrix [Figure 5.10(b)], mediated by both dislocation slips and twinning; (4) crack branching [Figure 5.10(c)]; (5) the formation of tortuous crack propagation paths by merging microcracks (evolved from microvoids) into main propagating cracks [Figure 5.10(d)]. The synergy of these mechanisms eventually leads to ductile fracture of the alloy, featuring a dimpled fracture morphology [310]. Likewise, the formation of microvoids by debonding intermetallic  $\sigma$  inclusions from the fcc matrix is also noted in the precipitate-containing CrFeNiV HEA [316]. Moreover, the breakage of brittle  $\sigma$  precipitates is also in part account for crack initiation in this alloy. Both cracking mechanisms, depicted in Figure 5.11, together lead to ductile fracture, rather than intergranular or cleavage fracture, in the alloy.

## 5.3.6 In metastable alloys

In the mechanically metastable Fe₄5Mn₃0Co₁0Cr₁0 HEA, it was revealed that the asynchronous FCC □HCP martensitic transformation in adjacent grains act as the primary trigger to cracking at grain boundaries [317]. The specific cracking process is illustrated with a series of schematics in Figure 5.12(a). Consider generically two touching FCC grains with distinct cryptographic orientations and propensities to the inception of dislocation slip and martensitic transformation. The one more prone to dislocation slip yet less to martensitic transformation is referred to as the compliant grain, whereas the other more prone to martensitic transformation yet less to slip is referred to as the stiff grain. Upon straining, a relatively large fraction of HCP martensite yet less slip forms in the stiff grain. By contrast, plenty of slip yet less martensite forms in the compliant grain. Since martensitic transformation is usually accompanied by a volumetric contraction, the asymmetrical character of the transformation as well as distinct crystallographic orientations in two adjacent grains inevitably creates a localized strain gradient (justified, for example, by a high density of geometrically necessary dislocations [317]) at where they meet −

the grain boundary. This strain gradient promotes the nucleation and coalescence of microvoids at the grain boundary, ultimately resulting in cracking. The progressive steps of such a fracture mechanism are evidenced in Figure 5.12(b) by an array of SEM images taken at various load levels during in-situ uniaxial tension, in which the lower-left and upper-right grains can be regarded as the stiff and compliant grains, respectively. In actual tests, the matrix-inclusion decohesion is another cracking mechanism in addition to grain boundary decohesion. Nevertheless, this mechanism is secondary in consideration of its scale as a result of a small fraction of inclusions is much smaller than the widespread phase transformation.

## 5.4 Summary and outlook

Analogous to many other metal alloys used today, HEAs as a large family of novel metallic materials may also fail in a brittle manner by cleavage and intergranular fracture or in a ductile manner by the nucleation, growth, and coalescence of microvoids. The HEAs with a single fcc phase normally exhibit greatest fracture resistance with high fracture toughness and impact toughness. On the other extreme, the fracture toughness and impact toughness in most single bcc-phased HEAs are rather low, making them poor fracture-resistant materials. In the middle, the HEAs with multiple phases could have their fracture toughness and impact toughness vary from very small numbers to very large numbers, covering wider fracture-resistance space. Obviously, the fracture behaviors of multi-phase HEAs are much more complex and elusive that those in single-phase ones. The same is also true to the fracture mechanism. The brittle fracture mechanisms in bcc HEAs are quite straightforward to understand. The ductile fracture mechanisms in certain representative fcc HEAs have been exhaustively studied and revealed with advanced microscopic techniques. On the other hand, due to the fact that cracks in multi-phase HEAs may interact in significantly different manners with their microstructures such as the phases and phase interfaces, the fracture mechanisms in these HEAs are least understood.

As of now, the fracture resistance of HEAs has been quantified with the fracture toughness,  $K_{IC}$ , conditional fracture toughness,  $K_Q$ , impact toughness, and crack-tip-opening angle (CTOA). The diversified usages of fracture-resistance parameters, particularly those non-standard ones like  $K_Q$ , create difficulty in ranking the fracture resistance of different HEAs. In future research, it is recommend to follow ASTM or other standards to test and report standard fracture/impact toughness, preferably  $K_{IC}$ . The use of  $K_Q$  should be minimized. Occasionally, different

fracture/impact toughness values were reported for the same alloy in the works by different authors, for example, the AlCoCrFeNi in Refs. [305] and [301] as well as the Al<sub>0.1</sub>CoCrFeNi in Refs. [292] and [293]. This is an implication that certain fracture tests performed were not rigorous and unreliable. More cautions should be taken in future tests to ensure data reliability and reproducibility. The fracture mechanisms revealed for HEAs so far do not distinguish HEAs from conventional dilute alloys. The severe lattice-distortion and sluggish diffusion are two important effects in HEAs. How these effects would affect the deformation, crack initiation, and crack propagation in HEAs is still unclear and barely studied. Tracking down the roles of these core effects in influencing the fracture resistance of HEAs is also a critical direction for the future research.

## **Table Captions**

**Table 5.1** Impact toughness and associated information (phase constitution, processing, temperature T, yield strength  $\sigma_y$ , fracture elongation  $\varepsilon_f$ , and test method) for a variety of high entropy alloys.

**Table 5.2** Fracture toughness  $K_{IC}$ , conditional fracture toughness  $K_Q$ , and associated information (phase constitution, processing, temperature T, yield strength  $\sigma_y$ , fracture elongation  $\varepsilon_f$ , and test method) for a variety of high entropy alloys.

## **Figure Captions**

- Figure 5.1 Ashby plot of the valid fracture toughness,  $K_{IC}$ , against the yield strength, depicting the damage- tolerance domains of HEAs as well as conventional metals and alloys and other material classes [308]. The dashed lines represent the process-zone size  $\frac{1}{\pi} \left( \frac{K_{IC}}{\sigma_f} \right)^2$  at the crack tip. The graphing of HEA domains is based on the data in Table 5.2, with the  $K_Q$  data and some extreme strengths estimated from  $\sigma_y = \frac{H}{3}$  excluded.
- Figure 5.2 Impact energy plotted against the yield strengths for HEAs in comparison with other metals and alloys [308]. The graphing of HEA domains is based on the data in Table 5.1.
- Figure 5.3 Transgranular cleavage with river markings and facets in the Al<sub>1.5</sub>CoCrFeNi HEA with bcc and B2 phases failed at room temperature [293].
- Figure 5.4 Intergranular fracture in the bcc TiZrNbTa HEA failed at room temperature [304].
- Figure 5.5 Hybrid fracture blending dimples and cleavage in the AlCoCrFeNi HEA with a fcc phase and two distinct bcc phases failed at room temperature [305].
- Figure 5.6 Ductile fracture characteristic of numerous dimples in the fcc CoCrFeNiMo HEA [315], failed at room temperature.
- Figure 5.7 Deformation and fracture mechanisms in the (a-e) fcc CrMnFeCoNi and (f) fcc Fe<sub>40</sub>Mn<sub>40</sub>Co<sub>10</sub>Cr<sub>10</sub> revealed by in-situ TEM observations. (a) Formation of a stacking-fault parallelepiped, with faces lying on three sets of {111} planes [312]. (b) Blockage of fast-moving partial dislocations by planar slip bands of perfect dislocations [312]. (c) Dislocation arrays are made sessile by being enclosed inside Twin 1 and Twin 2 [313]. (d) Deflection and blockage of the propagating crack at deformation twin boundaries [313]. (e) Crack bridging [312]. (f) Crack propagation along the twin boundary [314].
- Figure 5.8 (a) Back-scattered image (BEI) of the overall microstructure of the spark-plasmasintered AlCoCrFeNi HEA consisting of spinodally modulated bcc regions

enclosed by fcc "nets" [305]. (b) Secondary electron image (SEI) of the magnified bcc region revealing a spinodally modulated structure composed of ordered and disordered bcc phases [305]. (c) Crack propagation trajectory observed in a fracture test [305].

- Figure 5.9 Microstructures and crack propagation in the CoCrFeNiNb<sub>0.5</sub> HEA with hierarchical, lamellar eutectic Laves and fcc phases [300]. (a) The dark field optical microscopy (OM) image of the eutectic structure. (b) Scanning electron microscopy (SEM) image of the eutectic structure with the top and bottom insets showing the fine and coarse lamella regions, respectively. The crack propagation paths in the (c) fine lamella region and (d) coarse lamella region, which contribute to intrinsic toughening. (e) Extrinsic toughening by crack deflection and bridging.
- Figure 5.10 Crack initiation and propagation in the CoCrFeNiMo<sub>0.2</sub> HEA with a fcc matrix and Cr-rich precipitates [310]. (a) SEM observation of microvoid nucleation by the debonding of the Cr-rich intermetallic particles. (b) Crack tip blunting by plastic deformation. (c) Crack branching. (d) Formation of the tortuous crack propagation path by merging microcracks (evolved from microvoids) into the main crack.
- Figure 5.11 Crack initiation by precipitate-matrix deboning and the breakage of brittle  $\sigma$  precipitates in the precipitate-containing CrFeNiV HEA, which fractured in a ductile fashion [316].
- Figure 5.12 Cracking formation in the mechanically metastable (FCC□HCP martensitic transformation) Fe<sub>45</sub>Mn<sub>35</sub>Co<sub>10</sub>Cr<sub>10</sub> HEA [317]. (a) Schematics and (b) in-situ SEM images progressively showing the cracking mechanism at the grain boundary, triggered by the asynchronous phase transformation in two adjacent grains of different crystallographic orientations.

## 6 Fatigue

Fatigue is the weakening of a material under repeated loading and unloading, and is broadly classified as high-cycle fatigue ( $\sim 10^4 - 10^8$  cycles) and low-cycle fatigue ( $< 10^4$  cycles). High-cycle fatigue takes place when a material is cyclically deformed in the elastic regime at relatively low stress levels (usually less than 2/3 of the yield stress). By contrast, the applied stress in low-cycle fatigue normally exceeds the yield point of a material to induce repeated plastic deformation in it.

Three approaches are commonly used to characterize the fatigue behavior of a material: the stress-life method, the strain-life method, and the linear-elastic fracture mechanics (LEFM) method [318]. High-cycle fatigue is normally quantified by the stress-life method through plotting the magnitude of the cyclic stress (S) against the number of cycles to failure (N), i.e, the S-N curve. Some materials, such as steel and titanium, can manifest a plateau stress on the S-N curve below which the material will not fail for any number of cycles. This plateau stress is referred to as fatigue limit, fatigue strength, or endurance limit. In some other materials, such as aluminum, such a plateau stress is absent. In this case, fatigue limit is customarily decided to be the stress magnitude at a fatigue cycle of  $10^7$ . Owing to plastic deformation, low-cycle fatigue needs to be assessed with a strain-life method, usually presenting the plastic strain ( $\Delta \varepsilon_p$ ) against the number of cycles to failure ( $N_f$ ). Regardless of high cycles or low cycles, a fatigue failure needs to successively experience crack initiation, crack propagation, and ultimate failure, just like material fracture under monotonic loading. Accordingly, both high-cycle fatigue and low-cycle fatigue may be characterized by the LEFM method, specifically, recording the variations of crack-growth rates,  $\frac{da}{dN}$ , with the applied stress intensity factor range,  $\Delta K$ .

The fatigue behavior of HEAs with a variety of microstructures, including the fcc single phase, bcc single phase, multiple phases, and eutectic microstructures, has been studied in air and reported. The vast majority of fatigue studies focuses on high-cycle fatigue using the stress-life method, with some on fatigue-crack-growth behavior and few on low-cycle fatigue. Prior to elaborating the fatigue behavior of each category of HEAs, a few commonly used terms are defined as follows,

$$R = \frac{\sigma_{min}}{\sigma_{max}} \text{ or } \frac{\varepsilon_{min}}{\varepsilon_{max}} \text{ is the fatigue ratio,}$$

$$\sigma_a = \frac{\sigma_{max} - \sigma_{min}}{2} \text{ is the stress magnitude,}$$

$$\varepsilon_a = \frac{\varepsilon_{max} - \varepsilon_{min}}{2}$$
 is the strain magnitude,

$$\Delta K = K_{max} - K_{min}$$
 is the stress intensity factor range,

where  $\sigma_{min}$  and  $\sigma_{max}$  are the minimum and maximum loading stresses,  $\varepsilon_{min}$  and  $\varepsilon_{max}$  are the minimum and maximum loading strains,  $K_{min}$  and  $K_{max}$  are the minimum and maximum stress intensity factors.

# 6.1 Fatigue of face-centered-cubic high-entropy alloys

## 6.1.1 Low-cycle fatigue

The low-cycle fatigue of the fcc CoCuFeMnNi HEA with Cu-rich nano-clusters was examined with uniaxial tensile tests at a strain ratio of R = -1, with the strain amplitude,  $\varepsilon_a$ , varying at four different levels, i.e., 0.5%, 0.75%, 1.0%, and 1.5% [319]. As many other traditional alloys, the low-cycle fatigue behavior of the CoCrFeMnNi HEA follows the classical Coffin-Manson relation

$$\varepsilon_a = \varepsilon_f' (2N_f)^c, \tag{6.1}$$

where  $\varepsilon_f'$  is a constant known as fatigue ductility coefficient,  $2N_f$  is the number of reversals to failure, and c is a constant known as fatigue ductility exponent. Fitting the Coffin-Manson equation to the low-cycle fatigue data gives c = 0.34, slightly lower than the typical range of 0.5-0.7 found for steels [320]. Microstructural analyses suggested that planar slip in this alloy assisted in slip reversibility and thus fatigue resistance whereas the presence of Cu-rich nano-clusters arrested slip reversibility and therefore deteriorated fatigue resistance. It was found additionally that the annealing twin boundaries are less vulnerable to fatigue damage and was supposed to improve the alloy's fatigue performance when present in a large quantity [319].

# 6.1.2 High-cycle fatigue

Among many other HEAs, the high-cycle fatigue behaviors of the fcc CoCrFeMnNi HEAs are mostly studied to date. The studies include the alloys with a single fcc phase as well as those with a fcc matrix and different types of second-phase precipitates, produced by different synthesis techniques and thermo-mechanical treatments. The fatigue strength ( $\sigma_a$ ) and fatigue ratio ( $\frac{\sigma_{af}}{\sigma_{UTS}}$ ) of these alloys, along with other key information such as the processing history, phase constitution,

fatigue testing condition, and strengths are compiled in Table 6.1. Their S-N data in the forms of stress amplitude,  $\sigma_a$ , versus reversals to failure,  $2N_f$ , are all plotted Figure 6.1.

Even though all the data are for the CoCrFeMnNi HEA and its precipitate-containing derivatives, very different fatigue behaviors are noticed in alloys from different reports, primarily due to the variation in microstructures and testing conditions. As a matter of fact, apart from the expectedly minor effect of synthesis techniques and thermo-mechanical processing histories, the phase constitution, grain size, stress ratio R, and fatigue frequency are four major factors that could alter the fatigue properties of the alloys. Though the deconvolution of all four factor is infeasible, the effect of some of these factors can still be inferred from Figure 6.1. Firstly, by separately examining the two groups of alloys, one being those comprised of a single fcc phase (solid circles) and the other being those additionally containing second-phase precipitates (hollow circles), the general trend seen is that the increase in both the grain size and fatigue frequency deteriorates the fatigue resistance. Then, at similar other conditions, the comparison of the single-fcc alloys with those having additional precipitates suggests that the fatigue resistance is worsened by the secondphase precipitates. The stress ratio (R) effect is not unambiguous because of its intermingling with other factors. But, in certain traditional alloys, it was reported that a negative R value (e.g., -1) in comparison with a positive R value (e.g., 0.1) can impart better fatigue resistance than can [321, 322].

In addition, the Basquin equation

$$\sigma_a = A(2N_f)^b, \tag{6.2}$$

was fitted to the measurement data, and the values of the two constants, A and b, for all alloys are listed in Table 6.1.

#### 6.1.3 Fatigue crack growth

The fatigue crack growth of the CoCrFeMnNi HEA at both 293 K and 198 K were examined by carrying out cyclic fatigue tests at a stress ratio R = 0.1 and a frequency of 25 Hz on homogenized and recrystallized disc-shaped compact-tension specimens, according to ASTM E647 [323, 324]. The fatigue crack growth rate,  $\frac{da}{dN_f}$ , as a function of the applied stress intensity range,  $\Delta K$ , for the alloy at both temperatures is replotted in Figure 6.2(a) and the relevant data are compiled in Table 6.2 [324].

Examining Region I, the near threshold region, it is found that reducing the temperature from 293 K to 198 K increases the fatigue threshold of the alloy  $\Delta K_{th}$  from  $\sim 4.8$  MPa· $m^{0.5}$  to 6.3 MPa· $m^{0.5}$ . As  $\Delta K_{th}$  reflects the threshold stress intensity range below which crack growth is suppressed, this result is a clear indication that the cryogenic temperature can markedly improve the alloy's resistance to initial crack growth. This statement is also true in the whole Region I: at a given  $\Delta K$ , the alloy at 198 K constantly exhibits a crack growth rate around one order of magnitude smaller than the alloy at 293 K.

The excellent cryogenic-temperature fatigue property of the alloy in Region I is essentially in accordance with prior findings on its enhanced strengths, ductility, and fracture toughness retrieved from monotonic testing at cryogenic temperatures [18, 47]. Nevertheless, the underlying microstructural mechanisms for the cyclic and monotonic material deformation of the CoCrFeMnNi HEA are different. In cryogenic-temperature fatigue tests, the nanoscale deformation twining, which are routinely found in monotonic tests, disappears [324]. Instead, the planar slip of dislocations was believed to be the dominant deformation mechanism in the cyclically strained alloys at both temperatures, as typified by the cyclic slip steps with sharp edges in Figure 6.2(b) and its inset.

But, salient differences were observed on the crack propagation paths and fracture surface morphologies of the specimens tested at two different temperatures. SEM imaging in Region I of the room-temperature fatigued alloy revealed that cracks propagate predominantly in a transgranular manner [Figure 6.2(b)] with small-scale intergranular crack growths [inset of Figure 6.2(b)]. Conversely, the crack growth in the cryogenic-temperature fatigued alloy primarily follows intergranular paths, as evidenced in Figure 6.2(c). It is easily envisaged that an intergranular crack propagation mode is inclined to engender greater surface asperities between two facing crack flanks than a transgranular mode. Thus, the intergranular fracture in the cryogenic-temperature fatigued alloy indeed promotes roughness-induced crack closure, a well acknowledged crack closure mechanism in the low stress intensity range to lower the crack driving force at the crack tip, thereby strengthening its fatigue resistance [325]. On the contrary, the roughness-induced crack-closure mechanism is minimal in a transgranular fracture mode that produces very limited asperities on fracture surfaces, as in the room-temperature fatigued alloy. Besides, the high strength of the cryogenic-temperature alloy is helpful for retaining the roughness whilst the low strength of the room-temperature alloy makes it susceptible to roughness flattening

by plastic deformation [324]. These factors function jointly to cause greater fatigue resistance of the CoCrFeMnNi HEA at the cryogenic temperature than that at room temperature in Region I.

In Region II, i.e., the stable crack growth region, the CoCrFeMnNi HEA exhibit fairly comparable fatigue crack growth rates at room and cryogenic temperatures. The crack-growth behavior in this region is often described by the Paris power law,

$$\frac{da}{dN_f} = C\Delta K^m, (6.3)$$

where C and m are constants. Fitting the Paris law to the  $\frac{da}{dN_f} - \Delta K$  data in Region II yields m = 3.5 for the alloy tested at 293 K and m = 4.5 for the one tested at 198 K.

Apart from the CoCrFeMnNi HEA, the fatigue crack growth behaviors of the other two fcc HEAs, CoCrFeNi and CoCrFeNiMo<sub>0.2</sub>, at room temperature were also examined at the same stress ratio of R = 0.1 and a similar frequency of 6 Hz using the single-edge-notched tension (SENT) thin plate specimens [326]. Figure 6.2(d) compares the crack growths of all three fcc HEAs at room temperature. Clearly, at a given stress intensity range  $\Delta K$  in Region II, the CoCrFeNi HEA undergoes the fast crack growth, followed by the CoCrFeNiMo<sub>0.2</sub>, then the CoCrFeMnNi. It was suggested that the addition of Mo into the CoCrFeNi lowers the alloy's stacking fault energy [327] and increases the lattice friction and shear modulus, which synergistically promote slip planarity, eventually resulting in enhanced slip reversibility at the crack tip and thus better fatigue crack growth resistance [326]. Considering that planar slip also prevails in the fatigue deformation of the CoCrFeMnNi HEA, it is reasonable to conjecture that its significantly improved fatigue crack growth resistance relative to the CoCrFeNi is ascribed to the same mechanism.

## 6.1.4 Fatigue mechanism

Cyclic deformation in the fcc HEAs (e.g., CoCrFeMnNi, CoCuFeMnNi, and CoCrFeNiMo<sub>0.2</sub>) typically features planar slip. Therefore, they should share a similar fatigue mechanism. Here we take the CoCrFeMnNi as example to illustrate the fatigue mechanism in these fcc HEAs. Under straining, a localized dislocation slip line can act as the fatigue crack initiation site. Since multiple slip lines exist in the alloy, fatigue cracks are anticipated to initiate simultaneously at different locations and coalesce as they grow. The initiation of multiple fatigue cracks at slip lines and their coalescence are evidenced in Figure 6.3(a). Dislocation planarity also

makes fatigue crack propagation no longer follow a typical mode-I mode. Instead, mode-II type crack propagation characteristic of a zig-zag path constitutes the fatigue crack propagation mechanism. Such a mechanism is schematically illustrated in Figure 6.3(b). Considering an initiated crack, the stress field at the crack tip promotes localized dislocation slip, which can further evolves into extrusion/intrusion and eventually a sub-crack upon cyclic loading. Then, the main crack propagates and merges with the sub-crack to form a zig-zag propagation path.

Apart from planar dislocation slip, some researchers also suggested that annealing and deformation twins in the CoCrFeMnNi could serve as the initiate sites and propagation paths of fatigue cracks [328-330]. The competition of planar slip and twin boundaries in initiating and propagating fatigue cracks is elucidated in Figure 6.4 [331]. The SEM images in Figure 6.4(a) and (b), respectively, present the initiation and propagation of fatigue cracks along planar slip bands, which penetrates a twin ahead, and along a twin boundary. Statistical analyses of over a hundred of such SEM and EBSD images with fatigue cracks along either slips bands and/or twin boundaries revealed that the Schmid factor difference between the matrix and twin governs the dominance of which cracking mechanism. Depicted in Figure 6.4(c), irrespective of grain size, the increase in the Schimid factor difference favors twin-boundary cracking and vice versa. At intermediate Schimid factor differences, the dominance of any one of the two fatigue cracking mechanisms is weakened and both categories of cracks can coexist, as indicated by the shaded band in Figure 6.4(c). Furthermore, as the grain size reduces, the threshold value of Schimid factor difference migrates toward smaller values, implying that twin-boundary cracking is facilitated in fine-grained alloys.

In addition, like many other metals and alloys, high-angle grain boundaries are also weak spots prone to fatigue-crack initiation in HEAs. When second-phase precipitates is present in the alloy, they act as additional fatigue crack initiation sites [330].

# 6.2 Fatigue of body-centered-cubic high-entropy alloys

# 6.2.1 High-cycle fatigue

The bcc HfNbTaTiZr HEA is a refractory alloy possessing both high strength and satisfactory ductility, specifically having a yield strength of  $\sim 950$  MPa and an uniform elongation of  $\sim 0.15$  [332, 333]. The high-cycle fatigue properties of this alloy, after being cold-rolled and annealed, were evaluated with four-point bending tests at room temperature [332]. The fatigue

tests on this alloy were intended to carry out at a stress ratio R = 0.1 and a frequency of 10 Hz. Nevertheless, the samples could not be fatigue-failed unless the maximum applied stress,  $\sigma_{max}$ , exceeded the yield stress. As a result, plastic deformation indeed appears in the alloy during the high-cycle fatigue testing, contrasting the elastic deformation constraint in the generic high-cycle fatigue definition. An associated consequence is that the commonly used elastic beam bending equation

$$\sigma_{max} = \frac{3P(S_o - S_i)}{wh^2},\tag{6.4}$$

turns invalid for estimating  $\sigma_{max}$  on the plastically deformed fatigue samples, where P is the applied load,  $S_o$  is the outer span distance,  $S_i$  is the inner span distance, w is the specimen width, and h is the thickness. In other words, the stress distribution through the sample thickness no longer follows a linear elastic distribution. Rather, plastic yielding will take place at the locations where  $\sigma_{max}$  is in excess of the yield stress. The stress distribution in a plastically bent beam is schematically illustrated in Figure 6.5(a), where the nonlinear zones from  $\rho_P$  to  $\frac{h}{2}$  and  $-\rho_P$  to  $-\frac{h}{2}$  indicate the plastic zones.

In this scenario, an elasto-plastic model has to be employed to estimate  $\sigma_{max}$ . With the model outlined in Refs. [332, 334], the maximum stress in the plastic regime,  $\sigma_{max}^p$ , was evaluated and plotted as a function of the number of cycles to failure,  $N_f$ , in Figure 6.5(b). It is seen that all  $\sigma_{max}^p$  data are located in a narrow range between the yield strength,  $\sigma_y$ , and the ultimate tensile strength,  $\sigma_{UTS}$ . The  $\sigma_{max}^p - N_f$  data also exhibit a typical trend that the fatigue life increases with the decreasing stress level until reaching a plateau. In terms of the maximum stress, the fatigue endurance is 966 MPa at  $10^7$  cycles. Plotting the widely used S-N curve in the form of stress amplitude  $\sigma_a^p$  against  $N_f$ , however, does not yield a declining trend as usually observed. Instead, all fatigue data stay around a constant  $\sigma_a^p$  of  $\sim$  430 MPa, as shown in Figure 6.5(c). This is firstly because the plastic deformation confines both  $\sigma_{max}^p$  and  $\sigma_a^p$  in a narrow range, secondly because the actual stress ratio,  $R^p$ , considering the plastic stress is not fixed at the intended value of 0.1. Rather,  $R^p$  varies from 0.105 to 0.145. In terms of the stress amplitude, the fatigue endurance of the HfNbTaTiZr HEA may be thought of as  $\sim$  430 MPa.

It is easily envisioned that in the elasto-plastically fatigued HEA samples, the fatigue failure is majorly dictated by the plastic deformation rather than elasticity as usual. The impact of plastic deformation on the fatigue life of the HfNbTaTiZr HEA can be easily perceived from

a plot of plastic width ratio,  $Pl_w$ , against  $N_f$  in Figure 6.5(d). The plot was generated using the data above a stress level that the specimens assuredly failed, i.e.,  $\sigma_{max}^p > 977 \, MPa$  as marked by the dashed line in Figure 6.5(b) [332].  $Pl_w = 1 - \frac{\rho_p}{\frac{h}{2}}$ , where  $\rho_p$ , the distance from the neutral plane to the initial yielding location, can be evaluated from

$$\int_{\rho_p}^{h/2} \sigma_p(\varepsilon(z)) z dz = \frac{P(S_o - S_i)}{4w} - \frac{\sigma_y \rho_p^2}{3}, \tag{6.5}$$

where  $\sigma_p(\varepsilon(z))$  is the flow stress as a function of the strain. After obtaining a continuous  $\sigma_p(\varepsilon(z))$  function by performing a polynomial regression to the measured uniaxial true plastic flow stress-true plastic strain data, the left side of Equation (6.5) can be evaluated and  $\rho_p$  is thus determined [332]. From Figure 6.5(d), it is clear that the increased plastic width tends to reduce the fatigue life of the alloy. The reliance of the fatigue life of the HfNbTaTiZr HEA on the plastic zone width can be empirically described by  $Pl_w \cdot N_f^{\beta_1} = C_1$ , where  $\beta_1$  and  $C_1$  are constant.

#### 6.2.2 Fatigue crack growth

The fatigue crack growth of the bcc HfNbTaTiZr HEA was studied with the four-point bending tests of single-edge-notched bending (SENB) specimens at a constant stress ratio of R = 0.10 and loading frequency of f = 10 Hz in air and at room temperature [335]. Figure 6.6(a) displays the resulting crack propagation rate,  $da/dN_f$ , as a function of the applied stress intensity factor range,  $\Delta K$ , which obviously gives a Paris slope of m = 2.2 and a fatigue threshold of  $\Delta K_{th} = 2.5 \, MPa \cdot m^{0.5}$ .

# 6.2.3 Fatigue mechanism

The EBSD images of the embryonic and mature cracks confirmed that fatigue cracks initiated in an intergranular manner at grain boundaries on the tensile surface of the sample [332]. Unlike the very flat fracture surface usually seen in intergranular fractures, torn crystallographic structures were noticed on the crack initiation site of the HfNbTaTiZr HEA. The formed non-flat texture is presumably caused by the intersection of the activated slip planes with the grain boundary. Once initiated, the fatigue cracks propagate through grains in a transgranular manner. The crystallographic crack propagation is evidenced by the facets noticed on the fracture surface of the ally failed at  $\Delta K = 3.6 MPa$  in Figure 6.6(b), while numerous tear edges observed on the

fracture surface at  $\Delta K = 10.6 \, MPa$  in Figure 6.6(c) were presumed to be caused by the activation of slip systems unfavorably oriented relative to the model-I loading [335].

# 6.3 Fatigue of metastable high-entropy alloys

## 6.3.1 Low-cycle fatigue

The low-cycle fatigue was conducted on the metastable, dual-phase Fe<sub>50</sub>Mn<sub>30</sub>Co<sub>10</sub>Cr<sub>10</sub> HEA. This transformation-induced plasticity-assisted HEA (TRIP-HEA) consists of a metastable fcc phase ( $\gamma$ ) and a hcp martensite phase ( $\varepsilon$ ), and is best known for its simultaneous achievement of the high strength and ductility via a synergy of interface hardening and transformation-induced hardening as deformation drives a martensitic transformation from  $\gamma$  to  $\varepsilon$  [19].

Two different sets of alloys, one with fine grains (average grain size  $d \approx 5 \ \mu m$ ) and  $\sim 3$  vol% initial  $\varepsilon$  phase and the other with coarse grains (average grain size  $d \approx 10 \ \mu m$ ) and  $< 1 \ \text{vol}\%$  initial  $\varepsilon$  phase, were obtained through different thermo-mechanical processing routes. Their low-cycle fatigue behaviors along with dynamic microstructural evolution were investigated by performing full reversed push-pull loading in a strain-controlled mode, with the applied strain magnitude ( $\frac{\Delta \varepsilon}{2}$ ) varying from 0.23% - 0.6%. The phase evolution upon cyclic deformation is similar to that under monotonic deformation [19], namely, the martensitic transformation marches on till the volume fraction of the  $\varepsilon$  phase reaches beyond 85 vol% [19, 103], as representatively shown by the coarse-grained alloy in Figure 6.7(a). Nevertheless, the mechanical manifestations are different for the two different loading modes. Under the monotonic loading, extensive strain hardening was observed [19]. On the other hand, no appreciable strain hardening in both the fine-grained and coarse-grained HEAs was observed under low-cycle fatigue, as shown in Figure 6.7(b) and (c), respectively [103].

It is, therefore, inferred that the underlying deformation mechanisms for the monotonically and cyclically (in the low-cycle fatigue regime) deformed  $Fe_{50}Mn_{30}Co_{10}Cr_{10}$  HEA are distinct. It was postulated that the absence of strain hardening in the cyclically deformed alloy in the low-cycle fatigue regime is due to the planar nature of slip and partial reversibility of deformation, which impair the interaction between the  $\varepsilon$ -martensite and dislocations [103]. But, this postulation is not quite convincing and may still require further justification.

#### 6.3.2 High-cycle fatigue

The group led by R.S. Mishra modified the  $Fe_{50}Mn_{30}Co_{10}Cr_{10}$  HEA to another two metastable compositions –  $Fe_{42}Mn_{28}Cr_{15}Co_{10}Si_5$  [93, 99] and  $Fe_{38.5}Mn_{20}Co_{20}Cr_{15}Si_5Cu_{1.5}$  [336], in which Si and Cu are used to tune the phase stability of the FCC phase. With the use of multi-pass friction stir processing (FSP), mean grain sizes of ~ 1.97  $\mu$ m and ~ 0.77  $\mu$ m were achieved for the  $Fe_{42}Mn_{28}Cr_{15}Co_{10}Si_5$  [93] and  $Fe_{38.5}Mn_{20}Co_{20}Cr_{15}Si_5Cu_{1.5}$  HEAs, respectively [336]. The high-cycle bending fatigue data of the both alloys, conducted at R = -1 and a frequency of 20 Hz, are provided in Figure 6.8(a), from which it is seen that the fatigue strengths of the  $Fe_{42}Mn_{28}Cr_{15}Co_{10}Si_5$  and  $Fe_{38.5}Mn_{20}Co_{20}Cr_{15}Si_5Cu_{1.5}$  HEAs are ~ 535 MPa and 700 MPa. Taking into account of the ultimate tensile strengths of 1158 MPa for the former and 1126 MPa for the latter, their respective fatigue ratios are 0.46 and 0.62, respectively. In comparison, the  $Fe_{38.5}Mn_{20}Co_{20}Cr_{15}Si_5Cu_{1.5}$  HEA has both higher fatigue strength and fatigue ratio than the  $Fe_{42}Mn_{28}Cr_{15}Co_{10}Si_5$  HEA. Superimposed are the Basquin fits with Equation (6.2), with the values of fitting parameters listed in Table 6.1.

#### 6.3.3 Fatigue crack growth

The Fe<sub>30</sub>Mn<sub>10</sub>Co<sub>10</sub>Cr HEA is another metastable HEA with a fcc matrix ( $\gamma$ ) and a hcp martensite phase ( $\varepsilon$ ). Its fatigue crack growth behavior was investigated on compact tension samples with a stress ratio R = 0.1 and a frequency of 1 Hz, in accordance with ASTM standard E647 [94, 323]. Its crack growth rate,  $\frac{da}{dN_f}$ , as a function of the applied stress intensity range,  $\Delta K$ , is given in Figure 6.9. By fitting Equation (6.3) to the data, the Paris slope is determined to be m = 3.5. The examination of the crack propagation revealed a straight and smooth path in this alloy, in a sharp contrast to the zig-zag crack propagation in the conventional austenitic steels (e.g., Fe<sub>30</sub>Mn6<sub>Si</sub>) with a similar deformation-induced  $\gamma \to \varepsilon$  martensitic transformation [94, 337]. However, the microstructural evolution inspection around the crack tip revealed that extensive plastic deformation had taken place in the  $\varepsilon$  phase. The high plastic deformability of the  $\varepsilon$  phase in the present HEA contrasts its brittleness in conventional metastable austenitic steels, and was believed to slow down the fatigue-crack growth [94]. Like the Fe<sub>50</sub>Mn<sub>30</sub>Co<sub>10</sub>Cr<sub>10</sub> HEA undergoing low-cycle fatigue, deformation twins observed in the monotonic deformation of the same alloy [19] is absent under the cyclic fatigue [94].

## 6.3.4 Fatigue mechanism

The good high-cycle fatigue property of the metastable Fe42Mn28Cr15Co10Si5 HEA is attributed to the delay of crack propagation by crack blunting, crack branching, and crack deflection at the crack tip [93], as illustrated in Figure 6.8(b). One source of crack blunting, branching, and deflection is the localized work hardening entitled by the prevailing FCC □ HCP transformation in the plastic zone [93]. The other source is the formation of deformation twins in the HCP phase in the plastic zone, a direct result of which is that cracks branch or deflect along the formed twin boundaries, as demonstrated in Figure 6.8(c). Likewise, the FCC □ HCP martensitic transformation plays a crucial role in retarding fatigue crack propagation in the metastable Fe38.5Mn20Co20Cr15Si5Cu1.5 HEA [336]. Figure 6.8(d) clearly shows that pronounced FCC □ HCP transformation has taken place in the vicinity of the crack tip. Furthermore, the ultrafine grains in this alloy contribute to delaying fatigue crack initiation.

# 6.4 Fatigue of eutectic high-entropy alloys

# 6.4.1 High-cycle fatigue

The as-cast AlCoCrFeNi<sub>2.1</sub> HEA, abbreviated as EHEA<sub>c</sub>, features a eutectic structure comprising ordered fcc (L1<sub>2</sub>) and bcc (B2) lamellae [338]. Its lamellar structure along with the fraction of each phase is shown by the EBSD image in Figure 6.10(a). The magnified eutectic structure further reveals that the bcc phase contains numerous Cr-rich nanoprecipitates [338], as pointed out by the arrow in the BSE image of Figure 6.10(b). Subjecting EHEA<sub>c</sub> to 50% cold-rolling followed by heat treatment at 700 °C for 12 h induced the recrystallization of both fcc and bcc phases, ultimately leading to a hierarchical eutectic structure in the worked HEA, hereafter referred to as EHEA<sub>w</sub>. The recrystallized eutectic structure in EHEA<sub>w</sub> is illustrated by the EBSD image in Figure 6.10(c). The structural hierarchy can be viewed from the enlarged BSE image in Figure 6.10(d), from which it is seen that B2 particles of various morphologies precipitate out in the ordered fcc lamellae while Cr-rich nanoparticles are detected within the ordered bcc lamellae.

The high-cycle bending fatigue of both EHEA<sub>c</sub> and EHEA<sub>w</sub> was investigated with a custom-made tabletop mini-fatigue fixture at R = -1 and 20 Hz frequency [338]. The resulting S-N curves for both alloys are presented in Figure 6.10(e). It is clear that the hierarchy in the eutectic structure bestow improved fatigue life on EHEA<sub>w</sub> in comparison to EHEA<sub>c</sub> at any identical stress

amplitude. Also, EHEA<sub>w</sub> possesses an endurance limit of  $\sim 500$  MPa, which is 28.2% higher than  $\sim 390$  MPa for EHEA<sub>c</sub>. Lines in Figure 6.10(e) are Basquin fits with Equation (6.2), with the values of fitting parameters given in Table 6.1.

#### 6.4.2 Fatigue mechanism

The fatigue mechanism of both alloys were investigated by examining crack initiation and propagation separately, according to that the total number of cycles to failure can be decomposed into number of cycles to crack initiation and number of cycles to crack propagation, i.e.,  $N_f = N_i + N_p$ . For addressing the number of cycles to crack initiation,  $N_i$ , the full history of fatigue cycles at  $\sigma_a = 600 \, MPa$  for EHEA<sub>c</sub> and 700 MPa for EHEA<sub>w</sub> is plotted in Figure 6.10(f). The crack initiation can be detected as an abrupt change in the slope of the curves. The fatigue cycles at which crack initiation is detected for EHEA<sub>c</sub> and EHEA<sub>w</sub> are 30,000 and 85,000 cycles, respectively, as indicated in Figure 6.10(f). Clearly, the hierarchical eutectic structure substantially postpones crack initiation in EHEA<sub>w</sub>, even at a higher stress amplitude than that in EHEA<sub>c</sub>.

It is known that fatigue cracks usually initiate along persistent slip bands (PSBs) or at the locations that PSBs interact with grain boundaries or twin boundaries [338, 339]. In the eutectic structure of EHEA<sub>c</sub>, clearly defined PSBs can be easily trigged in the fcc phase through planar slips, as depicted in Figure 6.10(g). These straight, well-defined PSBs in EHEA<sub>c</sub> are low energy pathways for facilitated fatigue crack initiation either along them or at the fcc-bcc interfaces. On the other hand, planar slips and thus straight PSBs are hindered in EHEA<sub>w</sub> due to the presence of B2 particles in the fcc phase. Instead, the B2 particles tend to bend or deviate PSBs, as shown in Figure 6.10(h), through which PSBs are broken into small segments to delay the crack initiation.

The B2 particles in the fcc phase is also supposedly to improve the number of cycles to crack propagation  $(N_p)$  in EHEA<sub>w</sub> by deflecting the crack propagation paths. Counterintuitively, Figure 6.10(f) sees a shorter  $N_p$  in EHEA<sub>w</sub> than in EHEA<sub>c</sub>. This reason for this unexpected tendency is still unclear and may deserve further investigations.

# 6.5 Fatigue of multi-phase Al-Cr-Fe-Ni high-entropy alloys

# 6.5.1 High-cycle fatigue

In the Al-Cr-Co-Fe-Ni HEA system, the high-cycle fatigue properties of the Al<sub>0.5</sub>CoCrCuFeNi [340, 341], Al<sub>0.3</sub>CoCrFeNi [342], and Al<sub>0.7</sub>CoCrFeNi [343] have been characterized. As shown in Figure 6.11(b), the Al<sub>0.5</sub>CoCrCuFeNi has a duplex microstructure comprising of a dendritic fcc phase (dark color) and a Cu-rich interdendritic fcc phase (light color) [340]. The Al<sub>0.3</sub>CoCrFeNi is characteristic of a triplex microstructure containing the ultrafine-grained fcc matrix phase, and nano-sized B2 and tetragonal Fe-Cr-rich σ precipitates formed at grain interiors and boundaries, as shown by the EBSD phase map in Figure 6.11(c) [342]. The homogenized Al<sub>0.7</sub>CoCrFeNi [343] consists of fcc and B2 phases while the annealed Al<sub>0.7</sub>CoCrFeNi is composed of fcc and B2 phases plus nano-sized L12 precipitates, as shown in Figure 6.11(d) and (e), respectively.

The room-temperature bending fatigue properties were examined at R = 0.1 and a frequency of 10 Hz for the Al<sub>0.5</sub>CoCrCuFeNi HEA [340, 341] whereas at R = -1 and 20 Hz frequency for the Al<sub>0.3</sub>CoCrFeNi [342] and Al<sub>0.7</sub>CoCrFeNi HEA [343]. The *S-N* curves along with Basquin fits for all alloys are given in Figure 6.11(d) [340-342], while detailed fatigue data along with other associated information are listed in Table 6.1. When comparing the Al<sub>0.3</sub>CoCrFeNi with the Al<sub>0.7</sub>CoCrFeNi of two distinct microstructures, it is clear that they all have comparable fatigue performance, with the fatigue strengths in the range of 410 - 460 MPa. It may imply that the fatigue properties of the Al<sub>x</sub>CoCrFeNi HEAs are insensitive to microstructural alternations. On the other hand, both the Al<sub>0.3</sub>CoCrFeNi and Al<sub>0.7</sub>CoCrFeNi HEAs manifests superior fatigue resistance to the Al<sub>0.5</sub>CoCrCuFeNi HEA, who has a fatigue strength of 360 MPa. Note that the Al<sub>0.5</sub>CoCrCuFeNi HEA made from high purity raw materials (> 99.9%) and with minimized preexisting defects is selected for comparison. The same HEAs made from less pure raw materials were reported to exhibit great scatter in their *S-N* fatigue data due to the presence of pre-existing defects such as aluminum oxides, cracks and pores introduced during casting or cold-rolling [340, 341].

#### 6.5.2 Fatigue crack growth

The fatigue crack growth of the as-cast Al<sub>0.2</sub>CrFeNiTi<sub>0.2</sub> and AlCrFeNi<sub>2</sub>Cu HEAs, both having a dendritic structure composed primarily of fcc and bcc phases, was studied at a frequency of 20 Hz according to ASTM E647 [303, 323]. At a stress ratio R = 0.1, the crack growth rate,  $\frac{da}{d}N_f$ , as a function of the stress intensity range,  $\Delta K$ , for both alloys is comparatively plotted in Figure 6.12(a) [303]. Compared to the Al<sub>0.2</sub>CrFeNiTi<sub>0.2</sub> HEA, which has a fatigue threshold of  $\Delta K_{th} = 16~MPa \cdot m^{0.5}$  and Paris slope of m = 4.9, the AlCrFeNi<sub>2</sub>Cu HEA possess a slightly larger  $\Delta K_{th}$  of 17  $MPa \cdot m^{0.5}$  and smaller m of 3.4. In both the near threshold region (Region I) and the stable crack growth region (Region II), the latter shows greater crack growth resistance than the former. As in many other conventional metals [344-346], Figure 6.12(b) shows that increasing the stress ratio, R, tends to shift the entire crack growth curve towards the small  $\Delta K$  region (smaller  $\Delta K_{th}$ ), thereby deteriorating the crack propagation resistance of the alloy. More fatigue crack growth data of these two alloys can be found from Table 6.2.

Fractographic examinations with SEM revealed that the AlCrFeNi<sub>2</sub>Cu HEA exhibited fatigue striation in the Paris law regime, and a combination of faceted brittle cleavage and ductile dimple-like features in the final failure stage, whereas the fracture surfaces of the Al<sub>0.2</sub>CrFeNiTi<sub>0.2</sub> HEA is characteristic of much more extensive faceted brittle appearance with very limited ductile dimple-like features [303]. The observed fractographic features are well correlated with their respective crack growth rates, i.e., the relatively large-scale ductile fracture features in the AlCrFeNi<sub>2</sub>Cu HEA retards the crack growth rate in this alloy whilst the predominance of brittle fracture features in the Al<sub>0.2</sub>CrFeNiTi<sub>0.2</sub> HEA makes it amenable to fast crack growth.

#### 6.5.3 Fatigue mechanisms

#### 6.5.3.1 In Al<sub>0.5</sub>CoCrCuFeNi

A very first act to comprehend the fatigue mechanism is to examine fractographs. Figure 6.13(a) gives the overall view of the fatigue-failed surface of the Al<sub>0.5</sub>CoCrCuFeNi HEA made from high purity raw materials (> 99.9%) [341]. Like many other crystalline metals, three distinct regions can be recognized: the crack initiation region, the stable crack propagation region, and the fast fracture region. The zoomed-in image of each region is given separately in Figure 6.13(b) and (c). In Figure 6.13(b), it is obvious the fatigue cracks initiate from multiple pores (and/or oxide

inclusions), thereafter leading to varyingly oriented striations in the course of crack propagation. In the stable crack propagation region in Figure 6.13(c), a mix of fatigue striations and cleavage facets is seen, indicating that the fatigue cracks propagate in both ductile and brittle manners. Finally, the fast fracture region in Figure 6.13(d) manifests numerous dimples, implying ductile fracture in this region. The initiation of fatigue cracks from oxides is confirmed by a spotlighted oxide in Figure 6.13(e) [341], around which fatigue cracks initiate and extensive plastic deformation is noted. In addition, fatigue cracks are also noticed to form along slip bands as shown in Figure 6.13(f) [341].

Further TEM analyses of the undeformed structure revealed that the HEA contained nanotwins and tangled dislocations even prior to fatigue testing. Cyclic deformation triggered the evolution of more pronounced nanotwins and tangled dislocations. It was anticipated that a large amount of nanotwins had already been induced by cyclic deformation prior to crack initiation. The nanotwins promote working hardening, delay crack initiation, and contribute to the fatigue resistance of the alloy [18, 341].

# 6.5.3.2 In Al<sub>0.3</sub>CoCrFeNi

In the Al<sub>0.3</sub>CoCrFeNi HEA with fcc, B2 and  $\sigma$  phases, fatigue cracks were observed to initiate and propagate along the interface between the fcc matrix and hard second phase particles (B2 and  $\sigma$ ), as illustrated in Figure 6.14(a) [342]. These interfacial cracks are believed to be transformed from the accumulation of numerous geometrically necessary dislocations (GNDs) at the phase interfaces, which are necessary to accommodate compatible deformation of different phases [342]. Analogous to the duplex Al<sub>0.5</sub>CoCrCuFeNi HEA, extensive micro- and nano-sized deformation twins were observed in the fcc matrix of the triplex Al<sub>0.3</sub>CoCrFeNi HEA as shown in Figure 6.14(b), which can intensify working hardening, and thus give rise to a high fatigue strength [342]. The pile-up of dislocations at fcc/B2 or fcc/ $\sigma$  interfaces is thought to advocate the formation of deformation nano-twins [342].

## 6.5.3.3 In Al<sub>0.7</sub>CoCrFeNi

The crack trajectories of the Al<sub>0.7</sub>CoCrFeNi HEA with two different microstructures, one consisting of fcc and B2 phases while the other comprising fcc, B2, and L1<sub>2</sub> nano-sized particles, are shown in Figure 6.15(a) and (b), respectively [343]. In both cases, the cracks can initiate from

two locations, that is, at the fcc/B2 lamellar phase boundaries and at persistent slip bands (PSBs). Crack propagation in a zigzag pattern along the persistent slip bands is observed for both cases. By measuring the angles made by intersecting persistent slip bands, it is confirmed the activation of various {111}<10> slip systems. The presence of the L1<sub>2</sub> nano-sized particles seems not affect the fatigue mechanism appreciably. It was inferred that these nano-sized precipitates were sheared by dislocations during cyclic deformation, thereby not resulting in appreciable difference in the fatigue performance of the alloy with two distinct microstructures.

# 6.6 Fatigue of films

The fatigue characterization of HEA films is still nascent. Two preliminary studies were carried out on the fcc CoCrFeNi film [347] and the (FeCoNi)<sub>25</sub>(AlTiZr)<sub>75</sub> film with a mixture of fcc and the amorphous phases [348], by means of dynamic nanoindentation testing. As the surface of thin films is cyclically loaded at a given frequency, fatigue failure will take place at certain cycles.

The fatigue failure in the  $\sim 2.98~\mu m$  CoCrFeNi film sputtered on the Si substrate was probed by monitoring the changing rate of the nanoindentation penetration depth with respect to the fatigue cycle (i.e.,  $\frac{dh}{dc}$ ) as fatigue marches on [347]. It was revealed that the nanotwined CoCrFeNi films with a grain size of  $\sim 7.8~nm$  exhibit history-independent fatigue responses with  $\frac{dh}{dc}$  being almost zero throughout full cycles, in contrast to the progressive failure in the bulk, coarse-grained counterparts with positive  $\frac{dh}{dc}$  values, as schematically shown in Figure 6.16(a). The variations in  $\frac{dh}{dc}$  imply that the nanotwined CoCrFeNi film has superior fatigue resistance to its coarse-grained counterpart, as also confirmed by the atomic force micrographs of damaged surfaces [347].

Another way of examining the nanoindentation fatigue in films is to detect the sudden drop of the contact stiffness as fatigue cycle increases. This was adopted in the fatigue study of the  $(FeCoNi)_{25}(AlTiZr)_{75}$  film [348]. As shown in Figure 6.16(b), a sudden drop in the contact stiffness of the film is noticed to happen at the time of 312 s, corresponding to a fatigue life of  $1.40 \times 10^4$  cycles.

Like other thin films, the nanoindentation fatigue mechanism in HEA thin films is thought to follow three consecutive stages: compressional deformation stage, the buckling and layering stage, and the crack and delamination stage, as schematically depicted in Figure 6.16(c). The sudden drop of the contact stiffness, which signifies the initiation of the fatigue failure, occurs in the second stage.

## 6.7 Comparison

# 6.7.1 High-cycle fatigue

The fatigue strength  $\sigma_{af}$ , fatigue ratio  $\frac{\sigma_{af}}{\sigma_{UTS}}$ , and coefficients of the Basquin fitting equation of all HEAs characterized to date in air and at room temperature are compiled in Table 6.1. Alongside given is relevant information on processing, microstructure, testing, and uniaxial mechanical properties. The compilation only takes into account the alloys that have experienced cyclic elastic deformation but excluding the bcc HfNbTaTiZr HEA in which plasticity already set in. While the high-cycle fatigue *S-N* data of the HEAs categorized in the same group by phase constitution are compared and discussed in the preceding sections, the high-cycle fatigue of HEAs of distinct alloy categories are compared in Figure 6.17(a) by picking representative alloys from each category. For clarity, the *S-N* data for each HEA are overlaid with trend lines resembling Basquin fits. It is reminded that the HEAs in comparison have different grain sizes. Also, most of the HEAs have fatigue tests conducted at a stress ratio R = -1 with the only exception being the duplex Al<sub>0.5</sub>CoCrCuFeNi HEA with R = 0.1. The loading frequencies are in the rang of 10 - 30 Hz.

From Figure 6.17(a), it is seen that the Fe<sub>42</sub>Mn<sub>28</sub>Cr<sub>15</sub>Co<sub>10</sub>Si<sub>5</sub> HEA with a metastable fcc phase and a hcp martensite phase exhibits a highest fatigue strength of 535 MPa, followed by the wrought eutectic AlCoCrFeNi<sub>2.1</sub> (EHEA<sub>w</sub>) with a fatigue strength of 469 MPa, the triplex Al<sub>0.3</sub>CoCrFeNi at a level of 450 MPa, and the duplex Al<sub>0.7</sub>CoCrFeNi with 410 MPa. The duplex Al<sub>0.5</sub>CoCrCuFeNi have an intermediate fatigue strength of 361 MPa. The lowest fatigue strength occur to the fcc CoCrFeMnNi, with a value of 190.

To offset the strength effect in Figure 6.17(a), the fatigue ratio is obtained by normalizing the fatigue strength  $\sigma_{af}$  by the ultimate tensile strength  $\sigma_{UTS}$  and plotted in Figure 6.17(b). This time, the metastable Fe<sub>42</sub>Mn<sub>28</sub>Cr<sub>15</sub>Co<sub>10</sub>Si<sub>5</sub> remain on the top, followed by the triplex Al<sub>0.3</sub>CoCrFeNi HEA and then the duplex Al<sub>0.7</sub>CoCrFeNi. The duplex Al<sub>0.5</sub>CoCrCuFeNi sinks to the very bottom, just next to the fcc CoCrFeMnNi. The wrought eutectic AlCoCrFeNi<sub>2.1</sub> HEAs

(EHEA<sub>w</sub>) is located in the middle. Considering Figure 6.17(a) and (b) jointly, the metastable Fe<sub>42</sub>Mn<sub>28</sub>Cr<sub>15</sub>Co<sub>10</sub>Si<sub>5</sub> HEA possess superior fatigue resistance to all other HEAs. On the other hand, the fatigue resistance of fcc CoCrFeMnNi is close to the worst.

Prior comparisons with other crystalline and non-crystalline alloys indicate that the fatigue strength and fatigue ratio of the duplex Al<sub>0.5</sub>CoCrCuFeNi outperformed some steels, aluminum steels, nickel alloys, titanium alloys, and superalloys [258, 340, 341]. Considering that the duplex Al<sub>0.5</sub>CoCrCuFeNi HEA is a low performer in Figure 6.17(b) and a middle performer in Figure 6.17(a), it is not implausible to infer that the majority of HEAs investigated so far have superior fatigue resistance to many conventional metallic materials.

From Table 6.1, it is seen that the investigated HEAs have fatigue ratios,  $\frac{\sigma_{af}}{\sigma_{UTS}}$ , varying from 0.2 to 0.62. Comparing to many steels, aluminum alloys, magnesium alloys, nickel alloys, titanium alloys, and bulk metallic glasses which have  $0.15 \le \frac{\sigma_{af}}{\sigma_{UTS}} \le 0.35$  [332], HEAs shift up to a high-fatigue-ratio region.

## 6.7.2 Fatigue crack growth

Likewise, important fatigue-crack-growth properties of investigated HEAs such as the threshold stress intensity  $\Delta K_{th}$  and Paris slope m are complied in Table 6.2 along with associated information. The crack growth rate  $\frac{da}{d}N_f$  as a function of the stress intensity  $\Delta K$  for HEAs tested at room temperature, a stress ratio of R=0.1, and loading frequencies from 1 Hz to 25 Hz is selected to plot in Figure 6.18 for comparison. In terms of the threshold stress intensity  $\Delta K_{th}$ , the bcc HfNbTaTiZr holds a smallest value of 2.5  $MPa \cdot m^{0.5}$  (easiest fatigue crack initiation), followed by the fcc CoCrFeMnNi with  $\Delta K_{th}=4.8~MPa \cdot m^{0.5}$ , the duplex Al<sub>0.2</sub>CrFeNiTi<sub>0.2</sub> with  $\Delta K_{th}=16~MPa \cdot m^{0.5}$ , and lastly the duplex AlCrFeNi<sub>2</sub>Cu with  $\Delta K_{th}=17~MPa \cdot m^{0.5}$  (hardest fatigue crack initiation). In the nearly full stress intensity range, the duplex AlCrFeNi<sub>2</sub>Cu has the slowest fatigue growth rate while the highest is found to the fcc CoCrFeNi and CoCrFeNiMo<sub>0.2</sub>. All other HEAs have intermediate fatigue crack growth rates. Overall, the bcc HfNbTaTiZr HEAs has the most inferior fatigue-crack growth resistance while the resistance in the duplex AlCrFeNi<sub>2</sub>Cu is the most superior.

In prior comparisons, it was suggested that the fatigue-crack-growth resistance of the fcc CoCrFeMnNi HEA exceeded the Inconel 718 superalloy and was comparable to the 304L steel,

TWIP-XIP1000 steel, and Zr<sub>41.2</sub>Ti<sub>13.8</sub>Cu<sub>12.5</sub>Ni<sub>10</sub>Be<sub>22.5</sub> bulk metallic glass [258, 324]. Considering that the duplex Al<sub>0.2</sub>CrFeNiTi<sub>0.2</sub> and AlCrFeNi<sub>2</sub>Cu HEAs outperform the CoCrFeMnNi, it implies that the two Al-containing HEAs are in possession of favorable fatigue-crack-growth resistance in comparison with many conventional metal alloys.

# 6.8 Summary and outlook

The fatigue behaviors of a couple of bulk HEAs with varying compositions and microstructures have been investigated. The investigations essentially cover bulk HEAs with single face-centered cubic phase (e.g., CoCrFeMnNi), single body-centered cubic phase (e.g., HfNbTaTiZr), dual phases accompanying phase transformation (e.g., Fe<sub>50</sub>Mn<sub>30</sub>Co<sub>10</sub>Cr<sub>10</sub> and Fe<sub>42</sub>Mn<sub>28</sub>Cr<sub>15</sub>Co<sub>10</sub>Si<sub>5</sub>), eutectic phases (e.g., AlCoCrFeNi<sub>2.1</sub>), and multiple phases (e.g., Al<sub>0.3</sub>CoCrFeNi and AlCrFeNi<sub>2</sub>Cu). The investigation primarily focused on the high-cycle fatigue and fatigue crack growth, with few on the low-cycle fatigue. Nearly all the fatigue tests were conducted in air at room temperature with a few at cryogenic temperatures. Fatigue mechanisms in certain HEAs were suggested by virtue of fractographic or microstructural observations with microscopes such as scanning electron microscopes (SEM) and transmission electron microscopes (TEM). Overall, fatigue data in bulk HEAs are rather scattered, with some exhibiting superior fatigue resistance to many conventional metallic materials at comparable conditions. In addition, there are also some initial attempts in examining the fatigue behavior of HEA films [e.g., CoCrFeNi and (FeCoNi)<sub>25</sub>(AlTiZr)<sub>75</sub>] with nanoindentation techniques.

Nevertheless, what we can only draw from the existing scattered data is that certain HEAs may potentially serve as high fatigue-resistant structural components. But, this is not conclusive until we do more in-depth fatigue investigations, particularly in revealing the fatigue mechanisms linked with their excellent fatigue resistance. Fatigue mechanisms disclosed in alike alloys are sometimes contradictory. For instance, in one study of the fcc CoCuFeMnNi it was suggested that twin boundaries were resistant to fatigue damage [319] while in the other of CoCrFeMnNi they become crack initiation sites [331]. Besides, the present studies are mostly limited to in-air and room-temperature conditions. Considering that many HEAs particularly those known as refractory HEAs have great potential for high-temperature applications, such as in gas turbine engines, investigations of the thermal fatigue or the fatigue at elevated temperatures of these alloys should be considered in the future research. Likewise, some HEAs exhibit remarkable corrosion resistance

[349-352] and may be promising for applications in corrosive environments (e.g., bio-applications in human bodies). In consideration of this potential, it is also meaningful to evaluate the corrosion fatigue of HEAs with potential applications in corrosive environments.

# **Table Captions**

**Table 6.1** High-cycle fatigue properties (fatigue strength  $\sigma_{af}$ , fatigue ratio  $\frac{\sigma_{af}}{\sigma_{UTS}}$ , and coefficients of the Basquin equation) of HEAs in air and at room temperature. Alongside shown is the information on the thermomechanical processing, phase constitution, average grain size d, uniaxial yield strength  $\sigma_y$ , ultimate tensile strength  $\sigma_{UTS}$ , and fatigue testing parameters such as the stress ratio R and loading frequency f.

**Table 6.2** Fatigue crack growth properties (threshold stress intensity range  $\Delta K_{th}$  and Paris slope m) of HEAs. Alongside shown is the information on thermomechanical processing, phase constitution, grain size d, testing temperature T, stress ratio R, testing frequency f, and testing method.

# **Figure Captions**

- Figure 6.1 S-N data, in terms of the stress amplitude  $\sigma_a$  against the number of reversals to failure  $2N_f$ , of the CoCrFeMnNi HEAs tested at different conditions, lines indicating the Basquin fits. Associated alloy and testing information is found in Table 6.1.
- Figure 6.2 (a) Fatigue crack growth rate,  $\frac{da}{dN}$ , versus the applied stress intensity range,  $\Delta K$ , of the CoCrFeMnNi HEA at 293 K and 198 K [324]. Fractographs of the CoCrFeMnNi HEA fatigued at (b)  $\Delta K \approx 6 \, MPa \cdot m^{0.5}$  and 293 K and (b)  $\Delta K \approx 6.9 \, MPa \cdot m^{0.5}$  and 198 K [324]. (c) Comparison of the fatigue crack growth rates of three fcc HEAs, namely, the CoCrFeN, CoCrFeNiMo<sub>0.2</sub> and CoCrFeMnNi at room temperature. Lines are the Paris-law fits, and  $\Delta K_{th}$  is the threshold stress intensity range. Other details about the alloys and fatigue tests can be found in Table 6.2.
- Figure 6.3 Planar-slip governed fatigue mechanism in the fcc CoCrFeMnNi HEA [353]. (a) Concurrent fatigue crack nucleation and propagation along multiple planar slip lines, as indicated red lines. Microcracks formed at slip lines merge subsequently, leading to crack tips indicated by two white arrows. (b) Schematic illustration of fatigue crack propagation in a zig-zag fashion promoted by slip planarity.
- Figure 6.4 Competition between planar slip-band cracking and twin-boundary cracking in the fatigue of the CoCrFeMnNi HEA [331]. SEM images of (a) planar slip-band cracking with apparent extrusions/intrusions and (b) twin-boundary cracking. (c) The influence of Schmid factor difference and grain size on the competition between slip-band cracking and twin-boundary cracking.
- Figure 6.5 High-cycle fatigue behavior of the plastically deformed bcc HfNbTaTiZr HEA [332]. (a) Schematic stress distribution in a plastically bent beam, where the plastic zones range from  $\rho_P$  to  $\frac{h}{2}$  and from  $-\rho_P$  to  $-\frac{h}{2}$ . S-N data plotted in terms of (b) the maximum plastic stress  $\sigma_{max}^p$  versus the number of cycles to failure  $N_f$ , and (c) the

stress amplitude  $\sigma_a^p$  versus  $N_f$ . (d) Variation of the plastic width ratio,  $Pl_w = 1 - \frac{\rho_p}{\frac{h}{2}}$ , with  $N_f$  at  $\sigma_{max}^p > 977$  MPa, i.e., the data above the dashed line in (b).

- Figure 6.6 High-cycle fatigue in the bcc HfNbTaTiZr HEA [335]. (a) Crack growth rate. Fractographs at (b)  $\Delta K = 3.6 \, MPa$  and (c)  $\Delta K = 10.6 \, MPa$ .
- Figure 6.7 Low-cycle fatigue behavior of the metastable Fe<sub>50</sub>Mn<sub>30</sub>Co<sub>10</sub>Cr<sub>10</sub> HEA [103]. (a) Upon cyclic deformation at a strain amplitude  $\frac{\Delta \varepsilon}{2} = 0.6\%$ , about 95 vol% metastable fcc phase (γ) transforms into the hcp martensite phase (ε) in the coarse-grained HEA with an average grain size of ~10 μm, who originally contains less than 1 vol% ε. Stress amplitude  $\sigma_a$  against the number of fatigue cycles N at the strain amplitude 0.23%  $\leq \frac{\Delta \varepsilon}{2} \leq 0.6\%$  for (b) the fine-grained HEA with an average grain size of 5 μm and (c) the coarse-grained HEA with an average grain size of 10 μm.
- Figure 6.8 High-cycle fatigue behaviors of the metastable Fe<sub>42</sub>Mn<sub>28</sub>Cr<sub>15</sub>Co<sub>10</sub>Si<sub>5</sub> with a mean grain size of 1.97 μm [93] and Fe<sub>38.5</sub>Mn<sub>20</sub>Co<sub>20</sub>Cr<sub>15</sub>Si<sub>5</sub>Cu<sub>1.5</sub> with a mean grain size of 0.77 μm [336]. (a) *S-N* data in terms of the stress amplitude σ<sub>a</sub> against reversals to failure 2N<sub>f</sub>, the lines indicating the Basquin fits. Crack propagation trajectories in the Fe<sub>42</sub>Mn<sub>28</sub>Cr<sub>15</sub>Co<sub>10</sub>Si<sub>5</sub> HEA [93], revealing (b) crack deflection and branching and (c) crack branching along the twin boundaries. (d) EBSD phase map at the vicinity of the crack tip of the Fe<sub>38.5</sub>Mn<sub>20</sub>Co<sub>20</sub>Cr<sub>15</sub>Si<sub>5</sub>Cu<sub>1.5</sub> HEA [336].
- Figure 6.9 Fatigue crack growth rate along with the Paris law fit of the Fe<sub>30</sub>Mn<sub>10</sub>Co<sub>10</sub>Cr HEA, which is composed of a metastable fcc matrix and a hcp martensite phase [94].
- Figure 6.10 Microstructures and fatigue properties of the AlCoCrFeNi<sub>2.1</sub> eutectic HEA comprising ordered fcc (L1<sub>2</sub>) and bcc (B2) lamellae [338]. (a) EBSD phase map of the as-cast alloy, EHEA<sub>c</sub>. (b) BSE image of EHEA<sub>c</sub> with the arrow pointing to Crrich nanoprecipitates in the bcc phase. (c) EBSD phase map of the wrought alloy, EHEA<sub>w</sub>. (d) BSE image of EHEA<sub>w</sub> revealing Cr-rich nanoprecipitates in the bcc phase and B2 particles in the fcc phase. (e) *S-N* curves of EHEA<sub>c</sub> and EHEA<sub>w</sub> with

the Basquin fits. (f) Full history of fatigue cycles at  $\sigma_a = 600 \, MPa$  for EHEA<sub>c</sub> and 700 MPa for EHEA<sub>w</sub>. (g) BSE image of the fatigued EHEA<sub>c</sub> showing the formation of straight PSBs in the fcc phase. (h) BSE image of the fatigued EHEA<sub>w</sub> showing the formation of curved PSBs by the deflection of B2 particles in the fcc phase.

- Figure 6.11 (a) *S-N* curves of the Al<sub>0.5</sub>CoCrCuFeNi [341], Al<sub>0.3</sub>CoCrFeNi [342], and Al<sub>0.7</sub> CoCrFeNi [343] HEAs along with the Basquin fits. (b) SEM micrograph showing that the Al<sub>0.5</sub>CoCrCuFeNi HEA has a duplex microstructure comprising of a dendritic fcc phase (dark color) and a Cu-rich interdendritic fcc phase (light color) [340]. (c) EBSD phase map of the Al<sub>0.3</sub>CoCrFeNi HEA showing a triplex microstructure containing the ultrafine-grained fcc matrix phase, and nano-sized B2 and tetragonal Fe-Cr-rich σ precipitates [342]. EBSD phase maps and SEM micrographs of the Al<sub>0.7</sub>CoCrFeNi HEA with two different lamellar microstructures, (d) fcc and B2 phases, (e) fcc, B2, and nano-sized L1<sub>2</sub> precipitates [343].
- Figure 6.12 Fatigue crack growth behavior of the  $Al_{0.2}$ CrFeNiTi<sub>0.2</sub> and AlCrFeNi<sub>2</sub>Cu HEAs [303]. (a) Fatigue crack growth rate and Paris law fits of both HEAs at a stress ratio of R = 0.1. (b) Effect of the stress ratio R on the fatigue crack growth rate of the  $Al_{0.2}$ CrFeNiTi<sub>0.2</sub> HEA.
- Figure 6.13 Fracture morphologies of the Al<sub>0.5</sub>CoCrCuFeNi HEA made from high purity raw materials (> 99.9%), failed at  $\sigma_a = 495$  MPa [341]. (a) Overall view. (b) The crack initiation region. (c) The stable crack propagation region. (d) The fast fracture region. (e) Initiation of fatigue cracks from oxides. (f) Formation of cracks along slip bands.
- Figure 6.14 Fatigue mechanism in the Al<sub>0.3</sub>CoCrFeNi HEA with fcc, B2 and  $\sigma$  phases [342]. (a) Formation of fatigue cracks along the interface between the fcc matrix and hard second phase particles (B2 and  $\sigma$ ). (b) Extensive micro- and nano-sized deformation twins in the fcc matrix to intensify working hardening and thus fatigue resistance.

- Figure 6.15 The crack trajectories of the Al<sub>0.7</sub>CoCrFeNi HEA with two different microstructures [343]. (a) fcc and B2 phases. (b) fcc, B2, and L1<sub>2</sub> nano-sized particles.
- Figure 6.16 Nanoindentation fatigue of HEA thin films. (a) The changing rate of the nanoindentation penetration depth with respect to the fatigue cycle,  $\frac{dh}{dc}$ , against the fatigue cycle for the coarse-grained and nanotwined CoCrFeNi films at different impact energies [347]. (b) Variation of the contact stiffness over time for the (FeCoNi)<sub>25</sub>(AlTiZr)<sub>75</sub> film, on which the sudden drop in the contact stiffness marks the initiation of fatigue [348]. (c) Three stages of nanoindentation fatigue mechanics of thin films: compressional deformation stage, the buckling and layering stage, and the crack and delamination stag [348].
- Figure 6.17 Comparison of the high-cycle fatigue responses of different categories of HEAs classified by phase constitution. (a) S-N data in terms of stress amplitude  $\sigma_a$  versus reversals to failure  $2N_f$ . (b) Fatigue ratio  $\frac{\sigma_a}{\sigma_{UTS}}$  versus  $2N_f$ . For clarity, the data points in (a) and (b) are overlaid with trend lines.
- Figure 6.18 Comparison of fatigue crack growth rates of HEAs tested at similar conditions, i.e., room temperature and a stress ratio of R = 1.

#### 7 Small-scale mechanical behaviors

The small scale refers to the micro, submicron, and nano scales, contrary to the macro scale in millimeter and above. The mechanical behaviors of HEAs at small scales are of interest due to three major reasons. First, some HEAs are potentially useful in miniature structures and devices, e.g., microelectromechanical systems. Second, HEAs may exhibit different mechanical properties and deformation mechanisms at small scales than those at the macro scale, analogous to other metallic systems [354]. Third, certain material behaviors (e.g., incipient plasticity and hardness) or material forms (e.g., thin films) are conveniently measured by small-scale mechanical testing techniques, such as nanoindentation.

The small-scale mechanical behaviors of HEAs have not been studied in a systematic way compared to their macroscopic mechanical responses. To date, nano- and micro-pillar compression, nanoindentation, and in-situ transmission electron microscope (TEM) testing are predominant techniques used for characterizations. The majority of investigations are focused on fcc FeNiCrCoMn [111, 355, 356] and bcc NbMoTaW [59, 357, 358], with some others on fcc CoCrCuFeNi [359], fcc Al<sub>0.1</sub>CoCrFeNi [360], fcc Al<sub>0.3</sub>CoCrFeNi [253], bcc TiZrHfNb [361], and duplex Al<sub>0.7</sub>CoCrFeNi [362], as detailed in the following. Some aspects of the mechanical behaviors of these HEA systems have been covered in other chapters for the convenience of organizing contents of similar theme, e.g., naonindentation creep in Chapter 4, and in-situ TEM fracture in Chapter 5. The present chapter serves to discuss the remaining key aspects.

### 7.1 Nano- and micro-pillar compression

Strengthening mechanisms covered in Chapter 3 refer to intrinsic means of manipulating microstructures to improve the strength of HEAs. For a particular microstructure, the strength improvement normally scales with its characteristic length scale, for example, grain size for Hall-Petch strengthening, precipitate size for precipitation hardening, twin boundary spacing for twin boundary strengthening. These strength-microstructural length scaling relations are known as the intrinsic size effect, which governs the mechanical properties and deformation at all sample dimensions. In recent years, an extrinsic size effect was also revealed in some single crystalline and nanocrystalline metals and alloys [354, 363], which was primarily investigated by compressing nano- and/or micro-pillars with aspect ratios between 2:1 and 5:1 milled from the focused ion beam (FIB).

Pillar compression experiments were first introduced by Uchic et al. [363] and Greer et al. [364] to investigate the small-scale plasticity of the Ni micro-pillars and Au nanopillars. Following their work, compressions of micro- and nano-pillars have been conducted on various metallic systems, including fcc pure metals (e.g., Cu [365-367] and Al [368-370]), bcc pure metals (e.g., W [371], Nb [372], Ta [371], Mo [373, 374], and V [375]), nanocrystalline metals (e.g., Ni [376] and Ni-4%W [377]) among others, to investigate their plasticity in a small volume. Intriguingly, distinct scaling behaviors between the pillar strength and pillar diameter were reported for alloys of different crystal structures [354].

But, in general, power law scaling between the strength and pillar size was suggested for most metallic materials, which may be expressed in a generic form as [354, 378]

$$\sigma = AD^m, \tag{7.1}$$

or in a normalized form as [354, 366, 378]

$$\frac{\tau}{G} = A \left(\frac{D}{b}\right)^m,\tag{7.2}$$

where  $\sigma$  is the compressive flow stress,  $\tau$  is the resolved shear stress, G is the shear modulus, D is the pillar diameter, b is the magnitude of the Burgers vector, m is the size-effect exponent, and A is a constant. Note that m and A in Equations (7.1) and (7.2) do not necessarily have identical values for the same set of data.

# 7.1.1 Single crystalline face-centered cubic pillars

In-situ SEM micro-pillar compressions along different crystallographic orientations have been carried out on fcc FeNiCrCoMn single crystals with a circular or square cross section [111, 355] as well as cylindrical fcc CoCrCuFeNi single crystals. Equation (7.1) and its variant,  $\tau = AD^m$ , were employed to describe the correlation between the pillar strength and the pillar diameter in many cases [111, 355]. For a consistent comparison, we utilize the data available in the literature, or our best judgements when required information is unavailable, to convert the strength-pillar dimeter relation into the form as in Equation (7.2). Specifically, the stress needs to be resolved onto proper slip systems and normalized by the shear modulus, while the pillar size needs to be normalized by the magnitude of Burger's vector. Afterwards, conducting power law fitting to the  $\frac{\tau}{G} - \frac{D}{b}$  data for each HEA can give the value of the size-effect exponent, m. All information and results pertinent to these operations are compiled in Table 7.1.

For single crystalline fcc pure metal pillars, the compilation of the  $\frac{\tau}{G} - \frac{D}{b}$  data can almost give a universal power law correlation described in Equation (7.2), with a size-effect exponent of m = -0.66 [354]. From the ultimately calculated m values for single crystalline fcc HEAs in Table 7.1, it is seen that all single-phase fcc HEAs [111, 359] but the FeNiCrCoMn HEA by Raghavan et al. [355], as well as the fcc phase in a duplex HEA [362], have m close to the universal value of -0.66 for fcc pure metal single crystals. This turns out to be more evident after plotting the universal power law dependence in fcc pure metals (line) as well as  $\frac{\tau}{G} - \frac{D}{b}$  data of HEAs (symbols) together in Figure 7.1.

The exact reason for the deviation of the FeNiCrCoMn HEA by Raghavan et al. [355] is unclear and require further investigations. The loading orientation seems not be the cause, as a separate work on the same alloy showed that m is nearly independent of crystallographic orientations [111].

A cylindrical and a square FeNiCrCoMn micropillars are, respectively, imaged by the SEM following deformation to reveal deformation modes. For the cylindrical pillar loaded in the [11 3 5] crystallographic direction in Figure 7.2(a), the deformation is accommodated by the planar slip along the  $(1\underline{1}1)[110]$  slip system [355]. Likewise, planar slips on the  $\{111\}\langle 110\rangle$  slip system are also observed in the square pillar compressed in the  $[\underline{1}23]$  direction [111], as illustrated on the two orthogonal surfaces in Figure 7.2(b).

#### 7.1.2 Single crystalline body-centered cubic pillars

The single crystalline bcc NbMoTaW micropillars with the diameters ranging from 0.2-2 µm have been compressed along the [316] and [001] crystallographic orientations. The resulting engineering stress-strain curves of various sizes of pillars are illustrated by the [316] pillars in Figure 7.3(a) [59], from which several striking features are noticed. First, the yield strength and flow stress of the pillars increase expectedly with decreasing pillar size. Second, the strain hardening rate enhances as the pillars go smaller. Third, stress drops arise in the pillars of all sizes, and become gradually more prevalent and greater in magnitude as the pillar size reduces.

SEM observations of the post-compressed [316] pillars reveal distinct deformation modes in the large pillars and small pillars. Specifically, a single slip system traverse the 2  $\mu$ m and 1  $\mu$ m pillars, leaving parallel slip bands  $\sim 40-70^{\circ}$  off the loading axis, as representatively shown by the 2  $\mu$ m pillar in Figure 7.3(b). On the other hand, multiple slip systems are activated in the 0.5  $\mu$ m

and 0.25  $\mu$ m pillars, causing intersecting slip bands, as illustrated by the deformed 0.5  $\mu$ m pillar in Figure 7.3(c). The activation of multiple slip systems in the small pillars might be caused by a slight misalignment between the pillar top and the flat punch or by the tapering of the pillars ( $\sim 2$  – 3°). The interaction of multiple slip systems is most likely responsible for the improved strain hardening in the smaller pillars seen in Figure 7.3(a). Dislocation slips in the [001] pillars, on the other hand, exhibit wavy traces, which were inferred to be caused by the cross-slip of screw dislocations along (111) directions like in some pure bcc metals [59, 372].

For single crystalline bcc pure metal pillars investigated so far, a universal scaling between  $\frac{\tau}{G}$  and  $\frac{D}{b}$  does not exist as in fcc pure metal pillars [354]. Instead, based on Peierls barrier heights, they can be classified into three groups, with each group has a universal scaling relation [354]. These three groups are, Nb and V: low-barrier group with an average m = -0.82; Mo and Ta: mid-barrier group with an average m = -0.42; W: high-barrier group with an average m = -0.32[354]. In Figure 7.4, each group is represented as an average solid line. Following the same procedure in fcc HEA pillars, the flow stress (at 5% strain) and dimension data for the bcc NbMoTaW HEA pillars are transformed into  $\frac{\tau}{G}$  and  $\frac{D}{b}$  using the information in Table 7.1, and plotted in Figure 7.4 alongside three groups of bcc pure metal pillars for comparison. From Figure 7.4, it is clear that bcc HEA pillars are located above all bcc pure metal by having larger normalized strengths  $\frac{\tau}{G}$ , owing to solid solution strengthening. By shifting both the m=-0.32 curve for W and the m = -0.42 curve for Mo and Ta towards the HEA pillar data, it is seen that all HEA data fall closely around the m = -0.32 curve. It is also confirmed by the m values obtained for individual bcc HEAs in Table 7.1, which are all around -0.32. This trend is rational considering HEAs usually possess greater Peierls barrier heights than the pure metal with an identical crystal structure [53, 379].

# 7.1.3 Nanocrystalline single-phase pillars

Both the strength and ductility of metals at the micro scale may be further enhanced by introducing grain boundaries in nano-/micro-pillar samples, i.e., making nanocrystalline nano- or micro-pillars [376, 377, 380]. Zou et al. have milled 70 – 580 nm diameter nanocrystalline bcc NbMoTaW nanopillars out of the thermally stable nanocrystalline thin films produced from the normal direct current magnetron co-sputtering technique (Normal) and the ion beam-assisted deposition method (IBAD) [357, 381]. The pillars made from both processes possess strongly

textured, nanosize, columnar grains, as schematically illustrated for a large pillar in Figure 7.5(a) which contain many columnar grains, and for a small pillar in Figure 7.5(b) which contain only a couple of columnar grains.

Compressions of the nanocrystalline bcc NbMoTaW nanopillars indicate that their ductility and strengths increase concurrently with decreasing sample dimeters. The greater ductility in the small pillars than that in the large samples is attributed to that the large pillars are more vulnerable to intergranular fracture [e.g., Figure 7.5(c)] while small ones feature more uniform deformation [e.g., Figure 7.5(d)]. At the approximately identical pillar diameter of 500 nm, the nanocrystalline pillar produced from the ion beam-assisted deposition method (IBAD) has a yield strength of ~ 6.5 GPa, which is about twice that of the single crystal pillar, and six times that of the bulk polycrystalline sample. The nanocrystalline NbMoTaW nanopillars were also found to be the strongest among many other nano- and micro-pillars, including nanocrystalline nickel (Ni) [376, 377], copper (Cu) [380], platinum (Pt) [382], and rhodium (Rh) pillars [383], as well as single crystalline NbMoTaW [59], tungsten (W) [371, 372], gold (Au) [384], and nickel (Ni) pillars [385].

The strength-pillar diameter data in nanocrystalline metals are usually presented in the form of  $\frac{\tau}{G}$  versus D, considering the nonexistence of a unique Burger's vector in different grains. Unfortunately, for the  $\frac{\tau}{G} - D$  data reported in the literature, a consistent trend is not existent [354]. As shown in Figure 7.6 for the 30-nm grained nanocrystalline Ni pillars [376] and the 60-nm nanocrystalline Ni-4%W pillars [377], they literally exhibit the opposite power-law dependences: the normalized strength of the nanocrystalline Ni pillar increases with decreasing pillar diameter whereas an overall decreasing trend is noticed for the nanocrystalline Ni-4%W pillar. The nanocrystalline Ni-4%W pillar results in a positive size-effect exponent of 0.16 whilst the value is about -0.9 for the nanocrystalline Ni pillar. Plotting the same strength-pillar size data for the nanocrystalline NbMoTaW HEA pillars with grain sizes ranging from 70 nm to 1160 nm in Figure 7.6 manifests a "small is stronger" trend analogous to the Ni pillar. The size-effect exponent of the nanocrystalline NbMoTaW HEA pillars produced from both the normal direct current magnetron co-sputtering technique (Normal) and the ion beam-assisted film deposition (IBAD) [357] is evaluated to be -0.2, as documented in both Table 7.1 and Figure 7.6. Certainly, the NbMoTaW HEA has a bcc structure whereas Ni and Ni-4%W are fcc metals.

## 7.1.4 Multi-phase pillars

When a HEA contains more than one phase, mechanical properties of each individual phase or microstructural region may be characterized by nano-/micro-pillar compressions, in addition to macroscopic mechanical characterizations of the alloy as a whole. Doing so can help understand the mechanical characteristics of each constituent phase or microstructural region. To this end, nano- or micro-pillars need to be milled out of each phase or microstructural region using a focused ion beam (FIB) system, followed by pillar compressions.

For example, in the as-cast Al<sub>0.8</sub>CoCrCuFeNi HEA with two fcc phases plus one bcc phase [386], micropillars were milled out of three distinctive microstructural regions, i.e., one fcc dendritic region and two distinct interdendritic regions (each with more than one phase). Following the micropillar compressions, the yield strengths of the dendritic region and two interdendritic regions were determined to be ~764 MPa, ~958 MPa, and ~825 MPa, respectively, almost twice the strength of the bulk alloy (~470 MPa) [386].

The approach was also utilized to separately examine the small-scale mechanical behavior of the fcc and bcc phases present in the forged Al<sub>0.7</sub>CoCrFeNi HEA [362]. The size effect in each phase was investigated by compressing the pillars with diameters ranging from 400 nm to 2 µm (fcc phase along the [001] direction, bcc phase along the [324] direction). Each phase exhibits a classical smaller-is-stronger trend, with the smallest fcc pillar having a yield strength of ~1.2 GPa and the smallest bcc pillar of ~2.2 GPa, which are about 1.2 times and 1.5 times greater than their respective bulk counterparts. Fitting Equation (7.2) to the  $\frac{\tau}{G} - \frac{D}{b}$  data gives size-effect exponents m = -0.66 for the fcc micropillars and m = -0.28 for the bcc micropillars. m = -0.66 for the fcc phase is equivalent to the universal size-effect exponent suggested for nearly all fcc pure metals such as Ni, Cu, Al, and Au [354]. m = -0.28 for the bcc phase is lower than the value of most bcc pure metals (e.g., -0.42 for Mo and Ta, -0.82 for V and Nb [354, 362]), but indeed falls in the range of W, which has m ranging from -0.34 to -0.21 depending on the loading orientation [371, 372, 387]. The  $\frac{\tau}{G} - \frac{D}{b}$  data for the fcc- and bcc-phase pillars milled out of the Al<sub>0.7</sub>CoCrFeNi HEA are included in Figure 7.1 and Figure 7.4, respectively.

#### 7.1.5 Temperature effect on pillar strength

The strengths of nearly all metal alloys, in either a single crystalline form or a nanocrystalline form, deteriorate with increasing operating temperatures. Nanocrystalline metals

are particularly vulnerable to strengthen reduction at elevated temperatures (even at ambient and modest temperatures) due to pronounced grain boundary migration, grain boundary sliding, diffusion-mediated plasticity, and grain coarsening [388-392]. For assessing the potential high-temperature applications of the single crystalline and nanocrystaline NbMoTaW HEAs at small scales, their temperature-dependent strengths were investigated with micropillar compressions at temperatures ranging from 298 K to 873 K [358].

The temperature-induced variation of the yield strengths, defined as the flow stress at 0.2% offset strain, of the single crystalline and nanocrystalline NbMoTaW micropillars of  $\sim$ 1 µm in dimeter as well as the coarse-grained bulk polycrystalline NbMoTaW [16] is given in Figure 7.7(a). At all testing temperatures, the nanocrystalline pillars exhibit the highest strengths, followed by the single crystalline pillars and then the bulk polycrystalline samples [16]. In addition, the yield strength of the nanocrystalline pillars seems to reduce more slowly than that of the other two. Normalizing the yield strengths of three types of samples at all temperatures by their respective strengths at room temperature,  $\sigma_y^{RT}$ , leads to Figure 7.7(b). Now it become more clear that the nanocrystalline pillar samples have better strength retainment at elevated temperatures than the single crystalline pillars and bulk polycrystalline samples [16]. Specifically, as the temperature ramps from 298 K to 873 K, the strength of the nanocrystalline pillar reduces by ~20% while the reduction in the single crystalline pillars and the bulk polycrystalline samples are as high as ~50%. Also graphed in Figure 7.7(b) is the nanocrystalline Cu-Ta alloy for comparison [393], whose strength reduction rate with temperatures is close to the single crystalline pillars and bulk polycrystalline samples.

Given the high strength and remarkable resistance to temperature-induced strength softening, the nanocrystalline NbMoTaW micropillars are also compared against other nanocrystalline, ultrafine-grained, and coarse-grained metals and alloys. At first, the critical resolved shear stress normalized by the shear modulus,  $\frac{\tau}{G}$ , at the homologous temperature ( $\frac{T}{T_m}$ , with  $T_m$  being the melting temperature) ranging from 0 to 0.5 is plotted in Figure 7.8 for selected materials. Obviously, the nanocrystalline NbMoTaW micropillars outperform many coarse-grained [394] and nanostructured metals and alloys [393, 395-400]. Overall, the strength of the nanocrystalline NbMoTaW micropillars fall in the ultrastrength regime of  $\sim G/50 - G/30$ , approaching the theoretical strength of G/10. The nanocrystalline NbMoTaW micropillars also

outperform all other metal alloys in comparison in terms of specific strength,  $\frac{\sigma_y}{\rho}$ , where  $\rho$  is the density of a material, as demonstrated in Figure 7.9. The specific strength of the nanocrystalline NbMoTaW micropillars can reach ~ 0.4-0.5 MJ/kg, which is comparable to that of carbon lattices and carbon-ceramic lattices (~ 0.2-0.8 MJ/kg) [401].

#### 7.1.6 Deformation mechanism

The extrinsic size effect (smaller is stronger) in fcc pure metals is usually rationalized by two prominent mechanisms: mobile dislocation starvation in which surface nucleation of dislocations follows the annihilation of pre-existing dislocations at the free pillar surface [364, 402], and the single-arm source theory in which dislocations are created by the operation of single-arm sources (or partial Frank-Read sources) [403-405]. In bcc pure metals, the extrinsic size effect is believed to be associated with formation of mobile kinks, dislocation segments, and ultimately hard dislocation junctions whose size scales with the pillar diameter [406-408].

With the aid of in-situ TEM nanopillar (500 - 700 nm in diameter) compressions, deformation in the fcc Al<sub>0.1</sub>CoCrFeNi HEA, however, is proven to be mediated by dislocation avalanche, a microprocess opposite to mobile dislocation starvation [360]. The dislocation avalanche is in particular pertinent to stress drops observed during pillar compression, as to be explained in Figure 7.10. Figure 7.10(a) gives the recorded resolved shear stress as a function of loading time, which is divided into three stages (I, II, and III) based on the significance of stress drops. In Stage I, no stress drop is observed, the corresponding deformation mechanism captured by in-situ TEM imaging is provided in Figure 7.10(b). In this stage, dislocations generated from the pillar top cluster quickly to form a dislocation band (dark region indicated by the red arrows) and migrate downward with increasing load. The formation and migration of the dislocation band is made more evident by taking the difference of Image 2 and Image 1, as given by Image 1-2 in Figure 7.10(b). Stage II is characteristic of medium stress drops, corresponding to mild dislocation avalanches, as evidenced in Figure 7.10(c), particularly Image 3-4. In Stage III, dislocation avalanches have led to large stress drops and crystal slips as indicated by the SEM image in Figure 7.10(e) although Figure 7.10(d) does not clearly reveal the extent of dislocation avalanches in this stage. More detailed in-situ TEM examinations imply that the formation of dislocation avalanches is closely related to dislocation pileups in the front of dislocation bands, whose give-up triggers the avalanche.

#### 7.2 Nanoindentation

Instrumented nanoindentation is a mechanical testing technique widely used for characterizing many aspects of mechanical properties of materials by indenting small volumes. It can be applied to materials in both bulk and thin film forms. The applications of nanoindentation in HEAs involve the characterizations of Young's modulus and hardness [409-414], friction and wear [415], incipient plasticity [356, 361], strain rate sensitivity and activation volume [356, 361, 412, 416], indentation size effect [409], flow serration [259], creep [253, 255, 256, 417], and phase stability [413]. While some of these topics have been covered in other chapters (e.g., nanoindentation creep in Chapter 4), this section primarily focus on other important aspects, as will be detailed shortly.

#### 7.2.1 Young's modulus and hardness

The most common usage of nanoindentation is to map the Young's modulus and hardness of a material, either in a bulk or thin film form, using the classical Olive-Pharr method [418] executed in testing systems. Additionally, the determination of Young's modulus is facilitated by utilizing the load-displacement (P-h) data at shallow indentation where the indenter tip is spherical and the P-h curve can be well described by the Hertzian theory [419], which is given as

$$P = \frac{4}{3}E_r R^{1/2} h^{3/2},\tag{7.3}$$

where P is the applied indentation load, h is the penetration depth, R is the tip radius of the indenter, and  $E_r$  is reduced modulus of the indenter-sample system, given as

$$\frac{1}{E_r} = \frac{1 - v_i^2}{E_i} + \frac{1 - v_s^2}{E_s},\tag{7.4}$$

where  $E_i$  and  $v_i$  (1141 GPa and 0.07 for diamond) are the Young's modulus and Poisson's ratio of the indenter,  $E_s$  and  $v_s$  are the Young's modulus and Poisson's ratio of the material. Practically, P-h data at shallow indentation may be used in two distinct ways to reach Young's modulus. One way is through individual curve fitting with the Hertzian theory, specifically, fitting the Hertzian theory in Equation (7.3) to the P-h data prior to a pop-in event, as exemplified in Figure 7.14(a). The fitting constant, e.g., 3.65 in Figure 7.14(a), equals  $\frac{4}{3}E_rR^{1/2}$  in Equation (7.3) [356]. Knowing this equivalence and the value of R, the value of  $E_r$  can be calculated. Further with Equation (7.4) and appropriate treatment of  $v_s$ , the value of the material's Young's modulus,  $E_s$ , is obtained. The second approach follows the same principle but used a collection of P-h data pairs from many

more tests, with each data point from a single P-h curve at the first pop-in. All the data are plotted in the form of  $P - h^{3/2}$  and then are linearly fitted to obtain the slope constant. An example is demonstrated in Figure 7.11 for the FeCoCrNiMn HEA [356]. At this point, the method converge to the same point as the first method, i.e., the fitting slope [3.7 in Figure 7.11] is made equal to  $\frac{4}{3}E_rR^{1/2}$  to compute  $E_r$  and then  $E_s$ .

With the nanoindentation method, the Young's modulus and hardness of the FeCoCrNiMn HEA at varying temperatures were measured and given in Figure 7.12 [416]. From Figure 7.12(a), it is seen that the Young's modulli of both the nanocrystalline and the coarse-grained (measured on the elastically softest <110> grains) samples decrease with increasing temperature, following an alike linear fashion. The measurements from nanoindentation are essentially consistent with those measured by the resonant spectroscopy on the FeCoCrNiMn with grains  $\sim 4~\mu m$  [420] and  $\sim 15~\mu m$  [150] in size, though the moduli from nanoindentation is slightly smaller. A similar declining trend with increasing temperature is also noticed for the hardness of both the nanocrystalline FeCoCrNiMn and the <110> grain in the coarse-grained FeCoCrNiMn, as depicted in Figure 7.12(b). The difference is that hardness reduces much more pronouncedly than the Young's modulus. Besides, hardness of the nanocrystalline samples is about three times higher than that of the coarse-grained counterparts due to Hall-Petch hardening.

Phase transformation, if any, may also be detected by monitoring the change of Young's modulus with temperature. Any sharp change can be indicative of a phase transformation. Examples are provided in Figure 7.13 for the nanocrystalline fcc FeCoCrNiMn HEA, alongside shown are the coarse-grained and microcrystalline samples for comparison [413]. The Young's modulus hump of the nanocrystalline FeCoCrNiMn at ~ 773 – 973 K implies the formation of additional phases, and the followed reduction is a result of dissolution of the new nanophases and restoration of the single fcc phase. The phase transformation inferred from the Young's modulus-temperature variation is justified by phase evolution studies on the same nanocrystalline alloy [240].

#### 7.2.2 Incipient plasticity

Nanoindentation on a crystal often exhibits a distinct displacement burst (or pop-in) on the load-displacement (*P-h*) curve, as show in Figure 7.14(a) for the FeCoCrNiMn HEA for example [356]. Since the indented volume is rather small (of the order of nanometer) and most likely devoid

of dislocations, the pop-in event is believed to be associated with the nucleation of dislocation in the crystal [421-425]. Therefore, statistical analyses of pop-in events in a material is instructive to gain insights to the atomistic and energetic processes of dislocation nucleation in it [426-428].

The approach was adopted in the fcc FeCoCrNiMn HEA for extracting the activation energy and volume, from which the mechanism of the onset of plasticity can be inferred. The derivation of the activation volume first requires statistical nanoindentation on one or more individual grains (e.g., ~120 tests per grains) to obtain the cumulative probability of the maximum shear stress at the first pop-in normalized by the shear modulus,  $\tau_{max}/G$ . An example is given in Figure 7.14(b). According to the contact mechanics [419],  $\tau_{max}$  can be calculated from

$$\tau_{max} = 0.31 \left(\frac{6PE_r^2}{\pi^3 R^2}\right)^{1/3},\tag{7.5}$$

where P is the applied load, R is the tip radius of the indenter,  $E_r$  is the reduced modulus of the indenter-sample assembly, which is accessible from performing Hertzian fitting ( $P = \frac{4}{3}E_rR^{1/2}h^{3/2}$ ) to the elastic portion of a P-h curve, as exemplified in Figure 7.14(a).

In a theory proposed by Schuh and the coworkers [427, 428], the cumulative probability, F, is considered to be related to the pop-in load, P, by

$$ln[-ln(1-F)] = \alpha P^{1/3} + \beta, \tag{7.6}$$

where  $\beta$  is a weak function of P,  $\alpha$  is related to the activation volume, V, through

$$V = \frac{\pi}{0.47} \left(\frac{3R}{4E_r}\right)^{2/3} kT \cdot \alpha,\tag{7.7}$$

where k is the Boltzmann constant and T is temperature.

According to Equation (7.6), transforming the cumulative probability F into the form of ln[-ln(1-F)] and plotting it against  $P^{1/3}$  followed by the linear fitting with Equation (7.6) can give the value of  $\alpha$  from the slope, as demonstrated for the FeCoCrNiMn HEA indented at three different loading rates in Figure 7.14(c). Then, with known  $\alpha$ , the activation volume V is directly calculable from Equation (7.7). The activation volume V may also be alternatively determined through  $V = kT/\tau s$ , where the strain rate sensitivity s can be obtained from the slope of the linear fit to  $\tau_{max}$  averaged over a series of indentations versus the indentation strain rates [361].

The determination of the activation energy H (or activation enthalpy) relies on obtaining the cumulative probability curves at a range of temperatures. Then, at a specific level of cumulative probability, F, the pop-in load, P, and temperature, T, are related by

$$P^{1/3} = \gamma kT + \frac{\pi}{0.47} \left(\frac{3R}{4E_r}\right)^{2/3} \frac{H}{V'}$$
 (7.8)

where  $\gamma$  is a complex function whose form is not of particular importance. Fitting Equation (7.8) to the  $P^{1/3} - T$  data pairs at a specific level of F can lead to  $\frac{H}{V}$  from the intercept, as demonstrated in Figure 7.14(d) for the FeCoCrNiMn HEA. H then can be derived with known V. Note that fitting at different levels of F in principle will converges to a single intercept and thus a single  $\frac{H}{V}$  value, as also demonstrated in Figure 7.14(d).

With the above methods, the activation volume for pop-ins in the fcc FeCoCrNiMn was determined to be 34±7 ų, equivalent to 3 atoms whereas the corresponding activation energy is 1.72±0.35 eV [356]. It was rationalized that both values favored a vacancy or vacancy-like mediated heterogeneous dislocation nucleation, rather than a homogeneous dislocation nucleation, as the mechanism of the onset of plasticity in the fcc FeCoCrNiMn. The three-atom activation volume (as compared to one atom in fcc pure metals) as well as the slightly higher activation energy (as compared to 0.9-1.6 eV for fcc pure metals [356, 429]) in the fcc FeCoCrNiMn suggest that cooperative motion of several atoms, instead of the traditional direct atom-vacancy exchange, accommodates vacancy migration in the fcc FeCoCrNiMn HEA.

With the same approach, the activation volume in the bcc TiZrHfNb HEA was determined to be ~3-5 atomic volumes, slightly greater than 3 atomic volumes in the fcc FeCoCrNiMn [361]. Furthermore, the pop-in activation energy in the TiZrHfNb was also proved to be greater than that in the FeCoCrNiMn. These were attributed to the fact that the nucleation of full dislocations was favored in the bcc HEA whereas the plasticity in fcc HEAs was mediated by the nucleation of partial dislocations [361].

## 7.2.3 Nanoscale friction and wear

Nanoscratch can be configured in an instrumented nanoindentation system to quantify the friction and wear properties of a material. The method was employed to a bcc equiatomic TiZrHfNb HEA to study its coefficient of friction, wear rate, wear resistance, and associated mechanisms under both ramping and constant loading conditions [415].

The friction under a ramping load mode exhibits two distinct regimes: the elastic regime below the normal load of  $\sim 180~\mu m$  and plastic regime beyond. The elastic regime is characteristic of an ever-decreasing coefficient of friction (COF, defined as the ratio of the lateral force to normal

force) with increasing normal loads, whereas a steady-state coefficient of friction of  $\sim$  0.16 features the plastic regime. The same two-regime friction is also spotted for the friction tests at constant loads ranging from 10 to 1000  $\mu$ m, exhibiting also a steady-state COF value of  $\sim$  0.16. The two-regime friction behavior of the TiZrHfNb HEA is schematically illustrated in Figure 7.15. The emergence of the elastic-plastic friction regimes is rationalized as follows [415, 430]. In the elastic regime, the adhesion force existing at the indenter-material interface to shear the material ahead of moving indenter contribute predominantly to friction. On the other hand, both the adhesion force and an extra plowing force accompanied by plastic deformation of the material involves in the plastic regime. The steady-state coefficient of friction in the TiZrHfNb HEA was found to be fairly smaller than  $\sim$  0.27 and  $\sim$  0.24, respectively, for the Nb and C103 alloys tested under the same condition, and comparable to many hard amorphous alloys [431]. The low coefficient of friction in the TiZrHfNb HEA was believed to be attributed to its relatively high hardness and considerable elastic recovery.

The wear rate, W, in a nanoscratch test can be calculated through dividing the volume of removed materials, V, by the corresponding scratch distance, x. The wear resistance coefficient  $R_W$ , defined as the ratio of the hardness, H, to wear coefficient, K [431-433], can be computed from  $R_W = \frac{W}{F_n}$ , where  $F_n$  is the applied normal force, according to the recast Archard equation  $W = \frac{V}{x} = \frac{KF_n}{H}$  [415, 434, 435] for dry wear. With such a routine,  $R_W$  for the TiZrHfNb HEA was calculated to be  $7.81 \times 10^{10}$  Pa, evidently greater than  $4.02 \times 10^{10}$  Pa and  $5.46 \times 10^{10}$  Pa for Nb and C103, respectively. The remarkable wear resistance in the TiZrHfNb HEA is again ascribed to its high hardness.

#### 7.2.4 Thin film mechanics

It is particularly convenient to use the nanoindnetation technique to characterize the mechanical properties of thin film materials. Young's modulus, hardness, strain rate sensitivity, activation volume and their dependences on the composition and film thickness have been investigated with nanoindentation in such thin film HEAs as bcc NbMoTaW [436, 437],  $Al_xCoCrFeNi$  (x = 0, 0.1, 0.3) [438], and  $CoCrFeNiZr_x$  (x = 0, 0.3, 0.5, 1) [439]. In the  $Al_xCoCrFeNi$  (x = 0, 0.1, 0.3) thin films, it was reported that with increasing Al content, both the hardness and activation volume increases whereas the strain rate sensitivity decreases, which was ascribed to a combined effect of the reducing grain size and fraction of nanotwins [438]. The

increase in the Zr content in the  $\sim 1$  µm thick CoCrFeNiZr<sub>x</sub> (x = 0, 0.3, 0.5, 1) films drove the microstructure to evolve from crystal (x = 0) to crystal + amorphous (x = 0.3 and 0.5), and ultimately to amorphous (x = 1) [439]. Correspondingly, the hardness keeps increasing prior to x = 0.5, then, followed by a drop after the alloy's structure turns amorphous [439].

An external size effect was reported to the NbMoTaW HEA, that is, both the hardness and Young's modulus reduces with increasing film thickness, as shown in Figure 7.16(a). Nevertheless, the film thickness is not an independent variable in the work. Rather, it is correlated with the grain size in a positive linear manner, as illustrated in Figure 7.16(b). The first impression from the correlations in Figure 7.16 might be that the reduction in at least the hardness is caused by grain coarsening. However, the authors argued, without convincing justifications, that the grain boundary strengthening should be excluded, because in nanocrystalline metals with grain sizes less than 50 nm dislocations emitted from a grain boundary cannot accumulate in grain interiors but are absorbed by opposite grain boundaries [437, 440, 441]. The size effect eventually was rationalized as a combined result of solid solution hardening (increases with increasing grain size or film thickness), dislocation strengthening (independent of grain sizes or film thickness), and the dislocation source strength (decreases with increasing grain size or film thickness) [437].

## 7.3 Summary and outlook

Single crystalline HEA pillars at the nano and micro scales exhibit higher strengths than their bulk counterparts. As pure metal pillars, the variation of pillar strengths with pillar sizes in HEAs are well described by a power-law scaling,  $\frac{\tau}{G} = A \left(\frac{D}{b}\right)^m$ . Specifically, the  $\frac{\tau}{G} - \frac{D}{b}$  data of the single crystalline fcc HEA pillars fall on a universal power law with m = -0.66, which is also the exactly the size-effect exponent found for many fcc pure metal pillars [354]. The size-effect exponent in the single crystalline bcc HEA pillars is summarized to be m = -0.32, which is close the value reported for bcc pure metal pillars with large Peierls barrier heights (e.g., W). The studies of nanocrystalline HEA pillars have only been conducted on the NbMoTaW. Compared with their single crystalline and bulk counterparts, some striking excellences are found in their strengths, including significantly higher strengths at temperatures from room temperature to 873 K, better resistance to temperature-induced softening, and higher specific strengths.

Nevertheless, the small-scale mechanics of HEA pillars is still insufficiently investigated and many questions are still left obscure. First, more nano- and/or micro-pillar compression data

are needed to confirm or rebut the power law relations summarized for single crystalline fcc and bcc HEA pillars as well as nanocrystalline HEA pillars. Second, the understanding of strength-sample size relationships spanning fully from the macroscopic scale to the nanoscale is lacking. Third, deformation mechanisms in HEA nano- and micro-pillars and their differences with corresponding macroscopic deformation mechanisms are not clearly revealed, although dislocation avalanche was reported in the fcc Al<sub>0.1</sub>CoCrFeNi nanopillars. Fourth, differences in deformation mechanisms between fcc and bcc HEA pillars, which are responsible for their distinct strength-pillar size relationships, are far from understanding. Fifth, if the four core effects would play roles in affecting the strengths and deformation of HEA pillars and differentiate them from pure metal pillars is unclear. All these questions deserve further in-depth investigations. Clarifications of these questions are beneficial to finding the sample size, microstructure, and deformation mechanism that can achieve the highest strength in HEA pillars as well as to constructing predictive micromechanical models for HEAs.

The use of nanoindentation in HEAs at the nano- and micro-scales are mostly limited to some routine investigations by virtue of their convenience and high efficiency. Examples include the quick mapping of Young's moduli and harnesses in varying conditions such as different temperatures or film thicknesses, examination of nano-friction and wear behaviors, and estimate of activation volumes. Moving forward, nanoindentation should be leveraged to reveal more useful mechanical and structural information about HEAs at small scales.

## **Table Captions**

**Table 7.1** The estimated size-effect exponent m, along with alloy information, testing condition, slip system, pillar size D (diameter and edge length, respectively, for circular and square pillars), lattice constant a, the magnitude of Burger's vector b, shear modulus G, and Schmid factor S. m for single crystalline (sc) HEAs was obtained by fitting Equation (7.2) to the  $\frac{\tau}{G} \sim \frac{D}{b}$  data, but for nanocrystalline (nc) HEAs it was from the  $\frac{\tau}{G} \sim D$  fitting.

## **Figure Captions**

- Figure 7.1 The power-law dependence of the resolved shear stress normalized by shear modulus,  $\frac{\tau}{G}$ , on the pillar dimeter divided by the magnitude of Burger's vector,  $\frac{D}{b}$ , for single crystalline fcc pure metals and HEA pillars. The numbers enclosed by square brackets in the legend are loading crystallographic direction. Corresponding data for HEAs are found in Table 7.1.
- Figure 7.2 Planar slip traces on the {111}(110) slip system in the single crystalline fcc FeNiCrCoMn micropillars. (a) Cylindrical pillar compressed in the [11 3 5] crystallographic orientation [355]. (b) Square pillar compressed in the [123] orientation [380]. Both imaged by scanning electron microscopes (SEM).
- Figure 7.3 Compression of the single crystalline bcc NbMoTaW micropillars along the [316] crystallographic orientation [59]. (a) Engineering stress-strain curves of the 0.2-2 μm dimeter pillars. Scanning electron microscopy images of the deformed pillars with approximate diameters of (b) 2 μm and (c) 0.25 μm.
- Figure 7.4 The power-law dependence of the resolved shear stress normalized by shear modulus,  $\frac{\tau}{G}$ , on the pillar dimeter divided by the magnitude of Burger's vector,  $\frac{D}{b}$ , for the single crystalline bcc pure metal and HEA pillars. The numbers enclosed by square brackets in the legend are loading crystallographic direction. Corresponding data for HEAs are found in Table 7.1.
- Figure 7.5 Nanocrystalline bcc NbMoTaW nanopillars [357]. Schematics of (a) a larger pillar and (b) a small pillar containing textured, nanosize, columnar grains. Scanning electron microscopy images of the post-compressed (c) 1 µm and (d) 100 nm pillars.
- Figure 7.6 The power-law dependence of the resolved shear stress normalized by shear modulus,  $\frac{\tau}{G}$ , on the pillar dimeter, D, for the nanocrystalline Ni, Ni-4%W, and NbMoTaW HEA pillars. Normal and IBAD denote pillars produced from the normal direct current magnetron co-sputtering technique and the ion beam-assisted film deposition, respectively [358].

- Figure 7.7 (a) The temperature-dependent yield strengths of the single crystalline and nanocrystalline NbMoTaW HEA micropillars of ~ 1 μm in dimeter [358] as well as the coarse-grained bulk polycrystalline NbMoTaW [16]. (b) Temperature-induced strength reduction for the nanocrystalline and single crystalline NbMoTaW pillars [358], bulk polycrystalline NbMoTaW [16], and nanocrystalline Cu-Ta alloy [393].
- Figure 7.8 The critical resolved shear stress normalized by the shear modulus,  $\frac{\tau}{G}$ , as a function of the homologous temperature,  $\frac{T}{T_m}$ , for the single crystalline (sc) and nanocrystalline (nc) NbMoTaW HEA micropillars [358], nc Ni [397], and nc Cu-Ta alloy [393], ultrafine-grained (ufg) Al [396], ufg Cr [398], coarse-grained (cg) Mo and W [394]. All tested at a strain rate of  $\sim 10^{-3}$  s<sup>-1</sup>.
- Figure 7.9 The specific strength,  $\frac{\sigma_y}{\rho}$ , as a function of the temperature, T, for the single crystalline (sc) and nanocrystalline (nc) NbMoTaW HEA micropillars [358], nc Ni [397], and nc Cu-Ta alloy [393], ultrafine-grained (ufg) Al [396], ufg Cr [398], coarse-grained (cg) Mo and W [394]. All tested at a strain rate of  $\sim 10^{-3}$  s<sup>-1</sup>.
- Figure 7.10 In situ compression of a Al<sub>0.1</sub>CoCrFeNi pillar and the observation of dislocation avalanches by the transmission electron microscope (TEM) [360]. (a) Measured shear stress-time curve, on which three deformation stages (I, II, and II) are delimited. (b-d) TEM-observed deformation process at each stage. 1-2 and 3-4 are the differences of two consecutive TEM images (i.e., 1 and 2, 3 and 4), in which the positive and negative intensities are indicative of the creation and annihilation of dislocations, respectively. (e) Scanning electron microscopy (SEM) image showing a large slip step in the deformed nanopillar.
- Figure 7.11 An example linear fit to a collection of  $P h^{3/2}$  data at nanoindentation pop-ins for extracting the Young's modulus from the slope constant according to the Hertzian theory in Equation (7.3). The example is demonstrated by  $\sim 120$  nanoindentation tests on the fcc FeCoCrNiMn HEA [356].

- Figure 7.12 Young's modulus and hardness of the fcc FeCoCrNiMn HEA measured by nanoindentation [416]. (a) Temperature dependence of Young's modulus and (b) hardness of the nanocrystalline and the coarse-grained (measured on the elastically softest <110> grains) samples [416]. Alongside compared are the resonance spectroscopic measurements on the same alloy with grains  $\sim 4 \mu m$  [420] and  $\sim 15 \mu m$  [150] in size.
- Figure 7.13 Temperature dependence of the Young's moduli of the nanocrystalline, microcrystalline, and coarse-grained alloys [413], with the hump indicative of certain phase transformation in the nanocrystalline alloy.
- Figure 7.14 Incipient plasticity in the fcc FeCoCrNiMn HEA studied by nanoindentation [356]. (a) A typical load-displacement curve showing a pop-in event marking the onset of plasticity. The elastic portion prior to the pop-in is well fitted by the Hertzian theory [419]. (b) Representative cumulative probability of the normalized maximum shear stress by the shear modulus,  $\tau_{max}/G$ , at pop-ins of  $\sim$  120 indentations. (c) Linear fits to the ln[-ln(1-F)] versus  $P^{1/3}$  data at three different loading rates according to Equation (7.6), from which the pop-in activation volumes can be determined from the slopes. (d) Linear fits to the  $P^{1/3}$  versus T according to Equation (7.8), from which the pop-in activation energies can be retrieved from the intercepts. Note that the fits at three cumulative probability (F) levels converge to a single intercept, thus a single activation energy.
- Figure 7.15 Friction behavior of the bcc TiZrHfNb HEA studied by nanoscratch tests [415]. (a) Coefficient of friction (COF) of the high entropy (HE), Nb, and C103 alloys under a ramping load linearly increasing from 0 to 1000 μN. (b) COF of the HEA under constant loads from 10 to 1000 μN, with each point being the average COF under an individual constant load. In both loading modes, an elastic deformation dominated region (Region I) is followed by a plastic deformation dominated region (Region II).
- Figure 7.16 The size effect in the naoncrystalline NbMoTaW thin films [437]. (a) The variation of the hardness and Young's modulus (measured at a strain rate of 0.1 s<sup>-1</sup>) with the

film thickness. (b) The linear correlation between the film thickness and the grain size.

## 8 Other properties and potential applications

Some long-existing alloys prior to the coining of the high entropy alloy concept may also be classified as HEAs in a broader sense (or multi-principal element alloys or complex concentrated alloys). Some of these alloys, for example, the non-equimolar Co-Cr-Fe-Mo-Ni quinary alloys, have found wide engineering applications. We refer the readers to early discussions of such applications [1]. The present chapter focus itself on the discussion of applications of HEAs discovered after the concept was coined in 2004.

Overall, the vast majority of HEAs are still at the stage of laboratory investigations of their metallurgies, microstructures, properties, and suitability for practical applications, with none reported to be actually commercialized for engineering applications as of the writing of this article. Nevertheless, two parallel categories of endeavors are underway promoting engineering applications of certain promising HEAs. The first category, accounting for a significant portion of all endeavors, is the fundamental research to comprehensively understand the manufacturability, microstructures, and properties of HEAs. The second category is the application-oriented investigations. Some projects led by companies in collaboration with universities and research institutes are advancing the applications of HEAs. For example, Directed Vapor Technologies International Inc. is investigating the application of HEAs in thermal barrier coating systems under a Department of Energy (DOE) contract since 2015 [442]. QuesTek Innovations LLC, in collaboration with the University of Tennessee, is exploring HEAs for turbine applications also under a Department of Energy contract since 2016 [443].

In what follows, the potential structural and functional applications of HEAs in various forms (i.e., bulk, thin film, and powder) are summarized from the endeavors aforementioned. Some HEAs are believed to be potential in certain applications often because they possess key properties required by the applications. A tree map briefly summarizing the potential applications of HEAs along with their determining properties are given in Figure 8.1. Details in each application branch, along with an example alloy, are found in Table 8.1, as will be explained in the following.

## 8.1 Structural properties and applications

#### 8.1.1 Bulk alloys

The mechanical properties of bulk HEAs have been most extensively studied. Some properties reported in bulk HEAs imply their great promise in engineering applications across an array of industries such as machining, soldering, molding, automotive, aerospace, energy, extreme storage, mining, nuclear, ship, biomedical sector, among others.

Some HEAs, e.g., Al<sub>20</sub>Li<sub>20</sub>Mg<sub>10</sub>Sc<sub>20</sub>Ti<sub>30</sub> [444] produced by mechanical alloying, possess room-temperature hardness comparable to some ceramic materials, and can be potentially used in cutting tools. The high room-temperature hardness of some HEAs, e.g., NiCuCoFe<sub>0.25</sub>Mn<sub>1.75</sub> [445], also enables them promising brazing and soldering materials. The high hardness of certain HEAs, e.g., AlCoCrFeMoNi [446], can be better retained at temperatures up to 1000 °C compared to commercial alloys, making them ideal for high-temperature applications, such as hot-working molds and dies with minimal wear-out. Some HEAs, e.g. Co<sub>1.5</sub>CrFeNi<sub>1.5</sub>Ti [447], exhibit outstanding wear resistance, partially due to their high hardnesses.

HEAs made primarily of light metallic elements, such as Al, Mg, Ti, and Li, are potential lightweight structural components in both automotive and aerospace industries. Two example lightweight HEAs are the Al<sub>20</sub>Li<sub>20</sub>Mg<sub>10</sub>Sc<sub>20</sub>Ti<sub>30</sub> [448] and Al<sub>1.5</sub>CrFeMnTi [449], while many more can be found in Ref. [450]. HEAs that can achieve a good strength-ductility balance, e.g., Fe<sub>80x</sub>Mn<sub>x</sub>Co<sub>10</sub>Cr<sub>10</sub> [19], are also crucial to the advancement of modern transportation industries. A number of Al-containing HEAs, e.g., Al<sub>0.1</sub>CoCrFeNi [292], were reported to possess high energy absorption capacity under impact loading, and are thus promising materials for crash applications.

Some HEAs exhibit surprisingly extraordinary performance under extreme loading conditions. For instance, at cryogenic temperatures the well-known CrMnFeCoNi [18] manifests fracture toughness comparable or even exceeding that under ambient temperature, making it fairly suitable for applications under cryogenic conditions such as for storage tanks of liquefied oxygen, hydrogen, etc. On the other temperature extreme, refractory HEAs (e.g., TaNbHfZrTi [333, 451]) and high entropy superalloys (e.g., AlMo<sub>0.5</sub>NbTa<sub>0.5</sub>TiZr [452]) manifest remarkable creep resistance, and can retain their high strengths even at temperatures as high as 1400 °C [453]. These HEAs are prospective as replacement materials for commercial superalloys, such as Inconel 718 and Haynes 230, which cannot withstand temperatures greater than 1400 °C.

HEAs like FeNiMnCr [454] exhibit superior radiation resistance comparable to conventional single-phase Fe-Cr-Ni austenitic alloys, and are regarded as promising base compositions for demanding nuclear energy applications.

Moreover, exceptional corrosion resistance found in some HEAs render them favorable for a wide range of applications involving corrosive liquids, for example, boilers and heat exchangers that are subjected to high temperature corrosives, ship propellers that are constantly exposed to seawaters, medical devices and implants functioning in corrosive environments of human bodies [455]. Corrosion-resistant HEAs include Al<sub>0.1</sub>CrCoFeNi [456], AlCrFeCuCo [350], CrFe<sub>1.5</sub>MnNi<sub>0.5</sub> [352], AlCoCrFeNi [457], TiZrNbTaFe [458], among many others.

Biological applications of HEAs may be enable by meticulous alloy designs to warrant sufficient levels of biocompatibility, corrosion resistance, and mechanical performance. The equiatomic TiZrNbTa [459], TiZrNbTaFe [458], TiNbTaZrMo [460-462], and some of their non-equiatomic counterparts (e.g., Ti<sub>1.4</sub>Zr<sub>1.4</sub>Nb<sub>0.6</sub>Ta<sub>0.6</sub>Mo<sub>0.6</sub> [463]) were reported to achieve a satisfactory balance among these key properties pertinent to bio-applications. For instance, the equiatomic TiNbTaZrMo HEA exhibits superior biocompatibility to the CP-Ti, superior mechanical strength to the Ti-6Al-4V alloy [460] as well as good corrosion resistance under the isotonic sodium chloride solution at 310 K [464]. With these encouraging properties, these alloys are promising in such applications as orthopedic implants and biomedical devices.

#### 8.1.2 Thin films

In addition to bulk HEAs, high hardness and wear resistance were also reported in thin film HEAs and their nitrides. For example, high hardness, excellent wear resistance, and good resistance to brittle cracking have been reported in the AlCrCoFeNiMoTi<sub>0.75</sub>Si<sub>0.25</sub> [465] and AlCoCrFeNiTi HEAs [466]. The HEA nitride, (Al<sub>0.34</sub>Cr<sub>0.22</sub>Nb<sub>0.11</sub>Si<sub>0.11</sub>Ti<sub>0.22</sub>)<sub>50</sub>N<sub>50</sub>, furthermore, exhibits excellent oxidation resistance [467]. The excellence in hardness and wear resistance make these HEAs and their nitride ideal candidates for cutting tool coatings.

#### 8.2 Functional properties and applications

#### 8.2.1 Bulk alloys

Potential functional applications of a portion of HEAs are enabled by their extraordinary electrical, magnetic, energy conversion, hydrogen storage, superconducting, catalytic, and shape memory properties.

In the magnetic domain, the bulk FeCoNiMn<sub>0.25</sub>Al<sub>0.25</sub> HEA exhibits high saturated magnetization, low coercivity, and high Curie temperature [468]. High saturated magnetization and low resistivity are also found in the FeCoNi(AlSi)<sub>x</sub> ( $0 \le x \ge 0.8$  in molar ratio) [469], CoFeNiCrAg<sub>0.37</sub> [470], CoFeNiCrAu<sub>0.29</sub> [470], CoFeNiCr<sub>0.8</sub>Cu<sub>0.64</sub> [470], and CoFeMnNiX (X = Al, Cr, Ga, and Sn) [37]. The excellent magnetic properties of these alloys, particularly after combining with their special structural properties such as large ductility and good malleability, warrant their potential applications as soft magnets in nuclear energy, motors, magnetic resonance imaging, etc.

Some HEAs, such as Ni<sub>20</sub>Fe<sub>20</sub>Mo<sub>10</sub>Co<sub>35</sub>Cr<sub>15</sub> [471] and hcp Ir<sub>0.19</sub>Os<sub>0.22</sub>Re<sub>0.21</sub>Rh<sub>0.20</sub>Ru<sub>0.19</sub> [472], possess high electrocatalytic activities. When combining with the remarkable corrosion resistance, they may function as highly active and stable electrocatalyst for chemical and electrochemical reactions in energy conversion.

Hydrogen storage is another area in which HEAs might have great potential due to their capability of storing a large amount of hydrogen. The TiVZrNbHf HEA can retain a high hydrogen-to-metal molar ratio of 2.5 (i.e., forming MH<sub>2.5</sub> metal hydrides), which traditionally can only be accomplished in alloys based on rare-earth elements [473]. The high hydrogen storage capacity, attributed to hydrogen absorption in both tetrahedral and octahedral interstitial sites enabled by severe lattice distortion, suggests that this alloy is a promising hydrogen storage material.

The shape memory effect via martensitic transformation was first reported in the TiZrHfCoNiCu HEA [474]. A recently discovered shape memory HEA without the presence of platinum and gold, (Ni,Pd)<sub>50</sub>(Ti,Hf,Zr)<sub>50</sub>, has austenite finish temperatures beyond 700 °C [475]. This alloy could extend the shape memory effect to ultra-high temperatures and may find impactful usages in controlling the tolerance between turbine blades and the turbine case to improve the thrust-specific fuel consumption and regulating the size of the core exhaust nozzle to allow more efficient operation when a plane is in the air and reduce noise at touchdown.

HEAs could also advance the development of solid-state cooling systems by virtue of their impressive magnetocaloric effect [476, 477]. The hcp rare-earth GdDyErHoTb HEA, for example, was suggested to have a small magnetic hysteresis, large magnetocaloric effect (8.6 J kg<sup>-1</sup> K<sup>-1</sup> at the 5T magnetic field) and largest refrigerant capacity (~ 627 J kg<sup>-1</sup> at the 5T magnetic field) reported to date, and is a promising material for magnetic refrigeration applications [477].

Four different types of HEA superconductors, i.e., Type-A that crystallizes on a bcc lattice (e.g., Ta<sub>34</sub>Nb<sub>33</sub>Hf<sub>8</sub>Zr<sub>14</sub>Ti<sub>11</sub> [478]), Type-B that crystallizes on a α-Mn lattice [e.g., (HfTaWIr)<sub>0.6</sub>Re<sub>0.4</sub>[479]], Type-C that crystallizes on a CsCl lattice [e.g., (ScZrNbTa)<sub>0.65</sub>(RhPd)<sub>0.35</sub> [480]], and Type-D that crystallizes on a hcp lattice (e.g., Re<sub>0.56</sub>Nb<sub>0.11</sub>Ti<sub>0.11</sub>Zr<sub>0.11</sub>Hf<sub>0.11</sub>[481]), have also been reported to date. All known HEA superconductors have their superconducting transition temperatures, *T<sub>C</sub>*, varying from 1.9 to 9.3 K, located between those of amorphous alloys and simple binary alloys [482]. Compared to the binary alloy superconductors which have been commercialized as superconducting magnets, such as NbTi and Nb3S, the HEA superconductors known so far exhibit inferior upper critical magnetic fields [482]. Nnotheless, superior superconductors are anticipated to be found in the realm of HEAs considering the enormous compositional space.

### 8.2.2 Thin films

Some other HEAs are more functionally useful in a thin film form. For example, the NiCo<sub>0.6</sub>Fe<sub>0.2</sub>Cr<sub>1.5</sub>SiAlTi<sub>0.2</sub> coating was reported to have good oxidation resistance by forming a α-Al<sub>2</sub>O<sub>3</sub> protective layer on the surface, as well as a lower thermal conductivity and thus better heat insulation at elevated temperatures [483]. Overall, the properties of this HEA coating outperform the commonly used high-temperature CoCrAlY and NiCrAlY coatings, making it a promising substitute for overlay coatings in high-temperature applications [483].

The AlMoNbSiTaTiVZr HEA in the Cu/AlMoNbSiTaTiVZr/Si sandwich structure was found to be able to effectively prevent inter-diffusion between Cu and Si up to 700 °C for 30 min [484]. It, therefore, has great potential to act as a diffusion barrier in copper metallization and other similar applications.

Good electrical properties are also the characteristics of some HEA coatings. For instance, the Ni-Cr-Si-Al-Ta HEA could exhibit a temperature coefficient of resistance of as small as -10 ppm/ $^{\circ}$ C and an electrical resistivity of as high as 2215  $\mu\Omega$ ·cm, and are useful in thin film resistor applications [485].

#### 8.2.3 Powders

Certain HEAs, when they are present in a powder form, can manifest remarkable electromagnetic properties, potentially useful in electromagnetic wave absorption and interference shielding. In two independent studies [486, 487], FeCoNiCrAl powders made from mechanical

alloying were reported to have excellent microwave shielding and absorption at middle and high frequencies. FeCoNiCrAl powders are thus regarded as promising materials for electromagnetic wave absorption applications.

The quinary CoMoFeNiCu nanoparticles was also reported to possess very high catalytic reactivity [488]. Compared to the precious metal Ru catalysts, these HEA particles manifest substantially enhanced catalytic activity and stability when used for decomposing ammonia, with an improvement factor exceeding 20. Furthermore, their catalytic activity can be tuned to maximize the catalytic reactivity for specific needs by varying the Co/Mo ratio, making them promising for applications in a wide range of reaction conditions.

## 8.3 Summary and outlook

From the properties reported, great potential in structural and functional applications spanning diverse fields is found in HEAs of bulk, thin-film and powder forms. Some potential applications are critical in addressing pressing societal challenges (e.g., transportation), advancing energy sustainability (e.g., nuclear reactors and hydrogen storage), reinforcing national security (e.g. aerospace and ballistic applications), accelerating modern industrial progression (e.g., applications in cutting tools, magnetic refrigeration, and electronics), and addressing national health priorities (e.g., biomedical applications).

Despite the application promise in a wide variety of industries, huge gaps still exist from laboratory explorations to practical engineering applications. Laboratory investigations more or less focus on one or two primary properties crucial to a certain application whereas practical applications need to be justified by considering a combination of many properties. For example, HEAs used for energy conversion or shape memory also need to possess good strength and ductility to maintain structural integrity in harsh conditions. In this sense, more application-driven or application-focused research with investigating all necessary properties is required to close the gaps. Benchmarking against commercial materials, if any, is also an important step toward justifying HEAs in certain applications. Above all, the cost could generally be a critical issue for applications of HEAs, which requires meticulous considerations.

# **Table Captions**

**Table 8.1** Potential applications and associated properties of high entropy alloys, grouped by the application field and alloy form. For each category of applications, one typical example alloy is suggested.

# **Figure Captions**

Figure 8.1 Tree map of structural and functional applications along with determining properties for various forms of high entropy alloys.

### 9 Closing remarks

Fascinated by the enormously large compositional space and the great potential of offering innumerable microstructures and properties, there has been seeing a worldwide rush in the research of HEAs and their derivatives (e.g., medium-entropy alloys, high-entropy ceramics and polymers), particularly since 2010s, six years following the first introduction of the concept. While many avenues of research in this vibrant field are being opened each year or each month, a considerable portion of endeavors is still directed toward two very fundamental aspects. One predominant area is the exploration of the huge compositional space and microstructures with the aid of thermodynamics and kinetics, while the other is the characterization and comprehension of their mechanical behavior from fundamental and practical perspectives.

Expansive investigations of the mechanical behavior of HEAs at the early stage is unsurprising. Like many other metallic materials available in bulk, the envisaged applications of HEAs are primarily in the structural domain. However, the data or findings with regard to the mechanical behavior of HEAs are buried in hundreds of reports, intermingled with each other, and literally hinder researchers from gaining unobscured appreciations of key accomplishments achieved to date and guiding their next-step research. Through a thorough review in this regard, the present work highlights key findings and accomplishments in each sub-domain of the mechanical behavior of HEAs. These sub-domains cover not only the first- and second-tier mechanical properties of HEAs (e.g., strength, ductility, creep, fracture, and fatigue), but also the scientifically important physics that dictate these properties (e.g., deformation and strengthening mechanisms). The way that the content is organized as a whole and in each chapter is to facilitate a quick grasp of key discoveries in each topic of concern to the researchers in this field. Readers are, therefore, referred to each chapter or section for details of their concern.

Meanwhile, some generic comments about the mechanical behavior of HEAs are made here for the consideration of researchers in this field. From the perspective of fundamental physics, deformation and strengthening mechanisms found in HEAs still in general resemble those established in dilute alloys. Multi-principal elements in high concentration can alter deformation mechanisms on occasion (e.g., the prevalence of nano-twining and low stacking fault energies), but any convincing correlations between the atomic and/or lattice level structures (in particular the lattice distortion) and these deformation characteristics are not yet constructed. All strengthening mechanisms but the solid solution strengthening are not proven yet to be distinct from those in

dilute alloys. Strengthening models conventionally established for dilute alloys, including the Fleischer-type solid solution strengthening model, are constantly used in HEAs to account for their strengthening effects. Attempts of adapting existing solid solution strengthening models, including the Labusch-type models [118, 139] and the effective medium models [142, 146, 148, 489], gained some success. But these models remain phenomenological to HEAs, lacking key physical quantities characteristic of this particular family of alloys, such as the lattice distortion, elastic misfit, and local chemical order [119, 122], in their governing equations. In simple words, the fundamental differences between HEAs and conventional alloys have not yet been adequately and indisputably revealed, which will likely serve as an crucial line of endeavors in future fundamental research.

Considering application potential, hundreds of HEAs investigated by far, including those with a single fcc structure, a single bcc structure, and multi-phase structures, seems to exhibit no apparent advantages in both the first- and second-tier mechanical properties over conventional alloys already commercialized. Some unusual mechanical properties are sparsely reported, for example, the high fracture resistance at cryogenic temperatures in the fcc CrMnFeCoNi [18] and the remarkable high-temperature softening resistance in some bcc HEAs (e.g., [16]). For application-drive research, considering that exhaustive investigations of all HEA compositions is unlikely, the search of alloys with advantageous combinations of properties compared to traditional alloys should be the focus of future search. The search is supposed to be guided by increasingly mature fundamental understanding of this family of alloys for efficiency and effectiveness.

In addition, the high-throughput experimentation and computation have never ever been so critical in the investigation of bulk metallic materials. At present, the trial-and-error approach prevalently used in conventional bulky metals and alloys still prevail in searching and investigating HEAs. One of the fundamental differences between HEAs and conventional alloys, i.e., the nearly limitless compositions in the former, makes this approach very ineffective in dealing with HEAs. Taking the past decade of research as an example, the findings of very few alloys with compelling properties are at the expense of the consumption of a tremendous amount of resources after laboriously screening hundreds of compositions. In confrontation of the enormous HEA compositions, high-throughput experimentation and computation are effective tools for screening and eliminating. Unfortunately, the presently available high-throughput methods or tools are far

from enough for handling such a huge compositional database of bulky alloys. High-throughput experimentation is mostly limited to thin-film materials, while high-throughput experimentation lacks sound multi-scale coupling. Besides, the uses of high-throughput experimentation and computation are often decoupled. To address the high-throughput needs in the field of HEAs, the further evolution of high-throughput experimentation and computation platforms, particularly for bulky structural materials, is anticipated. Along this line, a large material library is also expected to be established, which will surely benefit the whole material science community.

#### 5 References

- [1] Miracle DB, Senkov ON. A critical review of high entropy alloys and related concepts. Acta Mater. 2017;122:448-511
- [2] Zhang Y, Zuo TT, Tang Z, Gao MC, Dahmen KA, Liaw PK, et al. Microstructures and properties of high-entropy alloys. Prog Mater Sci. 2014;61:1-93.
- [3] George EP, Raabe D, Ritchie RO. High-entropy alloys. Nat Rev Mater. 2019;4:515-34.
- [4] Yeh JW, Chen SK, Lin SJ, Gan JY, Chin TS, Shun TT, et al. Nanostructured high-entropy alloys with multiple principal elements: Novel alloy design concepts and outcomes. Adv Eng Mater. 2004;6:299-303.
- [5] Huang PK, Yeh JW, Shun TT, Chen SK. Multi-principal-element alloys with improved oxidation and wear resistance for thermal spray coating. Adv Eng Mater. 2004;6:74-8.
- [6] Hsu C-Y, Yeh J-W, Chen S-K, Shun T-T. Wear resistance and high-temperature compression strength of Fcc CuCoNiCrAl0.5Fe alloy with boron addition. Metall Mater Trans A. 2004;35:1465-9.
- [7] Chen TK, Shun TT, Yeh JW, Wong MS. Nanostructured nitride films of multi-element high-entropy alloys by reactive DC sputtering. Surf Coat Technol. 2004;188-189:193-200.
- [8] Yeh J-W, Lin S-J, Chin T-S, Gan J-Y, Chen S-K, Shun T-T, et al. Formation of simple crystal structures in Cu-Co-Ni-Cr-Al-Fe-Ti-V alloys with multiprincipal metallic elements. Metall Mater Trans A. 2004;35:2533-6.
- [9] Cantor B, Chang ITH, Knight P, Vincent AJB. Microstructural development in equiatomic multicomponent alloys. Mater Sci Eng A. 2004;375-377:213-8.
- [10] Cantor B. Multicomponent and high entropy alloys. Entropy. 2014;16.
- [11] Cantor B, Kim K, Warren PJ. Novel multicomponent amorphous alloys. Mater Sci Forum2002. p. 27-31.
- [12] Yeh J-W. Physical metallurgy of high-entropy alloys. JOM. 2015;67:2254-61.
- [13] Gao MC, Zhang C, Gao P, Zhang F, Ouyang LZ, Widom M, et al. Thermodynamics of concentrated solid solution alloys. Curr Opin Solid State Mater Sci. 2017;21:238-51.
- [14] Gorsse S, Miracle DB, Senkov ON. Mapping the world of complex concentrated alloys. Acta Mater. 2017;135:177-87.
- [15] Senkov ON, Miller JD, Miracle DB, Woodward C. Accelerated exploration of multi-principal element alloys for structural applications. Calphad. 2015;50:32-48.
- [16] Senkov ON, Wilks GB, Scott JM, Miracle DB. Mechanical properties of Nb25Mo25Ta25W25 and V20Nb20Mo20Ta20W20 refractory high entropy alloys. Intermetallics. 2011;19:698-706.
- [17] Middleburgh SC, King DM, Lumpkin GR, Cortie M, Edwards L. Segregation and migration of species in the CrCoFeNi high entropy alloy. J Alloys Compd. 2014;599:179-82.
- [18] Gludovatz B, Hohenwarter A, Catoor D, Chang EH, George EP, Ritchie RO. A fracture-resistant high-entropy alloy for cryogenic applications. Science. 2014;345:1153-8.
- [19] Li Z, Pradeep KG, Deng Y, Raabe D, Tasan CC. Metastable high-entropy dual-phase alloys overcome the strength–ductility trade-off. Nature. 2016;534:227.
- [20] Jien-Wei Y. Recent progress in high entropy alloys. Ann Chim Sci Mat. 2006;31:633-48.

- [21] Porter DA, Easterling KE, Sherif M. Phase transformations in metals and alloys. third ed. Boca Raton: CRC press: 2009.
- [22] Tong Y, Velisa G, Yang T, Jin K, Lu C, Bei H, et al. Probing local lattice distortion in medium-and high-entropy alloys. arXiv preprint arXiv:170707745. 2017.
- [23] Guo W, Dmowski W, Noh J-Y, Rack P, Liaw PK, Egami T. Local atomic structure of a high-entropy alloy: An X-Ray and neutron scattering study. Metall Mater Trans A. 2013;44:1994-7.
- [24] Yeh J-W, Chang S-Y, Hong Y-D, Chen S-K, Lin S-J. Anomalous decrease in X-ray diffraction intensities of Cu-Ni-Al-Co-Cr-Fe-Si alloy systems with multi-principal elements. Mater Chem Phys. 2007;103:41-6.
- [25] Owen LR, Pickering EJ, Playford HY, Stone HJ, Tucker MG, Jones NG. An assessment of the lattice strain in the CrMnFeCoNi high-entropy alloy. Acta Mater. 2017;122:11-8.
- [26] Eißmann N, Klöden B, Weißgärber T, Kieback B. High-entropy alloy CoCrFeMnNi produced by powder metallurgy. Powder Metall. 2017;60:184-97.
- [27] Dąbrowa J, Kucza W, Cieślak G, Kulik T, Danielewski M, Yeh J-W. Interdiffusion in the FCC-structured Al-Co-Cr-Fe-Ni high entropy alloys: Experimental studies and numerical simulations. J Alloys Compd. 2016;674:455-62.
- [28] Chen W, Zhang L. High-throughput determination of interdiffusion coefficients for Co-Cr-Fe-Mn-Ni high-entropy alloys. J Phase Equilib Diff. 2017;38:457-65.
- [29] Jin K, Zhang C, Zhang F, Bei H. Influence of compositional complexity on interdiffusion in Ni-containing concentrated solid-solution alloys. Mater Res Lett. 2018;6:293-9.
- [30] Tsai KY, Tsai MH, Yeh JW. Sluggish diffusion in Co-Cr-Fe-Mn-Ni high-entropy alloys. Acta Mater. 2013;61:4887-97.
- [31] Zhao YY, Chen HW, Lu ZP, Nieh TG. Thermal stability and coarsening of coherent particles in a precipitation-hardened (NiCoFeCr)94Ti2Al4 high-entropy alloy. Acta Mater. 2018;147:184-94.
- [32] Ranganathan S. Alloyed pleasures: multimetallic cocktails. Curr Sci. 2003;85:1404-6.
- [33] Senkov ON, Wilks GB, Miracle DB, Chuang CP, Liaw PK. Refractory high-entropy alloys. Intermetallics. 2010;18:1758-65.
- [34] Senkov ON, Miracle DB, Chaput KJ, Couzinie J-P. Development and exploration of refractory high entropy alloys—A review. J Mater Res. 2018;33:3092-128.
- [35] Tang Z, Gao MC, Diao H, Yang T, Liu J, Zuo T, et al. Aluminum alloying effects on lattice types, microstructures, and mechanical behavior of high-entropy alloys systems. JOM. 2013;65:1848-58.
- [36] Liu L, Zhu JB, Zhang C, Li JC, Jiang Q. Microstructure and the properties of FeCoCuNiSnx high entropy alloys. Mater Sci Eng A. 2012;548:64-8.
- [37] Zuo T, Gao MC, Ouyang L, Yang X, Cheng Y, Feng R, et al. Tailoring magnetic behavior of CoFeMnNiX (X = Al, Cr, Ga, and Sn) high entropy alloys by metal doping. Acta Mater. 2017;130:10-8.
- [38] Butler TM, Alfano JP, Martens RL, Weaver ML. High-temperature oxidation behavior of Al-Co-Cr-Ni-(Fe or Si) multicomponent high-entropy alloys. JOM. 2015;67:246-59.
- [39] Veronesi P, Colombini E, Rosa R, Leonelli C, Rosi F. Microwave assisted synthesis of Si-modified Mn25FexNi25Cu(50-x) high entropy alloys. Mater Lett. 2016;162:277-80.
- [40] Li BS, Wang YP, Ren MX, Yang C, Fu HZ. Effects of Mn, Ti and V on the microstructure and properties of AlCrFeCoNiCu high entropy alloy. Mater Sci Eng A. 2008;498:482-6.
- [41] Xiao DH, Zhou PF, Wu WQ, Diao HY, Gao MC, Song M, et al. Microstructure, mechanical and corrosion behaviors of AlCoCuFeNi-(Cr,Ti) high entropy alloys. Mater Design. 2017;116:438-47.
- [42] Loria EA. The processing-microstructure-property relationship for a multicomponent Nb–Ti–Al alloy. Mater Sci Eng A. 1999;271:430-8.
- [43] Lai LC, Lee CL, Perng TP. Preparation and hydrogenation of multicomponent AB2-type Zr–Mn–V–Co–Ni amorphous alloy. J Alloys Compd. 2000;307:266-71.
- [44] Kühn U, Eckert J, Mattern N, Schultz L. As-cast quasicrystalline phase in a Zr-based multicomponent bulk alloy. Appl Phys Lett. 2000;77:3176-8.
- [45] Kang B, Lee J, Ryu HJ, Hong SH. Microstructure, mechanical property and Hall-Petch relationship of a light-weight refractory Al0.1CrNbVMo high entropy alloy fabricated by powder metallurgical process. J Alloys Compd. 2018;767:1012-21.
- [46] Vaidya M, Trubel S, Murty BS, Wilde G, Divinski SV. Ni tracer diffusion in CoCrFeNi and CoCrFeMnNi high entropy alloys. J Alloys Compd. 2016;688:994-1001.

- [47] Otto F, Dlouhý A, Somsen C, Bei H, Eggeler G, George EP. The influences of temperature and microstructure on the tensile properties of a CoCrFeMnNi high-entropy alloy. Acta Mater. 2013;61:5743-55.
- [48] Chandan AK, Tripathy S, Ghosh M, Chowdhury SG. Evolution of substructure of a non-equiatomic FeMnCrCo high entropy alloy deformed at ambient temperature. Metall Mater Trans A. 2019;50:5079-90.
- [49] Xu XD, Liu P, Tang Z, Hirata A, Song SX, Nieh TG, et al. Transmission electron microscopy characterization of dislocation structure in a face-centered cubic high-entropy alloy Al0.1CoCrFeNi. Acta Mater. 2018;144:107-15.
- [50] Patriarca L, Ojha A, Sehitoglu H, Chumlyakov YI. Slip nucleation in single crystal FeNiCoCrMn high entropy alloy. Scripta Mater. 2016;112:54-7.
- [51] Abuzaid W, Sehitoglu H. Critical resolved shear stress for slip and twin nucleation in single crystalline FeNiCoCrMn high entropy alloy. Mater Charact. 2017;129:288-99.
- [52] Yoshida S, Ikeuchi T, Bhattacharjee T, Bai Y, Shibata A, Tsuji N. Effect of elemental combination on friction stress and Hall-Petch relationship in face-centered cubic high / medium entropy alloys. Acta Mater. 2019;171:201-15.
- [53] Wu Z, Bei H, Pharr GM, George EP. Temperature dependence of the mechanical properties of equiatomic solid solution alloys with face-centered cubic crystal structures. Acta Mater. 2014;81:428-41.
- [54] Smith TM, Hooshmand MS, Esser BD, Otto F, McComb DW, George EP, et al. Atomic-scale characterization and modeling of 60° dislocations in a high-entropy alloy. Acta Mater. 2016;110:352-63.
- [55] Rao SI, Woodward C, Parthasarathy TA, Senkov O. Atomistic simulations of dislocation behavior in a model FCC multicomponent concentrated solid solution alloy. Acta Mater. 2017;134:188-94.
- [56] Couzinié JP, Lilensten L, Champion Y, Dirras G, Perrière L, Guillot I. On the room temperature deformation mechanisms of a TiZrHfNbTa refractory high-entropy alloy. Mater Sci Eng A. 2015;645:255-63.
- [57] Dirras G, Gubicza J, Heczel A, Lilensten L, Couzinié JP, Perrière L, et al. Microstructural investigation of plastically deformed Ti20Zr20Hf20Nb20Ta20 high entropy alloy by X-ray diffraction and transmission electron microscopy. Mater Charact. 2015;108:1-7.
- [58] Rao SI, Varvenne C, Woodward C, Parthasarathy TA, Miracle D, Senkov ON, et al. Atomistic simulations of dislocations in a model BCC multicomponent concentrated solid solution alloy. Acta Mater. 2017;125:311-20.
- [59] Zou Y, Maiti S, Steurer W, Spolenak R. Size-dependent plasticity in an Nb25Mo25Ta25W25 refractory high-entropy alloy. Acta Mater. 2014;65:85-97.
- [60] Wang Q, Lu Y, Yu Q, Zhang Z. The exceptional strong face-centered cubic phase and semi-coherent phase boundary in a eutectic dual-phase high entropy alloy AlCoCrFeNi. Sci Rep. 2018;8:14910.
- [61] Gao X, Lu Y, Zhang B, Liang N, Wu G, Sha G, et al. Microstructural origins of high strength and high ductility in an AlCoCrFeNi2.1 eutectic high-entropy alloy. Acta Mater. 2017;141:59-66.
- [62] Shi P, Ren W, Zheng T, Ren Z, Hou X, Peng J, et al. Enhanced strength–ductility synergy in ultrafine-grained eutectic high-entropy alloys by inheriting microstructural lamellae. Nat Commun. 2019;10:489.
- [63] Choudhuri D, Gwalani B, Gorsse S, Komarasamy M, Mantri SA, Srinivasan SG, et al. Enhancing strength and strain hardenability via deformation twinning in fcc-based high entropy alloys reinforced with intermetallic compounds. Acta Mater. 2019;165:420-30.
- [64] Kim JH, Lim KR, Won JW, Na YS, Kim H-S. Mechanical properties and deformation twinning behavior of ascast CoCrFeMnNi high-entropy alloy at low and high temperatures. Mater Sci Eng A. 2018;712:108-13.
- [65] Laplanche G, Kostka A, Horst OM, Eggeler G, George EP. Microstructure evolution and critical stress for twinning in the CrMnFeCoNi high-entropy alloy. Acta Mater. 2016;118:152-63.
- [66] Sun SJ, Tian YZ, Lin HR, Yang HJ, Dong XG, Wang YH, et al. Transition of twinning behavior in CoCrFeMnNi high entropy alloy with grain refinement. Mater Sci Eng A. 2018;712:603-7.
- [67] Gutierrez-Urrutia I, Zaefferer S, Raabe D. The effect of grain size and grain orientation on deformation twinning in a Fe–22wt.% Mn–0.6wt.% C TWIP steel. Mater Sci Eng A. 2010;527:3552-60.
- [68] Naeita N, Takamura J. Deformation twinning in silver-and copper-alloy crystals. Philos Mag. 1974;29:1001-28.
- [69] Chen LB, Wei R, Tang K, Zhang J, Jiang F, He L, et al. Heavy carbon alloyed FCC-structured high entropy alloy with excellent combination of strength and ductility. Mater Sci Eng A. 2018;716:150-6.
- [70] Wu Z, Parish CM, Bei H. Nano-twin mediated plasticity in carbon-containing FeNiCoCrMn high entropy alloys. J Alloys Compd. 2015;647:815-22.
- [71] Chen J, Yao Z, Wang X, Lu Y, Wang X, Liu Y, et al. Effect of C content on microstructure and tensile properties of as-cast CoCrFeMnNi high entropy alloy. Mater Chem Phys. 2018;210:136-45.
- [72] Kumar N, Ying Q, Nie X, Mishra RS, Tang Z, Liaw PK, et al. High strain-rate compressive deformation behavior of the Al0.1CrFeCoNi high entropy alloy. Mater Design. 2015;86:598-602.
- [73] Liu SF, Wu Y, Wang HT, Lin WT, Shang YY, Liu JB, et al. Transformation-reinforced high-entropy alloys with superior mechanical properties via tailoring stacking fault energy. J Alloys Compd. 2019;792:444-55.

- [74] Deng Y, Tasan CC, Pradeep KG, Springer H, Kostka A, Raabe D. Design of a twinning-induced plasticity high entropy alloy. Acta Mater. 2015;94:124-33.
- [75] Stepanov ND, Shaysultanov DG, Chernichenko RS, Yurchenko NY, Zherebtsov SV, Tikhonovsky MA, et al. Effect of thermomechanical processing on microstructure and mechanical properties of the carbon-containing CoCrFeNiMn high entropy alloy. J Alloys Compd. 2017;693:394-405.
- [76] Jo YH, Jung S, Choi WM, Sohn SS, Kim HS, Lee BJ, et al. Cryogenic strength improvement by utilizing room-temperature deformation twinning in a partially recrystallized VCrMnFeCoNi high-entropy alloy. Nat Commun. 2017:8:15719.
- [77] Wu SW, Wang G, Yi J, Jia YD, Hussain I, Zhai QJ, et al. Strong grain-size effect on deformation twinning of an Al0.1CoCrFeNi high-entropy alloy. Mater Res Lett. 2017;5:276-83.
- [78] Chen W, Fu Z, Fang S, Wang Y, Xiao H, Zhu D. Processing, microstructure and properties of Al0.6CoNiFeTi0.4 high entropy alloy with nanoscale twins. Mater Sci Eng A. 2013;565:439-44.
- [79] Fu Z, Chen W, Fang S, Zhang D, Xiao H, Zhu D. Alloying behavior and deformation twinning in a CoNiFeCrAl0.6Ti0.4 high entropy alloy processed by spark plasma sintering. J Alloys Compd. 2013;553:316-23.
- [80] Yu PF, Cheng H, Zhang LJ, Zhang H, Jing Q, Ma MZ, et al. Effects of high pressure torsion on microstructures and properties of an Al0.1CoCrFeNi high-entropy alloy. Mater Sci Eng A. 2016;655:283-91.
- [81] Li D, Li C, Feng T, Zhang Y, Sha G, Lewandowski JJ, et al. High-entropy Al0.3CoCrFeNi alloy fibers with high tensile strength and ductility at ambient and cryogenic temperatures. Acta Mater. 2017;123:285-94.
- [82] Stepanov N, Tikhonovsky M, Yurchenko N, Zyabkin D, Klimova M, Zherebtsov S, et al. Effect of cryodeformation on structure and properties of CoCrFeNiMn high-entropy alloy. Intermetallics. 2015;59:8-17.
- [83] Zhang Z, Sheng H, Wang Z, Gludovatz B, Zhang Z, George EP, et al. Dislocation mechanisms and 3D twin architectures generate exceptional strength-ductility-toughness combination in CrCoNi medium-entropy alloy. Nat Commun. 2017;8:14390.
- [84] Wu W, Song M, Ni S, Wang J, Liu Y, Liu B, et al. Dual mechanisms of grain refinement in a FeCoCrNi high-entropy alloy processed by high-pressure torsion. Sci Rep. 2017;7:46720.
- [85] Wu W, Ni S, Liu Y, Liu B, Song M. Amorphization at twin-twin intersected region in FeCoCrNi high-entropy alloy subjected to high-pressure torsion. Mater Charact. 2017;127:111-5.
- [86] El Kadiri H, Kapil J, Oppedal AL, Hector LG, Agnew SR, Cherkaoui M, et al. The effect of twin–twin interactions on the nucleation and propagation of {101<sup>-</sup>2} twinning in magnesium. Acta Mater. 2013;61:3549-63.
- [87] Zhao YL, Yang T, Tong Y, Wang J, Luan JH, Jiao ZB, et al. Heterogeneous precipitation behavior and stacking-fault-mediated deformation in a CoCrNi-based medium-entropy alloy. Acta Mater. 2017;138:72-82.
- [88] Tong Y, Chen D, Han B, Wang J, Feng R, Yang T, et al. Outstanding tensile properties of a precipitation-strengthened FeCoNiCrTi0.2 high-entropy alloy at room and cryogenic temperatures. Acta Mater. 2019;165:228-40.
- [89] Huang H, Wu Y, He J, Wang H, Liu X, An K, et al. Phase-transformation ductilization of brittle high-entropy alloys via metastability engineering. Adv Mater. 2017;29:1701678.
- [90] Li Z, Körmann F, Grabowski B, Neugebauer J, Raabe D. Ab initio assisted design of quinary dual-phase high-entropy alloys with transformation-induced plasticity. Acta Mater. 2017;136:262-70.
- [91] Moon J, Qi Y, Tabachnikova E, Estrin Y, Choi W-M, Joo S-H, et al. Deformation-induced phase transformation of Co20Cr26Fe20Mn20Ni14 high-entropy alloy during high-pressure torsion at 77K. Mater Lett. 2017;202:86-8.
- [92] Lin Q, Liu J, An X, Wang H, Zhang Y, Liao X. Cryogenic-deformation-induced phase transformation in an FeCoCrNi high-entropy alloy. Mater Res Lett. 2018;6:236-43.
- [93] Liu K, Nene SS, Frank M, Sinha S, Mishra RS. Metastability-assisted fatigue behavior in a friction stir processed dual-phase high entropy alloy. Mater Res Lett. 2018;6:613-9.
- [94] Eguchi T, Koyama M, Fukushima Y, Tasan CC, Tsuzaki K. Fatigue crack growth behavior and associated microstructure in a metastable high-entropy alloy. Procedia Struct Integr. 2018;13:831-6.
- [95] Basu S, Li Z, Pradeep KG, Raabe D. Strain rate sensitivity of a TRIP-assisted dual-phase high-entropy alloy. Front Mater Sci. 2018:5.
- [96] Lilensten L, Couzinié J-P, Bourgon J, Perrière L, Dirras G, Prima F, et al. Design and tensile properties of a bcc Ti-rich high-entropy alloy with transformation-induced plasticity. Mater Res Lett. 2017;5:110-6.
- [97] Huang S, Li W, Holmström E, Vitos L. Phase-transition assisted mechanical behavior of TiZrHfTax high-entropy alloys. Sci Rep. 2018;8:12576.
- [98] Li Z, Tasan CC, Pradeep KG, Raabe D. A TRIP-assisted dual-phase high-entropy alloy: Grain size and phase fraction effects on deformation behavior. Acta Mater. 2017;131:323-35.
- [99] Nene SS, Liu K, Frank M, Mishra RS, Brennan RE, Cho KC, et al. Enhanced strength and ductility in a friction stir processing engineered dual phase high entropy alloy. Sci Rep. 2017;7:16167.

- [100] Nene SS, Sinha S, Frank M, Liu K, Mishra RS, McWilliams BA, et al. Unexpected strength–ductility response in an annealed, metastable, high-entropy alloy. Appl Mater Today, 2018;13:198-206.
- [101] Nene SS, Frank M, Liu K, Mishra RS, McWilliams BA, Cho KC. Extremely high strength and work hardening ability in a metastable high entropy alloy. Sci Rep. 2018;8:9920.
- [102] Li Z, Tasan CC, Springer H, Gault B, Raabe D. Interstitial atoms enable joint twinning and transformation induced plasticity in strong and ductile high-entropy alloys. Sci Rep. 2017;7:40704.
- [103] Niendorf T, Wegener T, Li Z, Raabe D. Unexpected cyclic stress-strain response of dual-phase high-entropy alloys induced by partial reversibility of deformation. Scripta Mater. 2018;143:63-7.
- [104] Fu Z, Jiang L, Wardini JL, MacDonald BE, Wen H, Xiong W, et al. A high-entropy alloy with hierarchical nanoprecipitates and ultrahigh strength. Sci Adv. 2018;4.
- [105] Wang M, Li Z, Raabe D. In-situ SEM observation of phase transformation and twinning mechanisms in an interstitial high-entropy alloy. Acta Mater. 2018;147:236-46.
- [106] Su J, Raabe D, Li Z. Hierarchical microstructure design to tune the mechanical behavior of an interstitial TRIP-TWIP high-entropy alloy. Acta Mater. 2019;163:40-54.
- [107] Huo W, Zhou H, Fang F, Hu X, Xie Z, Jiang J. Strain-rate effect upon the tensile behavior of CoCrFeNi high-entropy alloys. Mater Sci Eng A. 2017;689:366-9.
- [108] Gutierrez-Urrutia I, Raabe D. Dislocation and twin substructure evolution during strain hardening of an Fe–22wt.% Mn–0.6wt.% C TWIP steel observed by electron channeling contrast imaging. Acta Mater. 2011;59:6449-62.
- [109] Miao J, Slone CE, Smith TM, Niu C, Bei H, Ghazisaeidi M, et al. The evolution of the deformation substructure in a Ni-Co-Cr equiatomic solid solution alloy. Acta Mater. 2017;132:35-48.
- [110] Laplanche G, Kostka A, Reinhart C, Hunfeld J, Eggeler G, George EP. Reasons for the superior mechanical properties of medium-entropy CrCoNi compared to high-entropy CrMnFeCoNi. Acta Mater. 2017;128:292-303.
- [111] Okamoto NL, Fujimoto S, Kambara Y, Kawamura M, Chen ZMT, Matsunoshita H, et al. Size effect, critical resolved shear stress, stacking fault energy, and solid solution strengthening in the CrMnFeCoNi high-entropy alloy. Sci Rep. 2016;6:35863.
- [112] Liu S, Wei Y. The Gaussian distribution of lattice size and atomic level heterogeneity in high entropy alloys. Extreme Mech Lett. 2017;11:84-8.
- [113] Huang S, Li W, Lu S, Tian F, Shen J, Holmström E, et al. Temperature dependent stacking fault energy of FeCrCoNiMn high entropy alloy. Scripta Mater. 2015;108:44-7.
- [114] Zaddach AJ, Niu C, Koch CC, Irving DL. Mechanical properties and stacking fault energies of NiFeCrCoMn high-entropy alloy. JOM. 2013;65:1780-9.
- [115] Bhattacharjee PP, Sathiaraj GD, Zaid M, Gatti JR, Lee C, Tsai C-W, et al. Microstructure and texture evolution during annealing of equiatomic CoCrFeMnNi high-entropy alloy. J Alloys Compd. 2014;587:544-52.
- [116] Zhang YH, Zhuang Y, Hu A, Kai JJ, Liu CT. The origin of negative stacking fault energies and nano-twin formation in face-centered cubic high entropy alloys. Scripta Mater. 2017;130:96-9.
- [117] Zeng Y, Cai X, Koslowski M. Effects of the stacking fault energy fluctuations on the strengthening of alloys. Acta Mater. 2019;164:1-11.
- [118] Wu Z, Gao Y, Bei H. Thermal activation mechanisms and Labusch-type strengthening analysis for a family of high-entropy and equiatomic solid-solution alloys. Acta Mater. 2016;120:108-19.
- [119] Li Q-J, Sheng H, Ma E. Strengthening in multi-principal element alloys with local-chemical-order roughened dislocation pathways. Nat Commun. 2019;10:3563.
- [120] Ding J, Yu Q, Asta M, Ritchie RO. Tunable stacking fault energies by tailoring local chemical order in CrCoNi medium-entropy alloys. P Natl Acad Sci. 2018;115:8919.
- [121] Zhang R, Zhao S, Ding J, Chong Y, Jia T, Ophus C, et al. Short-range order and its impact on the CrCoNi medium-entropy alloy. Nature. 2020;581:283-7.
- [122] Ding Q, Zhang Y, Chen X, Fu X, Chen D, Chen S, et al. Tuning element distribution, structure and properties by composition in high-entropy alloys. Nature. 2019:574:223-7.
- [123] Khachaturyan AG. Theory of structural transformations in solids: Courier Corporation; 2013.
- [124] He F, Wang Z, Niu S, Wu Q, Li J, Wang J, et al. Strengthening the CoCrFeNiNb0.25 high entropy alloy by FCC precipitate. J Alloys Compd. 2016;667:53-7.
- [125] Ganji RS, Sai Karthik P, Bhanu Sankara Rao K, Rajulapati KV. Strengthening mechanisms in equiatomic ultrafine grained AlCoCrCuFeNi high-entropy alloy studied by micro- and nanoindentation methods. Acta Mater. 2017;125:58-68.
- [126] Zhao YY, Lei ZF, Lu ZP, Huang JC, Nieh TG. A simplified model connecting lattice distortion with friction stress of Nb-based equiatomic high-entropy alloys. Mater Res Lett. 2019;7:340-6.

- [127] Zhao YY, Nieh TG. Correlation between lattice distortion and friction stress in Ni-based equiatomic alloys. Intermetallics. 2017;86:45-50.
- [128] Sriharitha R, Murty BS, Kottada RS. Alloying, thermal stability and strengthening in spark plasma sintered AlxCoCrCuFeNi high entropy alloys. J Alloys Compd. 2014;583:419-26.
- [129] Nabarro FRN. Dislocations in a simple cubic lattice. Proc Phys Soc. 1947;59:256-72.
- [130] Dietze H-D. Die Temperaturabhängigkeit der Versetzungsstruktur. Z Phys. 1952;132:107-10.
- [131] Toda-Caraballo I, Rivera-Díaz-del-Castillo PEJ. Modelling solid solution hardening in high entropy alloys. Acta Mater. 2015;85:14-23.
- [132] Fleischer RL. Substitutional solution hardening. Acta Metall. 1963;11:203-9.
- [133] He JY, Wang H, Huang HL, Xu XD, Chen MW, Wu Y, et al. A precipitation-hardened high-entropy alloy with outstanding tensile properties. Acta Mater. 2016;102:187-96.
- [134] Juan C-C, Tseng K-K, Hsu W-L, Tsai M-H, Tsai C-W, Lin C-M, et al. Solution strengthening of ductile refractory HfMoxNbTaTiZr high-entropy alloys. Mater Lett. 2016;175:284-7.
- [135] Wang J, Liu B, Liu CT, Liu Y. Strengthening mechanism in a high-strength carbon-containing powder metallurgical high entropy alloy. Intermetallics. 2018;102:58-64.
- [136] Wu YD, Cai YH, Chen XH, Wang T, Si JJ, Wang L, et al. Phase composition and solid solution strengthening effect in TiZrNbMoV high-entropy alloys. Mater Design. 2015;83:651-60.
- [137] Lin C-M, Juan C-C, Chang C-H, Tsai C-W, Yeh J-W. Effect of Al addition on mechanical properties and microstructure of refractory AlxHfNbTaTiZr alloys. J Alloys Compd. 2015;624:100-7.
- [138] Labusch R. A statistical theory of solid solution hardening. Phys Status Solidi (b). 1970;41:659-69.
- [139] Toda-Caraballo I. A general formulation for solid solution hardening effect in multicomponent alloys. Scripta Mater. 2017;127:113-7.
- [140] Čižek L, Kratochvíl P, Smola B. Solid solution hardening of copper crystals. J Mater Sci. 1974;9:1517-20.
- [141] Gypen LA, Deruyttere A. Multi-component solid solution hardening. J Mater Sci. 1977;12:1034-8.
- [142] Varvenne C, Luque A, Curtin WA. Theory of strengthening in fcc high entropy alloys. Acta Mater. 2016;118:164-76.
- [143] Leyson GPM, Hector LG, Curtin WA. Solute strengthening from first principles and application to aluminum alloys. Acta Mater. 2012;60:3873-84.
- [144] Leyson GPM, Hector LG, Curtin WA. First-principles prediction of yield stress for basal slip in Mg–Al alloys. Acta Mater. 2012;60:5197-203.
- [145] Leyson GPM, Curtin WA, Hector Jr LG, Woodward CF. Quantitative prediction of solute strengthening in aluminium alloys. Nat Mater. 2010;9:750.
- [146] Varvenne C, Curtin WA. Strengthening of high entropy alloys by dilute solute additions: CoCrFeNiAlx and CoCrFeNiMnAlx alloys. Scripta Mater. 2017;138:92-5.
- [147] Maresca F, Curtin WA. Mechanistic origin of high retained strength in refractory BCC high entropy alloys up to 1900K. arXiv preprint arXiv:190102100. 2019.
- [148] Varvenne C, Curtin WA. Predicting yield strengths of noble metal high entropy alloys. Scripta Mater. 2018;142:92-5.
- [149] Yin B, Curtin WA. First-principles-based prediction of yield strength in the RhIrPdPtNiCu high-entropy alloy. Npj Comput Mater. 2019;5:14.
- [150] Laplanche G, Bonneville J, Varvenne C, Curtin WA, George EP. Thermal activation parameters of plastic flow reveal deformation mechanisms in the CrMnFeCoNi high-entropy alloy. Acta Mater. 2018;143:257-64.
- [151] Klimova M, Stepanov N, Shaysultanov D, Chernichenko R, Yurchenko N, Sanin V, et al. Microstructure and mechanical properties evolution of the Al, C-containing CoCrFeNiMn-type high-entropy alloy during cold rolling. Materials. 2017;11:53.
- [152] Wei R, Sun H, Han ZH, Chen C, Wang T, Guan SK, et al. Strengthening of Fe40Mn40Co10Cr10 high entropy alloy via Mo/C alloying. Mater Lett. 2018;219:85-8.
- [153] Wang Z, Baker I. Interstitial strengthening of a f.c.c. FeNiMnAlCr high entropy alloy. Mater Lett. 2016;180:153-6.
- [154] Ko JY, Hong SI. Microstructural evolution and mechanical performance of carbon-containing CoCrFeMnNi-C high entropy alloys. J Alloys Compd. 2018;743:115-25.
- [155] Stepanov ND, Yurchenko NY, Tikhonovsky MA, Salishchev GA. Effect of carbon content and annealing on structure and hardness of the CoCrFeNiMn-based high entropy alloys. J Alloys Compd. 2016;687:59-71.
- [156] Chen Y, Li Y, Cheng X, Xu Z, Wu C, Cheng B, et al. Interstitial strengthening of refractory ZrTiHfNb0.5Ta0.5Ox (x = 0.05, 0.1, 0.2) high-entropy alloys. Mater Lett. 2018;228:145-7.

- [157] Lei Z, Liu X, Wu Y, Wang H, Jiang S, Wang S, et al. Enhanced strength and ductility in a high-entropy alloy via ordered oxygen complexes. Nature. 2018;563:546-50.
- [158] Courtney TH. Mechanical behavior of materials: Waveland Press; 2005.
- [159] Fleischer RL. The flow stress of body-centered cubic metals: inherent lattice hardening or solution hardening? Acta Metall. 1967;15:1513-9.
- [160] Zhao YH, Liao XZ, Jin Z, Valiev RZ, Zhu YT. Microstructures and mechanical properties of ultrafine grained 7075 Al alloy processed by ECAP and their evolutions during annealing. Acta Mater. 2004;52:4589-99.
- [161] Wen H, Topping TD, Isheim D, Seidman DN, Lavernia EJ. Strengthening mechanisms in a high-strength bulk nanostructured Cu–Zn–Al alloy processed via cryomilling and spark plasma sintering. Acta Mater. 2013;61:2769-82.
- [162] Stokes AR, Wilson AJC. The diffraction of X rays by distorted crystal aggregates I. Proc Phys Soc. 1944;56:174-81.
- [163] Williamson GK, Smallman RE. III. Dislocation densities in some annealed and cold-worked metals from measurements on the X-ray debye-scherrer spectrum. Philos Mag. 1956;1:34-46.
- [164] Williamson GK, Hall WH. X-ray line broadening from filed aluminium and wolfram. Acta Metall. 1953;1:22-31.
- [165] particle size and strain analysis by x-ray diffraction.
- [166] Ham RK. The determination of dislocation densities in thin films. Philos Mag. 1961;6:1183-4.
- [167] Gao H, Huang Y, Nix WD, Hutchinson JW. Mechanism-based strain gradient plasticity— I. Theory. J Mech Phys Solids. 1999;47:1239-63.
- [168] Kubin LP, Mortensen A. Geometrically necessary dislocations and strain-gradient plasticity: a few critical issues. Scripta Mater. 2003;48:119-25.
- [169] Calcagnotto M, Ponge D, Demir E, Raabe D. Orientation gradients and geometrically necessary dislocations in ultrafine grained dual-phase steels studied by 2D and 3D EBSD. Mater Sci Eng A. 2010;527:2738-46.
- [170] Gao H, Huang Y. Geometrically necessary dislocation and size-dependent plasticity. Scripta Mater. 2003;48:113-8.
- [171] Demir E, Raabe D, Zaafarani N, Zaefferer S. Investigation of the indentation size effect through the measurement of the geometrically necessary dislocations beneath small indents of different depths using EBSD tomography. Acta Mater. 2009;57:559-69.
- [172] Kadkhodapour J, Schmauder S, Raabe D, Ziaei-Rad S, Weber U, Calcagnotto M. Experimental and numerical study on geometrically necessary dislocations and non-homogeneous mechanical properties of the ferrite phase in dual phase steels. Acta Mater. 2011;59:4387-94.
- [173] Callister Jr WD, Rethwisch DG. Fundamentals of materials science and engineering: an integrated approach: John Wiley & Sons; 2012.
- [174] Yoshida S, Bhattacharjee T, Bai Y, Tsuji N. Friction stress and Hall-Petch relationship in CoCrNi equi-atomic medium entropy alloy processed by severe plastic deformation and subsequent annealing. Scripta Mater. 2017;134:33-6
- [175] Cordero ZC, Knight BE, Schuh CA. Six decades of the Hall–Petch effect a survey of grain-size strengthening studies on pure metals. Int Mater Rev. 2016;61:495-512.
- [176] Hansen N. Hall-Petch relation and boundary strengthening. Scripta Mater. 2004;51:801-6.
- [177] Liu WH, Wu Y, He JY, Nieh TG, Lu ZP. Grain growth and the Hall-Petch relationship in a high-entropy FeCrNiCoMn alloy. Scripta Mater. 2013;68:526-9.
- [178] Kumar N, Komarasamy M, Nelaturu P, Tang Z, Liaw PK, Mishra RS. Friction stir processing of a high entropy alloy Al0.1CoCrFeNi. JOM. 2015;67:1007-13.
- [179] Wu D, Zhang J, Huang JC, Bei H, Nieh TG. Grain-boundary strengthening in nanocrystalline chromium and the Hall-Petch coefficient of body-centered cubic metals. Scripta Mater. 2013;68:118-21.
- [180] Huang Y-C, Su C-H, Wu S-K, Lin C. A Study on the hall–petch relationship and grain growth kinetics in FCC-structured high/medium entropy alloys. Entropy. 2019;21.
- [181] Fischmeister H, Karlsson B. Plasticity of two-phase materials with a coarse microstructure: Z METALLKD.; 1977.
- [182] Gavriljuk VG, Berns H. High nitrogen steels: structure, properties, manufacture, applications: Springer Science & Business Media; 2013.
- [183] Dieter GE, Bacon D. Mechanical metallurgy: McGraw-hill New York; 1986.
- [184] Shun T-T, Du Y-C. Age hardening of the Al0.3CoCrFeNiC0.1 high entropy alloy. J Alloys Compd. 2009;478:269-72.
- [185] Liu WH, Lu ZP, He JY, Luan JH, Wang ZJ, Liu B, et al. Ductile CoCrFeNiMox high entropy alloys strengthened by hard intermetallic phases. Acta Mater. 2016;116:332-42.

- [186] Gwalani B, Soni V, Lee M, Mantri SA, Ren Y, Banerjee R. Optimizing the coupled effects of Hall-Petch and precipitation strengthening in a Al0.3CoCrFeNi high entropy alloy. Mater Design. 2017;121:254-60.
- [187] Shun T-T, Hung C-H, Lee C-F. The effects of secondary elemental Mo or Ti addition in Al0.3CoCrFeNi high-entropy alloy on age hardening at 700°C. J Alloys Compd. 2010;495:55-8.
- [188] Ming K, Bi X, Wang J. Precipitation strengthening of ductile Cr15Fe20Co35Ni20Mo10 alloys. Scripta Mater. 2017;137:88-93.
- [189] He JY, Wang H, Wu Y, Liu XJ, Mao HH, Nieh TG, et al. Precipitation behavior and its effects on tensile properties of FeCoNiCr high-entropy alloys. Intermetallics. 2016;79:41-52.
- [190] Stepanov ND, Yurchenko NY, Panina ES, Tikhonovsky MA, Zherebtsov SV. Precipitation-strengthened refractory Al0.5CrNbTi2V0.5 high entropy alloy. Mater Lett. 2017;188:162-4.
- [191] Tsao LC, Chen CS, Chu CP. Age hardening reaction of the Al0.3CrFe1.5MnNi0.5 high entropy alloy. Mater Design. 2012;36:854-8.
- [192] Niu S, Kou H, Guo T, Zhang Y, Wang J, Li J. Strengthening of nanoprecipitations in an annealed Al0.5CoCrFeNi high entropy alloy. Mater Sci Eng A. 2016;671:82-6.
- [193] Ren B, Liu ZX, Cai B, Wang MX, Shi L. Aging behavior of a CuCr2Fe2NiMn high-entropy alloy. Mater Design. 2012;33:121-6.
- [194] He F, Wang Z, Cheng P, Wang Q, Li J, Dang Y, et al. Designing eutectic high entropy alloys of CoCrFeNiNbx. J Alloys Compd. 2016;656:284-9.
- [195] Liang Y-J, Wang L, Wen Y, Cheng B, Wu Q, Cao T, et al. High-content ductile coherent nanoprecipitates achieve ultrastrong high-entropy alloys. Nat Commun. 2018;9:4063.
- [196] Zhao YL, Yang T, Zhu JH, Chen D, Yang Y, Hu A, et al. Development of high-strength Co-free high-entropy alloys hardened by nanosized precipitates. Scripta Mater. 2018;148:51-5.
- [197] Shun T-T, Chang L-Y, Shiu M-H. Age-hardening of the CoCrFeNiMo0.85 high-entropy alloy. Mater Charact. 2013;81:92-6.
- [198] Booth-Morrison C, Dunand DC, Seidman DN. Coarsening resistance at 400°C of precipitation-strengthened Al–Zr–Sc–Er alloys. Acta Mater. 2011;59:7029-42.
- [199] Ashby M. Physics of strength and plasticity. Cambridge, Massachusetts: MIT Press; 1969.
- [200] Gladman T. The physical metallurgy of microalloyed steels: Maney Pub; 1997.
- [201] Kelly A. Strengthening methods in crystals: Elsevier Publishing Company; 1971.
- [202] Kamara AB, Ardell AJ, Wagner CNJ. Lattice misfits in four binary Ni-Base  $\gamma/\gamma 1$  alloys at ambient and elevated temperatures. Metall Mater Trans A. 1996;27:2888-96.
- [203] Huther W, Reppich B. Interaction of dislocations with coherent, stree-free ordered particles. Z Metallk. 1978;69:628-34.
- [204] Dao M, Lu L, Shen YF, Suresh S. Strength, strain-rate sensitivity and ductility of copper with nanoscale twins. Acta Mater. 2006;54:5421-32.
- [205] Shen YF, Lu L, Lu QH, Jin ZH, Lu K. Tensile properties of copper with nano-scale twins. Scripta Mater. 2005;52:989-94.
- [206] Remy L. Kinetics of f.c.c. deformation twinning and its relationship to stress-strain behaviour. Acta Metall. 1978:26:443-51.
- [207] Christian JW, Mahajan S. Deformation twinning. Prog Mater Sci. 1995;39:1-157.
- [208] Bouaziz O, Allain S, Scott C. Effect of grain and twin boundaries on the hardening mechanisms of twinning-induced plasticity steels. Scripta Mater. 2008;58:484-7.
- [209] Idrissi H, Renard K, Ryelandt L, Schryvers D, Jacques PJ. On the mechanism of twin formation in Fe–Mn–C TWIP steels. Acta Mater. 2010;58:2464-76.
- [210] Idrissi H, Renard K, Schryvers D, Jacques PJ. On the relationship between the twin internal structure and the work-hardening rate of TWIP steels. Scripta Mater. 2010;63:961-4.
- [211] Idrissi H, Ryelandt L, Veron M, Schryvers D, Jacques PJ. Is there a relationship between the stacking fault character and the activated mode of plasticity of Fe–Mn-based austenitic steels? Scripta Mater. 2009;60:941-4.
- [212] Renard K, Idrissi H, Schryvers D, Jacques PJ. On the stress state dependence of the twinning rate and work hardening in twinning-induced plasticity steels. Scripta Mater. 2012;66:966-71.
- [213] Joo SH, Kato H, Jang MJ, Moon J, Tsai CW, Yeh JW, et al. Tensile deformation behavior and deformation twinning of an equimolar CoCrFeMnNi high-entropy alloy. Mater Sci Eng A. 2017;689:122-33.
- [214] Fu Z, Chen W, Wen H, Zhang D, Chen Z, Zheng B, et al. Microstructure and strengthening mechanisms in an FCC structured single-phase nanocrystalline Co25Ni25Fe25Al7.5Cu17.5 high-entropy alloy. Acta Mater. 2016;107:59-71.

- [215] Li X, Wei Y, Lu L, Lu K, Gao H. Dislocation nucleation governed softening and maximum strength in nano-twinned metals. Nature. 2010:464:877.
- [216] Chen XH, Lu L, Lu K. Grain size dependence of tensile properties in ultrafine-grained Cu with nanoscale twins. Scripta Mater. 2011;64:311-4.
- [217] Gil Sevillano J. An alternative model for the strain hardening of FCC alloys that twin, validated for twinning-induced plasticity steel. Scripta Mater. 2009;60:336-9.
- [218] Yu Q, Wang J, Jiang Y. Inverse slip accompanying twinning and eetwinning during cyclic loading of magnesium single crystal. J Mater Sci. 2013;2013:8.
- [219] Tomita Y, Iwamoto T. Constitutive modeling of trip steel and its application to the improvement of mechanical properties. Int J Mech Sci. 1995;37:1295-305.
- [220] Zaefferer S, Ohlert J, Bleck W. A study of microstructure, transformation mechanisms and correlation between microstructure and mechanical properties of a low alloyed TRIP steel. Acta Mater. 2004;52:2765-78.
- [221] Herrera C, Ponge D, Raabe D. Design of a novel Mn-based 1GPa duplex stainless TRIP steel with 60% ductility by a reduction of austenite stability. Acta Mater. 2011;59:4653-64.
- [222] Bae JW, Seol JB, Moon J, Sohn SS, Jang MJ, Um HY, et al. Exceptional phase-transformation strengthening of ferrous medium-entropy alloys at cryogenic temperatures. Acta Mater. 2018;161:388-99.
- [223] Li Z, Raabe D. Influence of compositional inhomogeneity on mechanical behavior of an interstitial dual-phase high-entropy alloy. Mater Chem Phys. 2018;210:29-36.
- [224] Wei S, He F, Tasan CC. Metastability in high-entropy alloys: A review. J Mater Res. 2018;33:2924-37.
- [225] Rivera-Díaz-del-Castillo PEJ, Fu H. Strengthening mechanisms in high-entropy alloys: Perspectives for alloy design. J Mater Res. 2018;33:2970-82.
- [226] Olson GB, Cohen M. Kinetics of strain-induced martensitic nucleation. Metall Trans A. 1975;6:791.
- [227] Li S, Honarmandi P, Arróyave R, Rivera-Diaz-del-Castillo PEJ. Describing the deformation behaviour of TRIP and dual phase steels employing an irreversible thermodynamics formulation. Mater Sci Technol. 2015;31:1658-63.
- [228] Liu TK, Wu Z, Stoica AD, Xie Q, Wu W, Gao YF, et al. Twinning-mediated work hardening and texture evolution in CrCoFeMnNi high entropy alloys at cryogenic temperature. Mater Design. 2017;131:419-27.
- [229] Ye YF, Wang Q, Lu J, Liu CT, Yang Y. High-entropy alloy: challenges and prospects. Mater Today. 2016;19:349-62.
- [230] Chen J, Zhou X, Wang W, Liu B, Lv Y, Yang W, et al. A review on fundamental of high entropy alloys with promising high–temperature properties. J Alloys Compd. 2018;760:15-30.
- [231] Yu Y, He F, Qiao Z, Wang Z, Liu W, Yang J. Effects of temperature and microstructure on the triblogical properties of CoCrFeNiNbx eutectic high entropy alloys. J Alloys Compd. 2019;775:1376-85.
- [232] Woo W, Huang EW, Yeh J-W, Choo H, Lee C, Tu S-Y. In-situ neutron diffraction studies on high-temperature deformation behavior in a CoCrFeMnNi high entropy alloy. Intermetallics. 2015;62:1-6.
- [233] Reddy SR, Bapari S, Bhattacharjee PP, Chokshi AH. Superplastic-like flow in a fine-grained equiatomic CoCrFeMnNi high-entropy alloy. Mater Res Lett. 2017;5:408-14.
- [234] Shaysultanov DG, Stepanov ND, Kuznetsov AV, Salishchev GA, Senkov ON. Phase composition and superplastic behavior of a wrought AlCoCrCuFeNi high-entropy alloy. JOM. 2013;65:1815-28.
- [235] Chokshi AH. High temperature deformation in fine grained high entropy alloys. Mater Chem Phys. 2018;210:152-61.
- [236] Chang Y-J, Yeh A-C. The evolution of microstructures and high temperature properties of AlxCo1.5CrFeNi1.5Tiy high entropy alloys. J Alloys Compd. 2015;653:379-85.
- [237] He F, Wang Z, Wu Q, Li J, Wang J, Liu CT. Phase separation of metastable CoCrFeNi high entropy alloy at intermediate temperatures. Scripta Mater. 2017;126:15-9.
- [238] Vaidya M, Karati A, Marshal A, Pradeep KG, Murty BS. Phase evolution and stability of nanocrystalline CoCrFeNi and CoCrFeMnNi high entropy alloys. J Alloys Compd. 2019;770:1004-15.
- [239] Singh S, Wanderka N, Murty BS, Glatzel U, Banhart J. Decomposition in multi-component AlCoCrCuFeNi high-entropy alloy. Acta Mater. 2011;59:182-90.
- [240] Schuh B, Mendez-Martin F, Völker B, George EP, Clemens H, Pippan R, et al. Mechanical properties, microstructure and thermal stability of a nanocrystalline CoCrFeMnNi high-entropy alloy after severe plastic deformation. Acta Mater. 2015;96:258-68.
- [241] Stepanov ND, Shaysultanov DG, Ozerov MS, Zherebtsov SV, Salishchev GA. Second phase formation in the CoCrFeNiMn high entropy alloy after recrystallization annealing. Mater Lett. 2016;185:1-4.
- [242] Zhou W, Fu LM, Liu P, Xu XD, Chen B, Zhu GZ, et al. Deformation stimulated precipitation of a single-phase CoCrFeMnNi high entropy alloy. Intermetallics. 2017;85:90-7.

- [243] Kang YB, Shim SH, Lee KH, Hong SI. Dislocation creep behavior of CoCrFeMnNi high entropy alloy at intermediate temperatures. Mater Res Lett. 2018;6:689-95.
- [244] Tsao T-K, Yeh A-C, Kuo C-M, Kakehi K, Murakami H, Yeh J-W, et al. The high temperature tensile and creep behaviors of high entropy superalloy. Sci Rep. 2017;7:12658.
- [245] Cao C, Fu J, Tong T, Hao Y, Gu P, Hao H, et al. Intermediate-temperature creep deformation and microstructural evolution of an equiatomic FCC-structured CoCrFeNiMn high-entropy alloy. Entropy. 2018;20.
- [246] Dobeš F, Hadraba H, Chlup Z, Dlouhý A, Vilémová M, Matějíček J. Compressive creep behavior of an oxide-dispersion-strengthened CoCrFeMnNi high-entropy alloy. Mater Sci Eng A. 2018;732:99-104.
- [247] Cao T, Shang J, Zhao J, Cheng C, Wang R, Wang H. The influence of Al elements on the structure and the creep behavior of AlxCoCrFeNi high entropy alloys. Mater Lett. 2016;164:344-7.
- [248] Zhu C, Lu T. Deformation mechanism of a high-entropy alloy CoCrFeMnNi at intermediate high temperatures investigated by stress relaxation. Mater Res Express. 2018;6:036531.
- [249] He JY, Zhu C, Zhou DQ, Liu WH, Nieh TG, Lu ZP. Steady state flow of the FeCoNiCrMn high entropy alloy at elevated temperatures. Intermetallics. 2014;55:9-14.
- [250] He JY, Wang H, Wu Y, Liu XJ, Nieh TG, Lu ZP. High-temperature plastic flow of a precipitation-hardened FeCoNiCr high entropy alloy. Mater Sci Eng A. 2017;686:34-40.
- [251] Ma SG. Creep resistance and strain-rate sensitivity of a CoCrFeNiAl0.3 high-entropy alloy by nanoindentation. Mater Res Express. 2019;6:126508.
- [252] Xu Z, Zhang H, Li W, Mao A, Wang L, Song G, et al. Microstructure and nanoindentation creep behavior of CoCrFeMnNi high-entropy alloy fabricated by selective laser melting. Addit Manuf. 2019;28:766-71.
- [253] Zhang L, Yu P, Cheng H, Zhang H, Diao H, Shi Y, et al. Nanoindentation creep behavior of an Al0.3CoCrFeNi high-entropy alloy. Metall Mater Trans A. 2016;47:5871-5.
- [254] Lin PH, Chou HS, Huang JC, Chuang WS, Jang JSC, Nieh TG. Elevated-temperature creep of high-entropy alloys via nanoindentation. MRS Bull. 2019;44:860-6.
- [255] Lee D-H, Seok M-Y, Zhao Y, Choi I-C, He J, Lu Z, et al. Spherical nanoindentation creep behavior of nanocrystalline and coarse-grained CoCrFeMnNi high-entropy alloys. Acta Mater. 2016;109:314-22.
- [256] Ma Y, Feng YH, Debela TT, Peng GJ, Zhang TH. Nanoindentation study on the creep characteristics of highentropy alloy films: fcc versus bcc structures. Int J Refract Met Hard Mater. 2016;54:395-400.
- [257] Tsai MT, Huang JC, Lin PH, Liu TY, Liao YC, Jang JSC, et al. Creep of face-centered-cubic {111} and {100} grains in FeCoNiCrMn and FeCoNiCrMnAl alloys: Orientation and solid solution effects. Intermetallics. 2018;103:88-96.
- [258] Li W, Wang G, Wu S, Liaw PK. Creep, fatigue, and fracture behavior of high-entropy alloys. J Mater Res. 2018;33:3011-34.
- [259] Chen S, Li W, Xie X, Brechtl J, Chen B, Li P, et al. Nanoscale serration and creep characteristics of Al0.5CoCrCuFeNi high-entropy alloys. J Alloys Compd. 2018;752:464-75.
- [260] Mukherjee AK, Bird JE, Dorn JE. Experimental correlations for high-temperature creep. Berkeley, California: University of California; 1968.
- [261] Wang CL, Zhang M, Nieh TG. Nanoindentation creep of nanocrystalline nickel at elevated temperatures. J Phys D: Appl Phys. 2009;42:115405.
- [262] Wazzan AR. Lattice and grain boundary self-diffusion in nickel. J Appl Phys. 1965;36:3596-9.
- [263] Shahmir H, Nili-Ahmadabadi M, Shafiee A, Langdon TG. Effect of a minor titanium addition on the superplastic properties of a CoCrFeNiMn high-entropy alloy processed by high-pressure torsion. Mater Sci Eng A. 2018;718:468-76
- [264] Gladman T. Precipitation hardening in metals. Mater Sci Technol. 1999;15:30-6.
- [265] Laplanche G, Gadaud P, Horst O, Otto F, Eggeler G, George EP. Temperature dependencies of the elastic moduli and thermal expansion coefficient of an equiatomic, single-phase CoCrFeMnNi high-entropy alloy. J Alloys Compd. 2015;623:348-53.
- [266] Shahmir H, He J, Lu Z, Kawasaki M, Langdon TG. Evidence for superplasticity in a CoCrFeNiMn high-entropy alloy processed by high-pressure torsion. Mater Sci Eng A. 2017;685:342-8.
- [267] Wu Z, Bei H, Otto F, Pharr GM, George EP. Recovery, recrystallization, grain growth and phase stability of a family of FCC-structured multi-component equiatomic solid solution alloys. Intermetallics. 2014;46:131-40.
- [268] Wang Z, Fang Q, Li J, Liu B, Liu Y. Effect of lattice distortion on solid solution strengthening of BCC high-entropy alloys. J Mater Sci Technol. 2018;34:349-54.
- [269] Oh HS, Ma D, Leyson GP, Grabowski B, Park ES, Körmann F, et al. Lattice distortions in the FeCoNiCrMn high entropy alloy studied by theory and experiment. Entropy. 2016;18.

- [270] Komarasamy M, Kumar N, Mishra RS, Liaw PK. Anomalies in the deformation mechanism and kinetics of coarse-grained high entropy alloy. Mater Sci Eng A. 2016;654:256-63.
- [271] Tong Y, Jin K, Bei H, Ko JYP, Pagan DC, Zhang Y, et al. Local lattice distortion in NiCoCr, FeCoNiCr and FeCoNiCrMn concentrated alloys investigated by synchrotron X-ray diffraction. Mater Design. 2018;155:1-7.
- [272] Zhang C, Zhang F, Jin K, Bei H, Chen S, Cao W, et al. Understanding of the elemental diffusion behavior in concentrated solid solution alloys. J Phase Equilib Diff. 2017;38:434-44.
- [273] Kucza W, Dąbrowa J, Cieślak G, Berent K, Kulik T, Danielewski M. Studies of "sluggish diffusion" effect in Co-Cr-Fe-Mn-Ni, Co-Cr-Fe-Ni and Co-Fe-Mn-Ni high entropy alloys; determination of tracer diffusivities by combinatorial approach. J Alloys Compd. 2018;731:920-8.
- [274] Divinski SV, Reglitz G, Rösner H, Estrin Y, Wilde G. Ultra-fast diffusion channels in pure Ni severely deformed by equal-channel angular pressing. Acta Mater. 2011;59:1974-85.
- [275] Burton B. The influence of stacking fault energy on creep. Acta Metall. 1982;30:905-10.
- [276] Xie D, Feng R, Liaw PK, Bei H, Gao Y. Tensile creep behavior of an equiatomic CoCrNi medium entropy alloy. Intermetallics. 2020;121:106775.
- [277] Dwivedi A, Koch CC, Rajulapati KV. On the single phase fcc solid solution in nanocrystalline Cr-Nb-Ti-V-Zn high-entropy alloy. Mater Lett. 2016;183:44-7.
- [278] King DJM, Middleburgh SC, McGregor AG, Cortie MB. Predicting the formation and stability of single phase high-entropy alloys. Acta Mater. 2016;104:172-9.
- [279] Senkov ON, Senkova SV, Miracle DB, Woodward C. Mechanical properties of low-density, refractory multiprincipal element alloys of the Cr–Nb–Ti–V–Zr system. Mater Sci Eng A. 2013;565:51-62.
- [280] Senkov ON, Jensen JK, Pilchak AL, Miracle DB, Fraser HL. Compositional variation effects on the microstructure and properties of a refractory high-entropy superalloy AlMo0.5NbTa0.5TiZr. Mater Design. 2018;139:498-511.
- [281] Fazakas É, Zadorozhnyy V, Varga LK, Inoue A, Louzguine-Luzgin DV, Tian F, et al. Experimental and theoretical study of Ti20Zr20Hf20Nb20X20 (X=V or Cr) refractory high-entropy alloys. Int J Refract Met Hard Mater. 2014;47:131-8.
- [282] Tazuddin, Gurao NP, Biswas K. In the quest of single phase multi-component multiprincipal high entropy alloys. J Alloys Compd. 2017;697:434-42.
- [283] Murakumo T, Kobayashi T, Koizumi Y, Harada H. Creep behaviour of Ni-base single-crystal superalloys with various  $\gamma'$  volume fraction. Acta Mater. 2004;52:3737-44.
- [284] Zhang Z, Chen DL. Consideration of Orowan strengthening effect in particulate-reinforced metal matrix nanocomposites: A model for predicting their yield strength. Scripta Mater. 2006;54:1321-6.
- [285] Wang Q, Ma Y, Jiang B, Li X, Shi Y, Dong C, et al. A cuboidal B2 nanoprecipitation-enhanced body-centered-cubic alloy Al0.7CoCrFe2Ni with prominent tensile properties. Scripta Mater. 2016;120:85-9.
- [286] He JY, Liu WH, Wang H, Wu Y, Liu XJ, Nieh TG, et al. Effects of Al addition on structural evolution and tensile properties of the FeCoNiCrMn high-entropy alloy system. Acta Mater. 2014;62:105-13.
- [287] Hadraba H, Chlup Z, Dlouhy A, Dobes F, Roupcova P, Vilemova M, et al. Oxide dispersion strengthened CoCrFeNiMn high-entropy alloy. Mater Sci Eng A. 2017;689:252-6.
- [288] Kim WJ, Jeong HT, Park HK, Park K, Na TW, Choi E. The effect of Al to high-temperature deformation mechanisms and processing maps of Al0.5CoCrFeMnNi high entropy alloy. J Alloys Compd. 2019;802:152-65.
- [289] Zou Y, Okle P, Yu H, Sumigawa T, Kitamura T, Maiti S, et al. Fracture properties of a refractory high-entropy alloy: In situ micro-cantilever and atom probe tomography studies. Scripta Mater. 2017;128:95-9.
- [290] Chen C, Pang S, Cheng Y, Zhang T. Microstructure and mechanical properties of Al20-xCr20+0.5xFe20Co20Ni20+0.5x high entropy alloys. J Alloys Compd. 2016;659:279-87
- [291] ASTM E23-16b, Standard test methods for notched bar impact testing of metallic materials. West Conshohocken, PA: ASTM International; 2016.
- [292] Li D, Zhang Y. The ultrahigh charpy impact toughness of forged AlxCoCrFeNi high entropy alloys at room and cryogenic temperatures. Intermetallics. 2016;70:24-8.
- [293] Xia SQ, Gao MC, Zhang Y. Abnormal temperature dependence of impact toughness in AlxCoCrFeNi system high entropy alloys. Mater Chem Phys. 2018;210:213-21.
- [294] Anderson TL. Fracture mechanics: fundamentals and applications. third ed. Boca Raton: CRC press; 2005.
- [295] Liaw PK, McCabe DE, Landes JD. Determination of fracture toughness properties of 4340 steel. Int J Fract. 1985;27:R3-R8.

- [296] Logsdon WA, Liaw PK. Tensile, fracture toughness and fatigue crack growth rate properties of silicon carbide whisker and particulate reinforced aluminum metal matrix composites. Eng Fract Mech. 1986:24:737-51.
- [297] Liaw PK, Saxena A, Perrin J. Life extension technology for steam pipe systems—I. Development of material properties. Eng Fract Mech. 1993;45:759-86.
- [298] Liaw PK, Burke MG, Saxena A, Landes JD. Fracture toughness behavior of ex-service 2-1/4Cr-1Mo steels from a 22-year-old fossil power plant. Metall Trans A. 1991;22:455-68.
- [299] Liaw PK, Landes JD. Influence of prestrain history on fracture toughness properties of steels. Metall Trans A. 1986;17:473.
- [300] Chung D, Ding Z, Yang Y. Hierarchical eutectic structure enabling superior fracture toughness and superb strength in CoCrFeNiNb0.5 eutectic high entropy alloy at room temperature. Adv Eng Mater. 2018;0:1801060.
- [301] Mohanty S, Maity TN, Mukhopadhyay S, Sarkar S, Gurao NP, Bhowmick S, et al. Powder metallurgical processing of equiatomic AlCoCrFeNi high entropy alloy: Microstructure and mechanical properties. Mater Sci Eng A. 2017;679:299-313.
- [302] Roy U, Roy H, Daoud H, Glatzel U, Ray KK. Fracture toughness and fracture micromechanism in a cast AlCoCrCuFeNi high entropy alloy system. Mater Lett. 2014;132:186-9.
- [303] Seifi M, Li D, Yong Z, Liaw PK, Lewandowski JJ. Fracture toughness and fatigue crack growth behavior of ascast high-entropy alloys. JOM. 2015;67:2288-95.
- [304] Wang S-P, Ma E, Xu J. Notch fracture toughness of body-centered-cubic (TiZrNbTa)Mo high-entropy alloys. Intermetallics. 2018;103:78-87.
- [305] Zhang A, Han J, Meng J, Su B, Li P. Rapid preparation of AlCoCrFeNi high entropy alloy by spark plasma sintering from elemental powder mixture. Mater Lett. 2016;181:82-5.
- [306] Zhang H, He Y, Pan Y. Enhanced hardness and fracture toughness of the laser-solidified FeCoNiCrCuTiMoAlSiB0.5 high-entropy alloy by martensite strengthening. Scripta Mater. 2013;69:342-5.
- [307] ASTM E399-17, Standard test method for linear-elastic plane-strain fracture toughness KIc of metallic materials. West Conshohocken, PA: ASTM International; 2017.
- [308] Li W, Liaw PK, Gao Y. Fracture resistance of high entropy alloys: A review. Intermetallics. 2018;99:69-83.
- [309] ASTM E1820-17, Standard test method for measurement of fracture toughness. West Conshohocken, PA: ASTM International; 2017.
- [310] Li WP, Wang XG, Liu B, Fang QH, Jiang C. Fracture mechanisms of a Mo alloyed CoCrFeNi high entropy alloy: In-situ SEM investigation. Mater Sci Eng A. 2018;723:79-88.
- [311] Jo YH, Doh K-Y, Kim DG, Lee K, Kim DW, Sung H, et al. Cryogenic-temperature fracture toughness analysis of non-equi-atomic V10Cr10Fe45Co20Ni15 high-entropy alloy. J Alloys Compd. 2019;809:151864.
- [312] Zhang Z, Mao MM, Wang J, Gludovatz B, Zhang Z, Mao SX, et al. Nanoscale origins of the damage tolerance of the high-entropy alloy CrMnFeCoNi. Nat Commun. 2015;6:10143.
- [313] Kim S-W, Kim JH. In-situ observations of deformation twins and crack propagation in a CoCrFeNiMn highentropy alloy. Mater Sci Eng A. 2018;718:321-5.
- [314] Wang Y-B, Yang P-J, Sun X, Zhang H-L, Han W-Z. Fracture along deformation twin boundary in small-volume Fe40Mn40Co10Cr10 high entropy alloy. Adv Eng Mater. 2019;21:1801266.
- [315] Gao B, Zhang G, Guo T, Jiang C, Guo X, Tang S. Voiding and fracture in high-entropy alloy under multi-axis stress states. Mater Lett. 2019;237:220-3.
- [316] Jo YH, Choi WM, Kim DG, Zargaran A, Lee K, Sung H, et al. Utilization of brittle σ phase for strengthening and strain hardening in ductile VCrFeNi high-entropy alloy. Mater Sci Eng A. 2019;743:665-74.
- [317] Wei S, Kim J, Tasan CC. Boundary micro-cracking in metastable Fe45Mn35Co10Cr10 high-entropy alloys. Acta Mater. 2019;168:76-86.
- [318] Suresh S. Fatigue of materials: Cambridge university press; 1998.
- [319] Bahadur F, Biswas K, Gurao NP. Micro-mechanisms of microstructural damage due to low cycle fatigue in CoCuFeMnNi high entropy alloy. Int J Fatigue. 2020;130:105258.
- [320] Roessle ML, Fatemi A. Strain-controlled fatigue properties of steels and some simple approximations. Int J Fatigue. 2000;22:495-511.
- [321] Hou S-q, Xu J-q. Relationship among S-N curves corresponding to different mean stresses or stress ratios. J Zhejiang Univ Sci A. 2015;16:885-93.
- [322] Pallarés-Santasmartas L, Albizuri J, Avilés A, Avilés R. Mean stress effect on the axial fatigue strength of DIN 34CrNiMo6 quenched and tempered steel. Metals. 2018;8.
- [323] ASTM E647-15e1, Standard test method for measurement of fatigue crack growth rates. West Conshohocken, PA: ASTM International; 2015.

- [324] Thurston KVS, Gludovatz B, Hohenwarter A, Laplanche G, George EP, Ritchie RO. Effect of temperature on the fatigue-crack growth behavior of the high-entropy alloy CrMnFeCoNi. Intermetallics. 2017;88:65-72.
- [325] Ritchie RO. Mechanisms of fatigue-crack propagation in ductile and brittle solids. Int J Fract. 1999;100:55-83.
- [326] Li W, Long X, Huang S, Fang Q, Jiang C. Elevated fatigue crack growth resistance of Mo alloyed CoCrFeNi high entropy alloys. Eng Fract Mech. 2019;218:106579.
- [327] Wang Y, Liu B, Yan K, Wang M, Kabra S, Chiu Y-L, et al. Probing deformation mechanisms of a FeCoCrNi high-entropy alloy at 293 and 77 K using in situ neutron diffraction. Acta Mater. 2018;154:79-89.
- [328] Chlup Z, Fintová S, Hadraba H, Kuběna I, Vilémová M, Matějíček J. Fatigue behaviour and crack initiation in CoCrFeNiMn high-entropy alloy processed by powder metallurgy. Metals. 2019;9.
- [329] Kashaev N, Ventzke V, Petrov N, Horstmann M, Zherebtsov S, Shaysultanov D, et al. Fatigue behaviour of a laser beam welded CoCrFeNiMn-type high entropy alloy. Mater Sci Eng A. 2019;766:138358.
- [330] Kim Y-K, Ham G-S, Kim HS, Lee K-A. High-cycle fatigue and tensile deformation behaviors of coarse-grained equiatomic CoCrFeMnNi high entropy alloy and unexpected hardening behavior during cyclic loading. Intermetallics. 2019:111:106486.
- [331] Wang AG, An XH, Gu J, Wang XG, Li LL, Li WL, et al. Effect of grain size on fatigue cracking at twin boundaries in a CoCrFeMnNi high-entropy alloy. J Mater Sci Technol. 2020;39:1-6.
- [332] Guennec B, Kentheswaran V, Perrière L, Ueno A, Guillot I, Couzinié JP, et al. Four-point bending fatigue behavior of an equimolar BCC HfNbTaTiZr high-entropy alloy: Macroscopic and microscopic viewpoints. Materialia. 2018;4:348-60.
- [333] Chen SY, Tong Y, Tseng KK, Yeh JW, Poplawsky JD, Wen JG, et al. Phase transformations of HfNbTaTiZr high-entropy alloy at intermediate temperatures. Scripta Mater. 2019;158:50-6.
- [334] Štok B, Halilovič M. Analytical solutions in elasto-plastic bending of beams with rectangular cross section. Appl Math Model. 2009;33:1749-60.
- [335] Guennec B, Kentheswaran V, Perrière L, Ueno A, Guillot I, Couzinié JP, et al. Analysis of the fatigue crack growth mechanisms in equimolar body centered cubic HfNbTaTiZr high-entropy alloy: Discussions on its singularities and consequences on the crack propagation rate properties. Intermetallics. 2019;110:106459.
- [336] Liu K, Nene SS, Frank M, Sinha S, Mishra RS. Extremely high fatigue resistance in an ultrafine grained high entropy alloy. Appl Mater Today. 2019;15:525-30.
- [337] Ju Y-B, Koyama M, Sawaguchi T, Tsuzaki K, Noguchi H. Effects of \(\epsilon\)-martensitic transformation on crack tip deformation, plastic damage accumulation, and slip plane cracking associated with low-cycle fatigue crack growth. Int J Fatigue. 2017;103:533-45.
- [338] Shukla S, Wang T, Cotton S, Mishra RS. Hierarchical microstructure for improved fatigue properties in a eutectic high entropy alloy. Scripta Mater. 2018;156:105-9.
- [339] Sangid MD. The physics of fatigue crack initiation. Int J Fatigue. 2013;57:58-72.
- [340] Hemphill MA, Yuan T, Wang GY, Yeh JW, Tsai CW, Chuang A, et al. Fatigue behavior of Al0.5CoCrCuFeNi high entropy alloys. Acta Mater. 2012;60:5723-34.
- [341] Tang Z, Yuan T, Tsai C-W, Yeh J-W, Lundin CD, Liaw PK. Fatigue behavior of a wrought Al0.5CoCrCuFeNi two-phase high-entropy alloy. Acta Mater. 2015;99:247-58.
- [342] Liu K, Komarasamy M, Gwalani B, Shukla S, Mishra RS. Fatigue behavior of ultrafine grained triplex Al0.3CoCrFeNi high entropy alloy. Scripta Mater. 2019;158:116-20.
- [343] Liu K, Gwalani B, Komarasamy M, Shukla S, Wang T, Mishra RS. Effect of nano-sized precipitates on the fatigue property of a lamellar structured high entropy alloy. Mater Sci Eng A. 2019;760:225-30.
- [344] Hörnqvist M, Hansson T, Clevfors O. Fatigue crack growth testing using varying R-ratios. Procedia Eng. 2010;2:155-61.
- [345] Zhan W, Lu N, Zhang C. A new approximate model for the R-ratio effect on fatigue crack growth rate. Eng Fract Mech. 2014;119:85-96.
- [346] Boyce BL, Ritchie RO. Effect of load ratio and maximum stress intensity on the fatigue threshold in Ti-6Al-4V. Eng Fract Mech. 2001;68:129-47.
- [347] Huo W, Fang F, Liu X, Tan S, Xie Z, Jiang J. Fatigue resistance of nanotwinned high-entropy alloy films. Mater Sci Eng A. 2019;739:26-30.
- [348] Liu J-n, Xing Z-g, Wang H-d, Cui X-f, Jin G, Xu B-s. Microstructure and fatigue damage mechanism of FeCoNiAlTiZr high-entropy alloy film by nanoscale dynamic mechanical analysis. Vacuum. 2019;159:516-23.
- [349] Hsu Y-J, Chiang W-C, Wu J-K. Corrosion behavior of FeCoNiCrCux high-entropy alloys in 3.5% sodium chloride solution. Mater Chem Phys. 2005;92:112-7.
- [350] Qiu X-W, Zhang Y-P, He L, Liu C-g. Microstructure and corrosion resistance of AlCrFeCuCo high entropy alloy. J Alloys Compd. 2013;549:195-9.

- [351] Chou YL, Yeh JW, Shih HC. The effect of molybdenum on the corrosion behaviour of the high-entropy alloys Co1.5CrFeNi1.5Ti0.5Mox in aqueous environments. Corros Sci. 2010;52:2571-81.
- [352] Lee CP, Chang CC, Chen YY, Yeh JW, Shih HC. Effect of the aluminium content of AlxCrFe1.5MnNi0.5 highentropy alloys on the corrosion behaviour in aqueous environments. Corros Sci. 2008;50:2053-60.
- [353] Suzuki K, Koyama M, Hamada S, Tsuzaki K, Noguchi H. Planar slip-driven fatigue crack initiation and propagation in an equiatomic CrMnFeCoNi high-entropy alloy. Int J Fatigue. 2020;133:105418.
- [354] Greer JR, De Hosson JTM. Plasticity in small-sized metallic systems: Intrinsic versus extrinsic size effect. Prog Mater Sci. 2011;56:654-724.
- [355] Raghavan R, Kirchlechner C, Jaya BN, Feuerbacher M, Dehm G. Mechanical size effects in a single crystalline equiatomic FeCrCoMnNi high entropy alloy. Scripta Mater. 2017;129:52-5.
- [356] Zhu C, Lu ZP, Nieh TG. Incipient plasticity and dislocation nucleation of FeCoCrNiMn high-entropy alloy. Acta Mater. 2013;61:2993-3001.
- [357] Zou Y, Ma H, Spolenak R. Ultrastrong ductile and stable high-entropy alloys at small scales. Nat Commun. 2015;6:7748.
- [358] Zou Y, Wheeler JM, Ma H, Okle P, Spolenak R. Nanocrystalline high-entropy alloys: A new paradigm in high-temperature strength and stability. Nano Lett. 2017;17:1569-74.
- [359] Zhang H, Siu KW, Liao W, Wang Q, Yang Y, Lu Y. In situmechanical characterization of CoCrCuFeNi highentropy alloy micro/nano-pillars for their size-dependent mechanical behavior. Mater Res Express. 2016;3:094002.
- [360] Hu Y, Shu L, Yang Q, Guo W, Liaw PK, Dahmen KA, et al. Dislocation avalanche mechanism in slowly compressed high entropy alloy nanopillars. Comms Phys. 2018;1:61.
- [361] Ye YX, Lu ZP, Nieh TG. Dislocation nucleation during nanoindentation in a body-centered cubic TiZrHfNb high-entropy alloy. Scripta Mater. 2017;130:64-8.
- [362] Giwa AM, Liaw PK, Dahmen KA, Greer JR. Microstructure and small-scale size effects in plasticity of individual phases of Al0.7CoCrFeNi High Entropy alloy. Extreme Mech Lett. 2016;8:220-8.
- [363] Uchic MD, Dimiduk DM, Florando JN, Nix WD. Sample dimensions influence strength and crystal plasticity. Science. 2004;305:986.
- [364] Greer JR, Oliver WC, Nix WD. Size dependence of mechanical properties of gold at the micron scale in the absence of strain gradients. Acta Mater. 2005;53:1821-30.
- [365] Kiener D, Motz C, Rester M, Jenko M, Dehm G. FIB damage of Cu and possible consequences for miniaturized mechanical tests. Mater Sci Eng A. 2007;459:262-72.
- [366] Kiener D, Grosinger W, Dehm G, Pippan R. A further step towards an understanding of size-dependent crystal plasticity: In situ tension experiments of miniaturized single-crystal copper samples. Acta Mater. 2008;56:580-92.
- [367] Kiener D, Motz C, Schöberl T, Jenko M, Dehm G. Determination of mechanical properties of copper at the micron scale. Adv Eng Mater. 2006;8:1119-25.
- [368] Kunz A, Pathak S, Greer JR. Size effects in Al nanopillars: Single crystalline vs. bicrystalline. Acta Mater. 2011:59:4416-24.
- [369] Oh SH, Legros M, Kiener D, Dehm G. In situ observation of dislocation nucleation and escape in a submicrometre aluminium single crystal. Nat Mater. 2009;8:95.
- [370] Ng KS, Ngan AHW. Breakdown of Schmid's law in micropillars. Scripta Mater. 2008;59:796-9.
- [371] Schneider AS, Kaufmann D, Clark BG, Frick CP, Gruber PA, Mönig R, et al. Correlation between Critical Temperature and Strength of Small-Scale bcc Pillars. Phys Rev Lett. 2009;103:105501.
- [372] Kim J-Y, Jang D, Greer JR. Tensile and compressive behavior of tungsten, molybdenum, tantalum and niobium at the nanoscale. Acta Mater. 2010;58:2355-63.
- [373] Kim J-Y, Greer JR. Tensile and compressive behavior of gold and molybdenum single crystals at the nanoscale. Acta Mater. 2009;57:5245-53.
- [374] Bei H, Shim S, Miller MK, Pharr GM, George EP. Effects of focused ion beam milling on the nanomechanical behavior of a molybdenum-alloy single crystal. Appl Phys Lett. 2007;91:111915.
- [375] Han SM, Bozorg-Grayeli T, Groves JR, Nix WD. Size effects on strength and plasticity of vanadium nanopillars. Scripta Mater. 2010;63:1153-6.
- [376] Rinaldi A, Peralta P, Friesen C, Sieradzki K. Sample-size effects in the yield behavior of nanocrystalline nickel. Acta Mater. 2008;56:511-7.
- [377] Jang D, Greer JR. Size-induced weakening and grain boundary-assisted deformation in 60 nm grained Ni nanopillars. Scripta Mater. 2011;64:77-80.
- [378] Dehm G. Miniaturized single-crystalline fcc metals deformed in tension: New insights in size-dependent plasticity. Prog Mater Sci. 2009;54:664-88.

- [379] Chen SY, Wang L, Li WD, Tong Y, Tseng KK, Tsai CW, et al. Peierls barrier characteristic and anomalous strain hardening provoked by dynamic-strain-aging strengthening in a body-centered-cubic high-entropy alloy. Mater Res Lett. 2019:7:475-81.
- [380] Okamoto NL, Kashioka D, Hirato T, Inui H. Specimen- and grain-size dependence of compression deformation behavior in nanocrystalline copper. Int J Plast. 2014;56:173-83.
- [381] Smidt FA. Use of ion beam assisted deposition to modify the microstructure and properties of thin films. Int Mater Rev. 1990;35:61-128.
- [382] Gu XW, Loynachan CN, Wu Z, Zhang Y-W, Srolovitz DJ, Greer JR. Size-dependent deformation of nanocrystalline Pt nanopillars. Nano Lett. 2012;12:6385-92.
- [383] Alshehri O, Yavuz M, Tsui T. Manifestation of external size reduction effects on the yield point of nanocrystalline rhodium using nanopillars approach. Acta Mater. 2013;61:40-50.
- [384] Volkert CA, Lilleodden ET. Size effects in the deformation of sub-micron Au columns. Philos Mag. 2006;86:5567-79.
- [385] Frick CP, Clark BG, Orso S, Schneider AS, Arzt E. Size effect on strength and strain hardening of small-scale [111] nickel compression pillars. Mater Sci Eng A. 2008;489:319-29.
- [386] Liu Z, Guo S, Liu X, Ye J, Yang Y, Wang X-L, et al. Micromechanical characterization of casting-induced inhomogeneity in an Al0.8CoCrCuFeNi high-entropy alloy. Scripta Mater. 2011;64:868-71.
- [387] Schneider AS, Clark BG, Frick CP, Gruber PA, Arzt E. Effect of orientation and loading rate on compression behavior of small-scale Mo pillars. Mater Sci Eng A. 2009;508:241-6.
- [388] Van Swygenhoven H, Derlet PM. Grain-boundary sliding in nanocrystalline fcc metals. Phys Rev B. 2001;64:224105.
- [389] Shan Z, Stach EA, Wiezorek JMK, Knapp JA, Follstaedt DM, Mao SX. Grain boundary-mediated plasticity in nanocrystalline nickel. Science. 2004;305:654.
- [390] Rupert TJ, Gianola DS, Gan Y, Hemker KJ. Experimental observations of stress-driven grain boundary migration. Science. 2009;326:1686.
- [391] Gertsman VY, Birringer R. On the room-temperature grain growth in nanocrystalline copper. Scripta Metall Mater. 1994;30:577-81.
- [392] Mathaudhu SN, Boyce BL. Thermal stability: The next frontier for nanocrystalline materials. JOM. 2015;67:2785-7.
- [393] Darling KA, Rajagopalan M, Komarasamy M, Bhatia MA, Hornbuckle BC, Mishra RS, et al. Extreme creep resistance in a microstructurally stable nanocrystalline alloy. Nature. 2016;537:378.
- [394] Ashby MF. Mechanisms of deformation and fracture. In: Hutchinson JW, Wu TY, editors. Adv Appl Mech: Elsevier; 1983. p. 117-77.
- [395] Lu L, Chen X, Huang X, Lu K. Revealing the maximum strength in nanotwinned copper. Science. 2009;323:607. [396] Wheeler JM, Maier V, Durst K, Göken M, Michler J. Activation parameters for deformation of ultrafine-grained
- aluminium as determined by indentation strain rate jumps at elevated temperature. Mater Sci Eng A. 2013;585:108-13.
- [397] Wang YM, Hamza AV, Ma E. Temperature-dependent strain rate sensitivity and activation volume of nanocrystalline Ni. Acta Mater. 2006;54:2715-26.
- [398] Maier V, Hohenwarter A, Pippan R, Kiener D. Thermally activated deformation processes in body-centered cubic Cr How microstructure influences strain-rate sensitivity. Scripta Mater. 2015;106:42-5.
- [399] Wei Q, Zhang HT, Schuster BE, Ramesh KT, Valiev RZ, Kecskes LJ, et al. Microstructure and mechanical properties of super-strong nanocrystalline tungsten processed by high-pressure torsion. Acta Mater. 2006;54:4079-89.
- [400] Wei Q, Pan ZL, Wu XL, Schuster BE, Kecskes LJ, Valiev RZ. Microstructure and mechanical properties at different length scales and strain rates of nanocrystalline tantalum produced by high-pressure torsion. Acta Mater. 2011;59:2423-36.
- [401] Bauer J, Schroer A, Schwaiger R, Kraft O. Approaching theoretical strength in glassy carbon nanolattices. Nat Mater. 2016;15:438.
- [402] Greer JR, Nix WD. Nanoscale gold pillars strengthened through dislocation starvation. Phys Rev B. 2006;73:245410.
- [403] Rao SI, Dimiduk DM, Parthasarathy TA, Uchic MD, Tang M, Woodward C. Athermal mechanisms of size-dependent crystal flow gleaned from three-dimensional discrete dislocation simulations. Acta Mater. 2008;56:3245-59
- [404] Parthasarathy TA, Rao SI, Dimiduk DM, Uchic MD, Trinkle DR. Contribution to size effect of yield strength from the stochastics of dislocation source lengths in finite samples. Scripta Mater. 2007;56:313-6.

- [405] Rao SI, Dimiduk DM, Tang M, Uchic MD, Parthasarathy TA, Woodward C. Estimating the strength of single-ended dislocation sources in micron-sized single crystals. Philos Mag. 2007;87:4777-94.
- [406] Brinckmann S, Kim J-Y, Greer JR. Fundamental differences in mechanical behavior between two types of crystals at the nanoscale. Phys Rev Lett. 2008;100:155502.
- [407] Greer JR, Weinberger CR, Cai W. Comparing the strength of f.c.c. and b.c.c. sub-micrometer pillars: Compression experiments and dislocation dynamics simulations. Mater Sci Eng A. 2008;493:21-5.
- [408] Weinberger CR, Cai W. Surface-controlled dislocation multiplication in metal micropillars. P Natl Acad Sci. 2008;105:14304.
- [409] Wu D, Jang JSC, Nieh TG. Elastic and plastic deformations in a high entropy alloy investigated using a nanoindentation method. Intermetallics. 2016;68:118-27.
- [410] Lee D-H, Lee J-A, Zhao Y, Lu Z, Suh J-Y, Kim J-Y, et al. Annealing effect on plastic flow in nanocrystalline CoCrFeMnNi high-entropy alloy: A nanomechanical analysis. Acta Mater. 2017;140:443-51.
- [411] Lin S-Y, Chang S-Y, Chang C-J, Huang Y-C. Nanomechanical properties and deformation behaviors of multi-component (AlCrTaTiZr)NxSiy high-entropy coatings. Entropy. 2014;16:405-17.
- [412] Lee D-H, Choi I-C, Seok M-Y, He J, Lu Z, Suh J-Y, et al. Nanomechanical behavior and structural stability of a nanocrystalline CoCrFeNiMn high-entropy alloy processed by high-pressure torsion. J Mater Res. 2015;30:2804-15
- [413] Maier-Kiener V, Schuh B, George EP, Clemens H, Hohenwarter A. Nanoindentation testing as a powerful screening tool for assessing phase stability of nanocrystalline high-entropy alloys. Mater Design. 2017;115:479-85.
- [414] Hsueh H-T, Shen W-J, Tsai M-H, Yeh J-W. Effect of nitrogen content and substrate bias on mechanical and corrosion properties of high-entropy films (AlCrSiTiZr)100-xNx. Surf Coat Technol. 2012;206:4106-12.
- [415] Ye YX, Liu CZ, Wang H, Nieh TG. Friction and wear behavior of a single-phase equiatomic TiZrHfNb highentropy alloy studied using a nanoscratch technique. Acta Mater. 2018;147:78-89.
- [416] Maier-Kiener V, Schuh B, George EP, Clemens H, Hohenwarter A. Insights into the deformation behavior of the CrMnFeCoNi high-entropy alloy revealed by elevated temperature nanoindentation. J Mater Res. 2017;32:2658-67.
- [417] Ma Y, Peng GJ, Wen DH, Zhang TH. Nanoindentation creep behavior in a CoCrFeCuNi high-entropy alloy film with two different structure states. Mater Sci Eng A. 2015;621:111-7.
- [418] Oliver WC, Pharr GM. An improved technique for determining hardness and elastic modulus using load and displacement sensing indentation experiments. J Mater Res. 1992;7:1564-83.
- [419] Johnson KL, Johnson KL. Contact mechanics: Cambridge university press; 1987.
- [420] Haglund A, Koehler M, Catoor D, George EP, Keppens V. Polycrystalline elastic moduli of a high-entropy alloy at cryogenic temperatures. Intermetallics. 2015;58:62-4.
- [421] Wang W, Jiang CB, Lu K. Deformation behavior of Ni3Al single crystals during nanoindentation. Acta Mater. 2003;51:6169-80.
- [422] Shim S, Bei H, George EP, Pharr GM. A different type of indentation size effect. Scripta Mater. 2008;59:1095-8.
- [423] Chiu YL, Ngan AHW. Time-dependent characteristics of incipient plasticity in nanoindentation of a Ni3Al single crystal. Acta Mater. 2002;50:1599-611.
- [424] Zuo L, Ngan AHW, Zheng GP. Size Dependence of Incipient Dislocation Plasticity in Ni3Al. Phys Rev Lett. 2005;94:095501.
- [425] Lorenz D, Zeckzer A, Hilpert U, Grau P, Johansen H, Leipner HS. Pop-in effect as homogeneous nucleation of dislocations during nanoindentation. Phys Rev B. 2003;67:172101.
- [426] Schuh CA, Lund AC. Application of nucleation theory to the rate dependence of incipient plasticity during nanoindentation. J Mater Res. 2004;19:2152-8.
- [427] Mason JK, Lund AC, Schuh CA. Determining the activation energy and volume for the onset of plasticity during nanoindentation. Phys Rev B. 2006;73:054102.
- [428] Schuh CA, Mason JK, Lund AC. Quantitative insight into dislocation nucleation from high-temperature nanoindentation experiments. Nat Mater. 2005;4:617-21.
- [429] Balluffi RW. Vacancy defect mobilities and binding energies obtained from annealing studies. J Nucl Mater. 1978;69-70:240-63.
- [430] Bowden FP, Bowden FP, Tabor D. The friction and lubrication of solids: Oxford university press; 2001.
- [431] Hodge AM, Nieh TG. Evaluating abrasive wear of amorphous alloys using nanoscratch technique. Intermetallics. 2004;12:741-8.

- [432] Rabinowicz E, Dunn LA, Russell PG. A study of abrasive wear under three-body conditions. Wear. 1961;4:345-55.
- [433] Greer AL, Rutherford KL, Hutchings IM. Wear resistance of amorphous alloys and related materials. Int Mater Rev. 2002;47:87-112.
- [434] Mate CM. Tribology on the small scale: a bottom up approach to friction, lubrication, and wear: Oxford University Press; 2008.
- [435] Archard JF. Contact and rubbing of flat surfaces. J Appl Phys. 1953;24:981-8.
- [436] Feng X, Zhang J, Xia Z, Fu W, Wu K, Liu G, et al. Stable nanocrystalline NbMoTaW high entropy alloy thin films with excellent mechanical and electrical properties. Mater Lett. 2018;210:84-7.
- [437] Feng XB, Zhang JY, Wang YQ, Hou ZQ, Wu K, Liu G, et al. Size effects on the mechanical properties of nanocrystalline NbMoTaW refractory high entropy alloy thin films. Int J Plast. 2017;95:264-77.
- [438] Feng XB, Fu W, Zhang JY, Zhao JT, Li J, Wu K, et al. Effects of nanotwins on the mechanical properties of AlxCoCrFeNi high entropy alloy thin films. Scripta Mater. 2017;139:71-6.
- [439] Feng X, Fan S, Meng F, Surjadi JU, Cao K, Liao W, et al. Effect of Zr addition on microstructure and mechanical properties of CoCrFeNiZrx high-entropy alloy thin films. Appl Nanosci. 2019.
- [440] Carlton CE, Ferreira PJ. What is behind the inverse Hall–Petch effect in nanocrystalline materials? Acta Mater. 2007;55:3749-56.
- [441] Zhang JY, Cui JC, Liu G, Sun J. Deformation crossover in nanocrystalline Zr micropillars: The strongest external size. Scripta Mater. 2013;68:639-42.
- [442] Advanced bond coats for thermal barrier coating systems based on high entropy alloys. <a href="https://www.sbirgov/sbirsearch/detail/890837">https://www.sbirgov/sbirsearch/detail/890837</a>.
- [443] Exploration of high entropy alloys for turbine applications. <a href="https://www.sbirgov/sbirsearch/detail/1212591">https://www.sbirgov/sbirsearch/detail/1212591</a>.
- [444] Youssef KM, Zaddach AJ, Niu C, Irving DL, Koch CC. A novel low-density, high-hardness, high-entropy alloy with close-packed single-phase nanocrystalline structures. Mater Res Lett. 2015;3:95-9.
- [445] Bridges D, Zhang S, Lang S, Gao M, Yu Z, Feng Z, et al. Laser brazing of a nickel-based superalloy using a Ni-Mn-Fe-Co-Cu high entropy alloy filler metal. Mater Lett. 2018;215:11-4.
- [446] Yeh J-W, Lin S-J. Breakthrough applications of high-entropy materials. J Mater Res. 2018;33:3129-37.
- [447] Chuang M-H, Tsai M-H, Wang W-R, Lin S-J, Yeh J-W. Microstructure and wear behavior of AlxCo1.5CrFeNi1.5Tiy high-entropy alloys. Acta Mater. 2011;59:6308-17.
- [448] Gupta M, Tun K. An insight into the development of light weight high entropy alloys. Res Dev Mater Sci. 2017;2:9-11.
- [449] Feng R, Gao MC, Zhang C, Guo W, Poplawsky JD, Zhang F, et al. Phase stability and transformation in a light-weight high-entropy alloy. Acta Mater. 2018;146:280-93.
- [450] Feng R, Gao CM, Lee C, Mathes M, Zuo T, Chen S, et al. Design of light-weight high-entropy alloys. Entropy. 2016;18.
- [451] Chen S, Tseng K-K, Tong Y, Li W, Tsai C-W, Yeh J-W, et al. Grain growth and Hall-Petch relationship in a refractory HfNbTaZrTi high-entropy alloy. J Alloys Compd. 2019;795:19-26.
- [452] Senkov NO, Isheim D, Seidman ND, Pilchak LA. Development of a refractory high entropy superalloy. Entropy. 2016;18.
- [453] Manufacturing High Entropy Alloys: Pathway to Industrial Competitiveness.
- [454] Kumar NAPK, Li C, Leonard KJ, Bei H, Zinkle SJ. Microstructural stability and mechanical behavior of FeNiMnCr high entropy alloy under ion irradiation. Acta Mater. 2016;113:230-44.
- [455] Shi Y, Yang B, Liaw KP. Corrosion-resistant high-entropy alloys: A review. Metals. 2017;7.
- [456] Nair RB, Arora HS, Mukherjee S, Singh S, Singh H, Grewal HS. Exceptionally high cavitation erosion and corrosion resistance of a high entropy alloy. Ultrason Sonochem. 2018;41:252-60.
- [457] Kao Y-F, Lee T-D, Chen S-K, Chang Y-S. Electrochemical passive properties of AlxCoCrFeNi (x=0, 0.25, 0.50, 1.00) alloys in sulfuric acids. Corros Sci. 2010;52:1026-34.
- [458] Popescu G, Ghiban B, Popescu CA, Rosu L, Truscă R, Carcea I, et al. New TiZrNbTaFe high entropy alloy used for medical applications. IOP Conf Ser Mater Sci Eng. 2018;400:022049.
- [459] Nguyen VT, Qian M, Shi Z, Song T, Huang L, Zou J. A novel quaternary equiatomic Ti-Zr-Nb-Ta medium entropy alloy (MEA). Intermetallics. 2018;101:39-43.
- [460] Todai M, Nagase T, Hori T, Matsugaki A, Sekita A, Nakano T. Novel TiNbTaZrMo high-entropy alloys for metallic biomaterials. Scripta Mater. 2017;129:65-8.
- [461] Nagase T, Todai M, Hori T, Nakano T. Microstructure of equiatomic and non-equiatomic Ti-Nb-Ta-Zr-Mo high-entropy alloys for metallic biomaterials. J Alloys Compd. 2018;753:412-21.

- [462] Wang S-P, Xu J. TiZrNbTaMo high-entropy alloy designed for orthopedic implants: As-cast microstructure and mechanical properties. Mater Sci Eng C. 2017;73:80-9.
- [463] Hori T, Nagase T, Todai M, Matsugaki A, Nakano T. Development of non-equiatomic Ti-Nb-Ta-Zr-Mo high-entropy alloys for metallic biomaterials. Scripta Mater. 2019;172:83-7.
- [464] Nagase T, Mizuuchi K, Nakano T. Solidification microstructures of the ingots obtained by arc melting and cold crucible levitation melting in TiNbTaZr medium-entropy alloy and TiNbTaZrX (X = V, Mo, W) high-entropy alloys. Entropy. 2019;21.
- [465] ZHANG A-r, LIANG H-y, LI Y. Property of AlCrCoFeNiMoTi\_ (0.75) Si\_ (0.25) high-entropy alloy coating tool prepared by laser cladding. China Surf Eng. 2013:4.
- [466] Löbel M, Lindner T, Mehner T, Lampke T. Microstructure and wear resistance of AlCoCrFeNiTi high-entropy alloy coatings produced by HVOF. Coatings. 2017;7.
- [467] Shen W, Tsai M, Tsai K, Juan C, Tsai C, Yeh J, et al. Superior oxidation resistance of (Alo. 34Cr0. 22Nb0. 11Si0. 11Ti0. 22) 50N50 high-entropy nitride. J Electrochem Soc. 2013;160:C531-C5.
- [468] Li P, Wang A, Liu CT. A ductile high entropy alloy with attractive magnetic properties. J Alloys Compd. 2017;694:55-60.
- [469] Feng W, Qi Y, Wang S. Effects of short-range order on the magnetic and mechanical properties of FeCoNi(AlSi)x high entropy alloys. Metals. 2017;7.
- [470] Körmann F, Ma D, Belyea DD, Lucas MS, Miller CW, Grabowski B, et al. "Treasure maps" for magnetic highentropy-alloys from theory and experiment. Appl Phys Lett. 2015;107:142404.
- [471] Zhang G, Ming K, Kang J, Huang Q, Zhang Z, Zheng X, et al. High entropy alloy as a highly active and stable electrocatalyst for hydrogen evolution reaction. Electrochim Acta. 2018;279:19-23.
- [472] Yusenko KV, Riva S, Carvalho PA, Yusenko MV, Arnaboldi S, Sukhikh AS, et al. First hexagonal close packed high-entropy alloy with outstanding stability under extreme conditions and electrocatalytic activity for methanol oxidation. Scripta Mater. 2017;138:22-7.
- [473] Sahlberg M, Karlsson D, Zlotea C, Jansson U. Superior hydrogen storage in high entropy alloys. Sci Rep. 2016;6:36770.
- [474] Firstov GS, Kosorukova TA, Koval YN, Odnosum VV. High entropy shape memory alloys. Mater Today Proc. 2015;2:S499-S503.
- [475] Canadinc D, Trehern W, Ma J, Karaman I, Sun F, Chaudhry Z. Ultra-high temperature multi-component shape memory alloys. Scripta Mater. 2019;158:83-7.
- [476] Kurniawan M, Perrin A, Xu P, Keylin V, McHenry M. Curie temperature engineering in high entropy alloys for magnetocaloric applications. IEEE Magn Lett. 2016;7:1-5.
- [477] Yuan Y, Wu Y, Tong X, Zhang H, Wang H, Liu XJ, et al. Rare-earth high-entropy alloys with giant magnetocaloric effect. Acta Mater. 2017;125:481-9.
- [478] Koželj P, Vrtnik S, Jelen A, Jazbec S, Jagličić Z, Maiti S, et al. Discovery of a superconducting high-entropy alloy. Phys Rev Lett. 2014;113:107001.
- [479] Stolze K, Cevallos FA, Kong T, Cava RJ. High-entropy alloy superconductors on an α-Mn lattice. J Mater Chem C. 2018;6:10441-9.
- [480] Stolze K, Tao J, von Rohr FO, Kong T, Cava RJ. Sc-Zr-Nb-Rh-Pd and Sc-Zr-Nb-Ta-Rh-Pd high-entropy alloy superconductors on a CsCl-type lattice. Chem Mater. 2018;30:906-14.
- [481] Marik S, Motla K, Varghese M, Sajilesh KP, Singh D, Breard Y, et al. Superconductivity in a new hexagonal high-entropy alloy. Phys Rev Mater. 2019;3:060602.
- [482] Sun L, Cava RJ. High-entropy alloy superconductors: Status, opportunities, and challenges. Phys Rev Mater. 2019;3:090301.
- [483] Hsu W-L, Murakami H, Yeh J-W, Yeh A-C, Shimoda K. A heat-resistant NiCo0. 6Fe0. 2Cr1. 5SiAlTi0. 2 overlay coating for high-temperature applications. J Electrochem Soc. 2016;163:C752-C8.
- [484] Tsai M-H, Yeh J-W, Gan J-Y. Diffusion barrier properties of AlMoNbSiTaTiVZr high-entropy alloy layer between copper and silicon. Thin Solid Films. 2008;516:5527-30.
- [485] Lin R-C, Lee T-K, Wu D-H, Lee Y-C. A study of thin film resistors prepared using Ni-Cr-Si-Al-Ta high entropy alloy. Adv Mater Sci Eng. 2015;2015.
- [486] Yang P, Liu Y, Zhao X, Cheng J, Li H. Electromagnetic wave absorption properties of mechanically alloyed FeCoNiCrAl high entropy alloy powders. Adv Powder Technol. 2016;27:1128-33.
- [487] Zhang Y, Zhang B, Li K, Zhao G-L, Guo SM. Electromagnetic interference shielding effectiveness of high entropy AlCoCrFeNi alloy powder laden composites. J Alloys Compd. 2018;734:220-8.
- [488] Xie P, Yao Y, Huang Z, Liu Z, Zhang J, Li T, et al. Highly efficient decomposition of ammonia using high-entropy alloy catalysts. Nat Commun. 2019;10:4011.

- [489] Varvenne C, Leyson GPM, Ghazisaeidi M, Curtin WA. Solute strengthening in random alloys. Acta Mater. 2017:124:660-83.
- [490] Tsai M-H, Yeh J-W. High-entropy alloys: A critical review. Mater Res Lett. 2014;2:107-23.
- [491] Li Z, Ludwig A, Savan A, Springer H, Raabe D. Combinatorial metallurgical synthesis and processing of highentropy alloys. J Mater Res. 2018;33:3156-69.
- [492] Diao HY, Feng R, Dahmen KA, Liaw PK. Fundamental deformation behavior in high-entropy alloys: An overview. Curr Opin Solid State Mater Sci. 2017;21:252-66.
- [493] Praveen S, Bae JW, Asghari-Rad P, Park JM, Kim HS. Ultra-high tensile strength nanocrystalline CoCrNi equiatomic medium entropy alloy processed by high-pressure torsion. Mater Sci Eng A. 2018;735:394-7.
- [494] Sathiyamoorthi P, Moon J, Bae JW, Asghari-Rad P, Kim HS. Superior cryogenic tensile properties of ultrafine-grained CoCrNi medium-entropy alloy produced by high-pressure torsion and annealing. Scripta Mater. 2019;163:152-6.
- [495] Wu Z, Guo W, Jin K, Poplawsky JD, Gao Y, Bei H. Enhanced strength and ductility of a tungsten-doped CoCrNi medium-entropy alloy. J Mater Res. 2018;33:3301-9.
- [496] Gubicza J, Hung PT, Kawasaki M, Han J-K, Zhao Y, Xue Y, et al. Influence of severe plastic deformation on the microstructure and hardness of a CoCrFeNi high-entropy alloy: A comparison with CoCrFeNiMn. Mater Charact. 2019;154:304-14.
- [497] Liu J, Chen C, Xu Y, Wu S, Wang G, Wang H, et al. Deformation twinning behaviors of the low stacking fault energy high-entropy alloy: An in-situ TEM study. Scripta Mater. 2017;137:9-12.
- [498] Yu PF, Cheng H, Zhang LJ, Zhang H, Ma MZ, Li G, et al. Nanotwin's formation and growth in an AlCoCuFeNi high-entropy alloy. Scripta Mater. 2016;114:31-4.
- [499] Senkov ON, Scott JM, Senkova SV, Miracle DB, Woodward CF. Microstructure and room temperature properties of a high-entropy TaNbHfZrTi alloy. J Alloys Compd. 2011;509:6043-8.
- [500] Li J, Fang Q, Liu B, Liu Y. Transformation induced softening and plasticity in high entropy alloys. Acta Mater. 2018;147:35-41.
- [501] Niu C, LaRosa CR, Miao J, Mills MJ, Ghazisaeidi M. Magnetically-driven phase transformation strengthening in high entropy alloys. Nat Commun. 2018;9:1363.
- [502] Liu SF, Wu Y, Wang HT, He JY, Liu JB, Chen CX, et al. Stacking fault energy of face-centered-cubic high entropy alloys. Intermetallics. 2018;93:269-73.
- [503] Zhao S, Stocks GM, Zhang Y. Stacking fault energies of face-centered cubic concentrated solid solution alloys. Acta Mater. 2017;134:334-45.
- [504] Beyramali Kivy M, Asle Zaeem M. Generalized stacking fault energies, ductilities, and twinnabilities of CoCrFeNi-based face-centered cubic high entropy alloys. Scripta Mater. 2017;139:83-6.
- [505] Cai B, Liu B, Kabra S, Wang Y, Yan K, Lee PD, et al. Deformation mechanisms of Mo alloyed FeCoCrNi high entropy alloy: In situ neutron diffraction. Acta Mater. 2017;127:471-80.
- [506] Wang Z, Baker I, Cai Z, Chen S, Poplawsky JD, Guo W. The effect of interstitial carbon on the mechanical properties and dislocation substructure evolution in Fe40.4Ni11.3Mn34.8Al7.5Cr6 high entropy alloys. Acta Mater. 2016;120:228-39.
- [507] Sun SJ, Tian YZ, Lin HR, Dong XG, Wang YH, Zhang ZJ, et al. Enhanced strength and ductility of bulk CoCrFeMnNi high entropy alloy having fully recrystallized ultrafine-grained structure. Mater Design. 2017;133:122-7.
- [508] Yasuda HY, Miyamoto H, Cho K, Nagase T. Formation of ultrafine-grained microstructure in Al0.3CoCrFeNi high entropy alloys with grain boundary precipitates. Mater Lett. 2017;199:120-3.
- [509] Juan C-C, Tsai M-H, Tsai C-W, Hsu W-L, Lin C-M, Chen S-K, et al. Simultaneously increasing the strength and ductility of a refractory high-entropy alloy via grain refining. Mater Lett. 2016;184:200-3.
- [510] Kang B, Lee J, Ryu HJ, Hong SH. Ultra-high strength WNbMoTaV high-entropy alloys with fine grain structure fabricated by powder metallurgical process. Mater Sci Eng A. 2018;712:616-24.
- [511] Sathiyamoorthi P, Basu J, Kashyap S, Pradeep KG, Kottada RS. Thermal stability and grain boundary strengthening in ultrafine-grained CoCrFeNi high entropy alloy composite. Mater Design. 2017;134:426-33.
- [512] Wang Z, Genc A, Baker I. Direct versus indirect particle strengthening in a strong, ductile FeNiMnAlTi high entropy alloy. Mater Charact. 2017;132:156-61.
- [513] Gao N, Lu DH, Zhao YY, Liu XW, Liu GH, Wu Y, et al. Strengthening of a CrMnFeCoNi high-entropy alloy by carbide precipitation. J Alloys Compd. 2019;792:1028-35.
- [514] Lee D-H, Choi I-C, Yang G, Lu Z, Kawasaki M, Ramamurty U, et al. Activation energy for plastic flow in nanocrystalline CoCrFeMnNi high-entropy alloy: A high temperature nanoindentation study. Scripta Mater. 2018;156:129-33.

- [515] Liu WH, Yang T, Liu CT. Precipitation hardening in CoCrFeNi-based high entropy alloys. Mater Chem Phys. 2018:210:2-11.
- [516] Li RX, Liaw PK, Zhang Y. Synthesis of AlxCoCrFeNi high-entropy alloys by high-gravity combustion from oxides. Mater Sci Eng A. 2017;707:668-73.
- [517] Lv Y, Hu R, Yao Z, Chen J, Xu D, Liu Y, et al. Cooling rate effect on microstructure and mechanical properties of AlxCoCrFeNi high entropy alloys. Mater Design. 2017;132:392-9.
- [518] Wang W-R, Wang W-L, Yeh J-W. Phases, microstructure and mechanical properties of AlxCoCrFeNi highentropy alloys at elevated temperatures. J Alloys Compd. 2014;589:143-52.
- [519] Yang T, Xia S, Liu S, Wang C, Liu S, Zhang Y, et al. Effects of AL addition on microstructure and mechanical properties of AlxCoCrFeNi High-entropy alloy. Mater Sci Eng A. 2015;648:15-22.
- [520] Xiao Y, Zou Y, Ma H, Sologubenko AS, Maeder X, Spolenak R, et al. Nanostructured NbMoTaW high entropy alloy thin films: High strength and enhanced fracture toughness. Scripta Mater. 2019;168:51-5.
- [521] Wang S-P, Xu J. (TiZrNbTa)-Mo high-entropy alloys: Dependence of microstructure and mechanical properties on Mo concentration and modeling of solid solution strengthening. Intermetallics. 2018;95:59-72.
- [522] Tian YZ, Sun SJ, Lin HR, Zhang ZF. Fatigue behavior of CoCrFeMnNi high-entropy alloy under fully reversed cyclic deformation. J Mater Sci Technol. 2019;35:334-40.
- [523] Suzuki K, Koyama M, Noguchi H. Small fatigue crack growth in a high entropy alloy. Procedia Struct Integr. 2018;13:1065-70.
- [524] Li Z, Zhao S, Diao H, Liaw PK, Meyers MA. High-velocity deformation of Al0.3CoCrFeNi high-entropy alloy: Remarkable resistance to shear failure. Sci Rep. 2017;7:42742.
- [525] Senkov O, Scott J, Senkova S, Meisenkothen F, Miracle D, Woodward C. Microstructure and elevated temperature properties of a refractory TaNbHfZrTi alloy. J Mater Sci. 2012;47:4062-74.

## **Tables**

**Table 1.1** Differences between conventional dilute alloys and high-entropy alloys considered from different aspects.

Aspects	Conventional dilute alloys	HEAs		
compositional space	low-dimensional	high- and hyper-dimensional		
composition	limited	limitless		
alloy design strategy	based on one principal element	based on multiple principal elements		
concentration of secondary elements	dilute	concentrated		
solid solution	distinguishable solvent and solute atoms	indistinguishable solvent and solute atoms		
phase diagram	corners and edges	central region		
configurational entropy of mixing	low	high		
modulus mismatch	mild	severe		
atomic size mismatch	mild	severe		
lattice distortion	mild	severe		
microstructure	less diversified	more diversified		
properties	limited possibilities	numerous possibilities		
diffusion	relatively quick	sluggish		
solid solution strengthening	weak	strong		

 Table 1.2 Classification of high-entropy alloys based upon different features.

Based upon	Classification	Ref.
Composition	(i) Equimolar HEAs, (ii) non-equimolar HEAs	
Composition	(i) 3d transition metal HEAs, (ii) refractory metal HEAs, (iii) light metal HEAs, (iv) lanthanide transition metal HEAs, (v) HEA brasses and bronzes, (vi) precious metal HEAs, and (vii) interstitial compound HEAs	[1]
Microstructure	(i) single-phase HEAs, (ii) dual-phase HEAs, (iii) multi-phase HEAs	
Microstructure	(i) FCC AlCoCrCuFeNi and derivatives, (ii) FCC CoCrFeMnNi and derivatives, (iii) BCC refractory HEAs, (iv) HCP HEAs, (v) other HEAs	[26]
Microstructure	(i) terminal solutions, (ii) intermediate solutions, (iii) intermetallic compounds	[490 ]
Microstructure	(i) random solid solutions, (ii) ordered solid solutions, (iii) intermetallic phases	[490 ]
Microstructure	(i) simple disordered phases, (ii) simple ordered phases, (iii) complex ordered phases	[490 ]
Microstructure	(i) solid solutions, (ii) intermetallic compounds, (iii) a mixture of solid solutions and intermetallic compounds	[1]
Microstructure + properties	(i) FCC strong and ductile HEAs, (ii) BCC refractory HEAs, (iii) HCP HEAs, (iv) lightweight HEAs, (v) precious functional HEAs	[491 ]
Mechanical properties	(i) FCC 3d-transition metals, (ii) transition metals with larger-atomic-radius elements, (iii) BCC refractory metals, (iv) others	[492 ]
Phase stability	(i) stable HEAs, (ii) metastable HEAs	

 Table 2.1 High-entropy alloys reported with twining-mediated deformation.

Composition	Phase	Processing	T(K)	Twining initiation strain (%)	CRSS for twinning (MPa)	Ref.
CoCrNi	FCC	HPT	298	- ` ′	-	[493]
CoCrNi	FCC	HPT+AN	77	-	-	[494]
CoCrNi	FCC	Swaged+FR	77	6.7	260 ± 30	[110]
CoCrNi	FCC	Swaged+FR	293	12.9	260 ± 30	[110]
CoCrNi-3W	FCC	CR+AN	77	-	-	[495]
CoCrNi-3W	FCC	CR+AN	293	-	-	[495]
CoCrFeNi	FCC	HPT	298	-	-	[496]
CrMnFeCoNi	FCC	FR	77	~7.4	235 ± 10	[65]
CrMnFeCoNi	FCC	FR	293	~25	235 ± 10	[65]
CrMnFeCoNi	FCC	CR+FR	77	~20-38	-	[47]
CrMnFeCoNi	FCC	CR	77	15	-	[82]
CrMnFeCoNi	FCC	CR	293	40	-	[82]
CoCrFeMnNi	FCC	HF+CR+FR	298	-	-	[66]
CoCrFeMnNi	FCC	As-cast	295	-	87	[64]
CoCrFeMnNi	FCC	As-cast	473	-	102	[64]
CoCrFeMnNi	FCC	As-cast	673	-	116	[64]
CoCrFeMnNi	FCC	As-cast	773	-	121	[64]
$Fe_{20}Co_{27}Ni_{13}Cr_{20}Mn_{20}$	FCC	CR+FR	298	~18	-	[73]
$CoCrFeNiMnC_x$ (x > 0.1)	FCC+M <sub>7</sub> C <sub>3</sub>	-	298	-	-	[71]
FeNiCoCrMn-0.5C	FCC	CR+FR	77	~6.5	-	[70]
FeNiCoCrMn-0.5C	FCC	CR+FR	293	~32.5	-	[70]
CoNiFeCrAl <sub>0.6</sub> Ti <sub>0.4</sub>	FCC1+ FCC2+BCC	MA+SPS	298	-	-	[79]
VCrMnFeCoNi	FCC	CR+FR	298	-	-	[76]
$Fe_{40}Mn_{40}Co_{10}Cr_{10}$	FCC	CR+FR	298	~10	-	[314]
$(Fe_{40}Mn_{40}Co_{10}Cr_{10})_{96.7}C_{3.3}$	FCC	As-cast	298	-	-	[69]
Fe <sub>40</sub> Mn <sub>40</sub> Co <sub>10</sub> Cr <sub>10</sub> -1.0Mo-1.0C	FCC	As-cast	298	-		[152]
$Fe_{50}Mn_{30}Co_{10}Cr_{10}$	HCP+FCC	HR+Homo+ CR+FR	298	30	-	[19]
FeCoNiCrAl <sub>0.1</sub>	FCC	As-cast	298	-	-	[497]
Al <sub>0.1</sub> CoCrFeNi	FCC	As-cast	298	-	-	[77]
Al <sub>0.1</sub> CoCrFeNi	FCC	FR	298	-	-	[77]
Al <sub>0.3</sub> CoCrFeNi	FCC + B2 + $\sigma$	CR+FR	298	-	-	[63]
Al <sub>0.1</sub> CrFeCoNi	FCC	-	298	~5	-	[72]
Al <sub>0.1</sub> CoCrFeNi	FCC	-	298	~4.2	-	[72]
Al <sub>0.3</sub> CoCrFeNi	FCC+B2	HD	77	-	-	[81]
Al <sub>0.3</sub> CoCrFeNi	FCC+BCC+σ	CR+FR	298	-	-	[342]
Al <sub>0.5</sub> CoCrCuFeNi	FCC	CR	298	-		[341]
Al <sub>0.6</sub> CoNiFeTi <sub>0.4</sub>	FCC+BCC	MA+SPS	-	-	-	[78]
AlCoCuFeNi	BCC	MP	-	-	-	[498]
TaNbHfZrTi	BCC	HIP	298	-	-	[499]

Notes: "HR", "Homo", "CR", "MA", "SPS", "HD", "HIP", "HPT", "FR", "PR", "MP", and "AN" refer to hot-rolling, homogenization, cold-rolling, mechanical alloying, spark plasma sintering, hot-drawing, hot isostatic pression, high pressure torsion, fully recrystallization, partially recrystallization, melt-spinning, and annealing, respectively. CRSS denote the critical resolved shear stress.

 Table 2.2 High-entropy alloys reported with phase-transformation assisted deformation.

Alloy	Processing	Initial phase	Phase trans.	Benefits	Approach	Ref.
Fe <sub>50</sub> Mn <sub>30</sub> Co <sub>10</sub> Cr <sub>10</sub>	Melted in a vacuum induction furnace, cast, hot-rolled, homogenized, water-quenched, grain refined by cold rolling, annealed, and water-quenched	fcc+hcp	fcc→hc p	Strength, ductility, and work hardening	Modify the Mn content	[19, 95, 98, 99]
$Fe_{49.5}Mn_{30}Co_{10}Cr_{10}C_{0.5}$	Melted in a vacuum induction furnace, cast, hot-rolled, homogenized, water-quenched, cold-rolled, and tempered/annealed, and water- quenched	fcc+hcp	fcc→hc p	Strength, ductility, and work hardening	Modify the Mn content	[105, 106, 223]
$Co_{20Cr_{20Fe_{34Mn_{20}Ni_{6}}}$	Melted in a vacuum induction furnace, cast, hot-rolled, homogenized, and water-quenched	fcc+hcp	fcc→hc p	Strength, ductility, and work hardening	Tune SFE by composition al change	[90]
$Co_{25}Ni_{25}Fe_{25}Al_{7.5}Cu_{17.5}$	Molecular dynamic simulations	fcc	fcc→bcc	Strength, ductility, and work hardening	Low SFE	[500]
$Fe_{60}Co_{15}Ni_{15}Cr_{10}$	Melted in a vacuum induction furnace, cast, homogenized, pickled, cold-rolled, annealed, and water-quenched	fcc	fcc→bcc	Strength, ductility, and work hardening	Substitute Fe for (CoNi) and cryo- deformation	[222]
Fe <sub>20</sub> Co <sub>30</sub> Ni <sub>10</sub> Cr <sub>20</sub> Mn <sub>20</sub>	Arc-melted, drop-cast, homogenized, cold-rolled, annealed	fcc+hcp	fcc→hc p	Strength, ductility, and work hardening	Tune SFE by composition al change	[73]
Fe <sub>42</sub> Mn <sub>28</sub> Co <sub>10</sub> Cr <sub>15</sub> Si <sub>5</sub>	Arc-melted, drop-cast, and subjected to multi-pass FSP,	fcc+hcp	fcc→hc p	Strength, ductility, and work hardening	Add Si	[101]
$Fe_{39}Mn_{20}Co_{20}Cr_{15}Si_{5}AI \\ {}_{1}$	Arc-melted, drop-cast, and subjected to double-pass FSP, annealed, and water-quenched	fcc+hcp	fcc→hc p	Strength, ductility, and work hardening	Add Si and Al	[100]
FeCoCrNi	Melted by vacuum induction levitation, cast, annealed, and hotforged	fcc	fcc→hc p	n/a	Cryo- deformation	[92]
CrCoNi	Arc-melted, cast, homogenized, water-quenched, cold-rolled, and annealed	fcc	fcc→hc p	Strength	Cryo- deformation	[501]
Ta <sub>0.4</sub> HfZrTi	Arc-melted and drop-cast	bcc+hcp	bcc→hc p	Ductility and work hardening	Modify the Ta content	[89]
Ta <sub>0.5</sub> HfZrTi	Arc-melted and drop-cast	bcc+hcp	bcc→hc p	Ductility and work hardening	Modify the Ta content	[89]
Ta <sub>0.6</sub> HfZrTi	Arc-melted and drop-cast	bcc+hcp	bcc→hc p	Ductility and work hardening	Modify the Ta content	[89]

$Ti_{35}Zr_{27.5}Hf_{27.5}Nb_5Ta_5$	Melted by the arc and frequency induction technique, cast, cold-rolled, solution-treated, and air-quenched	bcc	bcc→ orthorh ombic phase	Work hardening	Composition al modification on TiZrHfNbTa	[96]
-------------------------------------	--	-----	-----------------------------------	----------------	---	------

Notes: SFE – stacking fault energy.

Table 2.3 High-entropy alloys reported with both twinning and phase transformation

Composition	T(K)	Phase	Phase trans.	Twin	Outcome	Ref.
Fe <sub>49.5</sub> Mn <sub>30</sub> Co <sub>10</sub> Cr <sub>10</sub> C <sub>0.5</sub>	298	fcc+hcp	fcc→hcp	Twin in fcc phase	Strength ↑  Ductility→  Strain Hardening↑	[102] [105] [106]
Fe <sub>50</sub> Mn <sub>30</sub> Co <sub>10</sub> Cr <sub>10</sub>	298	fcc+hcp	fcc→hcp	Twin in hcp phase	Strength ↑ Ductility ↓ Strain Hardening↑	[19]

Notes:  $\uparrow$ ,  $\downarrow$ , and  $\rightarrow$  indicate that the mechanical properties are better, worse, and similar to those in the alloys' equiatomic counterparts.

Table 2.4 Stacking fault energy (SFE) of the high-entropy alloys obtained by various techniques.

Composition	Structure	<i>T</i> (K)	SFE (mJ/m²)	Technique to calculate SFE	Ref.
NiFeCrCo	FCC	0	17.4-34.3	EMTO <sup>I</sup> +CPA <sup>II</sup> VASP <sup>III</sup>	[114]
CrMnFeCoNi	FCC	0	18.3-27.3	EMTO+CPA VASP	[114]
$Ni_{26}Fe_{20}Cr_{14}Co_{20}Mn_{20}$	FCC	0	57.7	EMTO+CPA VASP	[114]
$Ni_{23}Fe_{20}Cr_{17}Co_{20}Mn_{20}$	FCC	0	19.7	EMTO+CPA VASP	[114]
$Ni_{14}Fe_{20}Cr_{26}Co_{20}Mn_{20}$	FCC	0	3.5	EMTO+CPA VASP	[114]
$Ni_{14}Fe_{21.5}Cr_{21.5}Co_{21.5}Mn_{21.5}$	FCC	0	7.7	EMTO+CPA VASP	[114]
CoCrNi	FCC	0	-18, -49, -77	First-principles method +SQS <sup>IV</sup>	[116]
CoCrFeNi	FCC	0	-117, -82, -180	First-principles method +SQS	[116]
CoCrFeNi	HCP	0	-8, 43, 142	First-principles method +SQS	[116]
$Co_{25}Ni_{25}Fe_{25}Al_{7.5}Cu_{17.5}$	FCC	300	25.6 ±4.6	MD <sup>V</sup> simulation	[500]
FeCoNiCrCu	FCC	298	49±37	VASP	[112]
CrCoNi	FCC	293	22 ± 4	TEM <sup>VI</sup>	[110]
CrMnFeCoNi	FCC	77	30± 5	TEM	[111]
FeCrCoNiMn	FCC	298	~21	First-principles calculation	[113]
FeCrCoNiMn	FCC	77	~3.4	First-principles calculation	[113]
NiCoCr	FCC	298	18 ± 4	TEM	[502]
FeCoNiCr	FCC	298	27 ± 4	TEM	[502]
FeCoNiCrMn	FCC	298	26.5 ± 4.5	TEM	[502]
(FeCoNiCr) <sub>94</sub> Mn <sub>6</sub>	FCC	298	28 ± 4	TEM	[502]
(FeCoNiCr) <sub>86</sub> Mn <sub>14</sub>	FCC	298	29 ± 4	TEM	[502]
$Fe_{20}Co_{15}Ni_{25}Cr_{20}Mn_{20}$	FCC	298	38 ± 6	TEM	[502]
FeCoNiCrAl <sub>0.1</sub>	FCC	298	~ 30	TEM	[497]
CoCrNi	FCC	0	-24	Ab initio calculations	[83]
CoCrNi	FCC	0	-43-30	First principles calculation	[120]
CoCrNi	FCC	0	-62	DFT calculations	[503]
CoCrNi	FCC	0	-41	DFT calculations	[501]
CoCrFeNi	FCC	0	31.6 ± 0.9	DFTVII calculations	[504]
CoCrFeNiCu <sub>0.5</sub>	FCC	0	29.0 ± 1.9	DFT calculations	[504]
CoCrFeNiCu	FCC	0	27.5 ± 1.3	DFT calculations	[504]
CoCrFeNiCuAl <sub>0.3</sub>	FCC	0	33.8 ± 2.2	DFT calculations	[504]
CoCrFeNiCuAl <sub>0.5</sub>	FCC	0	32.0 ± 2.1	DFT calculations	[504]
CoCrFeNiCuTi <sub>0.5</sub>	FCC	0	37.4 ± 2.4	DFT calculations	[504]
CoCrFeNiAl <sub>0.25</sub>	FCC	0	38.7 ± 2.6	DFT calculations	[504]
CoCrFeNiAl <sub>0.3</sub>	FCC	0	35.2 ± 2.3	DFT calculations	[504]
CoCrFeNiAl <sub>0.375</sub>	FCC	0	33.7 ± 2.3	DFT calculations	[504]
CoCrFeNiAl <sub>0.3</sub> Ti <sub>0.1</sub>	FCC	0	42.4 ± 3.0	DFT calculations	[504]
$CoCrFeNiAl_{0.3}Mo_{0.1}$	FCC	0	37.2 ± 2.6	DFT calculations	[504]

CoCrFeNiMn	FCC	0	29.7 ± 1.2	DFT calculations	[504]
CoCrFeNiMnCu	FCC	0	27.0 ± 1.2	DFT calculations	[504]
CoCrFeNiPd	FCC	298	66	TEM	[122]
Al <sub>0.15</sub> CoCrFeNi	FCC	853	126.9	First principle calculation	[247]
Al <sub>0.15</sub> CoCrFeNi	FCC	898	132.8	First principle calculation	[247]
Al <sub>0.15</sub> CoCrFeNi	FCC	923	136.0	First principle calculation	[247]
Al <sub>0.15</sub> CoCrFeNi	FCC	948	139.3	First principle calculation	[247]
Al <sub>0.15</sub> CoCrFeNi	FCC	973	142.5	First principle calculation	[247]
Al <sub>0.60</sub> CoCrFeNi	FCC+BCC	853	147.4	First principle calculation	[247]
Al <sub>0.60</sub> CoCrFeNi	FCC+BCC	898	152.9	First principle calculation	[247]
Al <sub>0.60</sub> CoCrFeNi	FCC+BCC	923	155.9	First principle calculation	[247]
Al <sub>0.60</sub> CoCrFeNi	FCC+BCC	948	159.0	First principle calculation	[247]
Al <sub>0.60</sub> CoCrFeNi	FCC+BCC	973	162.0	First principle calculation	[247]
FeCoCrNiMo <sub>0.23</sub>	FCC	298	~19	Neutron diffraction	[505]
$Fe_{40.4}Ni_{11.3}Mn_{34.8}Al_{7.5}Cr_6$	FCC	298	22.2 ± 1.9	TEM	[153]
$(Fe_{40.4}Ni_{11.3}Mn_{34.8}Al_{7.5}Cr_6)_{99.93}C_{0.07}$	FCC	298	20.1 ± 1.0	TEM	[506]
$(Fe_{40.4}Ni_{11.3}Mn_{34.8}Al_{7.5}Cr_6)_{98.9}C_{1.1}$	FCC	298	10.2 ± 0.9	TEM	[506]
T	TT			777	

Notes: <sup>I</sup>: Exact muffin-tin orbital; <sup>II</sup>: Coherent potential approximation; <sup>III</sup>: Vienna ab initio simulation packages; IV: Special quasirandom structure; <sup>V</sup>: molecular dynamics; <sup>VI</sup>: Transmission-electron microscopy; <sup>VII</sup>: Density functional theory.

**Table 3.1** The values of the parameters used in the Taylor dislocation strengthening model for high entropy alloys. Alongside given is the information on the alloy processing condition, phase constitution, and estimated strength increment from the dislocation strengthening  $\Delta \sigma_{\rho i}$ , and associated references.

Alloy	Processing	Phase	<i>G</i> (MPa)	$\alpha_T$	<i>b</i> (nm)	$ ho_{dis} \ ( imes 10^{14}  m^{-2})$	$\Delta\sigma_{ ho i}$ (MPa)	Ref.
(FeCoNiCr) <sub>94</sub> Ti <sub>2</sub> Al <sub>4</sub>	Arc-melted, drop-cast, homogenized, cold-rolled 30%, annealed, aged, and water quenched	fcc matrix+L1₂- Ni₃(Ti, Al) precipitates	78.5	0.2	0.25 5	0	0	[133]
(FeCoNiCr) <sub>94</sub> Ti₂Al₄	Arc-melted, drop-casted, homogenized, cold-rolled 70%, aged, and water quenched	fcc matrix+L1 <sub>2</sub> - Ni <sub>3</sub> (Ti, Al) precipitates	78.5	0.2	0.25 5	5.02	274.5	[133]
Al <sub>10.5</sub> Cr <sub>21.1</sub> Fe <sub>21.1</sub> Co <sub>21.1</sub> Ni <sub>21.1</sub> Mo <sub>2.5</sub> C <sub>2.5</sub>	Melted in a vacuum induction furnace, gas-atomized into powder, cooled down, and powered hot extruded into bars	fcc+B2 and M <sub>23</sub> C <sub>6</sub>	74	0.2	0.26	5.42	276.2	[135]
AlCoCrCuFeNi	Mechanical alloying, followed by consolidation via SPS to produce ultrafine grained samples	fcc+B2	65	1.0	0.23	4.29	949	[125]
Fe <sub>49.5</sub> Mn <sub>30</sub> Co <sub>10</sub> Cr <sub>10</sub> C <sub>0</sub>	Cast, hot-rolled, homogenized, water-quenched, cold-rolled, tempered at 400 °C or annealed at 650 and 750 °C for various time	fcc+hcp	76	0.2	0.25 5	1.0	57	[106]

**Table 3.2** Hall-Petch intercepts and slopes, i.e.,  $\sigma_0$  and k in  $\sigma_y = \sigma_0 + k_S d^{-1/2}$ , of high entropy alloys and their subsets. Alongside given is the information on the alloy processing condition, phase constitution, grain size, testing temperature and associated references.

Alloy	Processing	Phase	<i>d</i> (μm)	<i>Т</i> (К)	$\sigma_0$ (MPa)	$k_S$ (MPa· $\mu$ m $^{0.5}$	Ref.
CoCrFeMnNi	Melted and solidified by magnetic levitation melting, solution-treated, hot-forged, (cold-rolled), annealed	fcc	0.5-89	293	194	490	[507]
CoCrFeMnNi	Arc-melted, drop-cast, solution-treated, cold-rolled, annealed	fcc	4.4-155	77 293 473 673 873 107 3	310 125 83 57 43 69	538 494 425 436 421 127	[47] [47] [47] [47] [47]
CoCrFeMnNi with 1 at.% C	Arc-melted, cast, solution- treated, cold-rolled, annealed	fcc	1.4-69.7	293	288	935	[75]
Al <sub>0.1</sub> CoCrFeNi	Induction-melted, hot isostatic pressing, friction stir processing	fcc	0.95- 1281	293	174	371	[178]
Al <sub>0.3</sub> CoCrFeNi	Arc-melted, drop-cast, cold- rolled, annealed	fcc	5.7-144	293	95	824	[186]
Al <sub>0.3</sub> CoCrFeNi	Prepared by a plasma arc furnace, homogenized, cold-rolled, annealed	fcc	0.8-148	293	144	674	[508]
CoCrNi	Arc-melted, cast, cold-rolled, homogenized, high-pressure torsion, annealed	fcc	0.32-500	293	218	265	[174]
HfNbTaZrTi	Arc-melted, drop-cast, cold- rolled, annealed	bcc	27-206	293	942	270	[451]
HfNbTaZrTi	Arc-melted, drop-cast, cold- rolled, annealed	bcc	38-250	293	919	240	[509]
WNbMoTaV	Ball-milled, spark plasma sintered	bcc	5.3-80	293	1050- 1078	1462-1774	[510]
Al <sub>0.1</sub> CrNbVMo	Ball-milled, spark plasma sintered, annealed	bcc	0.6-2.8	293	1680	811	[45]
(CoCrNi) <sub>94</sub> Al <sub>3</sub> Ti <sub>3</sub>	Arc-melted, drop-cast, homogenized, cold-rolled, annealed, aged	fcc+L1 <sub>2</sub> precipitat es	~67	293	216	568	[87]

Table 3.3 Hall-Petch intercepts and slopes based on the hardness, i.e.,  $H_0$  and  $k_H$  in  $H = H_0 + k_H d^{-1/2}$ , of high entropy alloys and their subsets. Alongside given is the information on the alloy

processing conditions, phase constitution, grain sizes, testing temperatures and associated references.

Alloy	Processing	Phase	<i>d</i> (μm)	T (K)	$H_0$ (Hv)	$k_H$ (Hv $\cdot$ µm $^{0.5}$	Ref.
CoCrFeMnNi	Arc-melted, drop-cast, cold- rolled, annealed	fcc	3.9-26.2	RT	125	69	[177, 180]
CoCrFeMnNi	Arc-melted, cast, homogenized, cold-rolled, annealed	fcc	3.7-210	RT	122	103	[180]
CoCrFePdNi	Arc-melted, cast, homogenized, cold-rolled, annealed	fcc	6.9-293	RT	193	85	[180]
Al <sub>0.3</sub> CoCrFeN i	Arc-melted, drop-cast, cold- rolled, annealed	fcc	5.7-144	RT	111	227	[186]
CoCrFeNi	Arc-melted, cast, homogenized, cold-rolled, annealed	fcc	4.2-154	RT	115	146	[180]
CoCrFeNi	Arc-melted, drop-cast, homogenized, cold-rolled, annealed	fcc	3.5-105	RT	118	166	[53]
CoCrFeNi	Spark plasma sintered	fcc+Cr <sub>7</sub> C <sub>3</sub> +Cr <sub>2</sub> O 3	0.12- 0.26	RT	108	163	[511]
CoFeMnNi	Arc-melted, cast, homogenized, cold-rolled, annealed	fcc	9.8-208	RT	112	104	[180]
NiCoCr	Arc-melted, cast, homogenized, cold-rolled, annealed	fcc	4.0-153	RT	129	249	[180]
NiCoCr	Arc-melted, drop-cast, homogenized, cold-rolled, annealed	fcc	1-73	RT	147	197	[53]
CoMnNi	Arc-melted, cast, homogenized, cold-rolled, annealed	fcc	17.2- 166.4	RT	126	127	[180]
CoFeNi	Arc-melted, drop-cast, homogenized, cold-rolled, annealed	fcc	27.8- 77.7	RT	97	131	[53]
FeNi	Arc-melted, drop-cast, homogenized, cold-rolled, annealed	fcc	34.9- 93.9	RT	105	113	[53]
CoNi	Arc-melted, drop-cast, homogenized, cold-rolled, annealed	fcc	4-75.8	RT	62	167	[53]
Ni	Arc-melted, drop-cast, homogenized, cold-rolled, annealed	fcc	27.6- 142.6	RT	69	34	[53]

**Table 3.4** Theoretically estimated precipitation hardening in high entropy alloys.  $\Delta \sigma_{cs}$ ,  $\Delta \sigma_{ms}$ ,  $\Delta \sigma_{os}$ ,  $\Delta \sigma_{sh}$ ,  $\Delta \sigma_{or}$ , and  $\Delta \sigma_{ppt}$  represent strengthening contributions from the particle-matrix

coherency, modulus mismatch, order strengthening, particle shearing mechanism, Orowan bypass mechanism, and the ultimate precipitation strengthening, respectively.

Alloy	Processing	Precipitates	Size (nm)	$\Delta\sigma_{cs}$ (MPa)	$\Delta\sigma_{ms}$ (MPa)	$\Delta\sigma_{os}$ (MPa)	$\Delta\sigma_{sh}$ (MPa)	$\Delta\sigma_{or}$ (MPa)	$\Delta\sigma_{ppt}$ (MPa)	F
CoNiCr) <sub>94</sub> Ti <sub>2</sub> Al <sub>4</sub>	Arc-melted, drop-cast, homogenized, cold-rolled	L1 <sub>2</sub> -Ni <sub>3</sub> (Ti, Al), morphology I	<40	216.8	29.8	305.6	305.6	n/a		
CONTC1 /94 1 12/A14	30%, annealed at 1273 K for 2 h, aged at 1073 K for 18 h, water quenched	L1₂-Ni₃(Ti, Al), morphology II	>70	346.5	35.6	254.8	382.1	n/a	326.7	[1
CoNiCr) <sub>94</sub> Ti <sub>2</sub> Al <sub>4</sub>	Arc-melted, drop-cast, homogenized, cold-rolled 70%, aged at 923 K for 4 h, water quenched	L1 <sub>2</sub> -Ni <sub>3</sub> (Ti, Al)	20-100	240.0	298	327.7	327.7	n/a	327.7	[1
CaNiCr) Ti Al	And moderal during and	L1 <sub>2</sub> -Ni <sub>3</sub> (Ti, Al)	12	n/a	n/a	n/a	244.3	n/a	244.3	۲,
CoNiCr) <sub>95</sub> Ti <sub>1</sub> Al <sub>4</sub>	Arc-melted, drop-cast,	L2 <sub>1</sub> -(Ni, Co) <sub>2</sub> TiAl	188	n/a	n/a	n/a	n/a	29.9	244.3	Į.
CoNiCr) <sub>91</sub> Ti₃Al <sub>6</sub>	homogenized, cold-rolled 30%, annealed at 1273 K for 2 h, and aged at varying	L1 <sub>2</sub> -Ni <sub>3</sub> (Ti, Al)	12	n/a	n/a	n/a	202.2	n/a	330.7	[1
CONTCT /91 1 13/A16		L2 <sub>1</sub> -(Ni, Co) <sub>2</sub> TiAl	231	n/a	n/a	n/a	n/a	330.7	330.7	Ŀ
CoNiCr) <sub>88</sub> Ti₃Al <sub>9</sub>	temperatures and time	$L1_2$ -Ni <sub>3</sub> (Ti, Al)	11	n/a	n/a	n/a	134.3	n/a	299.6	[1
CONTCT J88 F13 A19	temperatures and time	L2 <sub>1</sub> -(Ni, Co) <sub>2</sub> TiAl	350	n/a	n/a	n/a	n/a	299.6	233.0	Į.
I <sub>0.1</sub> CrNbVMo	Spark plasma sintered	alumina	71	n/a	n/a	n/a	n/a	86	86	[
2Ni <sub>12</sub> Mn <sub>36</sub> Al <sub>8</sub> Ti <sub>2</sub>	Arc-melted, drop-cast, cold- rolled 70%, annealed	(Ni, Al, Ti)-rich B2	223- 553	n/a	n/a	n/a	n/a	28	28	[!
eCoNiCrTi <sub>0.2</sub>	Arc-melted, drop-cast, homogenized, cold-rolled 80%, annealed, water- quenched, aged at 1073 K for 1h	Ni- and Ti-rich lamellar	1-8	n/a	n/a	410	2	0	412	[
. <sub>68</sub> Mn <sub>19.68</sub> Fe <sub>19.68</sub> . <sub>68</sub> Ni <sub>19.68</sub> Nb <sub>0.8</sub> C <sub>0.</sub>	Arc-melted, drop-cast, homogenized, cold-rolled 88%, annealed, water- quenched	NbC and M <sub>23</sub> C <sub>6</sub>	42	n/a	n/a	n/a	n/a	391	391	[9

**Table 3.5** The values of  $f_t$ ,  $k_{tb}$ , and  $\lambda_t$  used in the twin strengthening model  $\Delta\sigma_{tb} = f_t k_{tb} \lambda_t^{-1/2}$  for a number of high entropy alloys. Alongside given is the information on the alloy processing conditions, phase constitution, method to obtain  $k_{tb}$ , estimated strength increase  $\Delta\sigma_{tb}$ , and associated references.

Alloy	Processing	Phase	<i>f</i> <sub>t</sub> (%)	$\lambda_t$ (nm)	$k_{tb}$ (MPa· $\mu$ m $^{0.5}$	Method to obtain $k_{TB}$	$\Delta\sigma_{tb}$ (MPa)	Ref.
AlCoCrCuFeNi	Mechanical alloying, followed by consolidation via SPS to produce ultrafine grained samples	fcc+B2	11	43	270	Approximat e	143	[125]
Co <sub>25</sub> Ni <sub>25</sub> Fe <sub>25</sub> Al <sub>7.5</sub> Cu <sub>17.</sub>	Mechanical alloying followed by consolidation via SPS to produce nanocrystalline samples	fcc	5	61	350	Approximat e	71	[214]
$Fe_{49.5}Mn_{30}Co_{10}Cr_{10}C_0$	Cast, hot-rolled, homogenized, water-quenched, cold-rolled, tempered at 673 K or annealed at 923 and 1023 K for various time	fcc+hc p	n/a	68-126	195	Curve fitting	13- 468	[106]

**Table 4.1** Key deformation parameters, including the stress exponent (n), activation energy (Q), activation volume (V), strain rate sensitivity (m), and the inferred deformation mechanisms of high-entropy alloys.

position	Grain size	Structure	Testing	T(K)	$V^*(b^3)$	Q (KJ/mol)	n/m	Deformation Mechanism
FeMnNi	46 μm	FCC	Spherical nanoindentati on	298	4.6	-	2.91	Dislocation mediated
FeMnNi	49 nm	FCC	Spherical nanoindentati on	298	0.8	-	1.03	GB Diffusion
FeMnNi	33 nm	FCC	Spherical nanoindentati on	298	0.8	-	1.30	GB Diffusion
FeMnNi	10 nm	FCC	Tensile test	773–1073	-	113	m=0.31	Superplasticity
FeMnNi	1.4 μm	FCC	Strain rate jump	1023	-	-	$m \sim 0.59$ at $10^{-4}$ s <sup>-1</sup> – $m \sim 0.25$ at $10^{-2}$ s <sup>-1</sup>	Superplasticity
CrCuFeNi	2.1μm	L12+B2+ BCC	Tensile test	1073– 1273	-	273–394	1.8-2.7	Superplasticity
iCr)94Ti2Al4	15.7 μm	FCC	Strain rate jump	1023- 1173	_	> 600(1023- 1023 K )/ 350-450 (1148-1173 K)	6–9/4.5	Precipitation strengthening/ Dislocation climb
NiCrMn	12 μm	FCC	Strain rate jump	1023– 1123	67.6– 123.6/ 38.3–68.5	280(low strain rate regime )/ 330(high strain rate regime)	<=3/5	Dislocation glide/ Dislocation climb
FeMnNi	25 μm	FCC	Tensile creep	773–873	-	268(low– stress region )/380(high– stress region)	5-6/ 8.9-14	Dislocation climb/ dynamic recrystallization, precipitation and dislocation climb
FeMnNi	21.7 μm	FCC	Tensile creep	808–923	-	305–320(< 40 MPa)/235– 250(> 40 MPa)	~3/~6	Dislocation glide/ Dislocation climb

MPa)

CoCrFeNi	-	FCC	Stress relaxation	853–973	3.15–5.22	385	5.56	Cross-slip deformation mechanism
loCrFeNi	-	FCC+BCC	Stress relaxation	853–973	4.3–6.74	334	8.82	Cross-slip deformation mechanism
FeMnNi	800 nm	FCC	Compressive creep	973–1073	300 – 800	246(973– 1023 K)/ 704(1023– 1073 K)	6.3	Dislocation motion
MnNi–ODS	400 nm	FCC	Compressive creep	973–1073	-	210 (low stress region)/ 580(high stress region)	1.8/13.2	lattice diffusion/ Precipitation strengthening
$Co_{16.9}Cr_{7.4}Fe_8$ $_{9}Nb_{1.2}W_{0.4}C_{0.}$	-	FCC+L1 <sub>2</sub>	Tensile creep	1023– 1255	-	290	-	Precipitation strengthening
HfNbTa	80 μm	ВСС	Stress relaxation	298	30–50	-	-	Peierls mechanism
FeMnNi	100 –110 μm	FCC	Strain-rate jump	77–293	18–82	-	-	Labusch-type solution strengthening
CrFeNi	100 –110 μm	FCC	Strain–rate jump	77–293	19–77	-	-	Labusch-type solution strengthening
oCrNi	100 –110 μm	FCC	Strain-rate jump	77–293	15–50	-	-	Labusch–type solution strengthening
oCrNi	149 μm	FCC	Tensile creep	973–1023	100-200	370	5.3	Dislocation climb
าFeCoNi	17 μm	FCC	Repeated stress relaxation	77–423	60–500 (at yield stress)	-	-	Hall-Petch strengthening, solid solution strengthening, and forest hardening
loCrFeNi	millimeter	FCC	Repeated stress relaxation	298	263–284	-	-	Superplasticity
nFeCoNi	~10 nm	FCC	Tensile test	873-1073	-	~113	<i>m</i> =0.31	Superplasticity
CrCuFeNi	-	FCC+BCC	Berkevich nanoindentati	298	-	-	121–129	Dislocation glide-climb

CrCuFeNi	-	FCC+BCC	Berkevich nanoindentati on	473	-	-	84–97	dislocation glide-climb
FeNiAl <sub>0.3</sub>	15 – 20 μm	FCC	Berkevich nanoindentati on	298	-	-	<i>m</i> = 0.0048.	_
'FeNiCu	40 – 80 nm	FCC	Berkevich nanoindentati on	298	0.08 nm <sup>3</sup>	-	<i>m</i> = 0.035	-
eNiCuAl <sub>2.5</sub>	50 – 90 nm	ВСС	Berkevich nanoindentati on	298	0.51 nm <sup>3</sup>	-	<i>m</i> = 0.0048	_
°FeCuNi	40–80 nm	FCC	Spherical nanoindentati on	298	-	-	<i>m</i> = 0.41– 0.14	dislocation dominated
FeCuNi	60– 100 nm	FCC+BCC	Spherical nanoindentati on	298	-	-	<i>m</i> = 0.25– 0.27	dislocation dominated
Ni <sub>20</sub> Cr <sub>20</sub> Mn <sub>20</sub> 111)	50 μm	FCC	Berkevich nanoindentati on	873	7	>259	3.8	Dislocation climb
Ni <sub>20</sub> Cr <sub>20</sub> Mn <sub>20</sub> 111)	50 μm	FCC	Berkevich nanoindentati on	873	9	>239	5	Dislocation climb
i <sub>20</sub> Cr <sub>18</sub> Mn <sub>18</sub> Al 111)	10 μm	FCC+BCC	Berkevich nanoindentati on	873	8	>260	4.3	Dislocation climb
FeMnNi	1–2 μm	FCC	Berkevich nanoindentati on	298	-	-	14.34 – 18.34	Dislocation motion
FeMnNi	38 nm	FCC	Berkevich nanoindentati on	298–573	15–24	48–147	36–66	Grain boundary diffusion

**Table 5.1** Impact toughness and associated information (phase constitution, processing, temperature T, yield strength  $\sigma_y$ , fracture elongation  $\varepsilon_f$ , and test method) for a variety of high entropy alloys.

Composition	Phase	Processing	<i>T</i> (K)	$\sigma_{\!\scriptscriptstyle y}$ (MPa)	$arepsilon_f$	Impact energy (J)	Tes
			124	610	0.42	177	
			175	541	0.35	194	_
CoCrFeMnNi	fcc	Vacuum-induction	213	494	0.39	208	Charpy-im
		melted, cast	300	429	0.40	213	notched spec
			373	n/a	n/a	206	
			423	n/a	n/a	196	
$AI_{13}Cr_{23.5}Fe_{20}Co_{20}Ni_{23.5}$	fcc	Arc-melted, cast	RT	760 <sup>™</sup>	0.06 <sup>T</sup>	2.54	Impact tes
		Vacuum levitation	77	412 <sup>T</sup>	~ 0.9 <sup>T</sup>	289	Charman in
Al <sub>0.1</sub> CoCrFeNi <sup>(I)</sup>	fcc	melted, cast, hot forged	200	295 <sup>™</sup>	~ 0.65 <sup>T</sup>	318	Charpy-im
		at 1323 K	298	250 <sup>™</sup>	~ 0.54 <sup>T</sup>	420	notched spec
		Vacuum levitation	77	515 <sup>™</sup>	~ 0.74 <sup>T</sup>	328	
Al <sub>0.3</sub> CoCrFeNi	fcc	melted, cast, hot forged	200	310 <sup>T</sup>	~ 0.66 <sup>T</sup>	409	Charpy-im
		at 1323 K	298	220 <sup>T</sup>	~ 0.65 <sup>T</sup>	413	notched spec
		Maria de la Partira	77	n/a	n/a	398	Character to
CoCrFeNi	fcc	Vacuum levitation	200	n/a	n/a	322	Charpy-im
		melted, cast	298	155 <sup>™</sup>	0.6 <sup>T</sup>	287	notched spec
		Manusa Inditation	77	n/a	n/a	371	Charman in
Al <sub>0.1</sub> CoCrFeNi <sup>(II)</sup>	fcc	Vacuum levitation	200	n/a	n/a	327	Charpy-im
		melted, cast	298	n/a	n/a	294	notched spec
$Al_{18}Cr_{21}Fe_{20}Co_{20}Ni_{21}$	bcc	Arc-melted, cast	RT	~ 370 <sup>T</sup>	<b>0</b> <sup>T</sup>	0.29	Impact tes
$AI_{15.5}Cr_{22.25}Fe_{20}Co_{20}Ni_{22.2}$	fcc+bcc	Arc-melted, cast	RT	~ 590 <sup>T</sup>	<b>0</b> <sup>T</sup>	0.36	Impact tes
Al <sub>10.5</sub> Cr <sub>24.75</sub> Fe <sub>20</sub> Co <sub>20</sub> Ni <sub>24.7</sub>	fcc+bcc	Arc-melted, cast	RT	370 <sup>T</sup>	0.25 <sup>T</sup>	11.45	Impact tes
,			77	n/a	n/a	1.82	
AL 0.05 AL	(	Vacuum levitation	200	n/a	n/a	3.02	Charpy-im
Al <sub>0.75</sub> CoCrFeNi	fcc+B2	melted, cast	298	800-1400 <sup>c</sup>	0.35- 0.55 <sup>c</sup>	3.58	notched spec
			77	n/a	n/a	0.64	
AL C. C. T. A.	h	Vacuum levitation	200	n/a	n/a	0.64	Charpy-im
Al <sub>1.5</sub> CoCrFeNi	bcc+B2	melted, cast	298	1453- 1867 <sup>H</sup>	n/a	1.28	notched spec

Notes: RT indicates room temperature; the superscript <sup>T</sup>, <sup>C</sup>, and <sup>H</sup> represent that the data are sourced from tensile tests, compressive tests, and hardness (the yield strength is estimated from  $\sigma_y = \frac{H}{3}$ ); the superscript <sup>(I)</sup> and <sup>(II)</sup> denote the same alloy from different works.

**Table 5.2** Fracture toughness  $K_{IC}$ , conditional fracture toughness  $K_Q$ , and associated information (phase constitution, processing, temperature T, yield strength  $\sigma_y$ , fracture elongation  $\varepsilon_f$ , and test method) for a variety of high entropy alloys.

Composition	Phase	Processing	<i>T</i> (K)	$\sigma_y$ (MPa)	$oldsymbol{arepsilon}_f$	<i>K<sub>IC</sub></i> or <i>K<sub>Q</sub></i> (MPa m <sup>0.5</sup> )	Tes
CrMnFeCoNi	fcc	Arc-melted, cast, cold forged and rolled, recrystallized	77 200 298	759 <sup>T</sup> 518 <sup>T</sup> 410 <sup>T</sup>	0.71 <sup>T</sup> 0.6 <sup>T</sup> 0.57 <sup>T</sup>	219 221 217	J-R curve test (AS
		Vacuum induction melted, cast,	77	470 <sup>T</sup>	0.62 <sup>T</sup>	232	
$Fe_{45}Co_{20}Cr_{10}Ni_{15}V_{10}$	fcc	homogenized, cold- rolled, annealed, and water- quenched	298	294 <sup>⊤</sup>	0.36 <sup>T</sup>	219	J-R curve test (AS
$AI_{13}Cr_{23.5}Fe_{20}Co_{20}Ni_{23.5}$	fcc	Arc-melted, cast	298	760 <sup>™</sup>	0.06 <sup>T</sup>	53	K testing or (AS
FeCoNiCrAl <sub>3</sub>	bcc	Laser-solidified coating (1.5 mm thick)	298	2500 <sup>H</sup>	n/a	7.6	Nanc
$AI_{23}Co_{15}Cr_{23}Cu_8Fe_{15}Ni_{15}$	bcc	Vacuum induction melted, cast	298	1260 <sup>c</sup>	0.21 <sup>c</sup>	5.4-5.8	K testing on and CVNRB
Single-crystal NbMoTaW	bcc	Arc-melted, cast, homogenized	298	2640 <sup>H, MC</sup>	0.026 <sup>c</sup>	1.6	Bending o cantilever spe a
Bi-crystal NbMoTaW	bcc	Arc-melted, cast, homogenized	298	1058 <sup>H, MC</sup>	0.026 <sup>c</sup>	0.2	Bending o cantilever spe a
Nanocrystalline NbMoTaW	bcc	2-3 μm thick film deposited	298	~5700 <sup>MC</sup>	n/a	2.9-3.3	Bending o cantilever spe
TiZrNbTa	bcc	Arc-melted, cast	298	1020 <sup>c</sup>	> 0.5 <sup>c</sup>	28.5	K testing or (AS
(TiZrNbTa) <sub>95</sub> Mo <sub>5</sub>	bcc	Arc-melted, cast	298	1180 <sup>c</sup>	~ 0.51 <sup>c</sup>	22.5	K testing or (AS
(TiZrNbTa) <sub>90</sub> Mo <sub>10</sub>	bcc	Arc-melted, cast	298	1300 <sup>c</sup>	~ 0.26 <sup>c</sup>	20	K testing or (AS
(TiZrNbTa) <sub>80</sub> Mo <sub>20</sub>	bcc	Arc-melted, cast	298	1460 <sup>c</sup>	~ 0.07 <sup>c</sup>	18.7	K testing or (AS
$AI_{18}Cr_{21}Fe_{20}Co_{20}Ni_{21}$	two bcc	Arc-melted, cast	298	~ 370 <sup>T</sup>	<b>0</b> <sup>T</sup>	9	K testing or (AS
Al <sub>0.2</sub> CrFeNiTi <sub>0.2</sub>	fcc + bcc	Vacuum levitation melted, cast	298	1666 <sup>H</sup>	n/a	32 - 35	K testing or (AS
$AI_{15.5}Cr_{22.25}Fe_{20}Co_{20}Ni_{22.25}$	fcc + bcc	Arc-melted, cast	298	~ 590 <sup>T</sup>	<b>0</b> <sup>T</sup>	11	K testing or

							(AS
AlCrFeNi₂Cu	fcc + bcc	Vacuum levitation	298	1049 <sup>H</sup>	n/a	40-45	K testing o
- / tierr ervizeu	icc i bec	melted, cast	473	n/a	n/a	46-47	(AS
CoCrFeNiNb <sub>0.5</sub>	eutectic, fcc + Laves	Arc-melted, cast	298	1700 <sup>c</sup>	~ 0.7 <sup>c</sup>	11.4-14.8	J-R curve specimer
FeCoNiCrCuTiMoAlSiBe <sub>0.5</sub>	bcc + martensite	Laser-solidified coating (1.5 mm thick)	298	3770 <sup>H</sup>	n/a	50.9	Nanc
AlCoCrFeNi <sup>(I)</sup>	fcc + duplex bcc	SPS at 1473 K	298	1262 <sup>T</sup>	~ 0.29 <sup>T</sup>	25.2	K testing or (As
AlCoCrFeNi <sup>(II)</sup>	fcc + L1 <sub>2</sub> + tetragonal σ	SPS at 973-1273 K	298	333- 2667 <sup>H</sup>	n/a	1-3.9	K testing on (E
FoCrNi)/	foota	Vacuum induction melted, cast,	77	571-819 <sup>T</sup>	0.43- 0.73 <sup>T</sup>	244-278	J-R curve test
FeCrNiV	fcc + σ	homogenized, cold- rolled, and annealed	298	352-587 <sup>T</sup>	0.39- 0.64 <sup>T</sup>	160-189	(AS

Notes: The superscript <sup>T</sup>, <sup>C</sup>, <sup>H</sup>, and <sup>MC</sup> indicate that the data are sourced from tensile tests, compressive tests, hardness (the yield strength is estimated from  $\sigma_y = \frac{H}{3}$ ), and micro-compression tests, respectively; the superscript <sup>(I)</sup> and <sup>(II)</sup> indicate the same alloy from different works;  $K_Q$  is used for the shaded numbers in the fracture-toughness column;  $\varepsilon_f = 0.026$  for the Nb<sub>25</sub>Mo<sub>25</sub>Ta<sub>25</sub>W<sub>25</sub>HEAs are from their polycrystalline counterparts [16];

**Table 6.1** High-cycle fatigue properties (fatigue strength  $\sigma_{af}$ , fatigue ratio  $\frac{\sigma_{af}}{\sigma_{UTS}}$ , and coefficients of the Basquin equation) of HEAs in air and at room temperature. Alongside shown is the information on the thermomechanical processing, phase constitution, average grain size d, uniaxial yield strength  $\sigma_y$ , ultimate tensile strength  $\sigma_{UTS}$ , and fatigue testing parameters such as the stress ratio R and loading frequency f.

Composition	Processing	Phase	d (μm)	$\sigma_{\scriptscriptstyle{y}}$ (MPa)	$\sigma_{UTS}$ (MPa)	$\sigma_{af}$ (MPa)	$\frac{\sigma_{af}}{\sigma_{UTS}}$	Basqu fit
CoCrFeMnNi	Alloy powder ball-milled, compacted by SPS	fcc	0.6	n/a	n/a	450	n/a	A=10 b=- 0.04
CoCrFeMnNi	Magnetic levitation melted, cast, solution- treated, hot-forged, cold- rolled, annealed	fcc	30	300	676	190	0.28	A=54 b=- 0.05
CoCrFeMnNi	Vacuum induction melted, cast, hot-rolled, solution-treated, water quenched	fcc	41/77*	254	585	250	0.43	A=11 b=- 0.10
CoCrFeMnNi	Synthesized by SHS	fcc	250- 500	159	362	83	0.23	A=41 b=- 0.09
CoCrFeMnNi	Magnetic levitation melted, cast, solution- treated, hot-forged, cold- rolled, annealed	fcc+Cr-rich precipitates	0.65	800	888	280	0.32	A=43 b=- 0.18
CoCrFeMnNi	Vacuum induction melted, cast, hot-rolled, homogenized	fcc+CrMn <sub>2</sub> O <sub>4</sub> particles	245.5	293	626	126	0.2	A=17- b=- 0.17
CoCrFeMnNi (welded)	Synthesized by SHS	fcc+M <sub>7</sub> C <sub>3</sub> particles	100- 300	164	349	89	0.26	A=38 b=- 0.09
$Fe_{42}Mn_{28}Cr_{15}Co_{10}Si_5$	Cast, multi-pass FSP	metstable fcc⊡hcp	1.97	957	1158	535	0.46	A=14 b=- 0.05
Fe <sub>38.5</sub> Mn <sub>20</sub> Co <sub>20</sub> Cr <sub>15</sub> Si <sub>5</sub> Cu <sub>1.</sub>	Cast, multi-pass FSP	metstable fcc⊡hcp	0.77	850	1126	700	0.62	A=12 b=- 0.03
As-cast AlCoCrFeNi <sub>2.1</sub> (EHEA <sub>c</sub> )	Cast	eutectic, hierarchical fcc (L1 <sub>2</sub> )+bcc (B2)	n/a	746	1057	383	0.36	A=47 b=-0.
Wrought AlCoCrFeNi <sub>2.1</sub> (EHEA <sub>w</sub> )	Cast, cold-rolled, annealed	eutectic, hierarchical fcc (L1 <sub>2</sub> )+bcc (B2)	n/a	1110	1340	469	0.35	A=75. b=- 0.19

Al <sub>0.5</sub> CoCrCuFeNi	Arc-melted, cast annealed, quenched, cold-rolled	dendritic fcc + interdendritic fcc	n/a	1284	1344	361	0.27	A=34 b=- 0.16
Al <sub>0.3</sub> CoCrFeNi	Arc-melted, cast, solutionized, cold-rolled, annealed	fcc+B2 and $\sigma$ precipitates	0.71	900	1074	450	0.42	A=13. b=- 0.06
Al <sub>0.7</sub> CoCrFeNi	Arc-melted, cast, hot- rolled, cold-rolled, homogenized, water- quenched	fcc+B2	n/a	780	1040	410	0.36	A=34 b=- 0.12
Al <sub>0.7</sub> CoCrFeNi	Arc-melted, cast, hot- rolled, cold-rolled, homogenized, water- quenched, annealed	fcc+B2 and $L1_2$ precipitates	n/a	1050	1400	460	0.33	A=14 b=- 0.07

Note: FSP-friction stir processing; SPS-spark plasma sintering; SHS-self-propagating high-temperature synthesis; \*Two different mean grain sizes, 41 and 77  $\mu$ m were reported for the same set of fatigue data in two separate works.

**Table 6.2** Fatigue crack growth properties (threshold stress intensity range  $\Delta K_{th}$  and Paris slope m) of HEAs. Alongside shown is the information on thermomechanical processing, phase constitution, grain size d, testing temperature T, stress ratio R, testing frequency f, and testing method.

Processing	Phase	<i>d</i> (μm)	<i>T</i> (K)	R	f (Hz)	m	$\Delta K_{th} \ (MPa \cdot m^{0.5})$
Vacuum induction melted, cast, homogenized, swaged, annealed	fcc	7	198	0.1	25	4.5	6.3
Vacuum induction melted, cast, homogenized, swaged, annealed	fcc	7	293	0.1	25	3.5	4.8
Powder metallurgy	fcc	15	293	0.1	6	7.4	n/a
Powder metallurgy	fcc	12	293	0.1	6	6.0	n/a
Arc-melted, cast, cold-rolled, annealed	bcc	~60	293	0.1	10	2.2	2.5
Vacuum induction melted, cast, hot- rolled, homogenized, hot-rolled, solutionized, quenched	metastab le fcc @hcp	n/a	293	0.1	1	3.5	n/a
		,		0.1		4.9	16
Vacuum levitation melted, cast	tcc+bcc	n/a	293		20		7 5
				0.7		3.4	17
Vacuum levitation melted, cast	fcc+bcc	n/a	293	0.3	20	6.5	5
				0.7		14.5	7
	Vacuum induction melted, cast, homogenized, swaged, annealed Vacuum induction melted, cast, homogenized, swaged, annealed  Powder metallurgy  Powder metallurgy  Arc-melted, cast, cold-rolled, annealed  Vacuum induction melted, cast, hot-rolled, homogenized, hot-rolled, solutionized, quenched  Vacuum levitation melted, cast	Vacuum induction melted, cast, homogenized, swaged, annealed Vacuum induction melted, cast, homogenized, swaged, annealed  Powder metallurgy  fcc  Powder metallurgy  fcc  Arc-melted, cast, cold-rolled, annealed  Vacuum induction melted, cast, hot-rolled, homogenized, hot-rolled, solutionized, quenched  Vacuum levitation melted, cast  fcc  fcc  fcc  fcc  fcc  fcc  fcc  f	Processing Phase (μm)  Vacuum induction melted, cast, homogenized, swaged, annealed Vacuum induction melted, cast, homogenized, swaged, annealed  Powder metallurgy fcc 15  Powder metallurgy fcc 12  Arc-melted, cast, cold-rolled, annealed  Vacuum induction melted, cast, hotrolled, homogenized, hot-rolled, solutionized, quenched  Vacuum levitation melted, cast fcc+bcc n/a	Processing       Phase (μm)       T (K)         Vacuum induction melted, cast, homogenized, swaged, annealed       fcc       7       198         Vacuum induction melted, cast, homogenized, swaged, annealed       fcc       7       293         Powder metallurgy       fcc       15       293         Arc-melted, cast, cold-rolled, annealed       bcc       ~60       293         Vacuum induction melted, cast, hot-rolled, homogenized, hot-rolled, solutionized, quenched       le fcc       n/a       293         Vacuum levitation melted, cast       fcc+bcc       n/a       293	ProcessingPhase (μm)T (K) T (K)RVacuum induction melted, cast, homogenized, swaged, annealedfcc71980.1Vacuum induction melted, cast, homogenized, swaged, annealedfcc72930.1Powder metallurgyfcc152930.1Powder metallurgyfcc122930.1Arc-melted, cast, cold-rolled, annealedbcc~602930.1Vacuum induction melted, cast, hot- rolled, homogenized, hot-rolled, solutionized, quenchedmetastab le fccn/a2930.1Vacuum levitation melted, castfcc+bccn/a2930.3O.7 Vacuum levitation melted, castfcc+bccn/a2930.3	ProcessingPhase (μm)(μm)T (k)Rf (Hz)Vacuum induction melted, cast, homogenized, swaged, annealedfcc71980.125Vacuum induction melted, cast, homogenized, swaged, annealedfcc72930.125Powder metallurgyfcc152930.16Powder metallurgyfcc122930.16Arc-melted, cast, cold-rolled, annealedbcc~602930.110Vacuum induction melted, cast, hot- rolled, homogenized, hot-rolled, solutionized, quenchedmetastab le fccn/a2930.11Vacuum levitation melted, castfcc+bccn/a2930.320Vacuum levitation melted, castfcc+bccn/a2930.320	Processing         Phase (μm)         T (K)         R         f (Hz)         m           Vacuum induction melted, cast, homogenized, swaged, annealed         fcc         7         198         0.1         25         4.5           Vacuum induction melted, cast, homogenized, swaged, annealed         fcc         7         293         0.1         25         3.5           Powder metallurgy         fcc         15         293         0.1         6         7.4           Powder metallurgy         fcc         12         293         0.1         6         6.0           Arc-melted, cast, cold-rolled, annealed         bcc         ~60         293         0.1         10         2.2           Vacuum induction melted, cast, hot-rolled, solutionized, quenched         le fcc         n/a         293         0.1         1         3.5           Vacuum levitation melted, cast         fcc+bcc         n/a         293         0.1         4.9           Vacuum levitation melted, cast         fcc+bcc         n/a         293         0.3         20         5.3           0.7         25.8         0.1         3.4           Vacuum levitation melted, cast         fcc+bcc         n/a         293         0.3         20         6.5

Note: SENT-single-edge notched tension; DC(T)-disc-shaped compact-tension; SENB-single-edge notched bending; CT-compact tension;

**Table 7.1** The estimated size-effect exponent m, along with alloy information, testing condition, slip system, pillar size D (diameter and edge length, respectively, for circular and square pillars), lattice constant a, the magnitude of Burger's vector b, shear modulus G, and Schmid factor S. m for single crystalline (sc) HEAs was obtained by fitting Equation (7.2) to the  $\frac{\tau}{G} \sim \frac{D}{b}$  data, but for nanocrystalline (nc) HEAs it was from the  $\frac{\tau}{G} \sim D$  fitting.

Alloy	Phase	Structure	Pillar	Loading direction	Slip system	D (μm)	a (Å)	<i>b</i> (nm)	<i>G</i> (GPa)	S	m	R€
eNiCrCoMn	fcc	SC	cylinder	[11 3 5]	(1 <u>1</u> 1)[110]	1-10	3.59	0.2539	80	0.48	0.30	[5 35
eNiCrCoMn	fcc	SC	square	[ <u>1</u> 26]	(111)[ <u>1</u> 01]	1-8.3	3.59	0.2539	80	0.488	- 0.62	[11
eNiCrCoMn	fcc	SC	square	[ <u>1</u> 23]	(111)[ <u>1</u> 01]	1-8.3	3.59	0.2539	80	0.467	- 0.57	[11
oCrCuFeNi	fcc	SC	cylinder	[100]	{111}⟨110⟩	0.5-2	3.54	0.2503	70	0.408	- 0.55	[35
IbMoTaW	bcc	SC	cylinder	[316]	( <u>11</u> 2)[111]	0.25-2	3.222	0.2789	114	0.41	- 0.30	[5
IbMoTaW	bcc	SC	cylinder	[001]	( <u>11</u> 2)[111]	0.25-2	3.222	0.2789	114	0.47	- 0.33	[5
IbMoTaW (IBAD)	bcc	nc	cylinder	n/a	n/a	0.07- 0.75	3.222	n/a	212	n/a	- 0.20	[35
lbMoTaW (Normal)	bcc	nc	cylinder	n/a	n/a	0.07- 1.16	3.222	n/a	212	n/a	- 0.20	[35
<sub>0.7</sub> CoCrFeNi	fcc	SC	cylinder	[324]	(1 <u>1</u> 1)[011]	0.4-2	3.572	0.2526	75	0.422 a	- 0.71	[36
0./COCI FEINI	bcc	SC	cylinder	[001]	( <u>1</u> 01)[111]	0.4-2	2.868	0.2484	70	0.408	- 0.27	[36

Notes: sc and nc denote single crystalline and nanocrystalline, respectively; IBAD denotes the ion beam-assisted film deposition; Normal denotes the normal direct current magnetron co-sputtering technique; <sup>a</sup>: the value of 0.634 in Ref. [362] seems to be incorrectly calculated as the Schmid factor cannot exceed 0.5 in general; It is, therefore, recalculated here.

**Table 8.1** Potential applications and associated properties of high entropy alloys, grouped by the application field and alloy form. For each category of applications, one typical example alloy is suggested.

Field	Alloy form	Key properties	Potential applications	Example a
	•	High hardness	Cutting tools, brazing, and soldering materials	NiCuCoFe <sub>0.2</sub>
		Retained high hot hardness	Hot-working molds and dies	AlCoCrFeN
		Wear resistance	Hardfacing materials	Co <sub>1.5</sub> CrFeN
		High strength and low density	Weight-critical applications, such as in the transportation sector	$Al_{20}Li_{20}Mg_{10}$
		Strength-ductility balance	Automotive and aerospace sectors	Fe <sub>80x</sub> Mn <sub>x</sub> Co
	Bulk	High impact toughness	Crash and impact energy absorption	Al <sub>0.1</sub> CoCrI
Structural	Baik	High fracture toughness at cryogenic temperatures	Storage tanks for liquefied gases	CrMnFeC
		Retained high strength at elevated temperatures and creep resistance	Turbine blades and hypersonic vehicles	Refractory Tal and HE supe AlMo <sub>0.5</sub> NbT
		Radiation-damage resistance	Nuclear reactors	FeNiMn
		Corrosion resistance	Boilers, heat exchangers, and ship propellers	Al <sub>0.1</sub> CrCol
		Corrosion resistance and biocompatibility	Biomedical applications, such as orthopedic or dental implants	TiZrNbTa
	Thin film	High hardness and wear	Wear-resistant coatings, such as	AlCoCrFe
		resistance	cutting tool coatings	Alcocite
		High saturation magnetization and low resistivity	Magnetic applications	FeCoNiMn <sub>0</sub> .
	Bulk	High electrocatalytic activity and corrosion resistance	Energy conversion applications	Ni <sub>20</sub> Fe <sub>20</sub> Mo <sub>10</sub>
		High hydrogen storage capacity	Hydrogen storage	TiVZrNb
		Shape memory effect at large temperature ranges	Ultra-high temperature shape memory alloys	(Ni,Pd) <sub>50</sub> (Ti,I
F ations		Magnetocaloric effect	Magnetic refrigeration	GdDyErH
Functiona		Superconductivity	Superconductors	Ta <sub>34</sub> Nb <sub>33</sub> Hf <sub>8</sub>
l		Heat and oxidation resistance, and thermal expansion	Thermal barrier coatings in high- temperature applications	NiCo <sub>0.6</sub> Fe <sub>0.2</sub> Cr <sub>1</sub>
	Film	Thermal stability and sluggish diffusion	Diffusion barriers	AlMoNbSiT
		Good electrical properties	Thin-film resistors	Ni-Cr-Si-A
	Powder	Excellent electromagnetic properties	Electromagnetic wave absorption and interference shielding	FeCoNiC
		Catalytic reactivity and stability	Catalysts	CoMoFeN

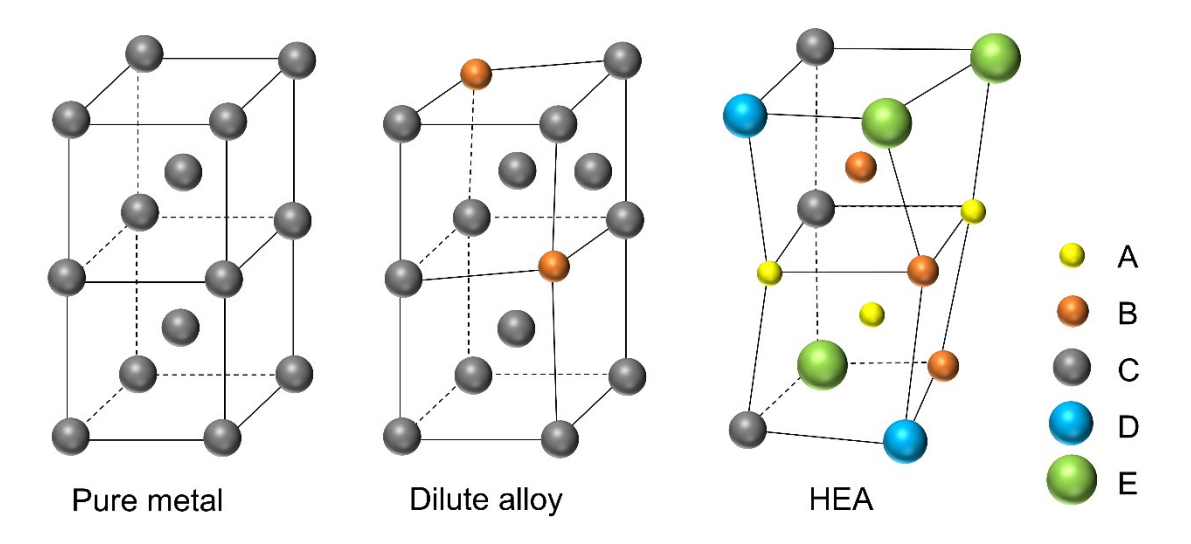


Figure 1.1 Schematics of lattice distortion in body-centered cubic pure metals, conventional dilute alloys, and high-entropy alloys. A-D represent different element species in general.

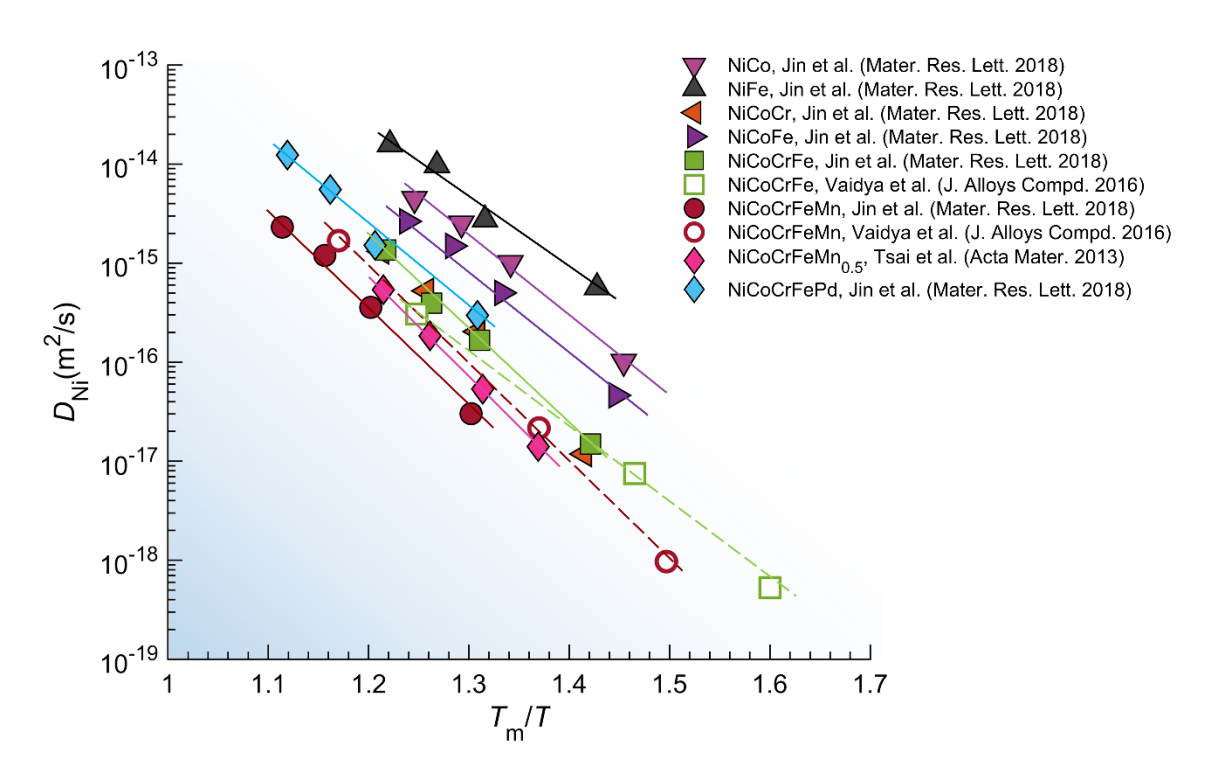


Figure 1.2 Diffusion coefficients of Ni,  $D_{Ni}$ , in a series of fcc alloys including high-entropy alloys against the inverse homologous temperature,  $T_m/T$ , including NiCo [29], NiFe [29], NiCoFe [29], NiCoFe [29], NiCoFeCr [29], NiCoFeCrMn [29], and NiCoFeCrPd [175], CoCrFeMnNi [271], CoCrFeNi [271], and FeCoCrNiMn<sub>0.5</sub> [27, 30].  $T_m$  denotes melting temperature.

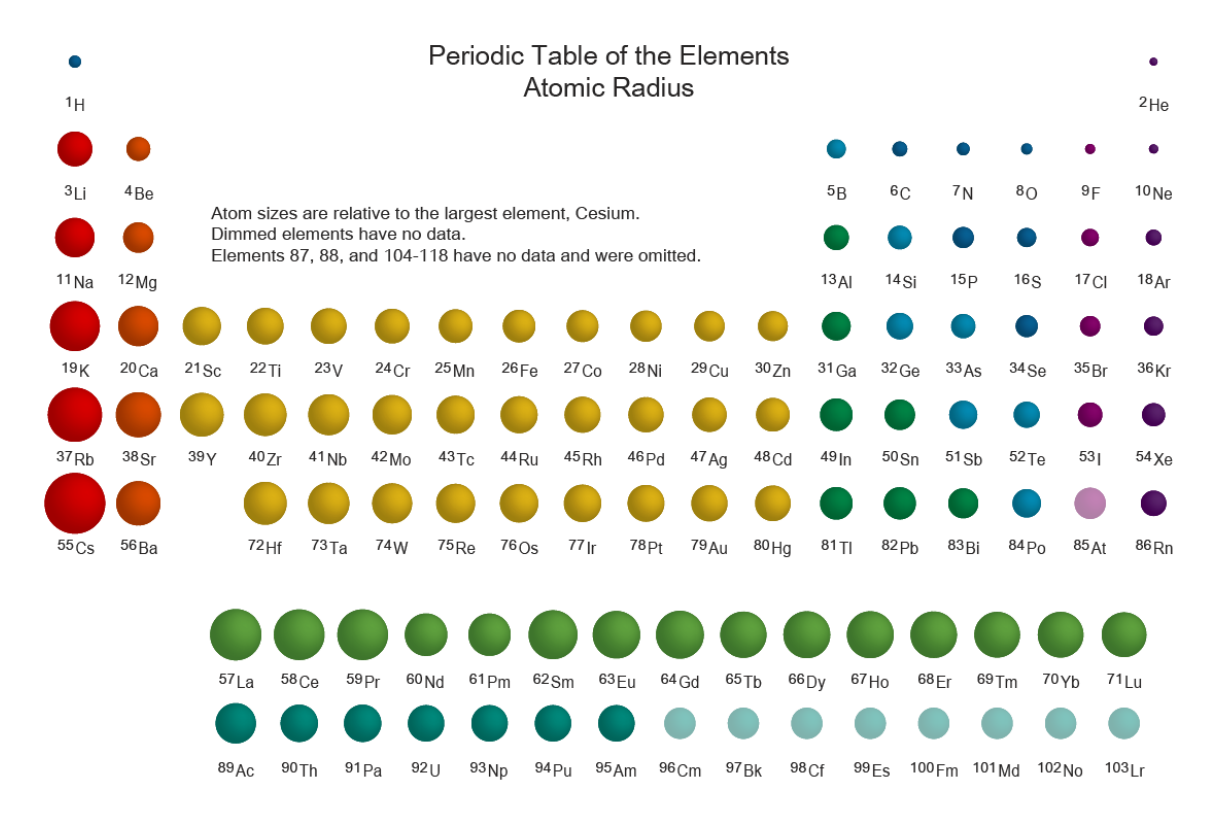


Figure 1.3 Periodic table of elements by atomic size. Courtesy of Sciencenotes.org at http://sciencenotes.org/printable-periodic-table/.

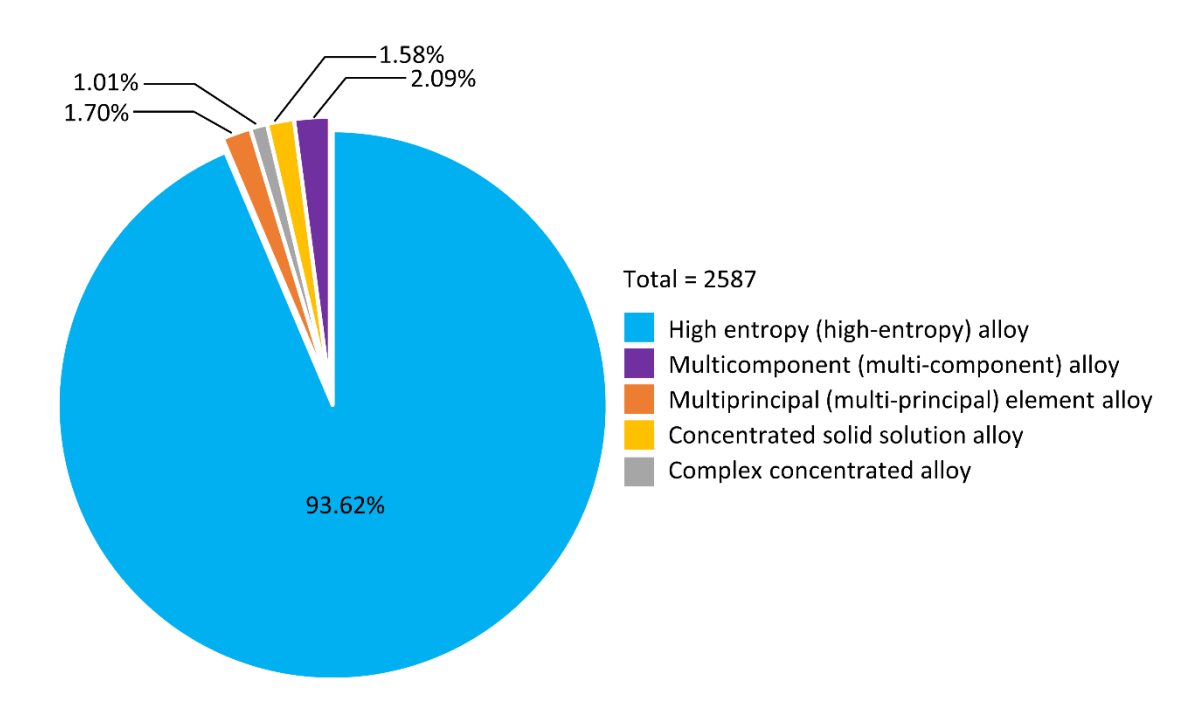


Figure 1.4 Percentages of different naming conventions for "high entropy alloys". The statistics is based on merely considering the usages of these terms in the titles of 2587 papers from 2004 to the end of 2019.

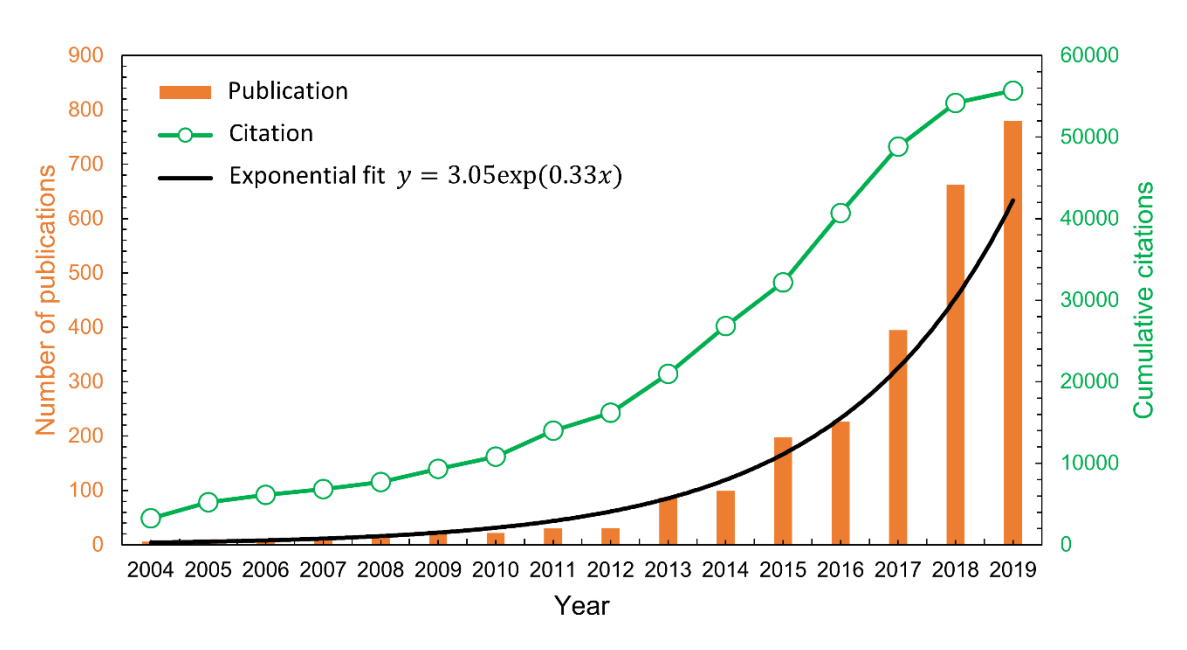


Figure 1.5 Number of HEA publications by year, along with cumulative citations over years from 2004 to the end of 2019. The growth of HEA articles can be described by an exponential rise of y = 3.05exp(0.33x).

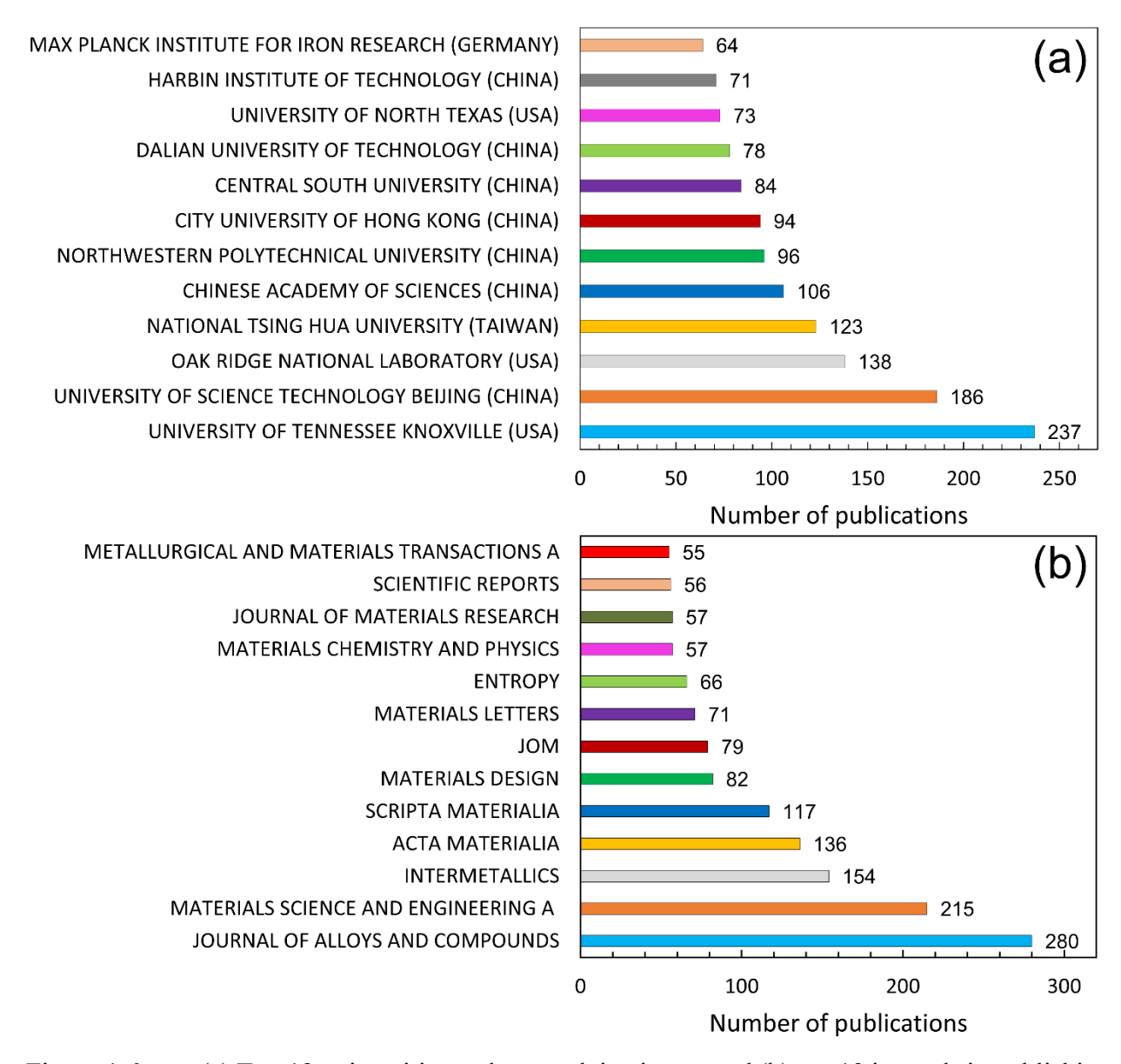


Figure 1.6 (a) Top 12 universities and research institutes, and (b) top 13 journals in publishing HEA articles, sorted by the number of publications from year 2004 to the end of 2019.

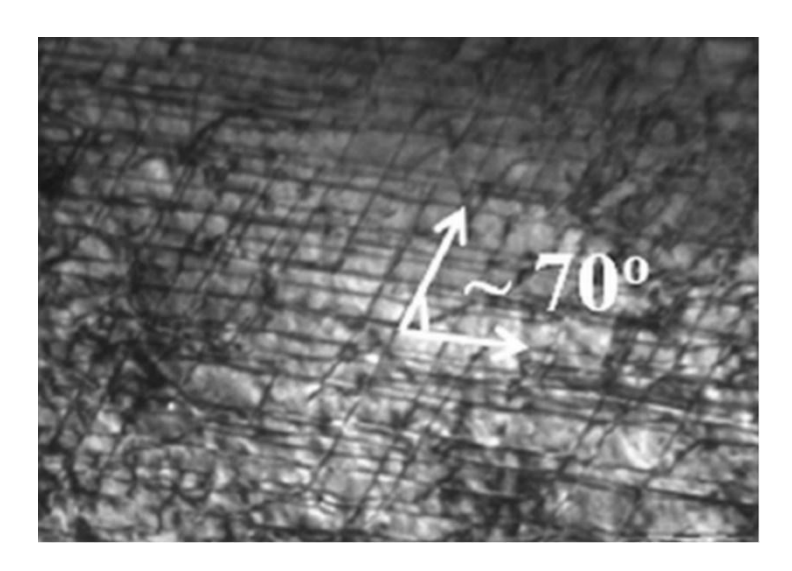


Figure 2.1 TEM image of the deformed (CoCrNi)<sub>94</sub>Al<sub>3</sub>Ti<sub>3</sub> medium-entropy alloy, indicating planar slip of dislocations along with intersecting slip lines in two different {111} planes [46].

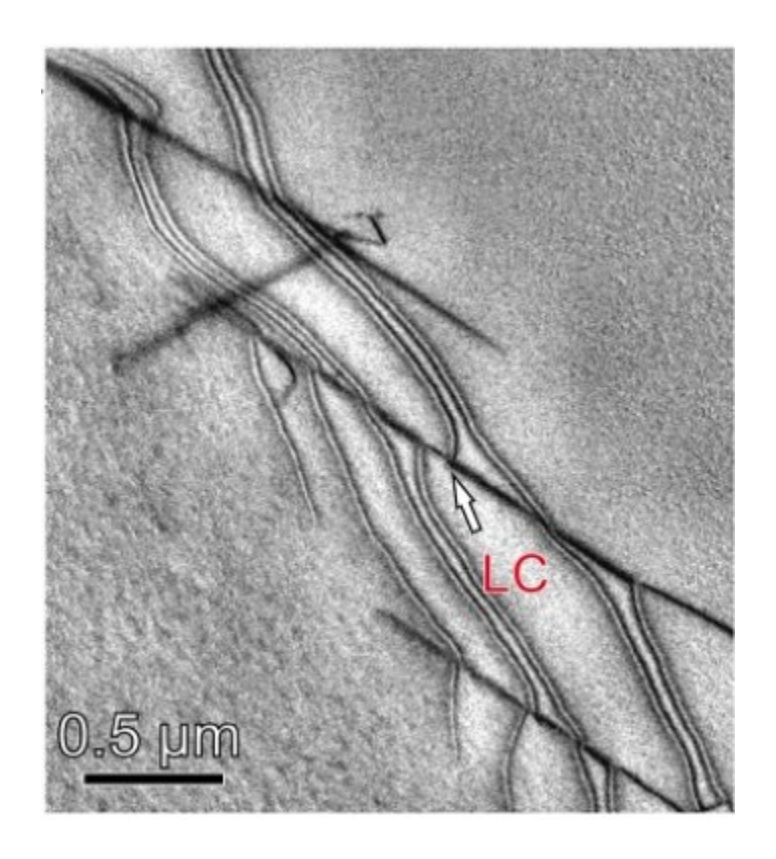


Figure 2.2 Lomer-Cottrell (LC) junctions (e.g., the one marked by an arrow) formed on two  $\{111\}$  slip plane intersections in the Al<sub>0.1</sub>CoCrFeNi high-entropy alloy [47].

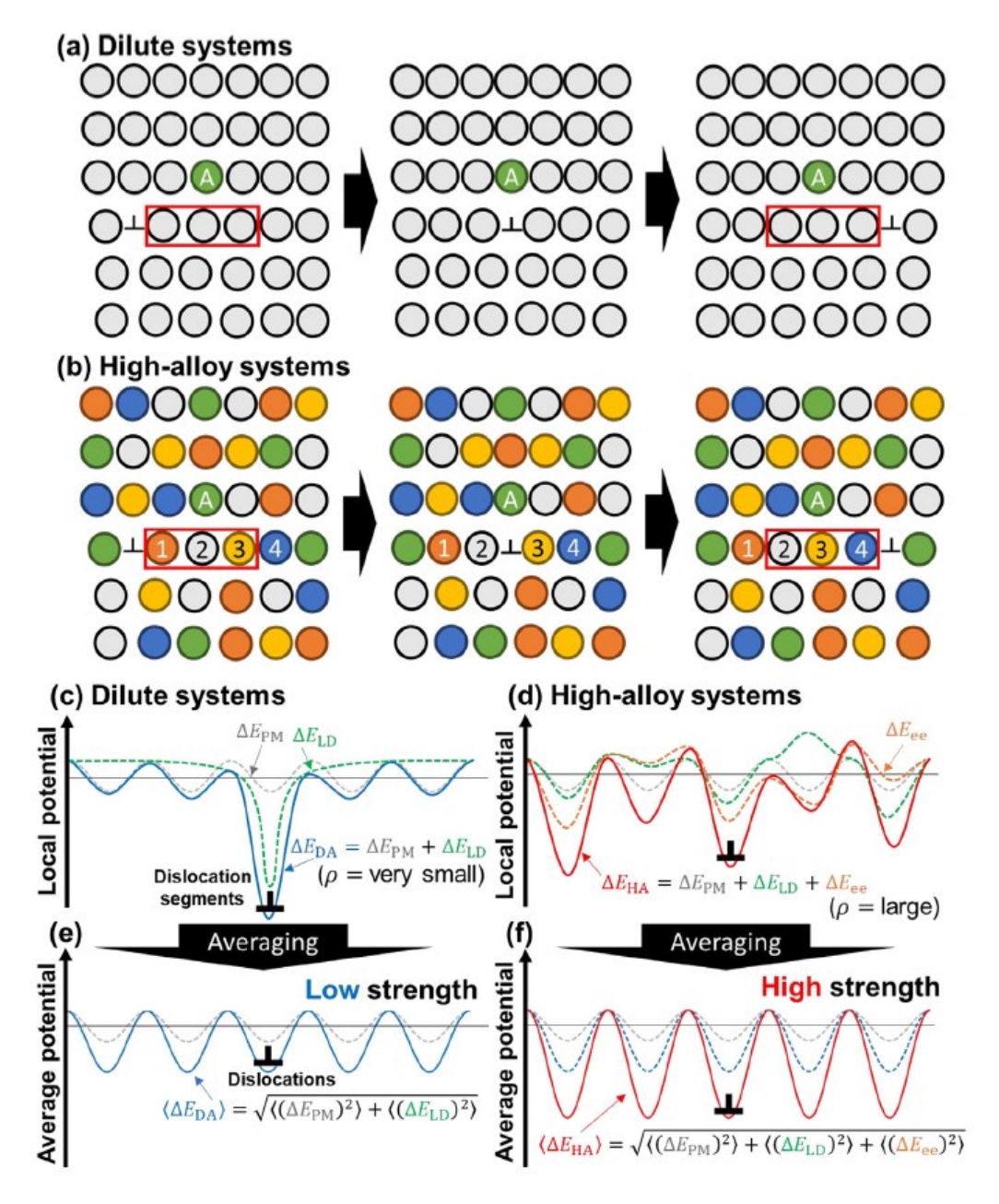


Figure 2.3 Schematics showing the changes in the arrangement of neighboring atoms caused by an edge dislocation slip in the face-centered-cubic crystal lattices of (a) a dilute solid solution and (b) a high-alloy system, respectively. Local Peierls potential energy profiles around a dislocation segment are schematically illustrated for the (c) dilute system and (d) high-alloy system [50]. Distributions of the average potential energies in the (e) dilute system and (f) high-alloy system, which were obtained by averaging the local potential energies shown in (c) and (d) along the dislocation line [50].

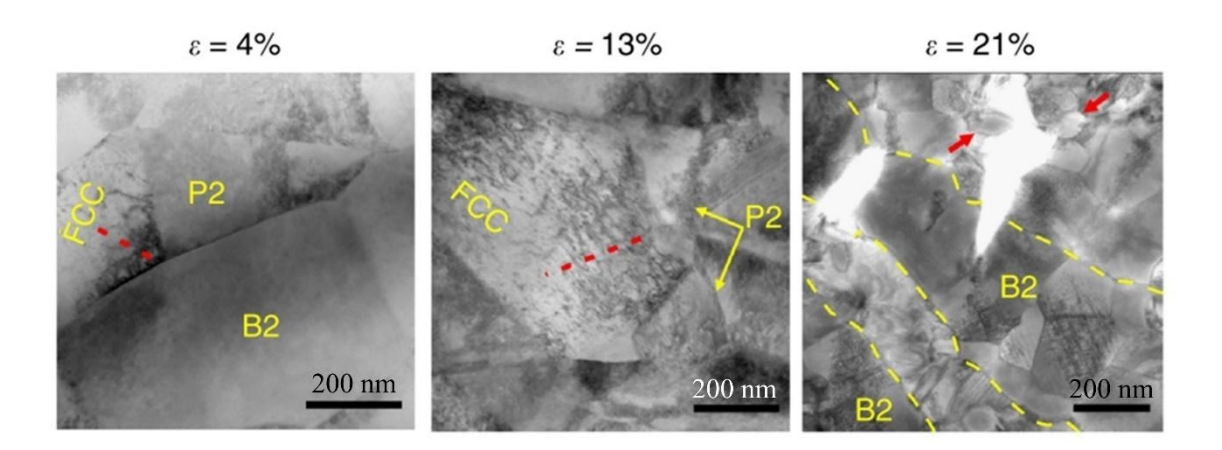


Figure 2.4 Deformation micro-mechanisms in the hierarchical AlCoCrFeNi<sub>2.1</sub> high-entropy alloy with the increasing tensile strain [60].

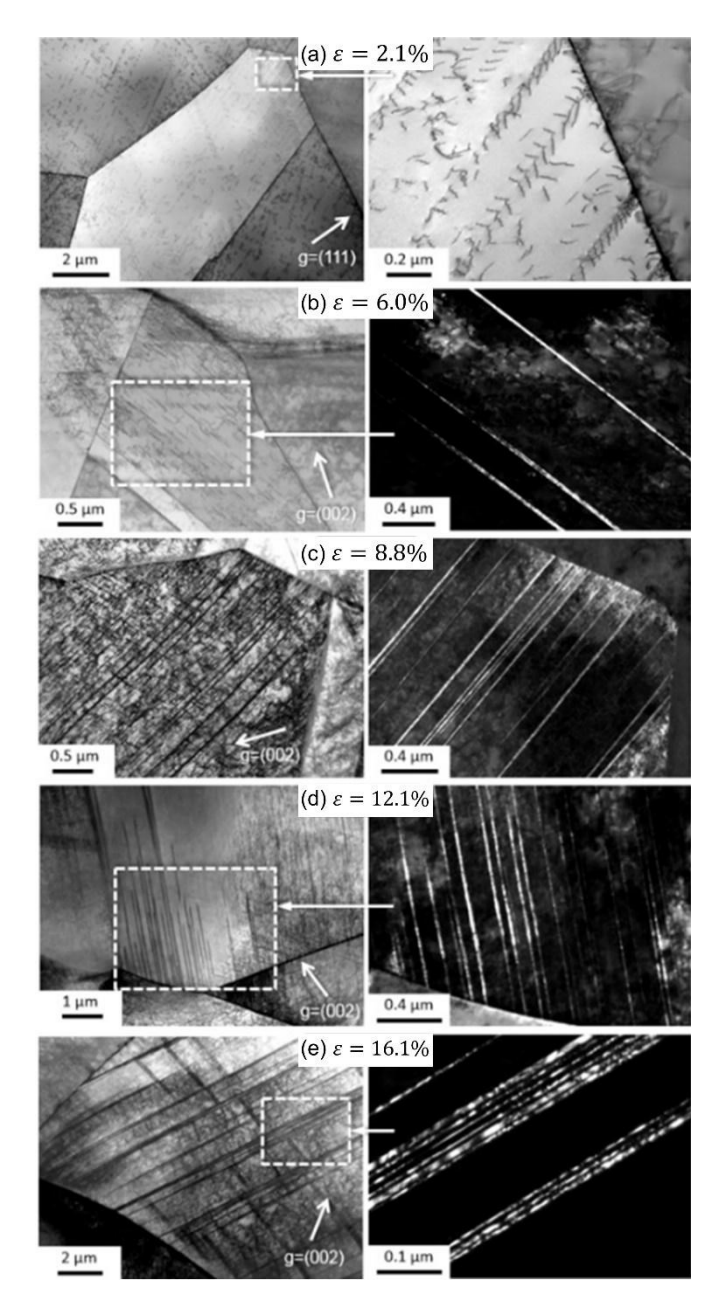


Figure 2.5 TEM micrographs showing the evolution of twins with true tensile strain at 77 K in the FeNiCoCrMn alloy [63]. (a) Both figures are bright-field images. (b-e) Figures on the left are bright-field images while those on the right are dark-field images. The dashed rectangles in the left column delineate areas that are magnified in right column.

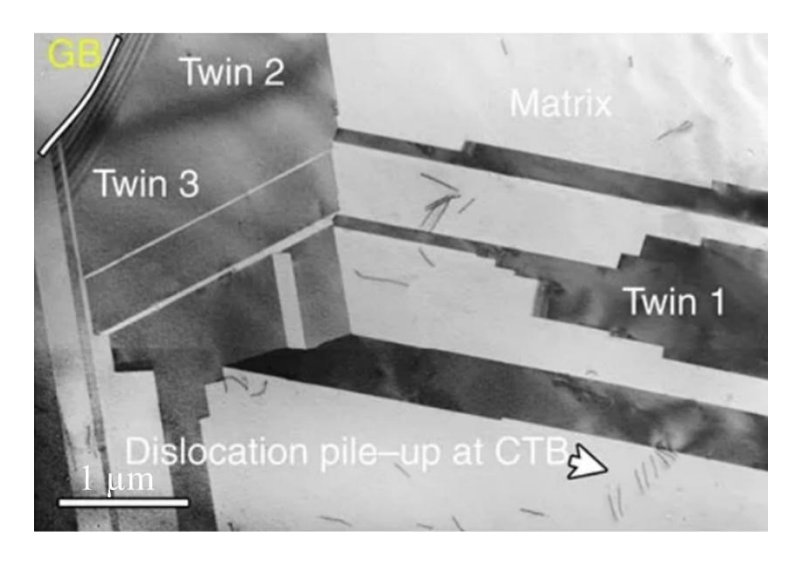


Figure 2.5 TEM micrographs showing the evolution of twins with true tensile strain at 77 K in the FeNiCoCrMn alloy [63]. (a) Both figures are bright-field images. (b-e) Figures on the left are bright-field images while those on the right are dark-field images. The dashed rectangles in the left column delineate areas that are magnified in right column.

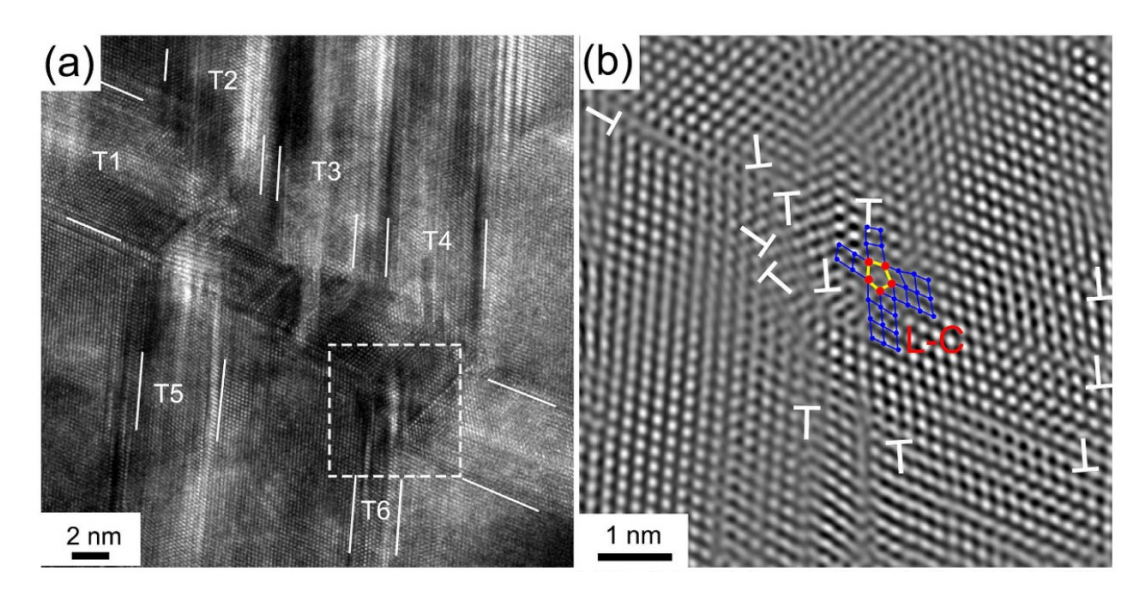


Figure 2.7 Twin-twin interactions in the FeCoCrNi alloy introduced by high-pressure torsion (HPT) [82]. (a) HRTEM image showing three incident twins (T2, T3, and T4) in the same direction interacting with one barrier twin (T1) and triggering the formation of T5 and T6 twins (twin boundaries highlighted by white lines). (b) Fourier filtered image of the framed part in (a), showing plenty of dislocations (marked with white "T") and an Lomer-Cottrell (LC) lock (indicated by five red spots). [82]

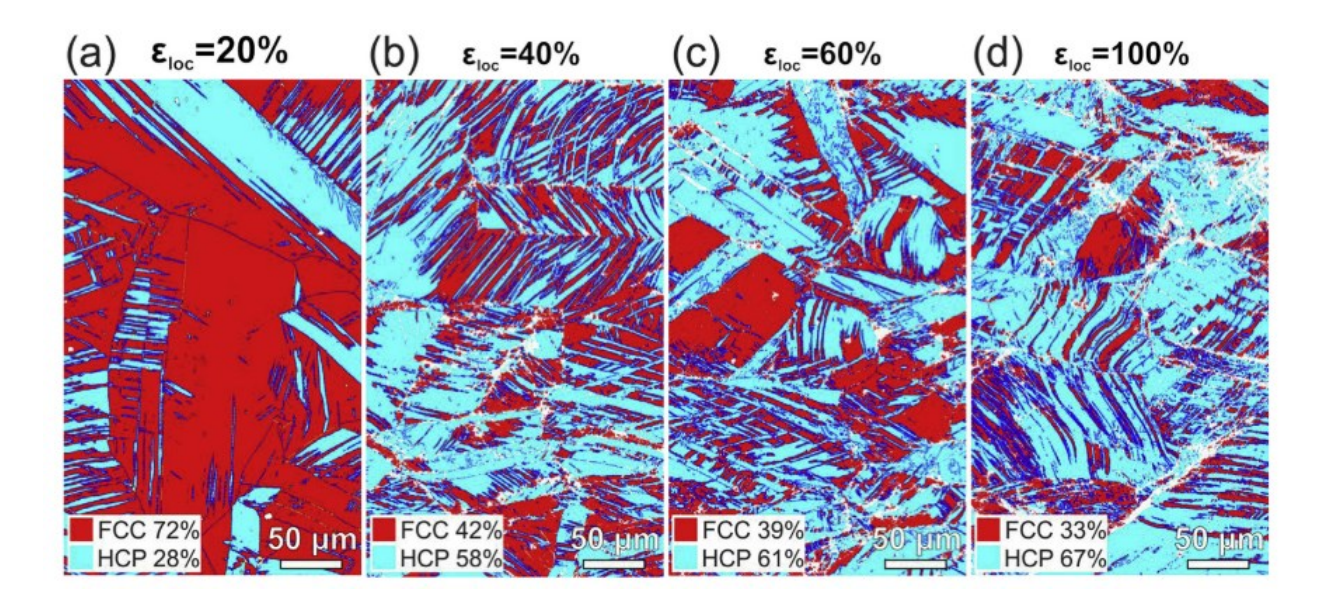


Figure 2.8 EBSD phase maps of the dual-phase  $Co_{20}Cr_{20}Fe_{34}Mn_{20}Ni_6$  alloy deformed at room temperature [88], reflecting the deformation-induced martensitic transformation as a function of deformation. The local strain,  $\varepsilon_{loc}$ , of (a) 20%, (b) 40%, (c) 60% and (d) 90% correspond to the early, medium and late uniform deformation and post-necking stages, respectively.

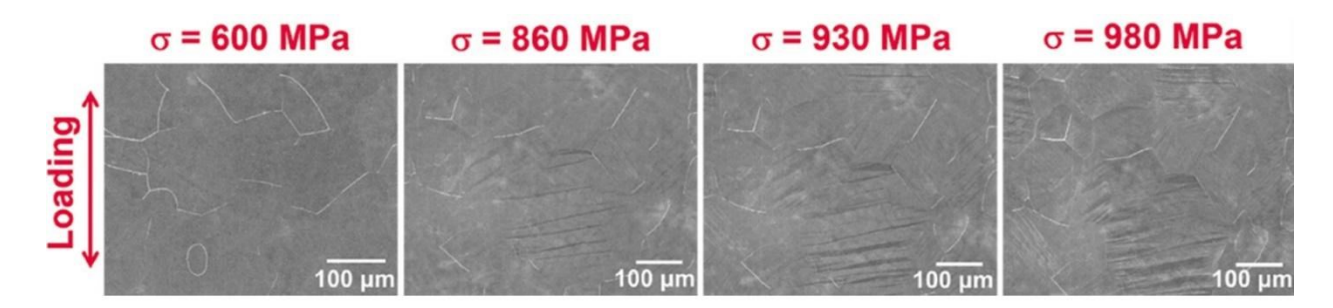


Figure 2.9 In-situ SEM observation reveals the martensitic phase transformation process in the Ta<sub>0.5</sub>HfZrTi alloy during continuous loading [87].

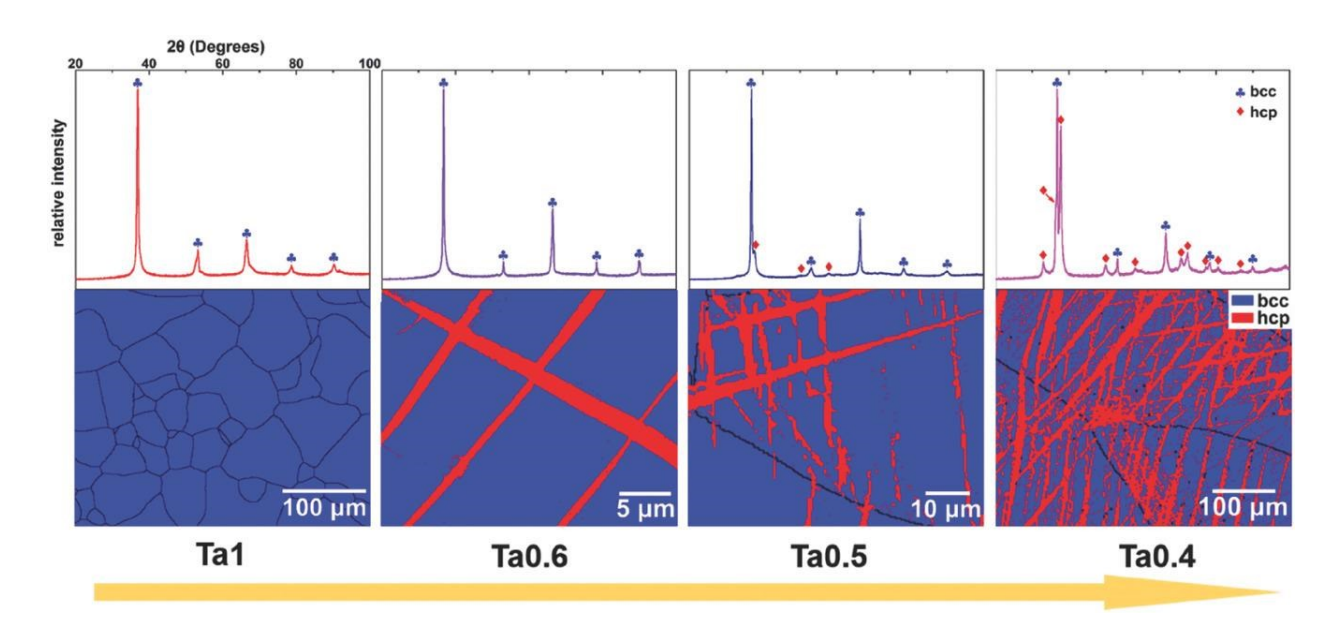


Figure 2.10 XRD patterns and EBSD images of the as-cast  $Ta_xHfZrTi$  (x = 1, 0.6, 0.5, and 0.4) alloys [87]. The Ta concentration significantly influences the phase constitution of this alloy system, rendering either single (bcc) or dual-phase (bcc + hcp) structure [87]. The decrease of the Ta content destabilizes the bcc matrix and promotes the formation of the hcp phase.

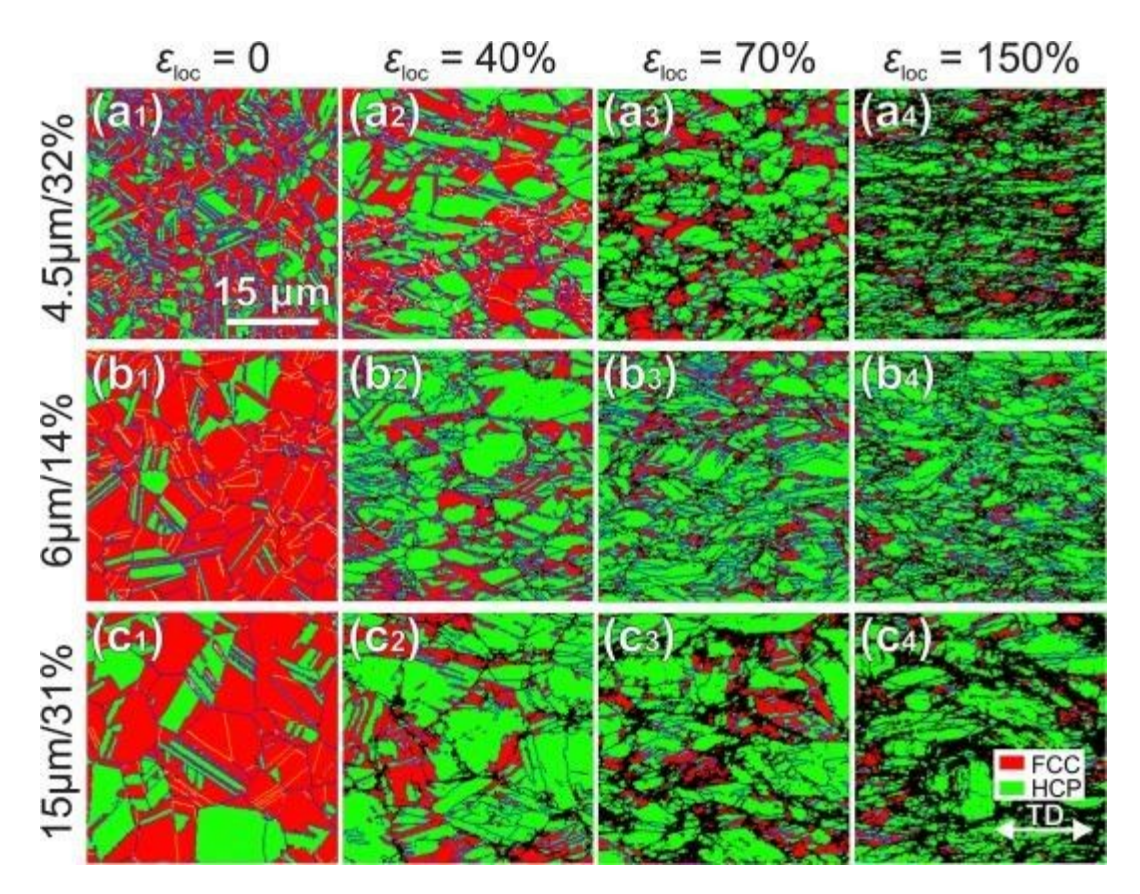


Figure 2.11 Representative EBSD phase maps showing the microstructural evolution with the increasing local strain,  $\varepsilon_{loc}$ , of the dual-phase Fe<sub>50</sub>Mn<sub>30</sub>Co<sub>10</sub>Cr<sub>10</sub> alloy with different fcc grain sizes and initially available hcp phase fractions: (a<sub>1-4</sub>) 4.5  $\mu$ m/32%; (b<sub>1-4</sub>) 6  $\mu$ m/14% and (c<sub>1-4</sub>) 15  $\mu$ m/31% [100].

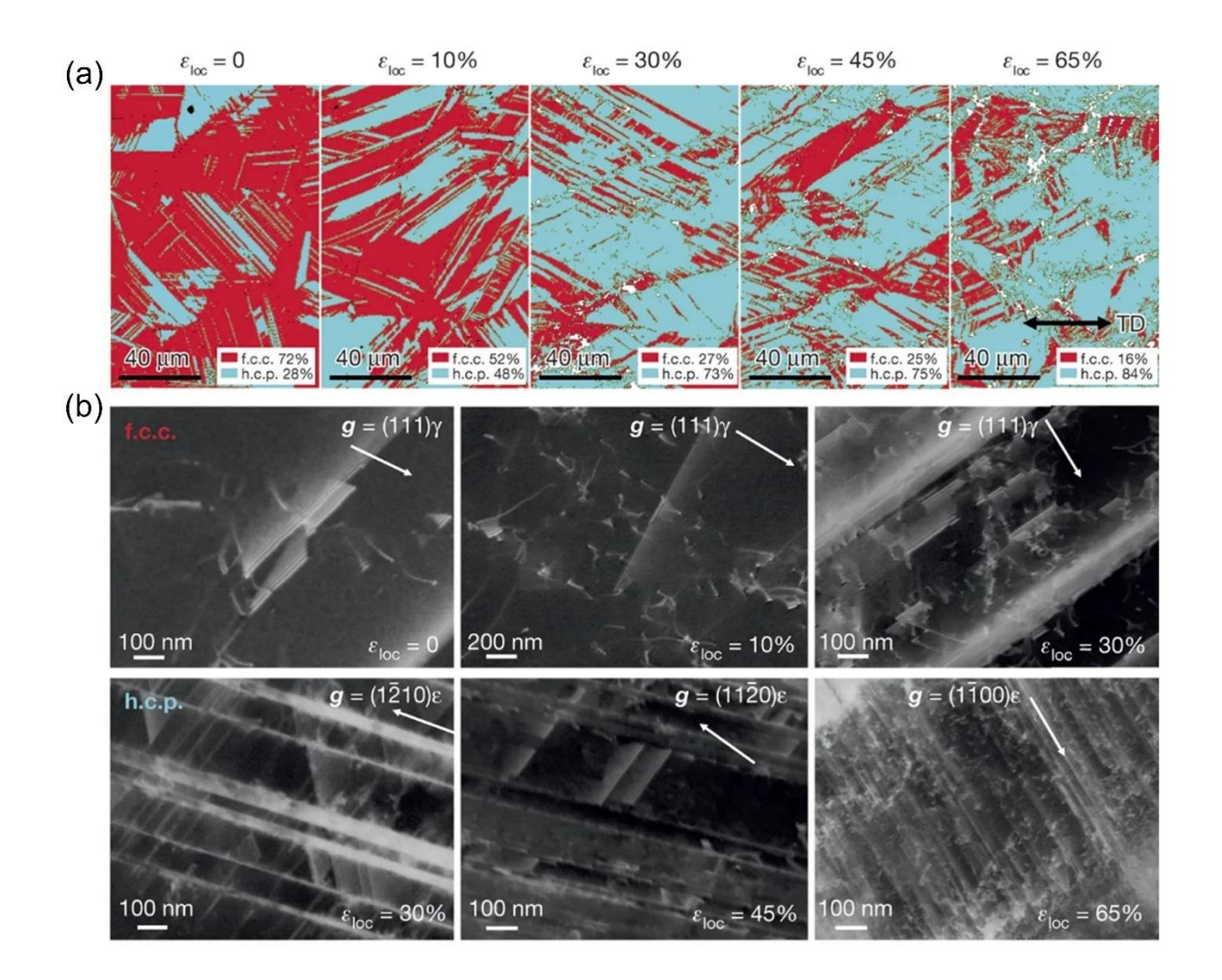


Figure 2.12 The deformation in the Fe<sub>50</sub>Mn<sub>30</sub>Co<sub>10</sub>Cr<sub>10</sub> alloy accommodated by phase transformation and twining [19]. (a) EBSD phase maps revealing the deformation-induced martensitic transformation as a function of deformation, with  $\varepsilon_{loc}$  and TD denoting the local strain and tensile direction, respectively. (b) ECCI analyses showing the evolution of defect substructures in the fcc and hcp phases, where the deformation-induced twinning is dominated in the hcp phase. g is the diffraction vector,  $\gamma$  is the fcc phase, and  $\varepsilon$  is the hcp phase.

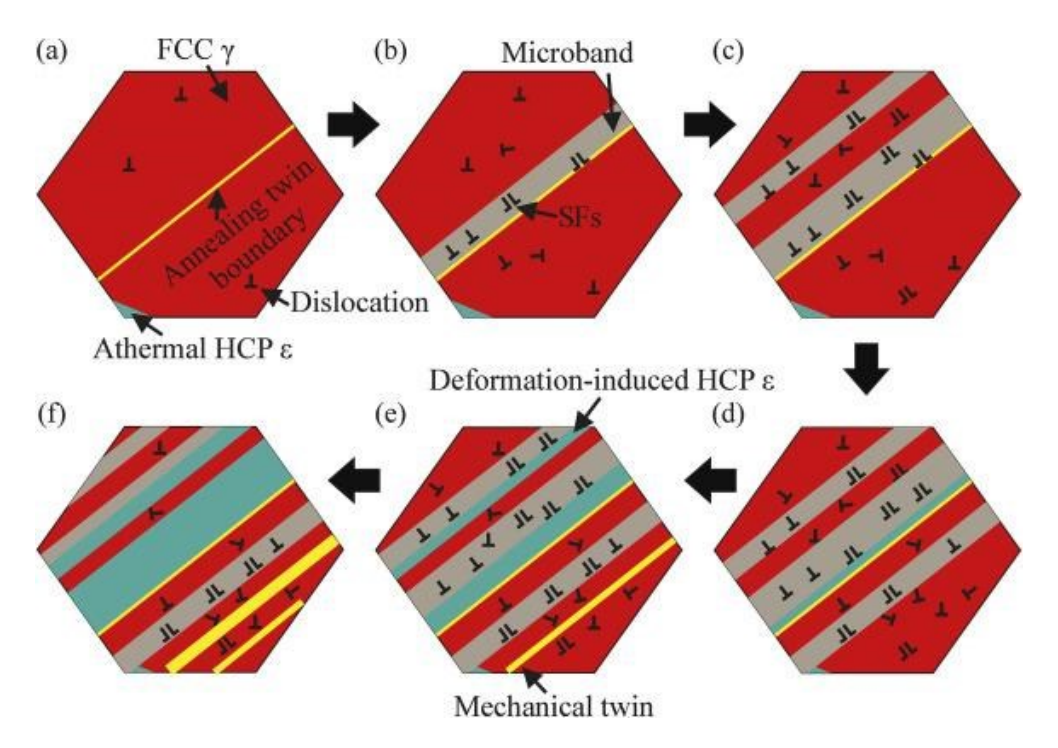


Figure 2.13 Schematic sketch of microstructural evolution with straining in an interstitial highentropy alloys [103]. Black arrows point in the direction of increasing strain values.

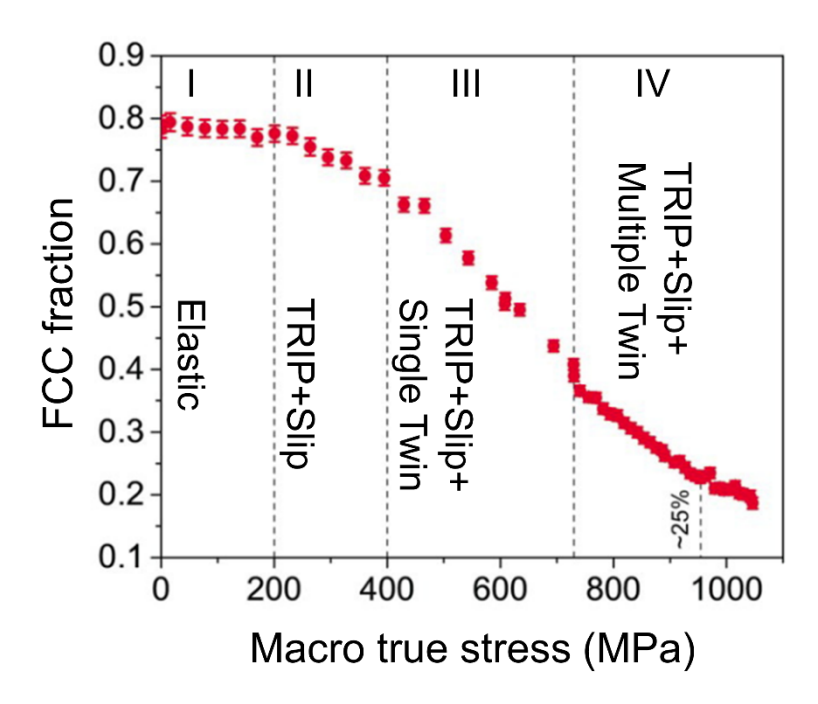


Figure 2.14 The dynamic evolution of the fcc phase fraction under tension in the TRIP-HEA  $Fe_{50}Mn_{30}Co_{10}Cr_{10}$  [102].

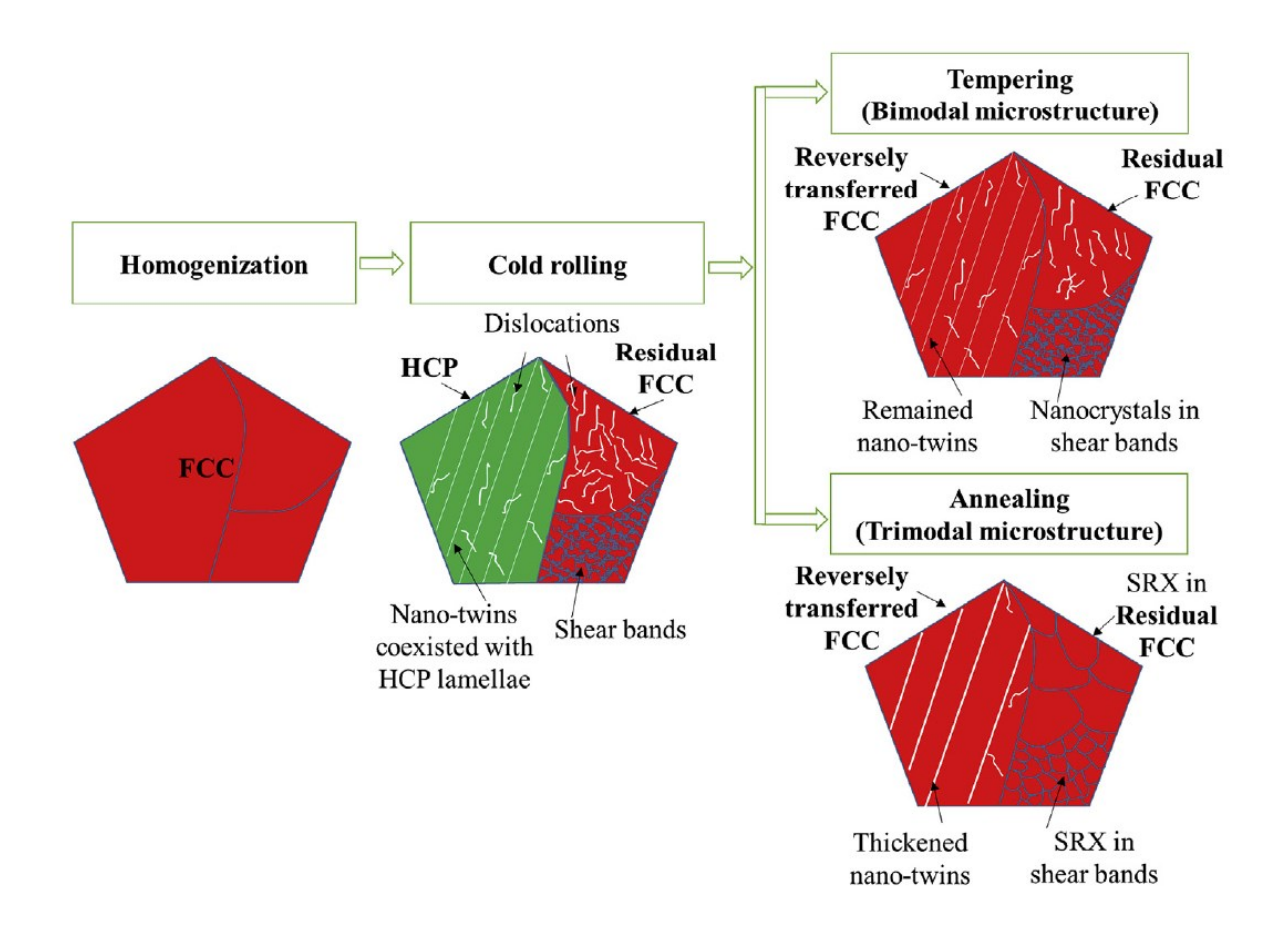


Figure 2.15 Schematic showing the thermomechanical processes for producing the bimodal and trimodal microstructures in the  $Fe_{49.5}Mn_{30}Co_{10}Cr_{10}C_{0.5}$  alloy [104].

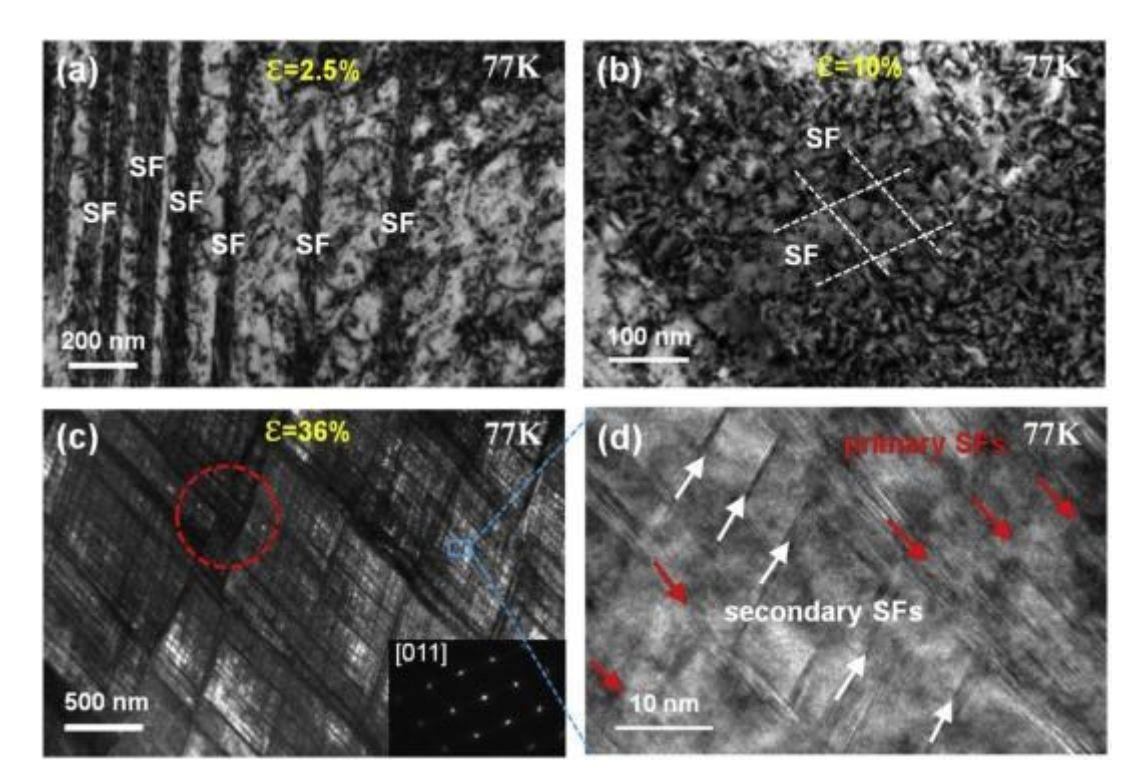


Figure 2.16 Bright-field TEM images of dislocation structures and stacking faults (SFs) in the precipitation-strengthened FeCoNiCrTi<sub>0.2</sub> alloy after deformed to a true strain of  $\sim$ 2.5% (a),  $\sim$ 10% (b) and  $\sim$ 36% (c) at 77 K [86]. The inset in (c) is a SAED pattern of the region in the red circle. (d) HRTEM image of the blue region in (c). (a) is taken under the two-beam condition to see dislocations, and (c–d) are taken along the zone axis of [011] to observe intersecting stacking faults.

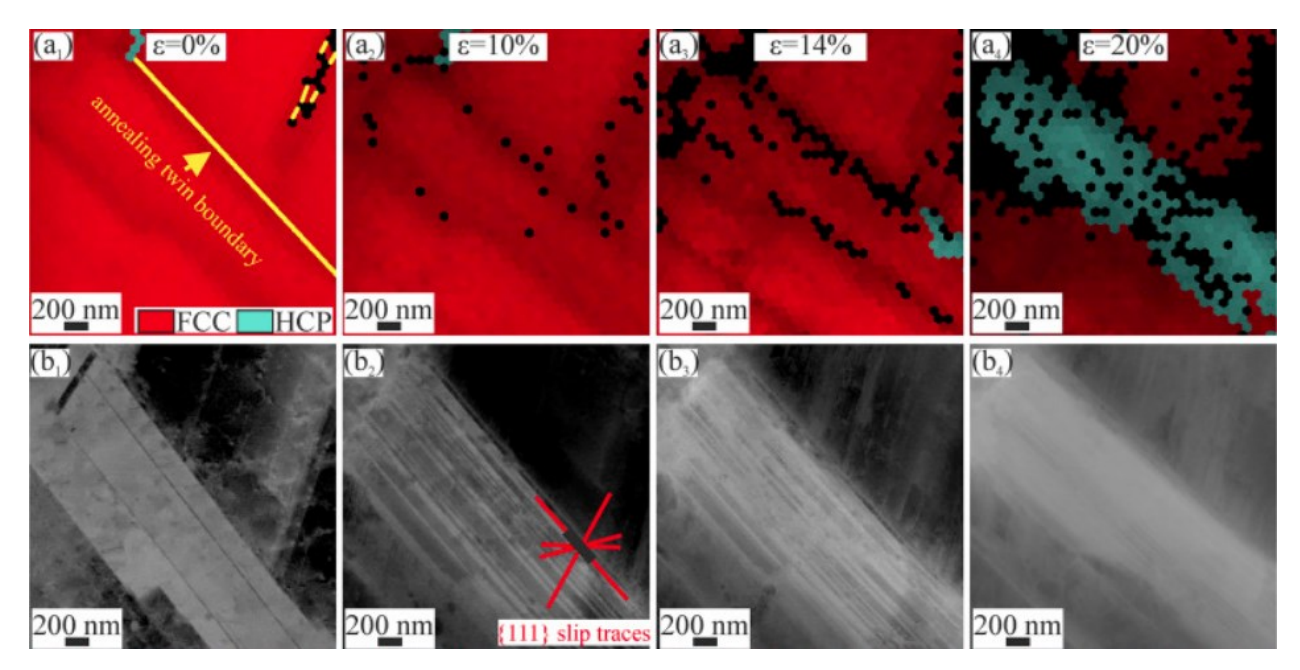


Figure 2.17 Interrupted in-situ EBSD and ECCI observations of deformation and phase transformation at varying strain levels in the interstitial  $Fe_{49.5}Mn_{30}Co_{10}Cr_{10}C_{0.5}$  high-entropy alloy [103]. (a) Overlay of phase map with image quality map. (b) ECC images.

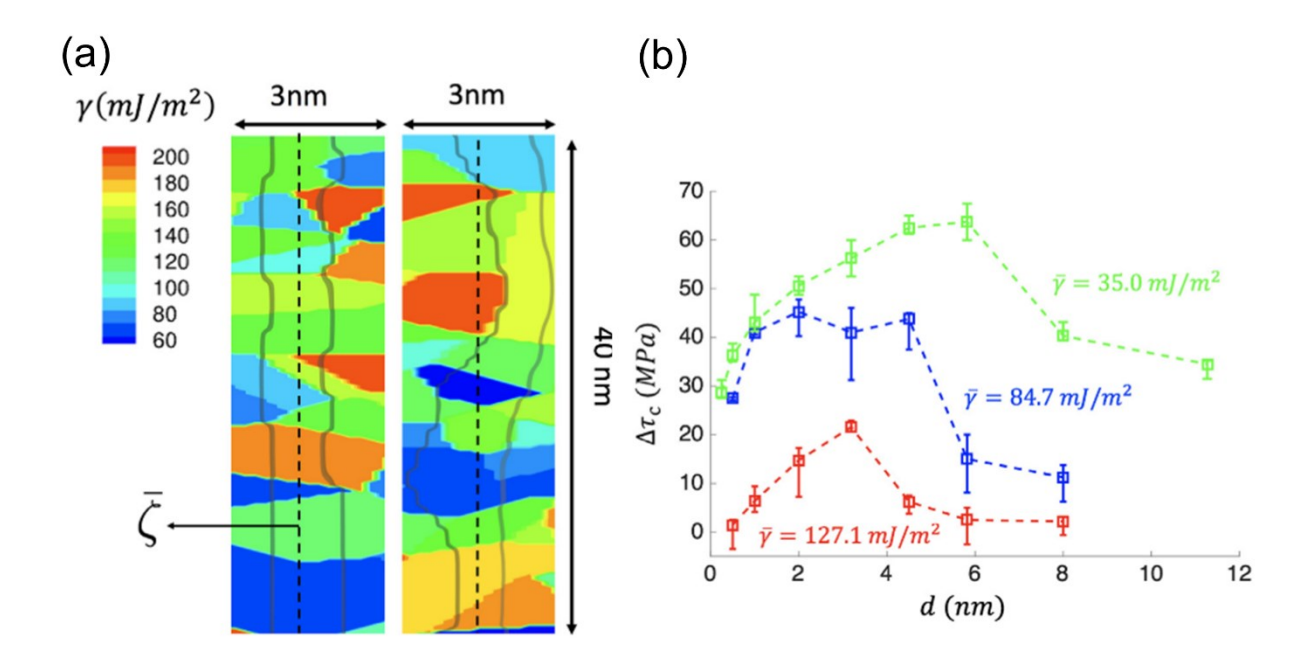


Figure 2.18 (a) Schockley partials revealed by theoretical calculations [115]. Left: the relaxed dislocation configuration at zero stress. Right: the dislocation configuration at an applied stress of 195 MPa. (b) The critical stress increment,  $\Delta \tau_c$ , as a function of the stacking fault region size d [115]. The stacking fault energies are chosen randomly from uniform distributions.

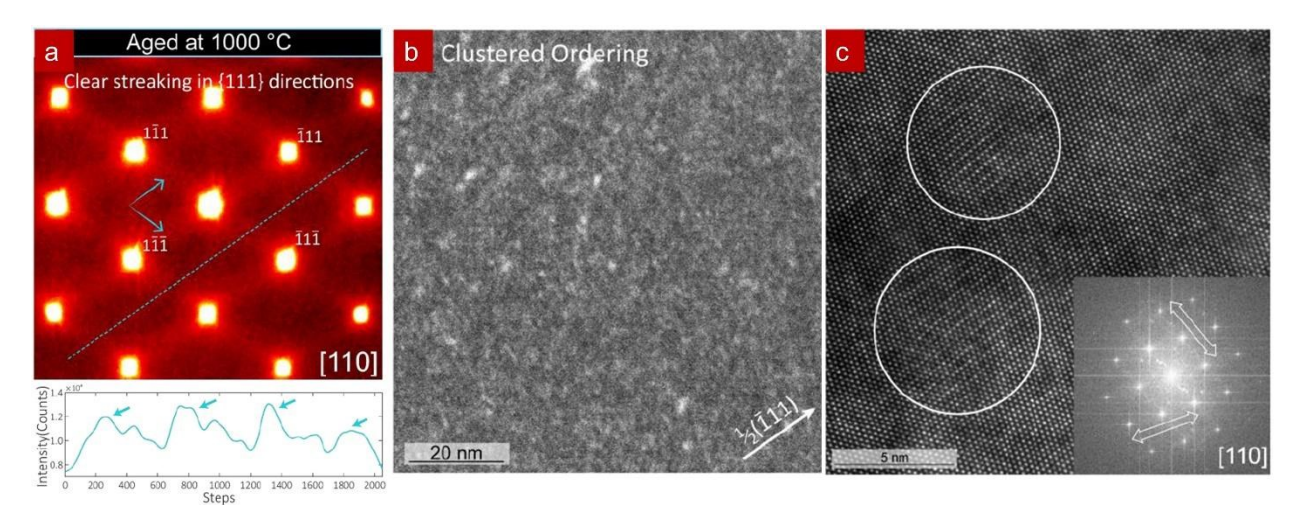


Figure 2.19 Short-range ordering observed in the CoCrNi alloy [119]. (a) Energy-filtered diffraction pattern taken from the sample aged at 1000 °C. The line plot shows the periodic intensity of the "diffuse superlattice" streaks. (b) Energy-filtered dark-filed image taken from the 1000 °C aged sample. (c) Typical high-resolution TEM image and the associated FFT image of the 1000 °C aged sample, where superlattices are marked by the white circles and the associated streaking along the {111} direction is marked by the white arrows in the FFT image.

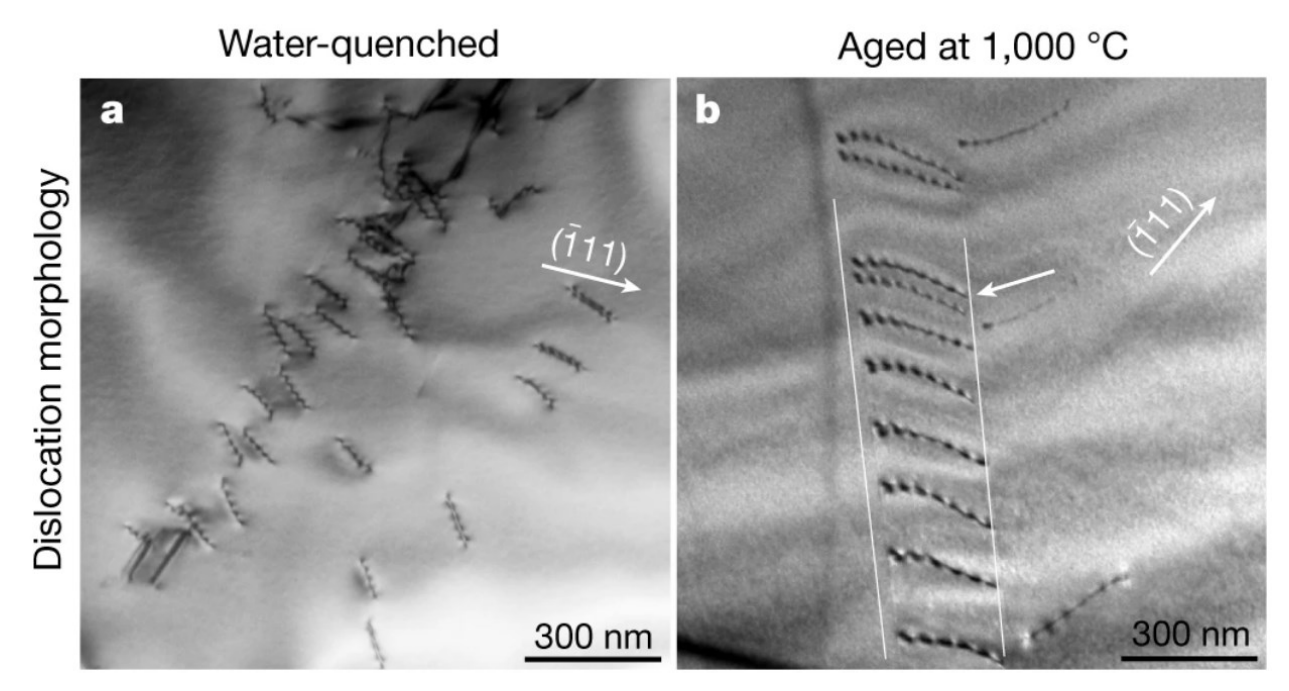


Figure 2.20 Dislocations in the water-quenched and 1,000 °C aged CoCrNi samples [119]. (a) Two-beam bright-field image, showing the representative wavy configuration of dislocations in the water-quenched sample. (b) Two-beam bright-field image, showing the representative planar configuration of dislocations in the 1,000 °C aged sample, with the leading dislocation pair indicated by the white arrow.

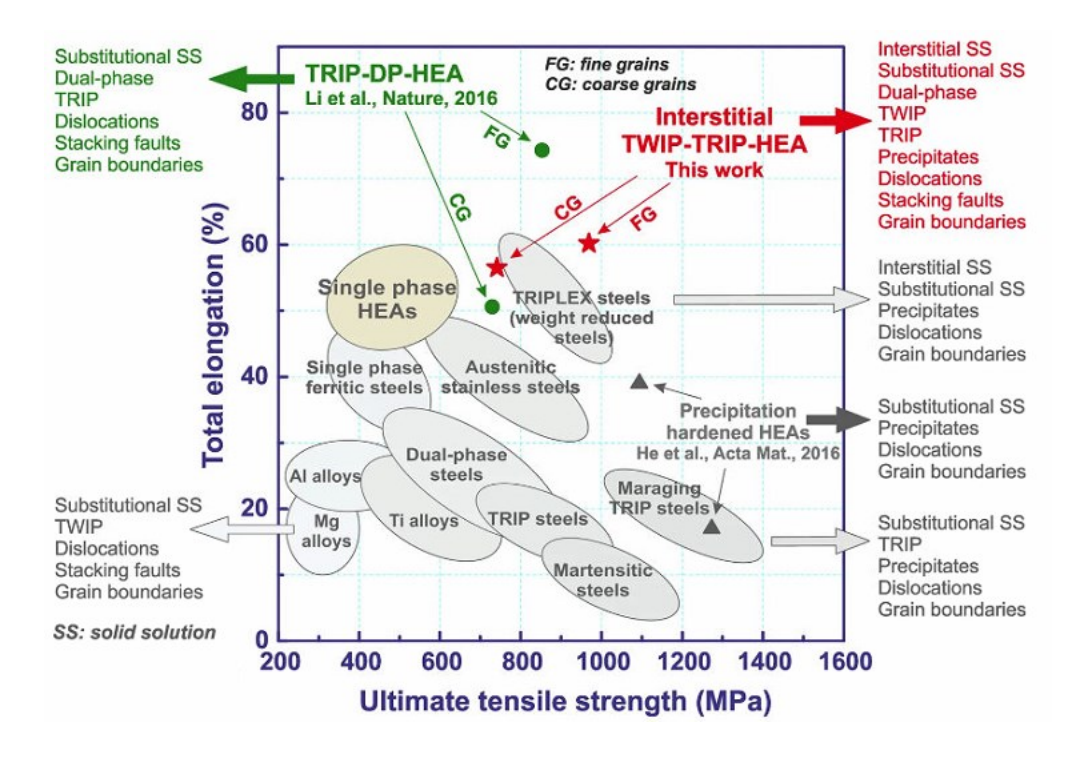


Figure 2.21 Strength-ductility profiles of various classes of metallic materials including highentropy alloys [100].

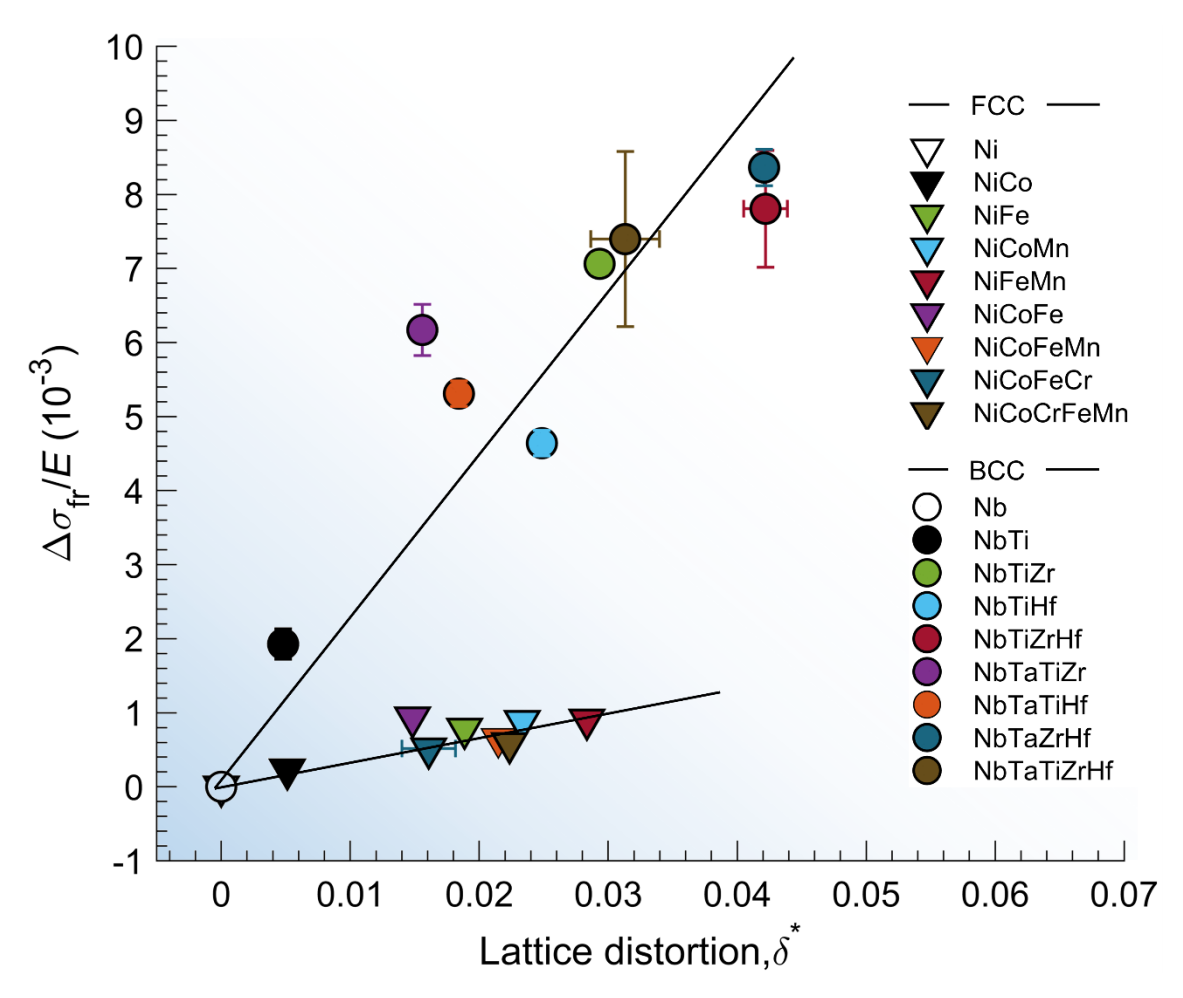


Figure 3.1 The linear correlations between the normalized lattice distortion stress,  $\Delta \sigma_{fr}/E$ , and the lattice distortion,  $\delta^*$ , for both the Ni-based fcc and Nb-based bcc equiatomic alloys [124].

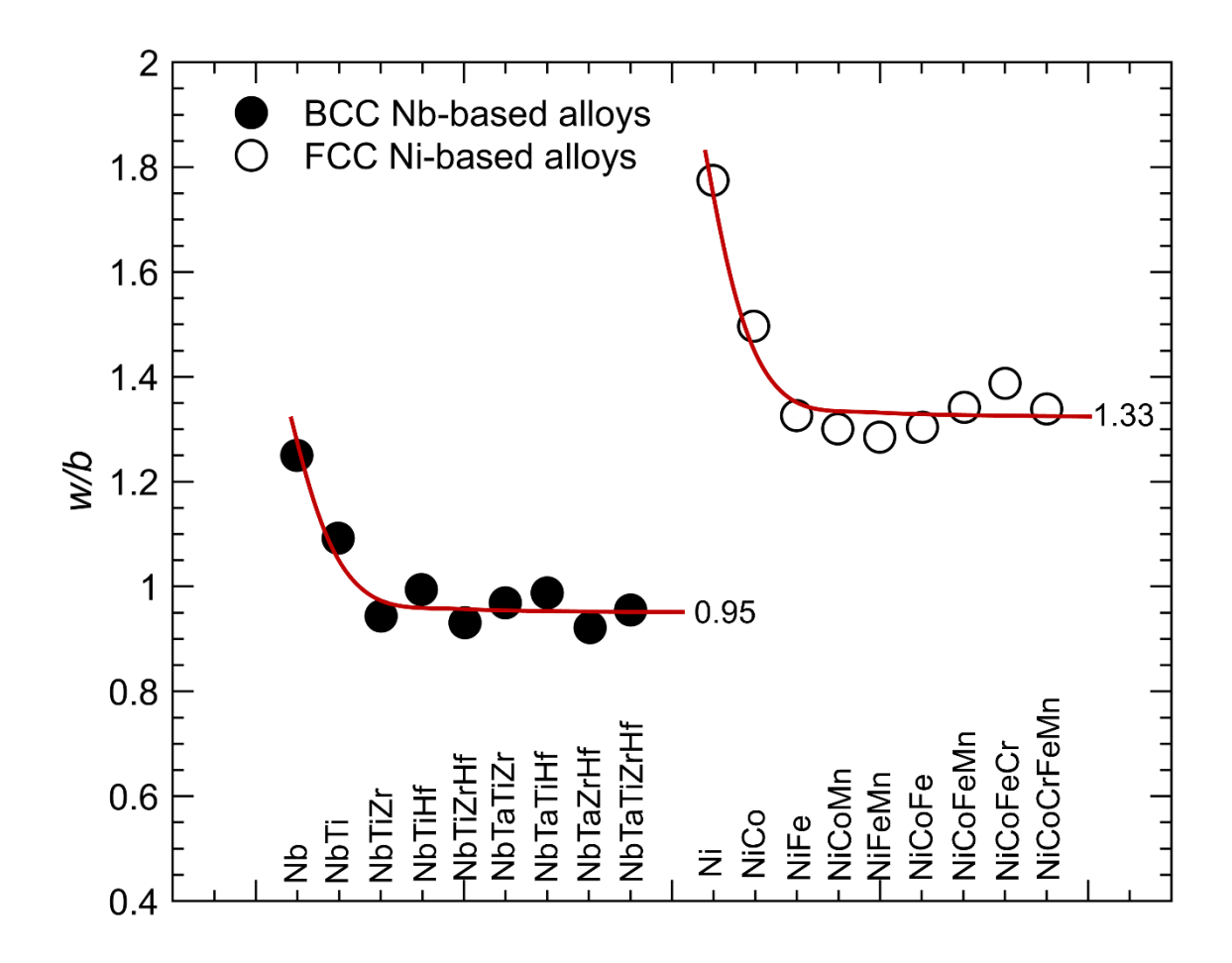


Figure 3.2 The normalized dislocation core width,  $w_d/b$ , for both the Ni-based fcc and Nb-based bcc equiatomic alloys [124].

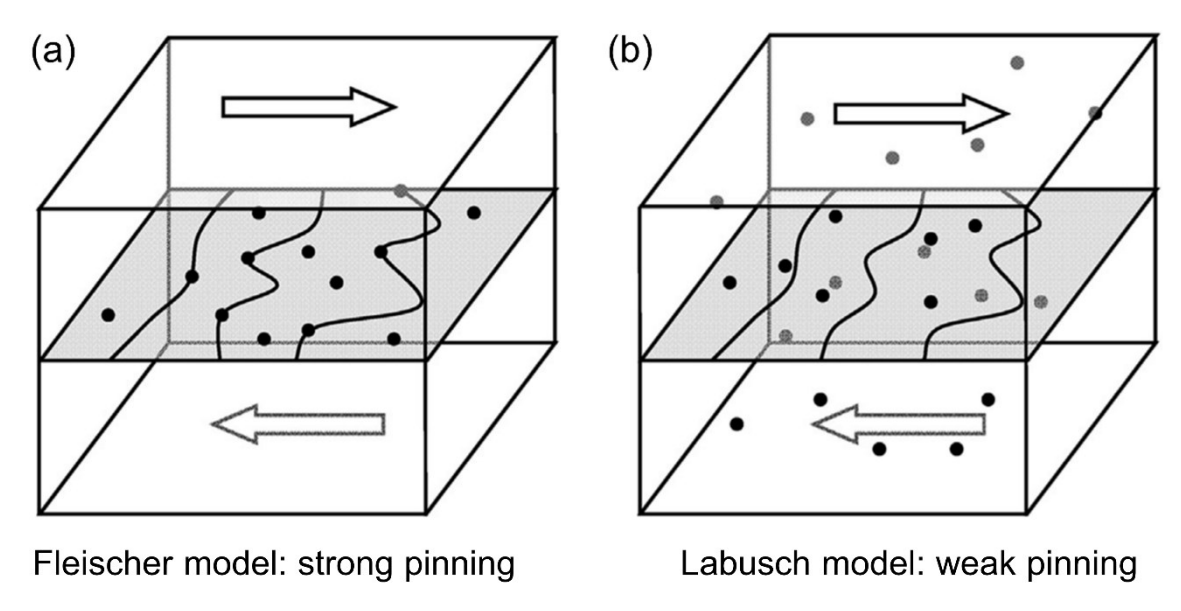


Figure 3.3 Schematics of the (a) Fleischer model and (b) Labusch model [116].

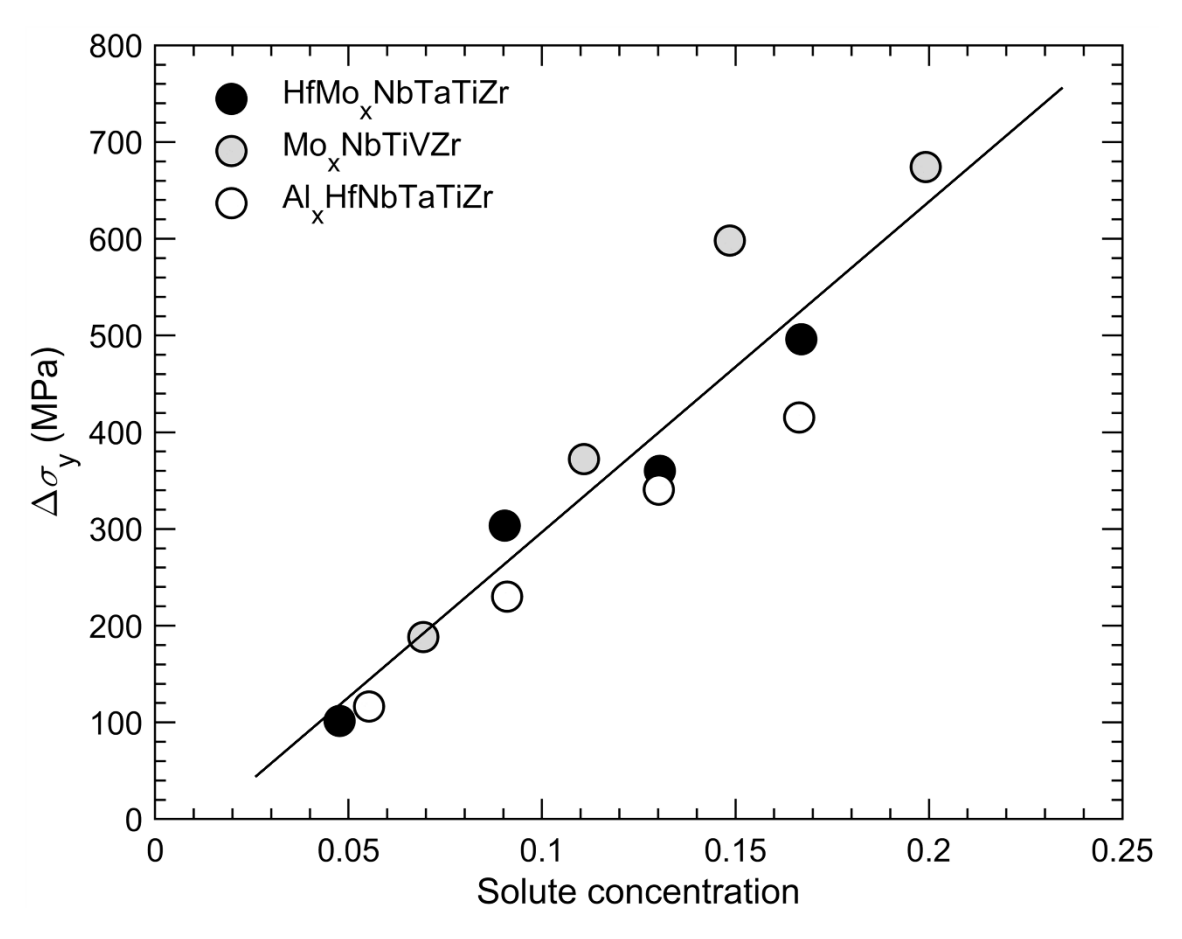


Figure 3.4 The linear scaling between the yield strength increase,  $\Delta \sigma_y$ , and the solute concentration in the HfMo<sub>x</sub>NbTaTiZr [132], MoxNbTiVZr [134], and Al<sub>x</sub>HfNbTaTiZr [135] HEAs.

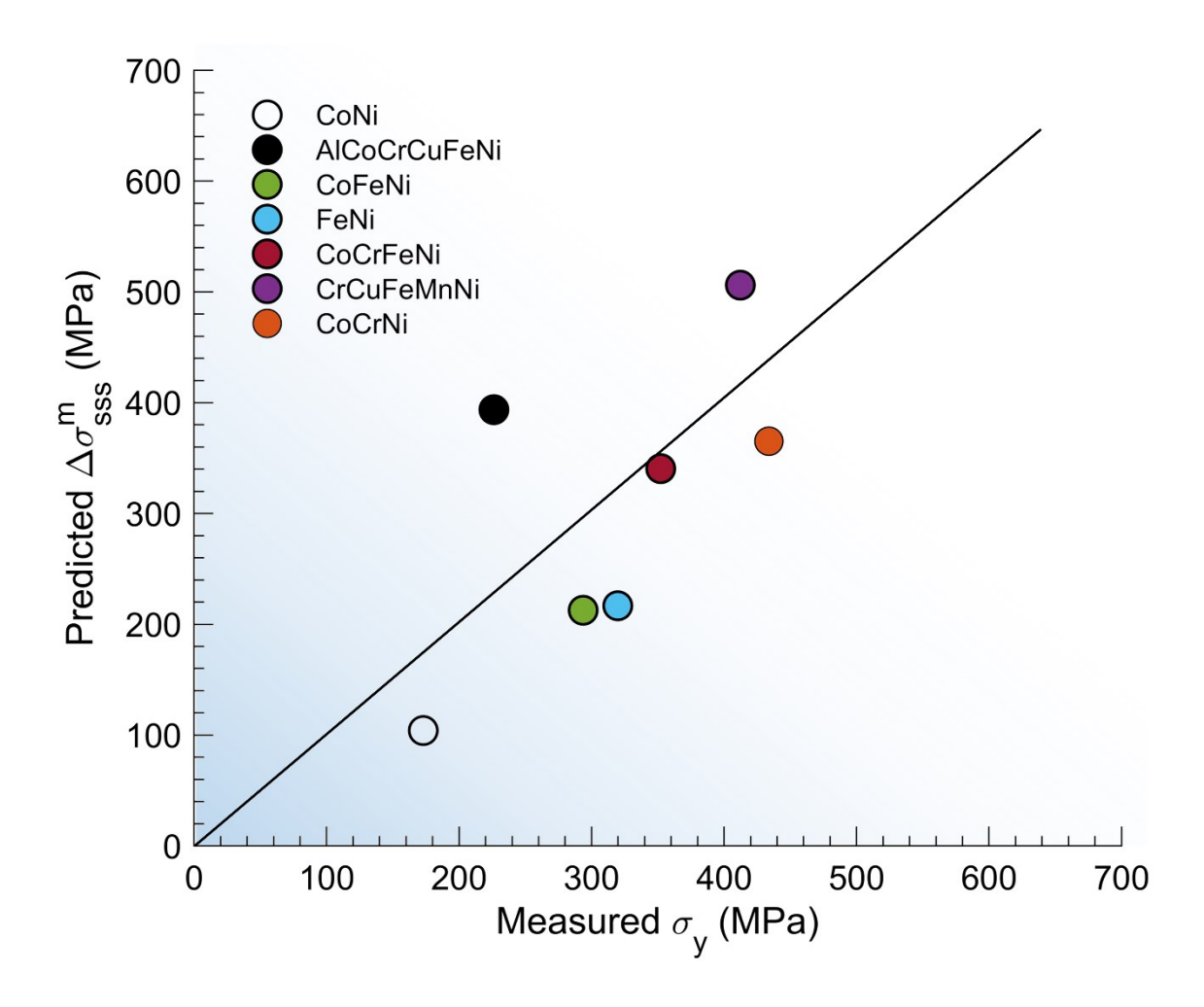


Figure 3.5 Experimental yield strength,  $\sigma_y$ , versus the predicted solid solution strengthening effect,  $\Delta \sigma_{sss}^m$ , for the single crystals of HEAs and their subsystems [137].

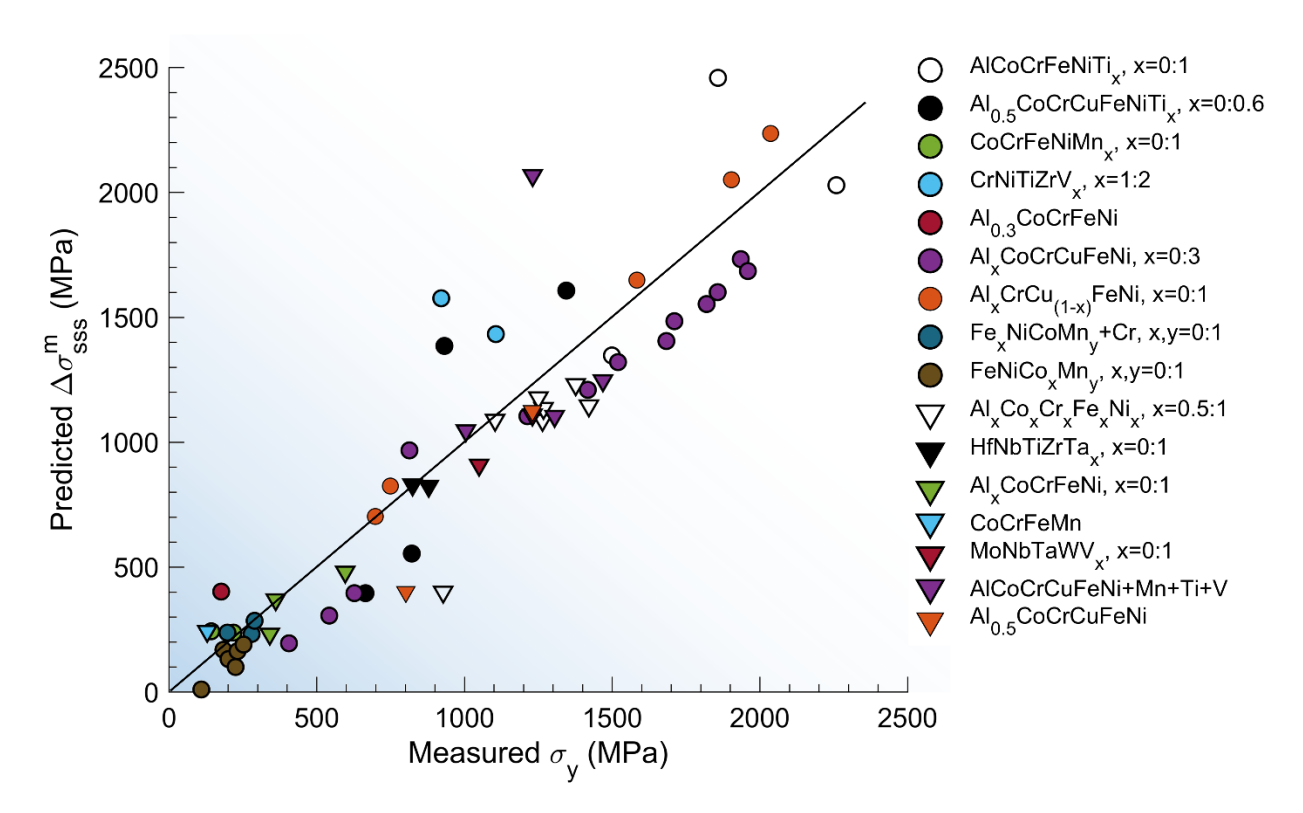


Figure 3.6 Experimental yield strength,  $\sigma_y$ , versus the predicted solid solution strengthening effect,  $\Delta \sigma_{sss}^m$ , for the polycrystalline HEAs [137]. Note that experimental  $\sigma_y$  in this case does not exclude the grain size effect.

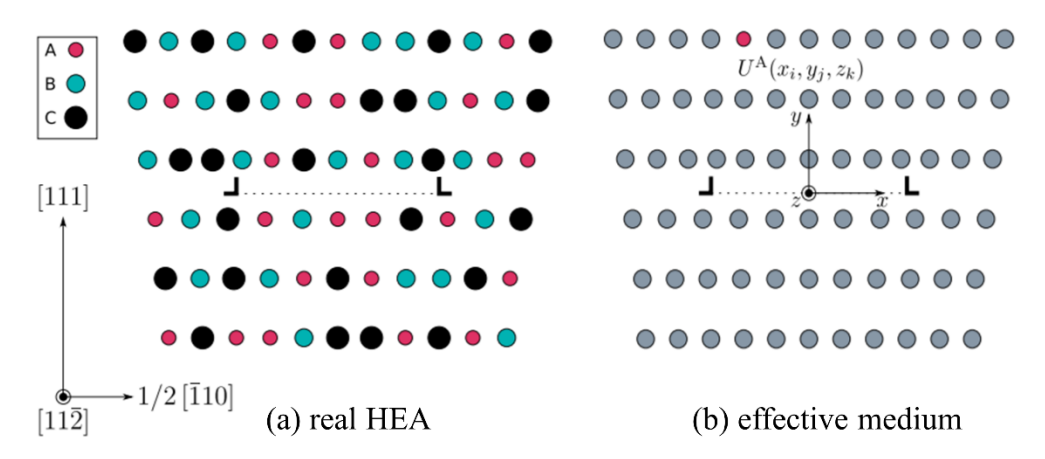


Figure 3.7 Schematics showing (a) the atom distribution in an actual 3-component HEA with a dissociated edge dislocation and (b) the effective matrix of the same alloy with "solute" A embedded at the position  $(x_i, y_j, z_k)$ , with an interaction energy  $U^A(x_i, y_j, z_k)$  with the dislocation [140].

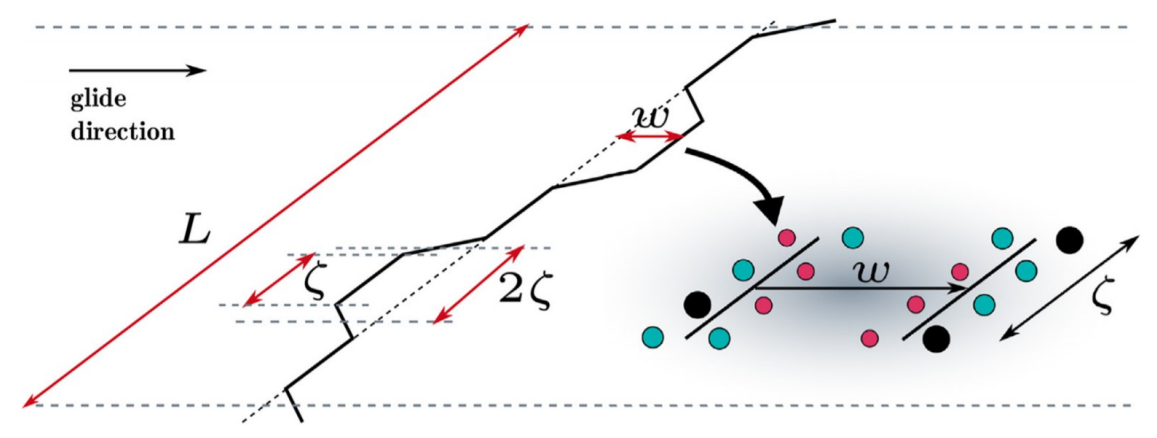


Figure 3.8 Schematic of the low-energy wavy dislocation configuration formed by moving a L long straight dislocation through the solute field with spatial fluctuations of concentrations. The total dislocation energy is minimized when  $\zeta$  and w reaches their characteristic values,  $\zeta_c$  and  $w_c$  [140].

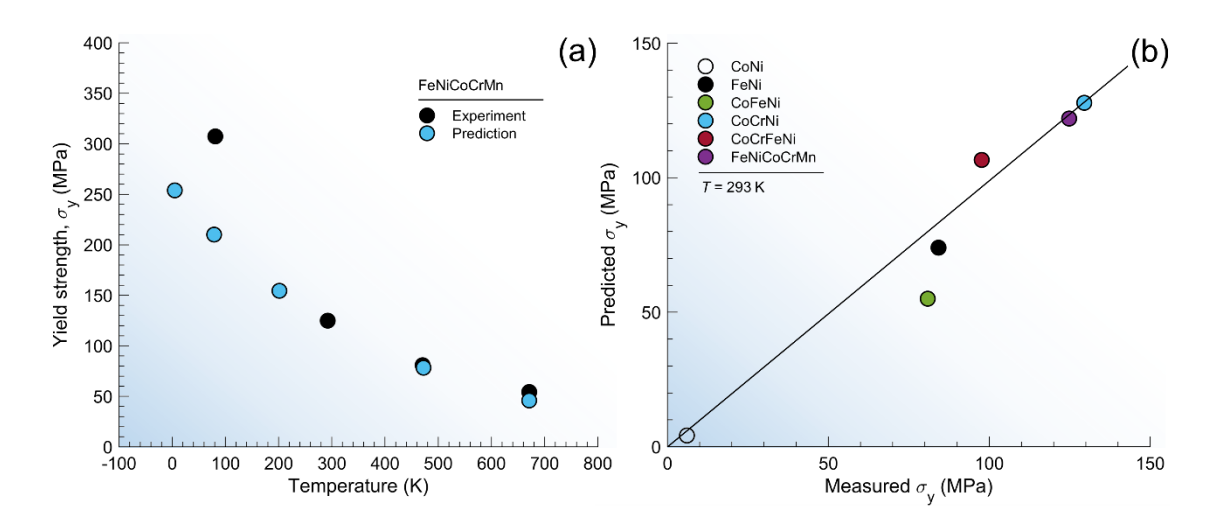


Figure 3.9 (a) Experimental vs. predicted yield strengths of the fcc FeNiCoCrMn HEA at varying temperatures [140]. (b) Experimental vs. predicted yield strengths of the fcc HEA in the Fe-Ni-Co-Cr-Mn family at 293 K [140]. Note that the Hall-Petch contribution to the strengths are subtracted.

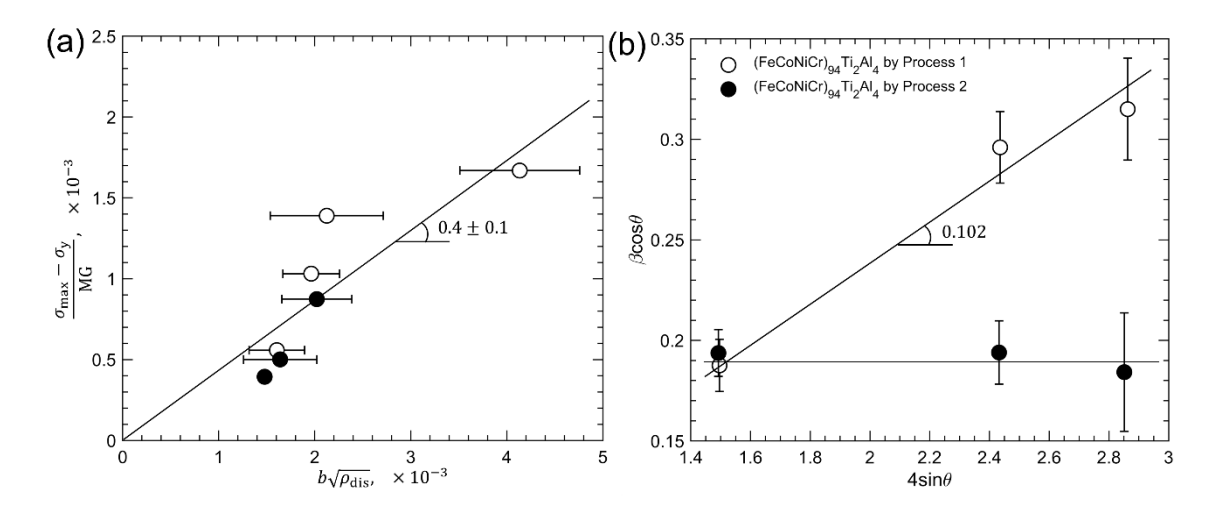


Figure 3.10 (a)  $\frac{\sigma_{max} - \sigma_y}{MG}$  plotted against  $b\sqrt{\rho_{dis}}$  for the fcc CrMnFeCoNi HEA, from which the value of  $\alpha$  in the Taylor hardening model can be determined from the slope of the linear fitting line [63]. (b) The line broadening parameter of X-ray diffraction peaks,  $\beta cos\theta$ , plotted against the diffraction angle parameter,  $4sin\theta$ , for the (FeCoNiCr)<sub>94</sub>Ti<sub>2</sub>Al<sub>4</sub> HEA processed by two different processing routes, i.e., Process 1 and Process 2 (refer to the text for the specifics of each process). A linear fitting to the  $\beta cos\theta - 4sin\theta$  data pairs leads to the evaluation of the micro strain,  $\varepsilon_M$ , from the slope [131].

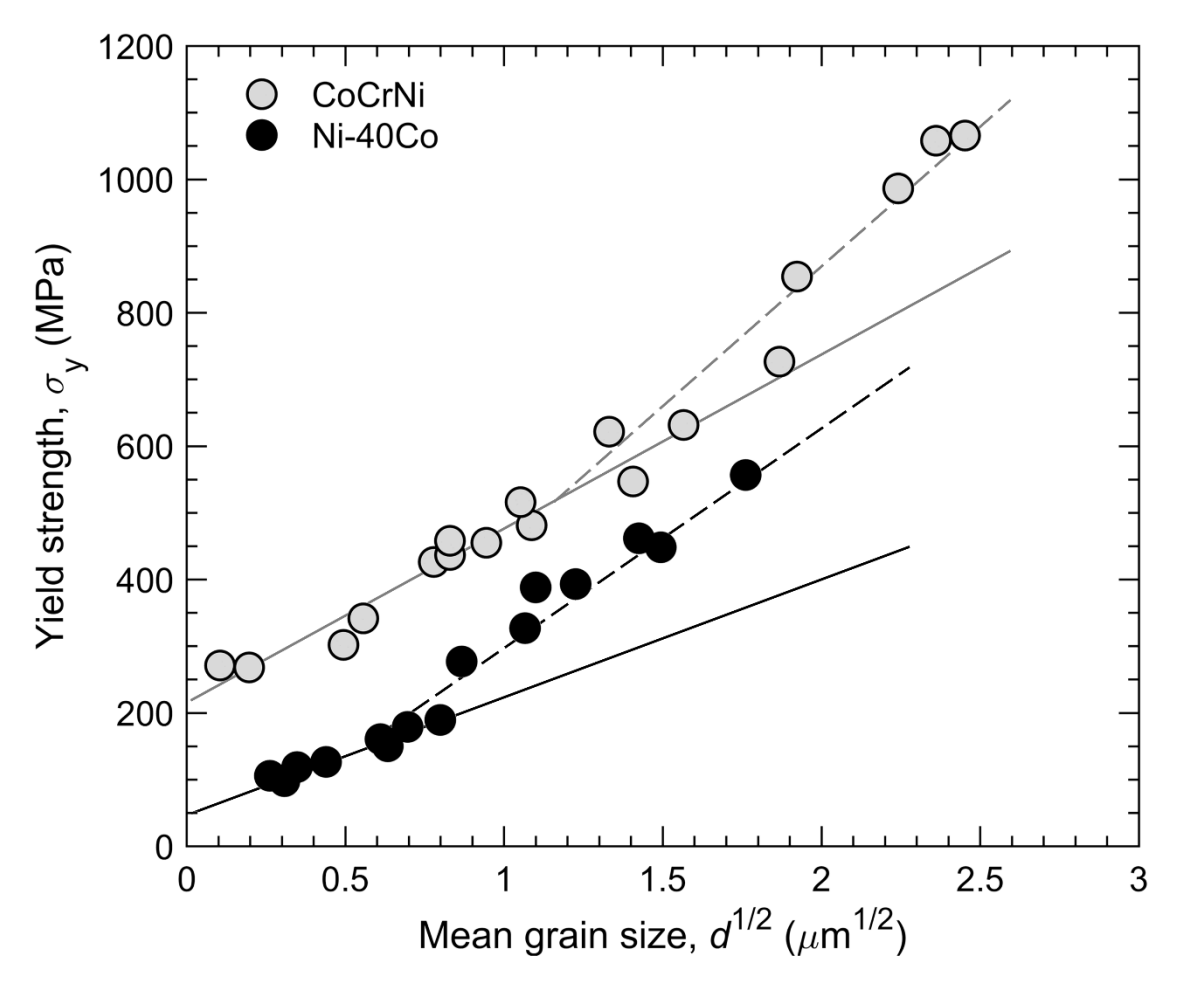


Figure 3.11 The Hall-Petch relation of the CoCrNi and Ni-40Co alloys, with the dashed lines indicating extra hardening at small grain sizes. The solid lines are the linear fitting for the values of  $\sigma_0$  and  $k_S$ , with the data in the extra-hardening region excluded for use [172].

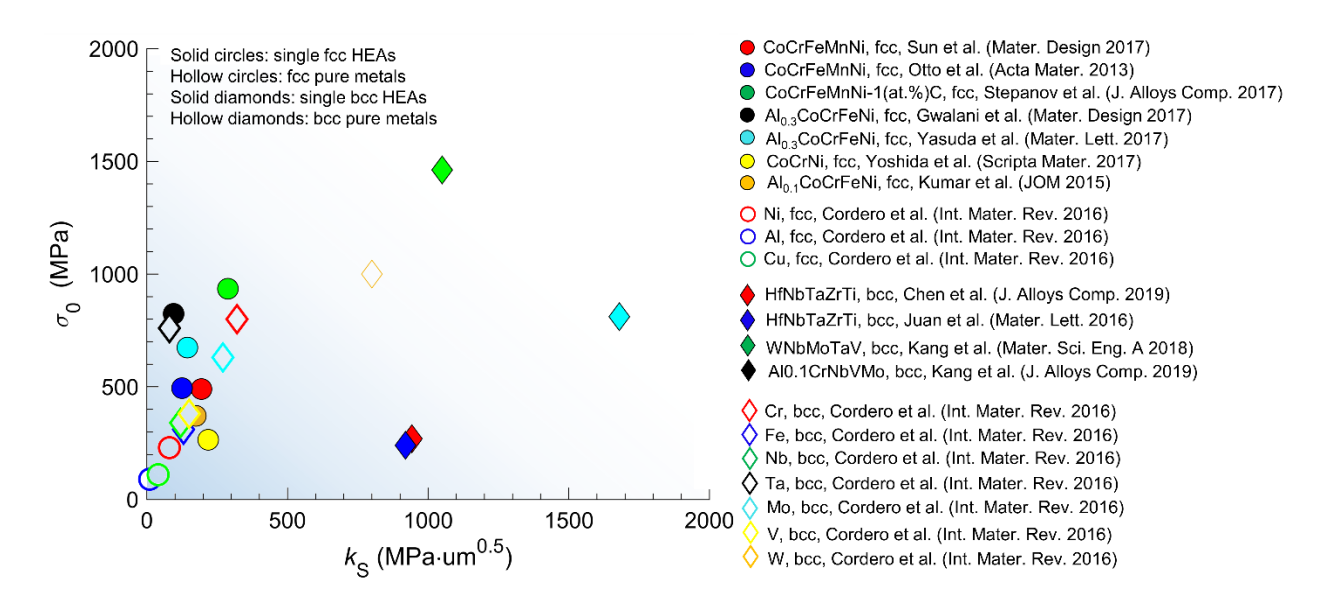


Figure 3.12 The friction stress,  $\sigma_0$ , versus the Hall-Petch coefficient,  $k_S$ , of the alloys listed in Table 3.2. Alongside plotted are the fcc pure metals Ni, Al, and Cu as well as bcc pure metals Cr, Fe, Nb, Ta, Mo, V, and W for comparison [173]

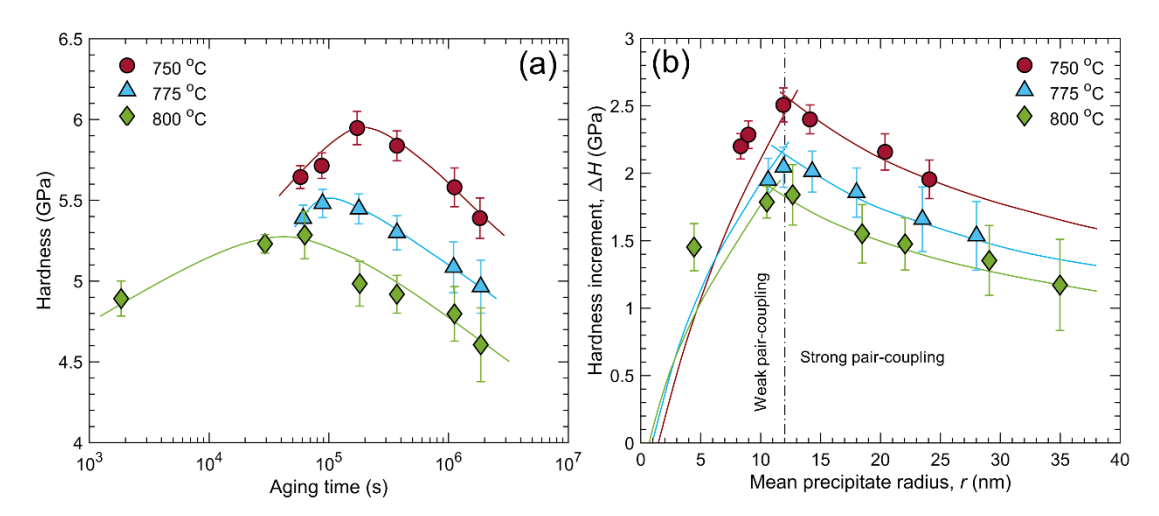


Figure 3.13 Precipitation hardening of the (FeCoNiCr)<sub>94</sub>Ti<sub>2</sub>Al<sub>4</sub> HEA at 750 °C, 775 °C, and 800 °C for varying aging durations [31]. (a) Variation of the nanoindentation hardness with the aging time at three temperatures, with the solid lines delineating the trends. (b) Hardness increment against the average precipitate radius at three temperatures, where the symbols represent measurement data whereas lines are theoretical predictions from Equations. (3.41) and (3.42).

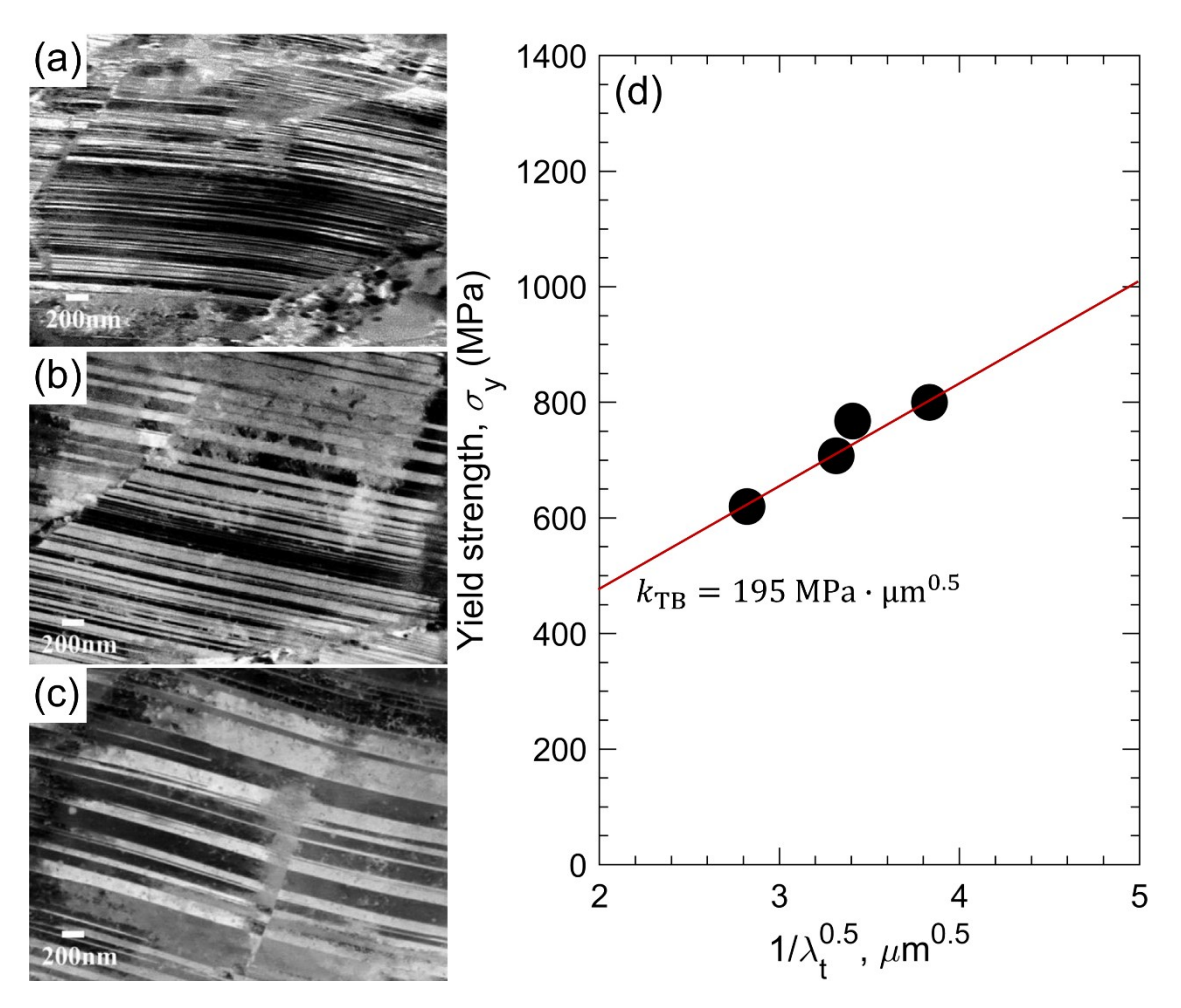


Figure 3.14 Electron channeling contrast (ECC) images of the nano-twins with varying spacing in the interstitial TRIP-TWIP Fe<sub>49.5</sub>Mn<sub>30</sub>Co<sub>10</sub>Cr<sub>10</sub>C<sub>0.5</sub> HEA (with fcc and hcp phases) annealed at (a) 650 °C for 3 min, (b) 650 °C for 10 min, and (c) 750 °C for 3 min. (d) The yield strength,  $\sigma_y$ , as a function of the twining spacing quantity,  $\lambda_t^{-1/2}$ , on which a liner curving fitting is performed to retrieve the twin boundary strengthening coefficient,  $k_{tb}$  [104].

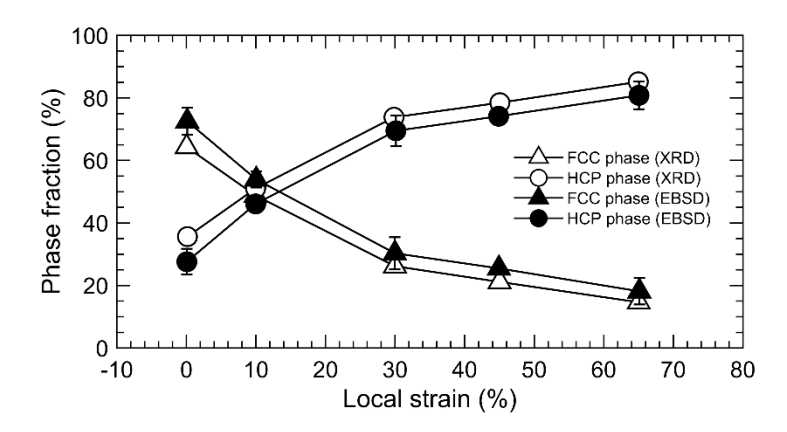


Figure 3.15 The volume fractions of the fcc parent phase and hcp martensitic phase in the  $Fe_{50}Mn_{30}Co_{10}Cr_{10}$  HEA at different local strain levels [96], which are quantified by both the X-ray diffractions and EBSD map.

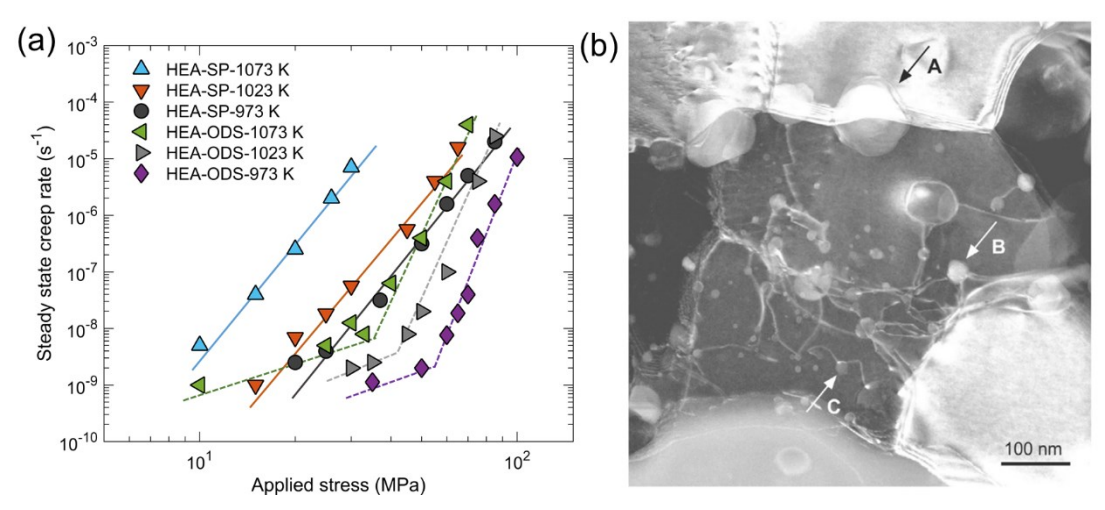


Figure 4.1 (a) Dependence of the creep rates of the HEA-SP and HEA-ODS alloys on the applied stress [245]. (b) STEM HAADF image of the microstructure formed during creep at 1073 K and 67 MPa, for an accumulated strain of 9% [245]. The arrows highlight three locations in which oxide particles interact with a grain boundary (location A), a low-angle dislocation boundary (location B) and an individual dislocation (location C).

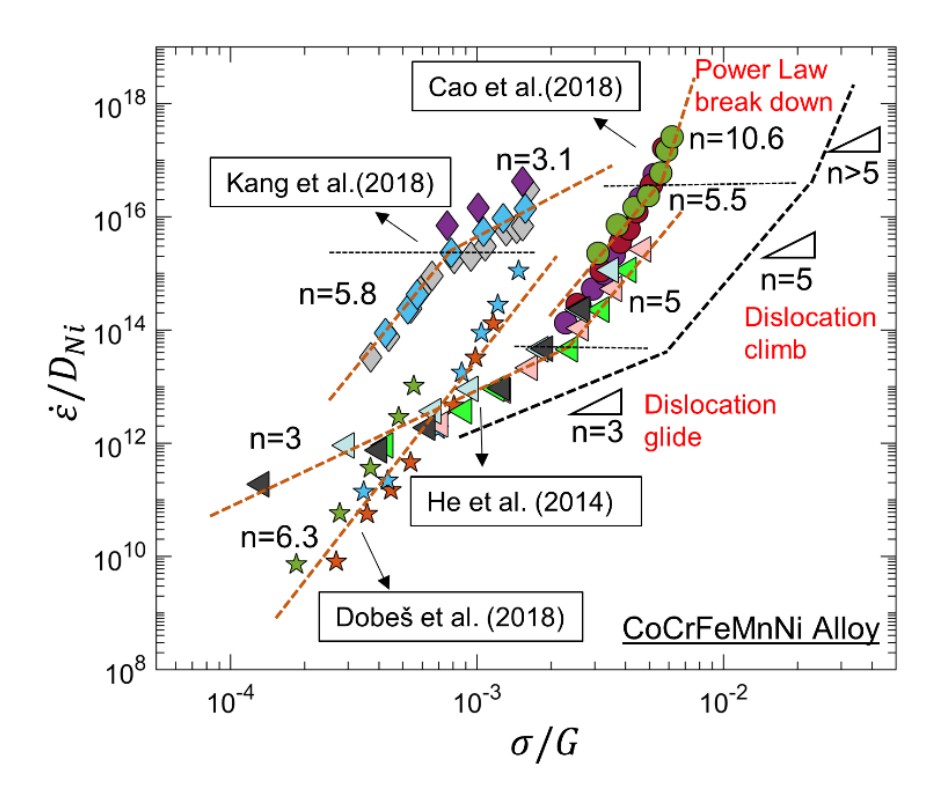


Figure 4.2 Dependence of the normalized creep rates by the diffusion coefficient on the normalized applied stresses for the CoCrFeMnNi alloy [242, 244, 245, 248].

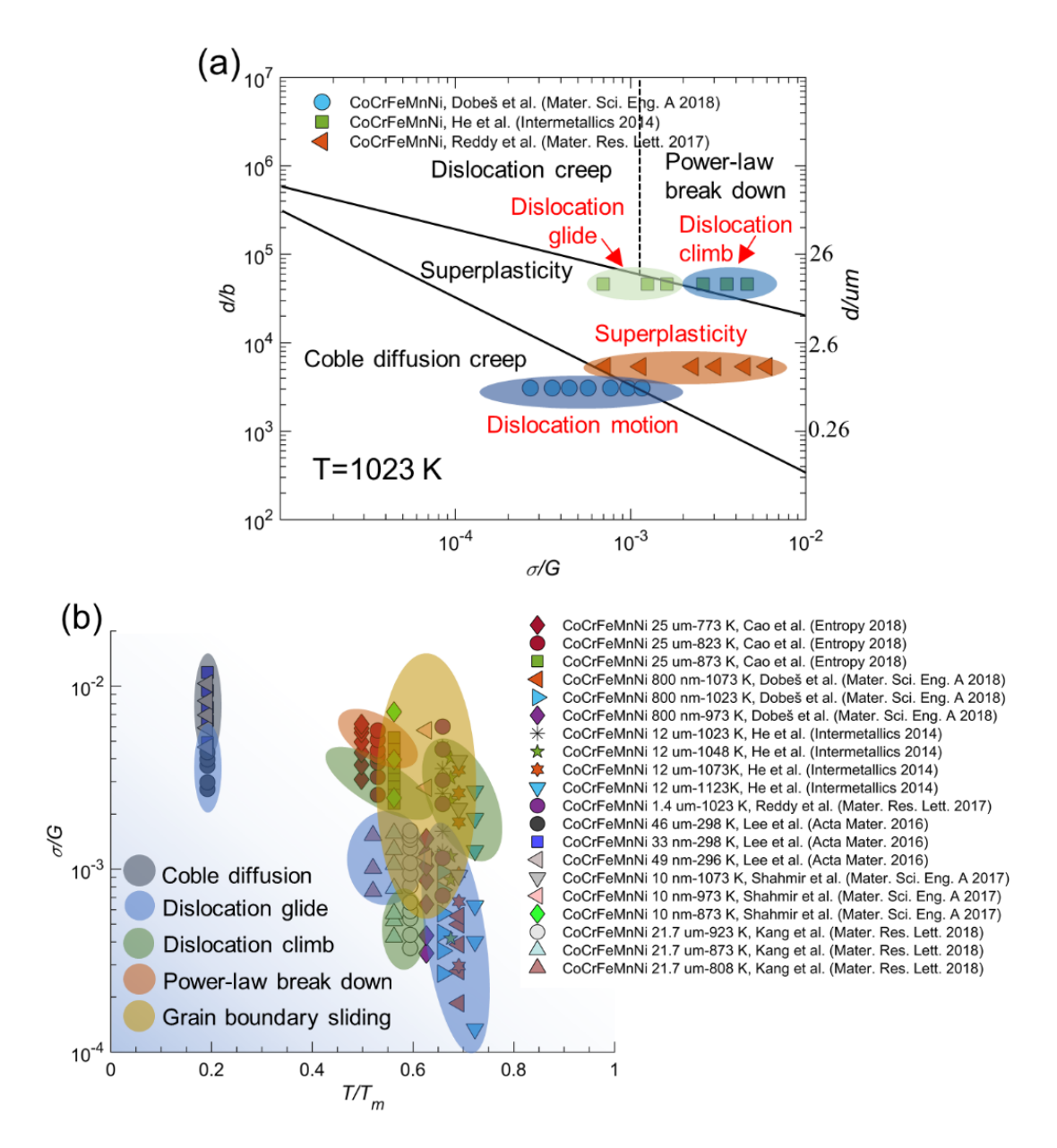


Figure 4.3 (a) Deformation mechanisms for the CoCrFeMnNi alloy [232, 234, 245, 248]. (b) Deformation mechanism map for the CoCrFeMnNi alloy at a fixed temperature of 1023 K [232, 242, 244, 245, 248, 254, 265]. The shaded areas correspond to four different deformation mechanisms in this alloy.

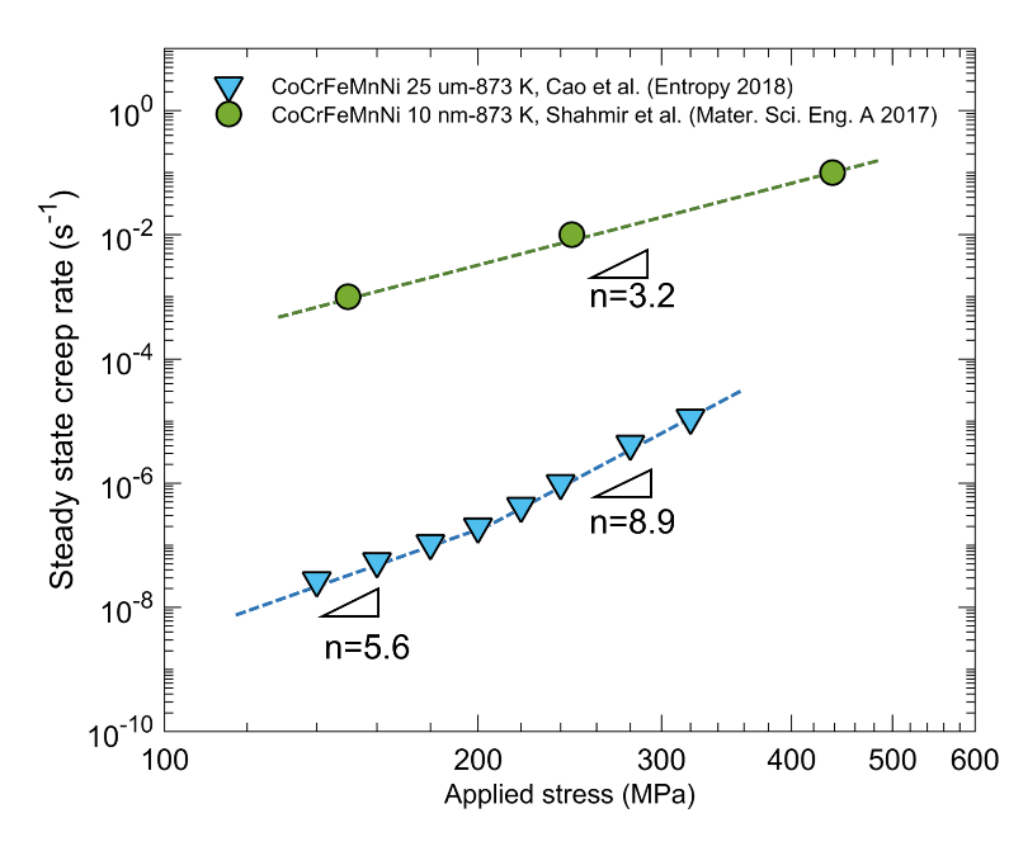


Figure 4.4 Variation of the strain rate with the stress in the CoCrFeMnNi HEA with initial grain sizes of 10 nm and 25  $\mu$ m, tested at 873 K [244, 265].

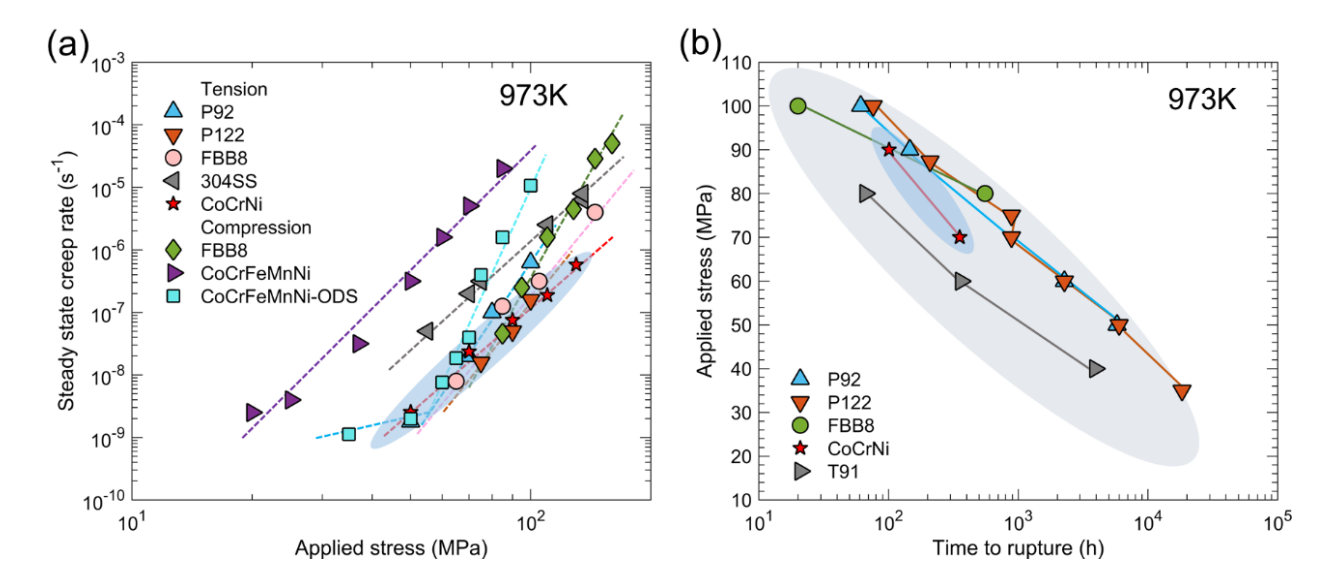


Figure 4.5 Comparison of creep behaviors. (a) Steady-state creep rate versus the applied stress for 304 stainless steel, commercial ferritic steels (P92, P122, and FBB8), CoCrFeMnNi alloy (with/without ODS), and CoCrNi alloy at 973 K [276]. (b) Applied stress versus time to rupture for commercial ferritic steels (P92, P122, T91, and FBB8), and CoCrNi alloy at 973 K [276].

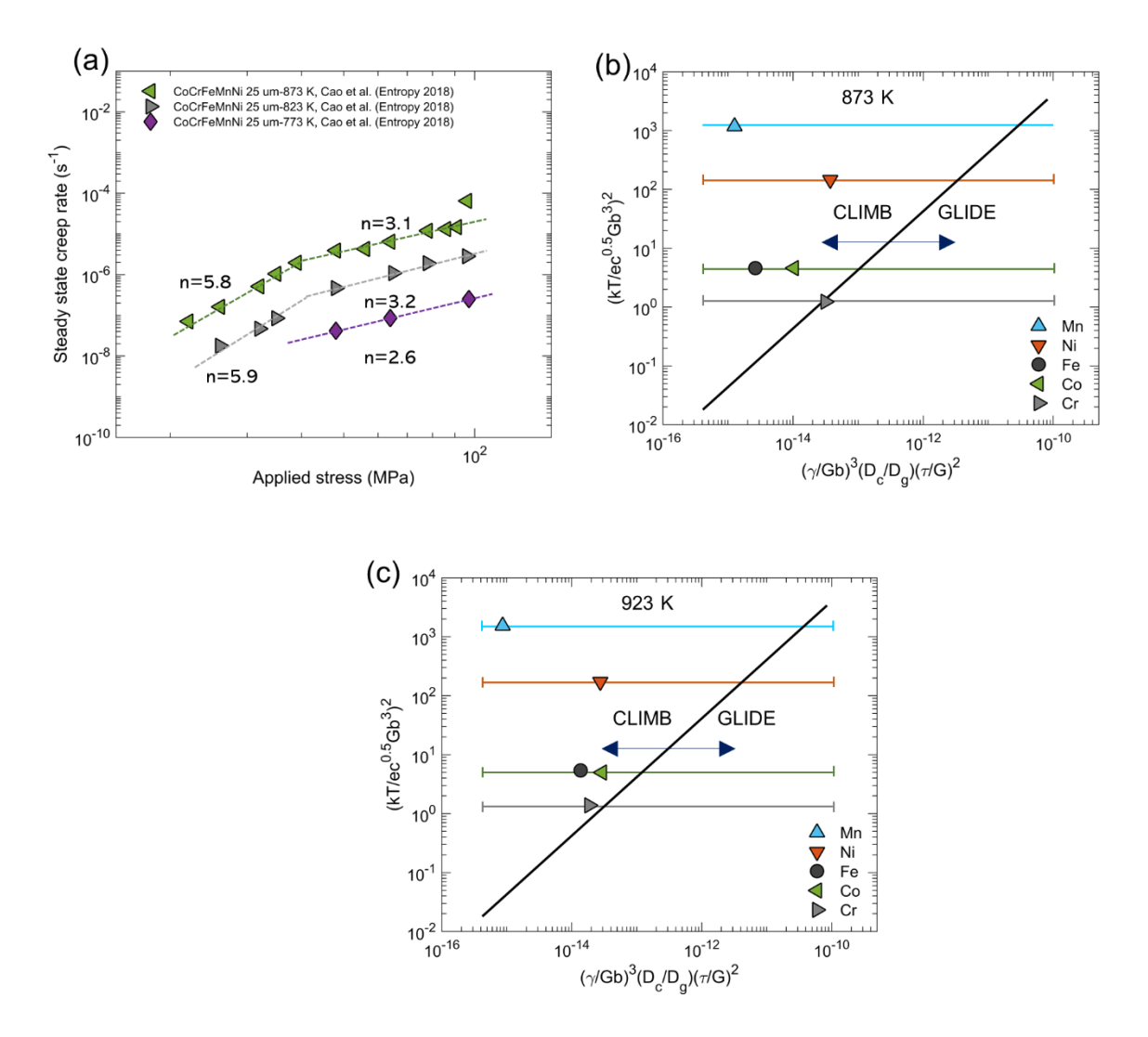


Figure 4.6 (a) The dependence of creep rates on the applied stress in the CoCrFeMnNi alloy.  $(\frac{kT}{ec^{0.5}Gb^3})^2$  versus  $(\frac{\gamma}{Gb})^3 \frac{D_C}{D_g} (\frac{\tau}{G})^2$  on a logarithmic scale at (b) 873 K (c) and 923 K for the CoCrFeMnNi alloy [242].

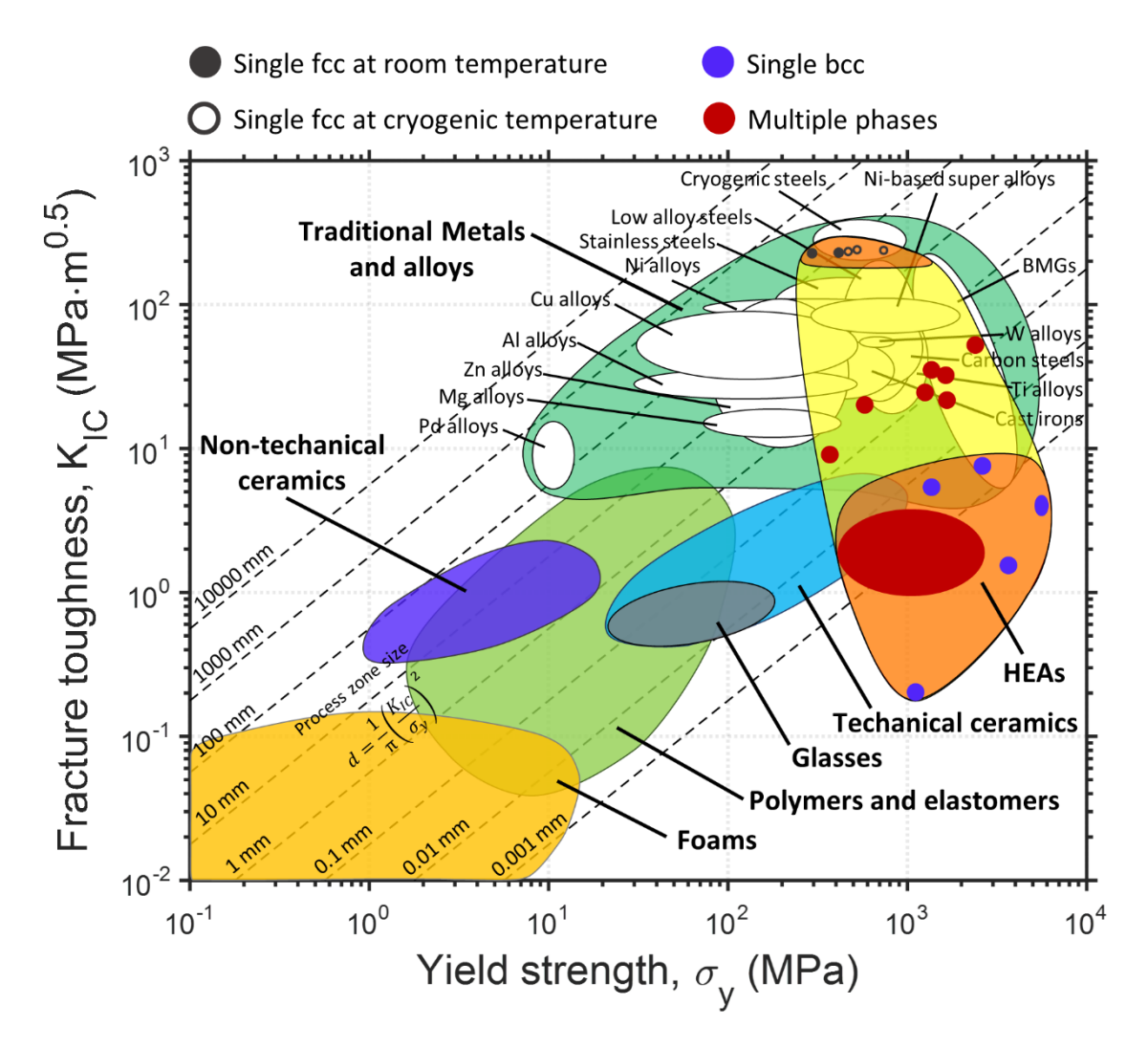


Figure 5.1 Ashby plot of the valid fracture toughness,  $K_{IC}$ , against the yield strength, depicting the damage- tolerance domains of HEAs as well as conventional metals and alloys and other material classes [308]. The dashed lines represent the process-zone size  $\frac{1}{\pi} \left( \frac{K_{IC}}{\sigma_f} \right)^2$  at the crack tip. The graphing of HEA domains is based on the data in Table 5.2, with the  $K_Q$  data and some extreme strengths estimated from  $\sigma_y = \frac{H}{3}$  excluded.

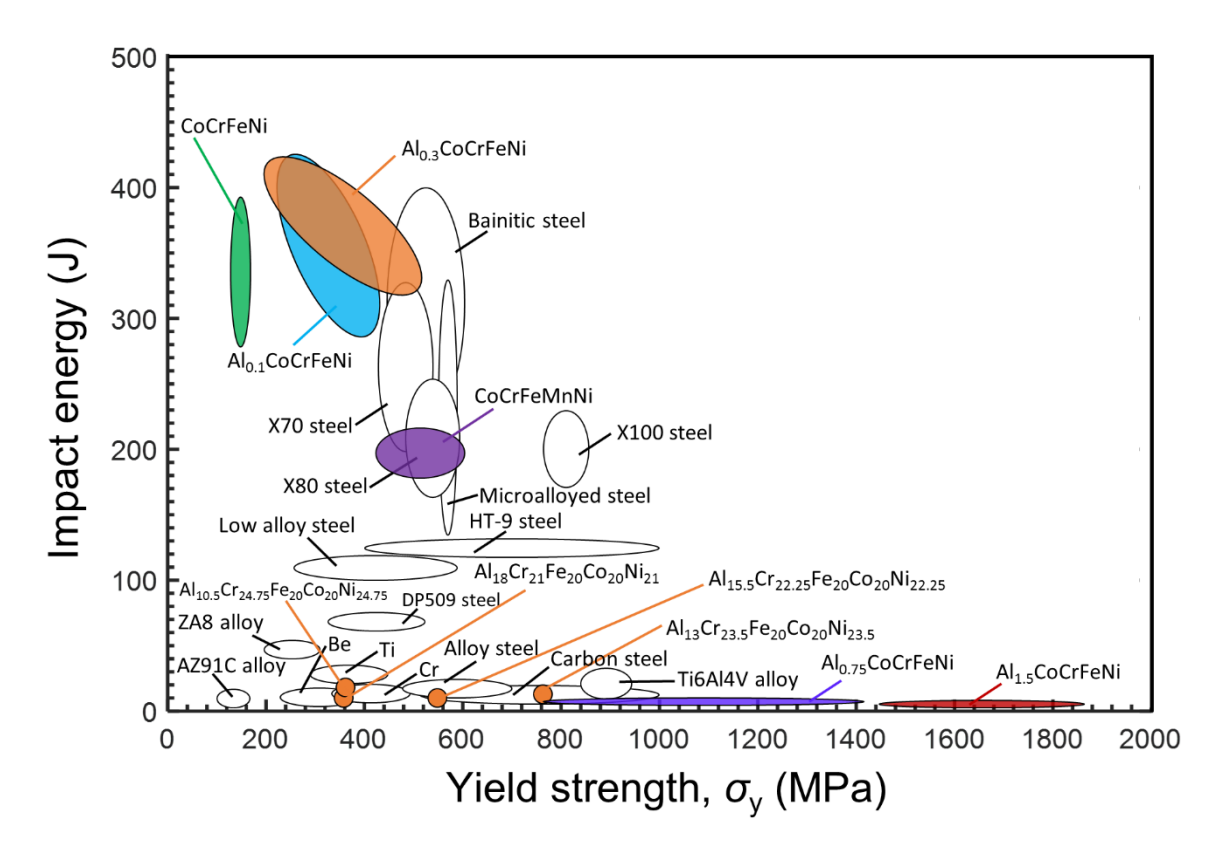


Figure 5.2 Impact energy plotted against the yield strengths for HEAs in comparison with other metals and alloys [308]. The graphing of HEA domains is based on the data in Table 5.1.

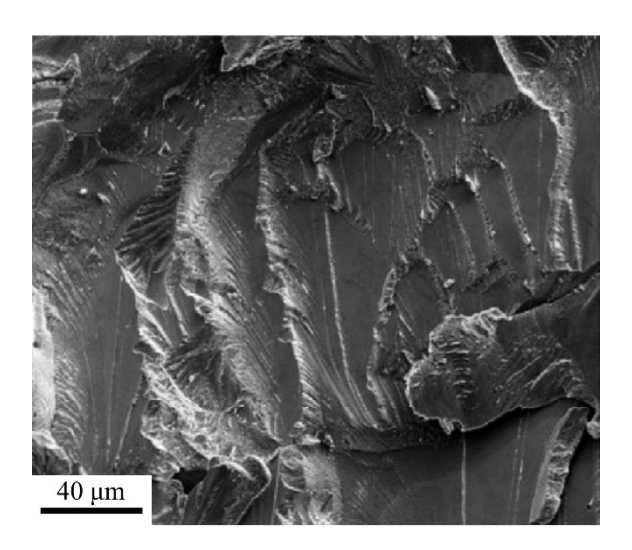


Figure 5.3 Transgranular cleavage with river markings and facets in the Al<sub>1.5</sub>CoCrFeNi HEA with bcc and B2 phases failed at room temperature [293].

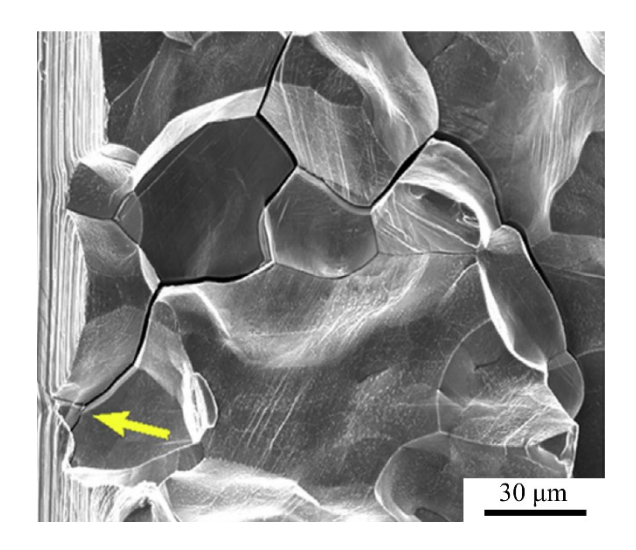


Figure 5.4 Intergranular fracture in the bcc TiZrNbTa HEA failed at room temperature [304].

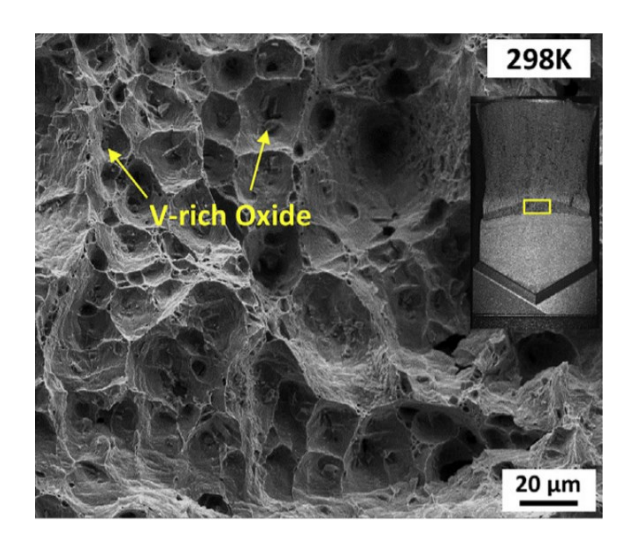


Figure 5.5 Hybrid fracture blending dimples and cleavage in the AlCoCrFeNi HEA with a fcc phase and two distinct bcc phases failed at room temperature [305].

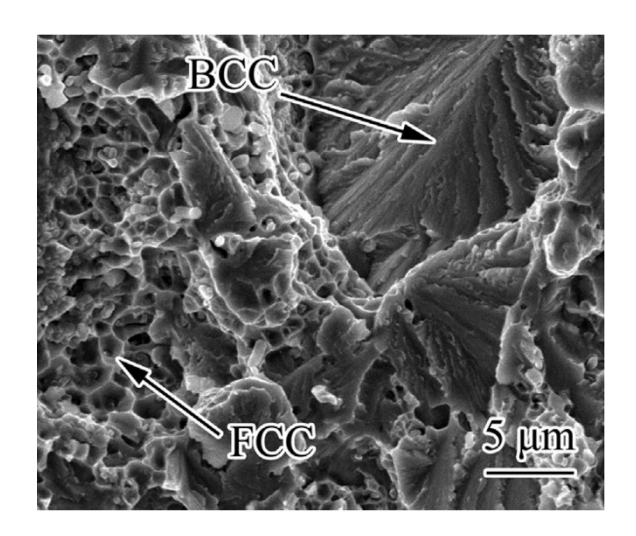


Figure 5.6 Ductile fracture characteristic of numerous dimples in the fcc CoCrFeNiMo HEA [315], failed at room temperature.

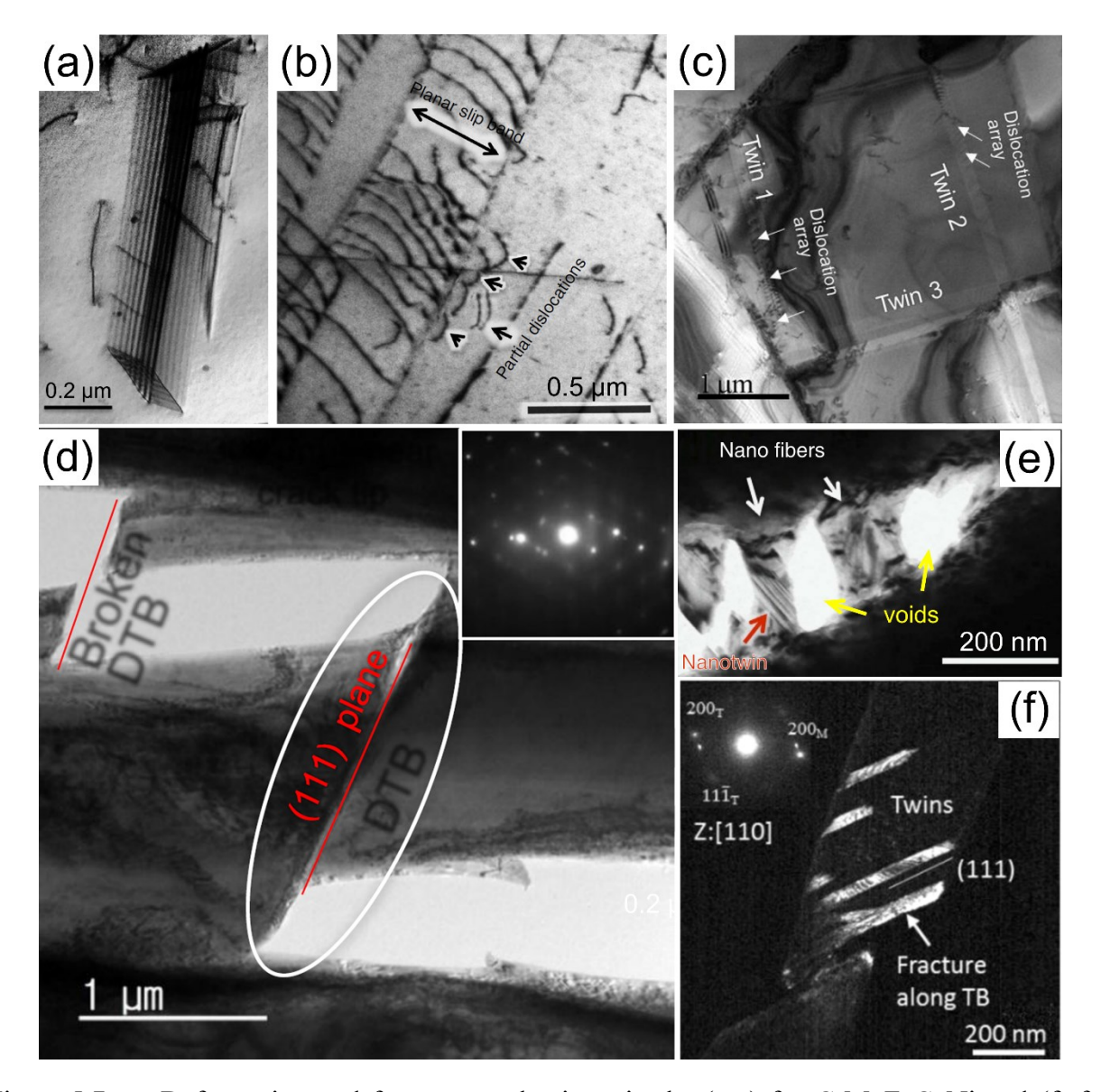


Figure 5.7 Deformation and fracture mechanisms in the (a-e) fcc CrMnFeCoNi and (f) fcc Fe<sub>40</sub>Mn<sub>40</sub>Co<sub>10</sub>Cr<sub>10</sub> revealed by in-situ TEM observations. (a) Formation of a stacking-fault parallelepiped, with faces lying on three sets of {111} planes [312]. (b) Blockage of fast-moving partial dislocations by planar slip bands of perfect dislocations [312]. (c) Dislocation arrays are made sessile by being enclosed inside Twin 1 and Twin 2 [313]. (d) Deflection and blockage of the propagating crack at deformation twin boundaries [313]. (e) Crack bridging [312]. (f) Crack propagation along the twin boundary [314].

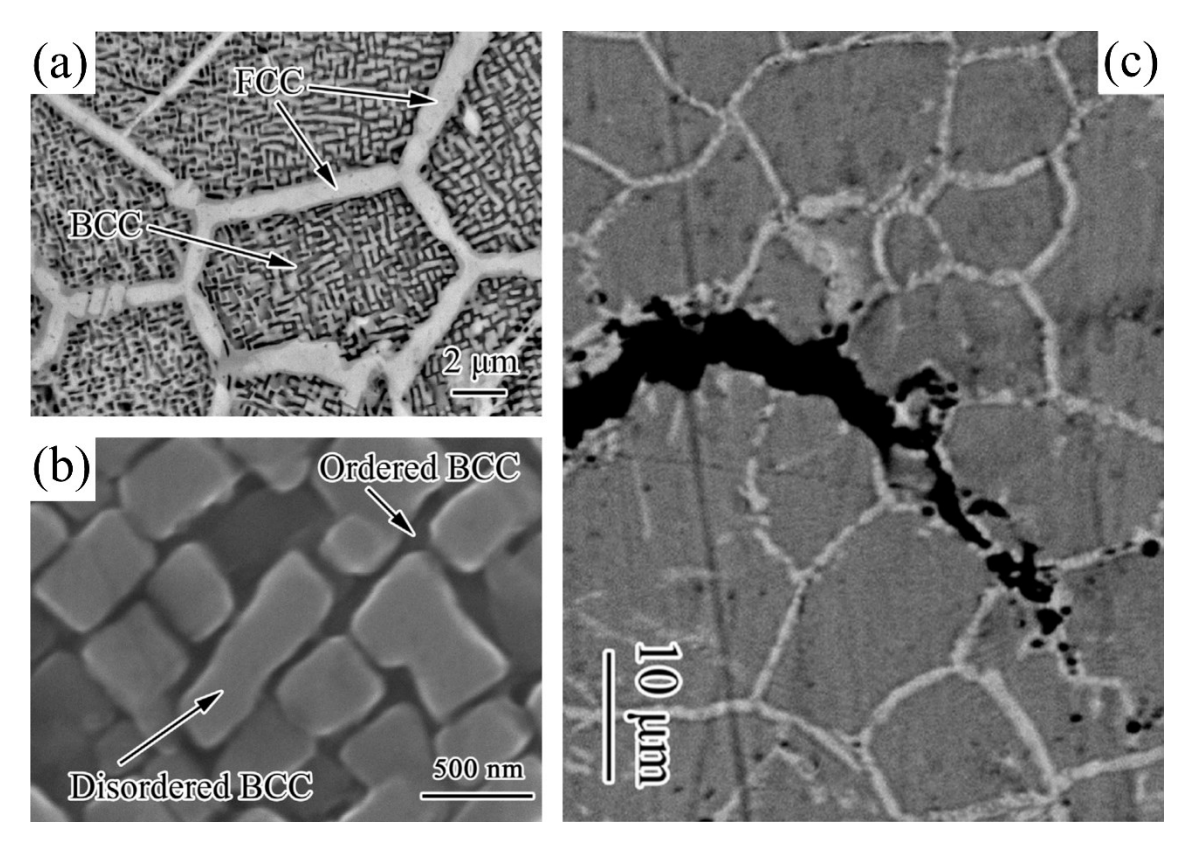


Figure 5.8 (a) Back-scattered image (BEI) of the overall microstructure of the spark-plasma-sintered AlCoCrFeNi HEA consisting of spinodally modulated bcc regions enclosed by fcc "nets" [305]. (b) Secondary electron image (SEI) of the magnified bcc region revealing a spinodally modulated structure composed of ordered and disordered bcc phases [305]. (c) Crack propagation trajectory observed in a fracture test [305].

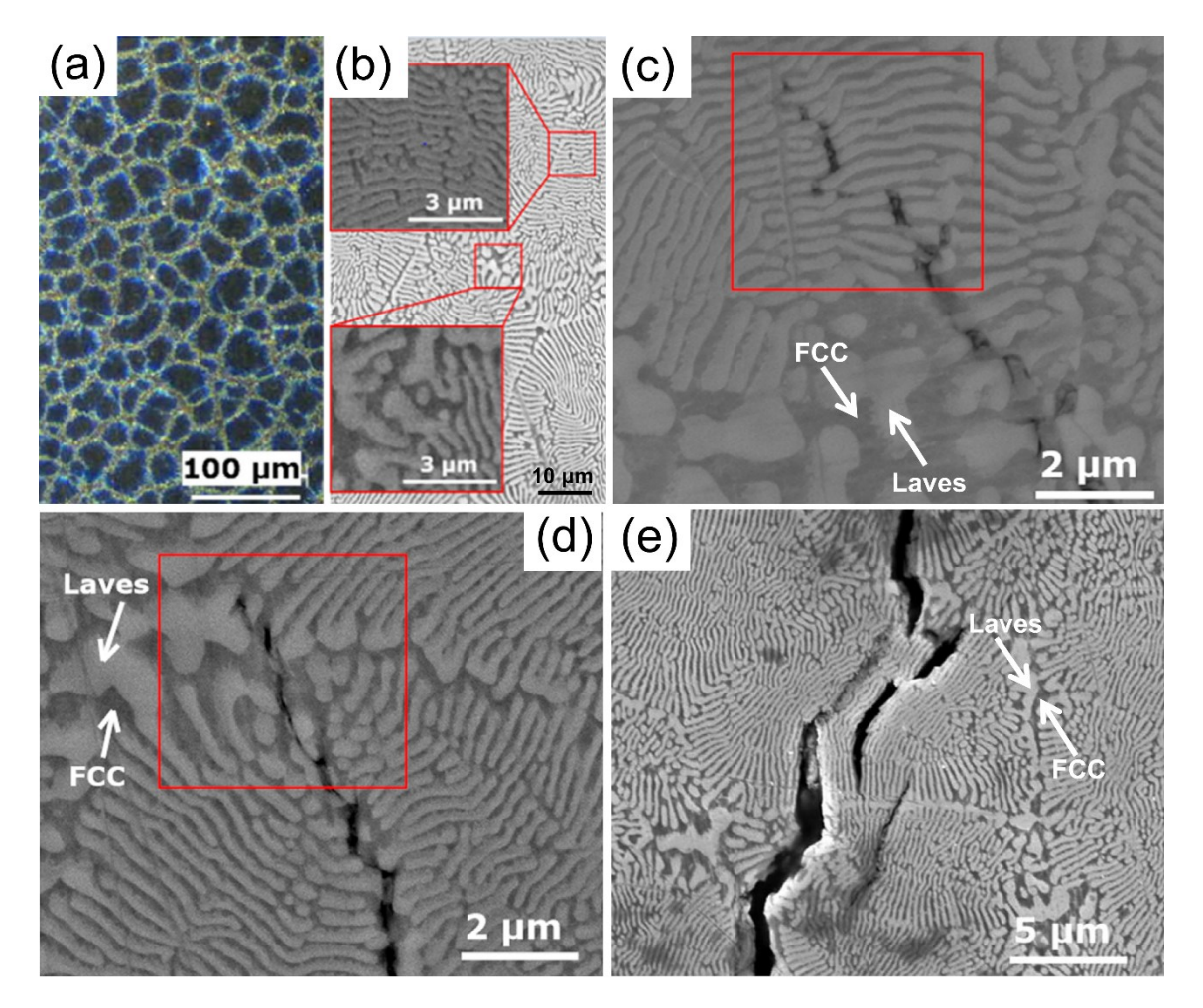


Figure 5.9 Microstructures and crack propagation in the CoCrFeNiNb<sub>0.5</sub> HEA with hierarchical, lamellar eutectic Laves and fcc phases [300]. (a) The dark field optical microscopy (OM) image of the eutectic structure. (b) Scanning electron microscopy (SEM) image of the eutectic structure with the top and bottom insets showing the fine and coarse lamella regions, respectively. The crack propagation paths in the (c) fine lamella region and (d) coarse lamella region, which contribute to intrinsic toughening. (e) Extrinsic toughening by crack deflection and bridging.

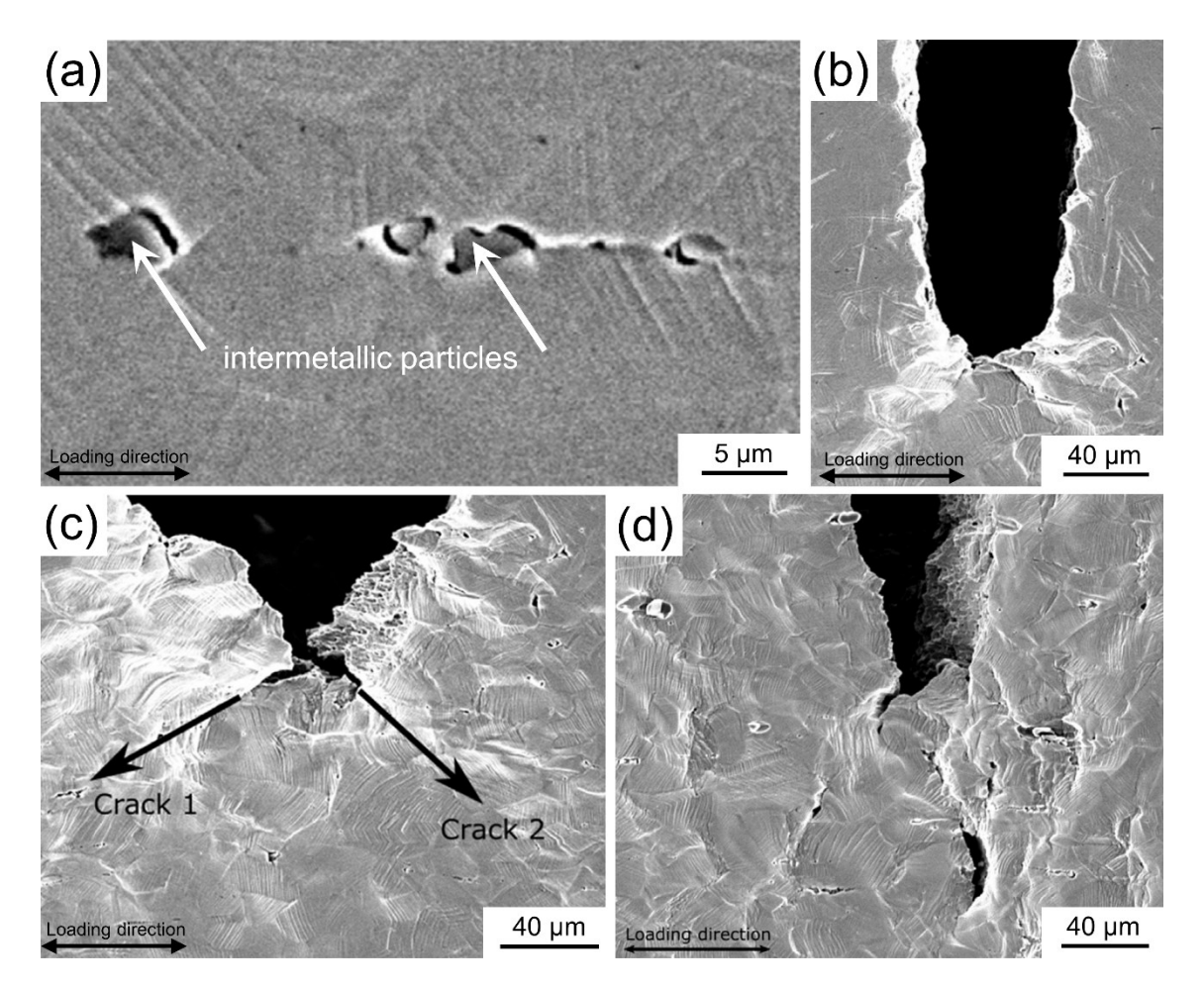


Figure 5.10 Crack initiation and propagation in the CoCrFeNiMo<sub>0.2</sub> HEA with a fcc matrix and Cr-rich precipitates [310]. (a) SEM observation of microvoid nucleation by the debonding of the Cr-rich intermetallic particles. (b) Crack tip blunting by plastic deformation. (c) Crack branching. (d) Formation of the tortuous crack propagation path by merging microcracks (evolved from microvoids) into the main crack.

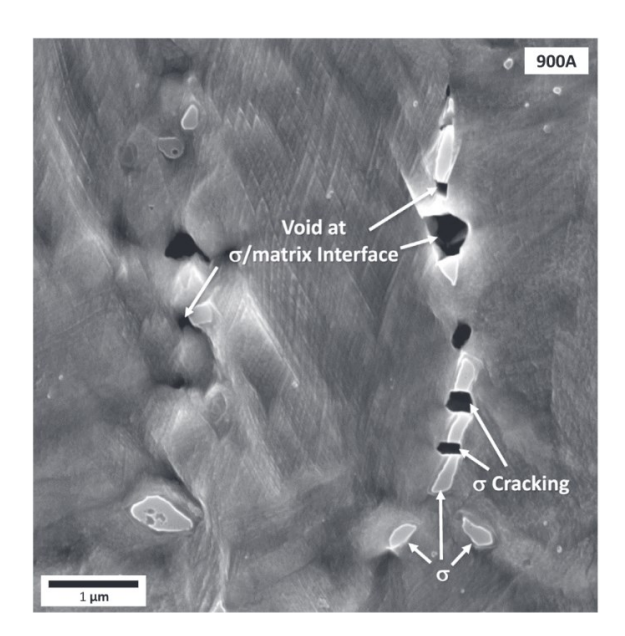


Figure 5.11 Crack initiation by precipitate-matrix deboning and the breakage of brittle  $\sigma$  precipitates in the precipitate-containing CrFeNiV HEA, which fractured in a ductile fashion [316].

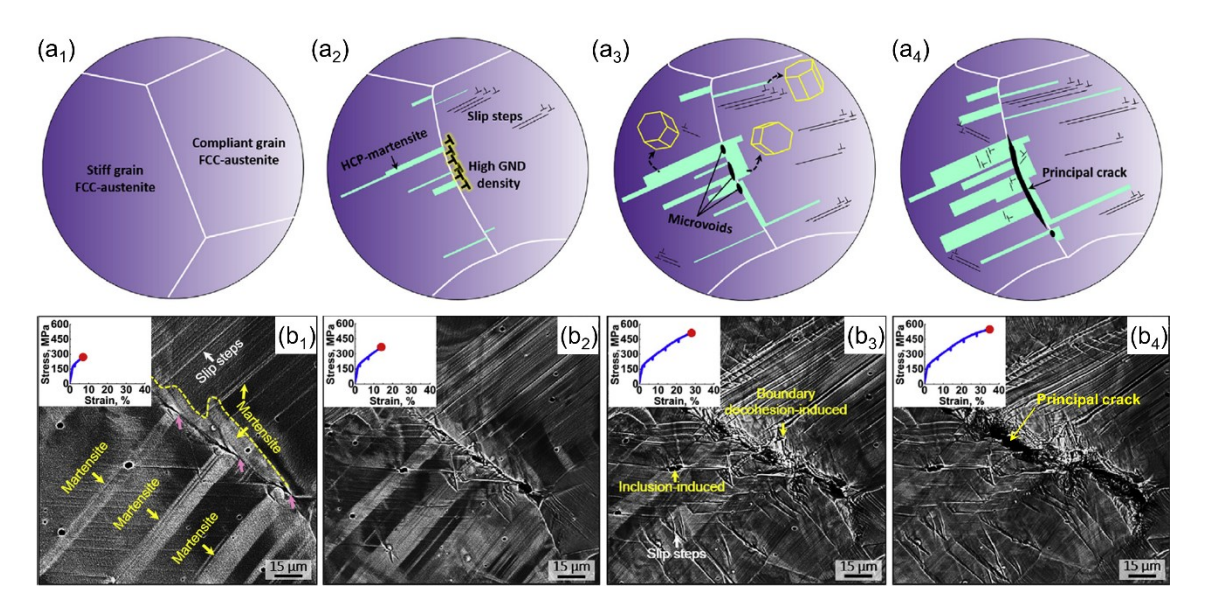


Figure 5.12 Cracking formation in the mechanically metastable (FCC $\square$ HCP martensitic transformation) Fe<sub>45</sub>Mn<sub>35</sub>Co<sub>10</sub>Cr<sub>10</sub> HEA [317]. (a) Schematics and (b) in-situ SEM images progressively showing the cracking mechanism at the grain boundary, triggered by the asynchronous phase transformation in two adjacent grains of different crystallographic orientations.

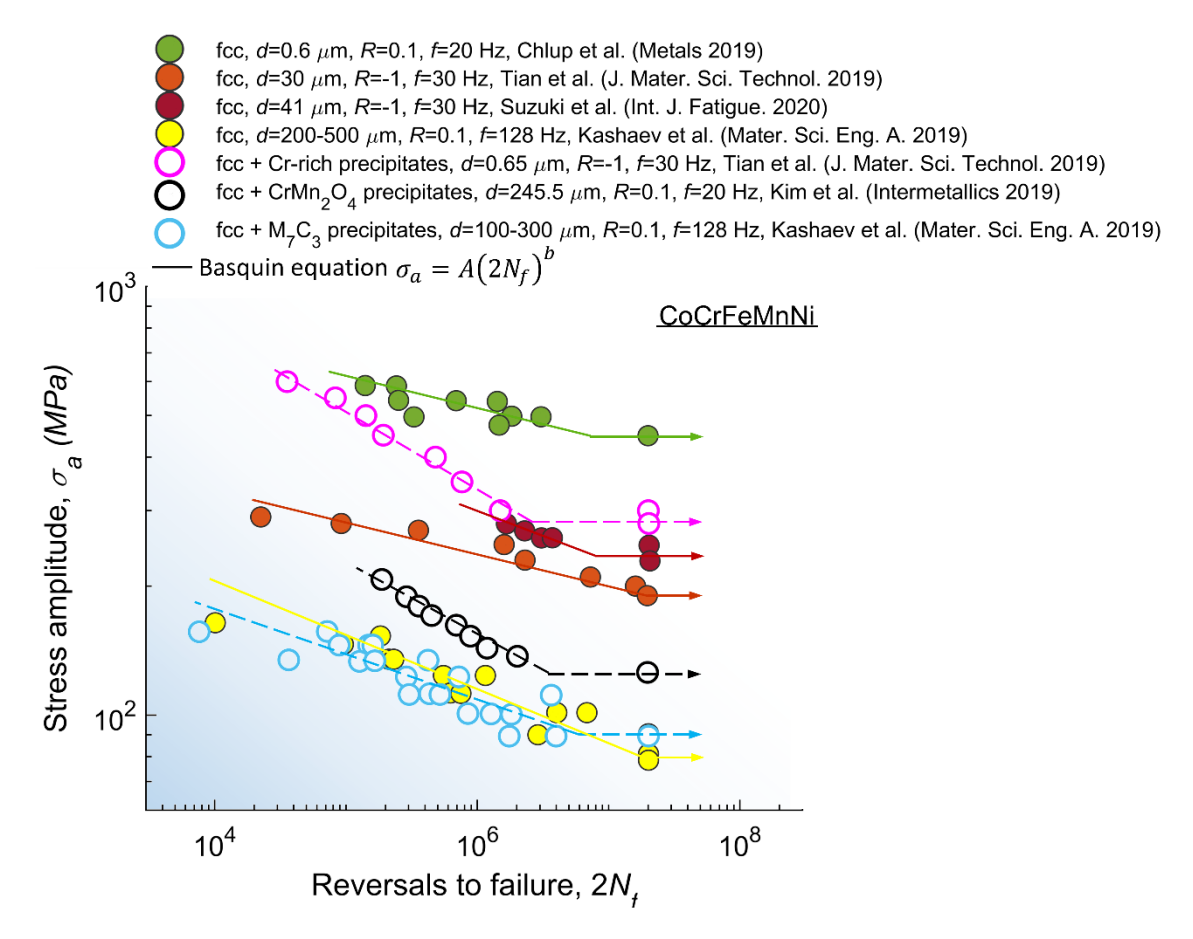


Figure 6.1 S - N data, in terms of the stress amplitude  $\sigma_a$  against the number of reversals to failure  $2N_f$ , of the CoCrFeMnNi HEAs tested at different conditions, lines indicating the Basquin fits. Associated alloy and testing information is found in Table 6.1.

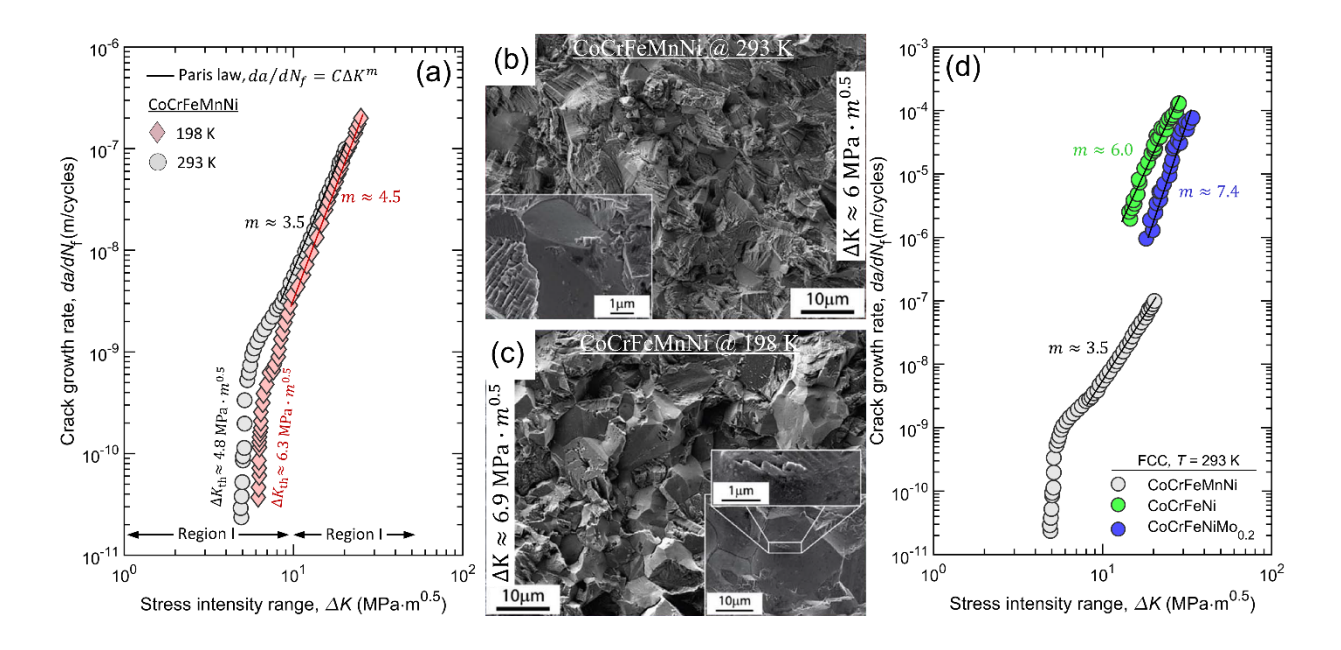


Figure 6.2 (a) Fatigue crack growth rate,  $\frac{da}{dN}$ , versus the applied stress intensity range,  $\Delta K$ , of the CoCrFeMnNi HEA at 293 K and 198 K [324]. Fractographs of the CoCrFeMnNi HEA fatigued at (b)  $\Delta K \approx 6 \, MPa \cdot m^{0.5}$  and 293 K and (b)  $\Delta K \approx 6.9 \, MPa \cdot m^{0.5}$  and 198 K [324]. (c) Comparison of the fatigue crack growth rates of three fcc HEAs, namely, the CoCrFeN, CoCrFeNiMo<sub>0.2</sub> and CoCrFeMnNi at room temperature. Lines are the Paris-law fits, and  $\Delta K_{th}$  is the threshold stress intensity range. Other details about the alloys and fatigue tests can be found in Table 6.2.

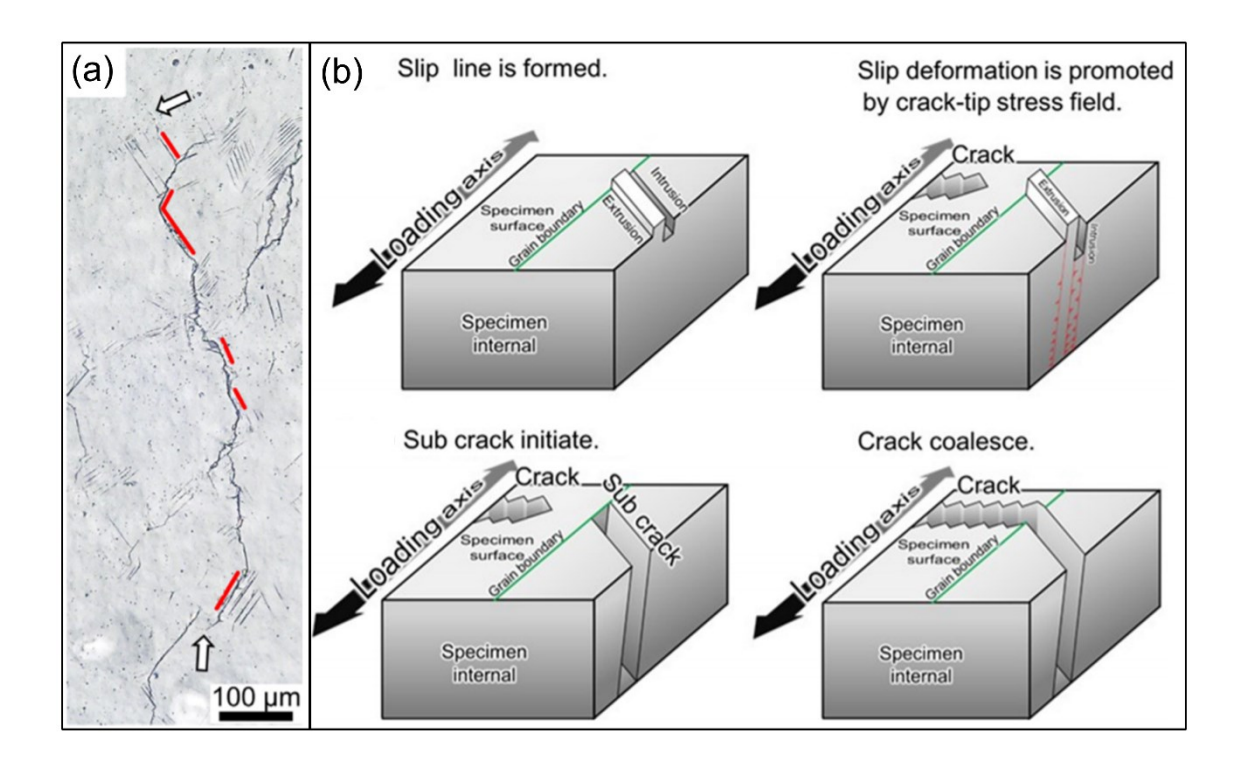


Figure 6.3 Planar-slip governed fatigue mechanism in the fcc CoCrFeMnNi HEA [489]. (a) Concurrent fatigue crack nucleation and propagation along multiple planar slip lines, as indicated red lines. Microcracks formed at slip lines merge subsequently, leading to crack tips indicated by two white arrows. (b) Schematic illustration of fatigue crack propagation in a zig-zag fashion promoted by slip planarity.

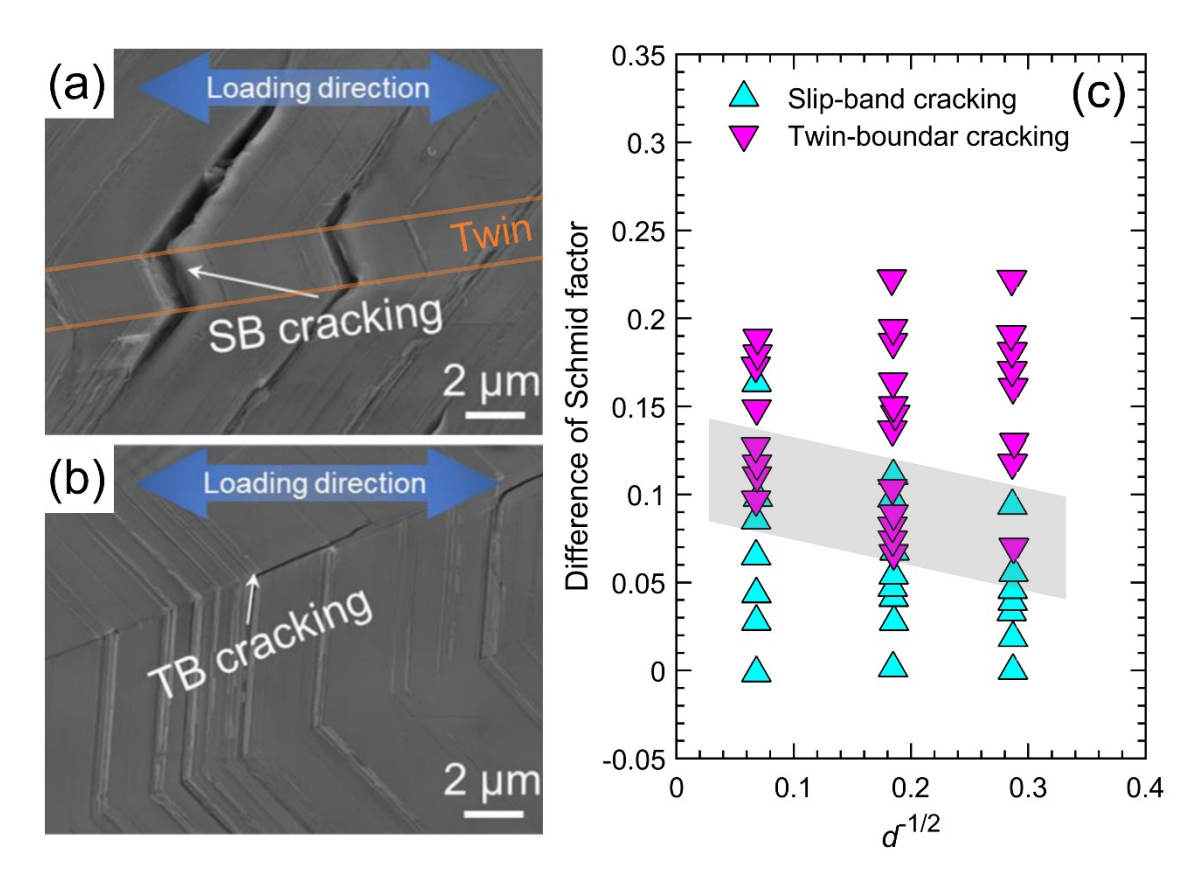


Figure 6.4 Competition between planar slip-band cracking and twin-boundary cracking in the fatigue of the CoCrFeMnNi HEA [331]. SEM images of (a) planar slip-band cracking with apparent extrusions/intrusions and (b) twin-boundary cracking. (c) The influence of Schmid factor difference and grain size on the competition between slip-band cracking and twin-boundary cracking.

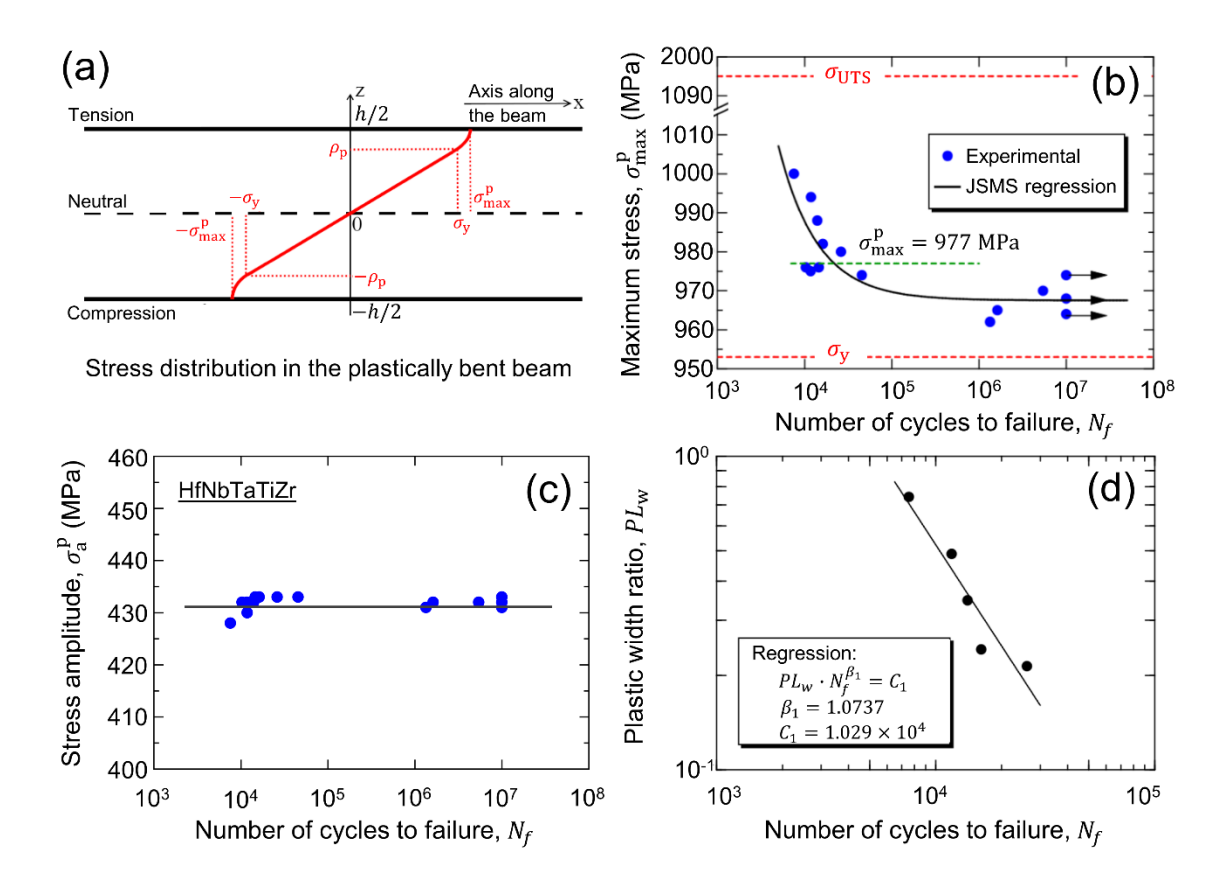


Figure 6.5 High-cycle fatigue behavior of the plastically deformed bcc HfNbTaTiZr HEA [332]. (a) Schematic stress distribution in a plastically bent beam, where the plastic zones range from  $\rho_P$  to  $\frac{h}{2}$  and from  $-\rho_P$  to  $-\frac{h}{2}$ . S-N data plotted in terms of (b) the maximum plastic stress  $\sigma_{max}^p$  versus the number of cycles to failure  $N_f$ , and (c) the stress amplitude  $\sigma_a^p$  versus  $N_f$ . (d) Variation of the plastic width ratio,  $Pl_w = 1 - \frac{\rho_p}{\frac{h}{2}}$ , with  $N_f$  at  $\sigma_{max}^p > 977$  MPa, i.e., the data above the dashed line in (b).

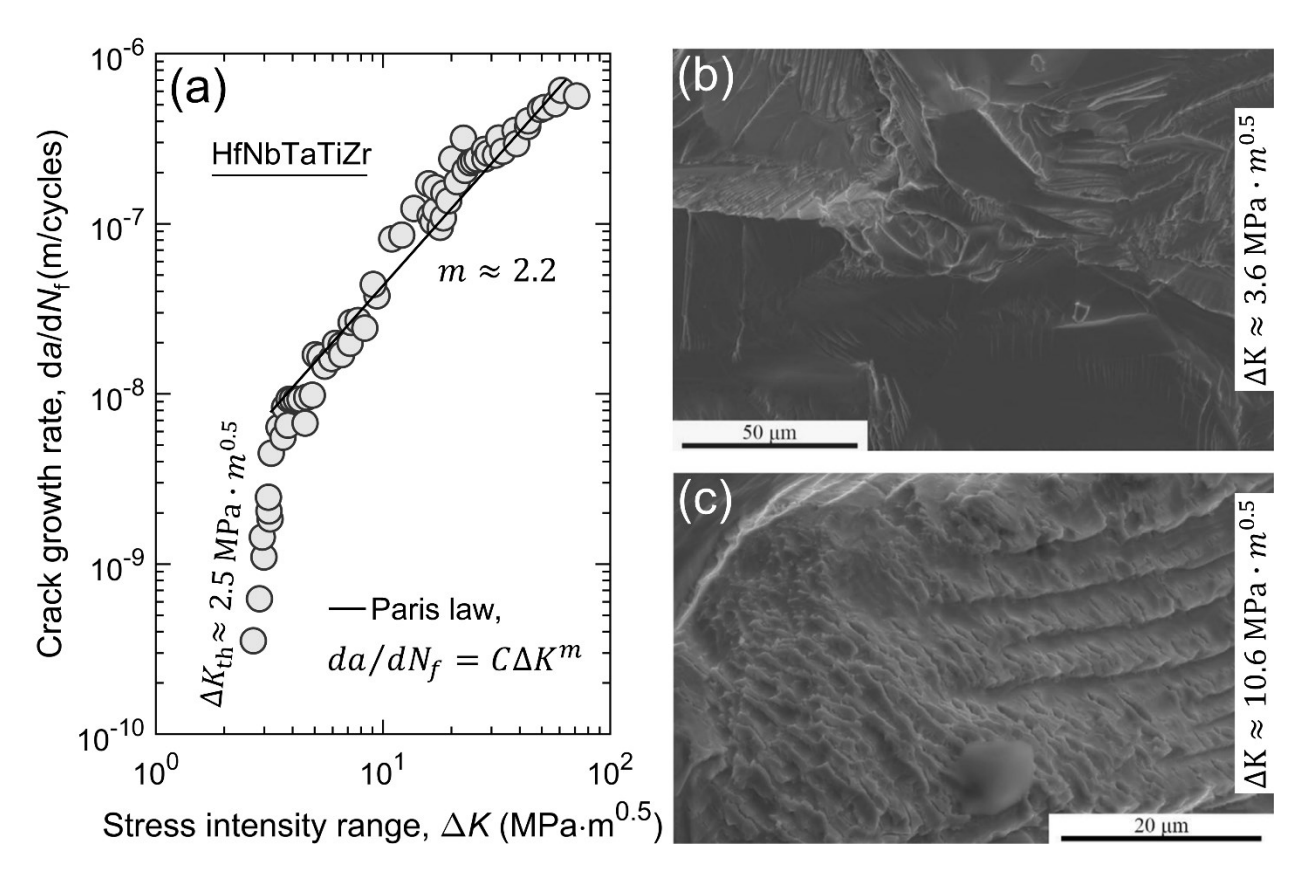


Figure 6.6 High-cycle fatigue in the bcc HfNbTaTiZr HEA [335]. (a) Crack growth rate. Fractographs at (b)  $\Delta K = 3.6 \, MPa$  and (c)  $\Delta K = 10.6 \, MPa$ .

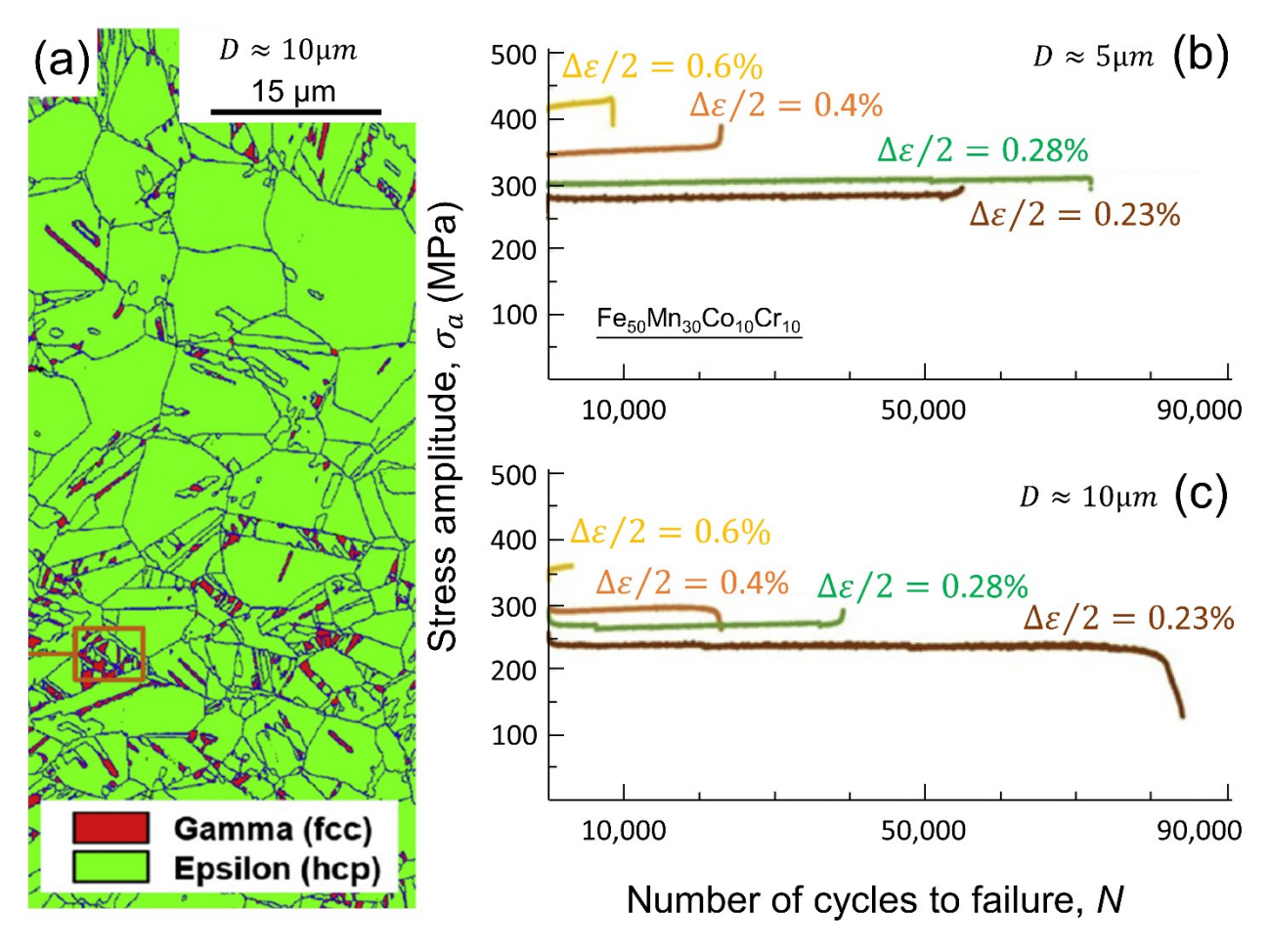


Figure 6.7 Low-cycle fatigue behavior of the metastable Fe<sub>50</sub>Mn<sub>30</sub>Co<sub>10</sub>Cr<sub>10</sub> HEA [101]. (a) Upon cyclic deformation at a strain amplitude  $\frac{\Delta \varepsilon}{2} = 0.6\%$ , about 95 vol% metastable fcc phase ( $\gamma$ ) transforms into the hcp martensite phase ( $\varepsilon$ ) in the coarse-grained HEA with an average grain size of ~10 µm, who originally contains less than 1 vol%  $\varepsilon$ . Stress amplitude  $\sigma_a$  against the number of fatigue cycles N at the strain amplitude 0.23%  $\leq \frac{\Delta \varepsilon}{2} \leq 0.6\%$  for (b) the fine-grained HEA with an average grain size of 5 µm and (c) the coarse-grained HEA with an average grain size of 10 µm.

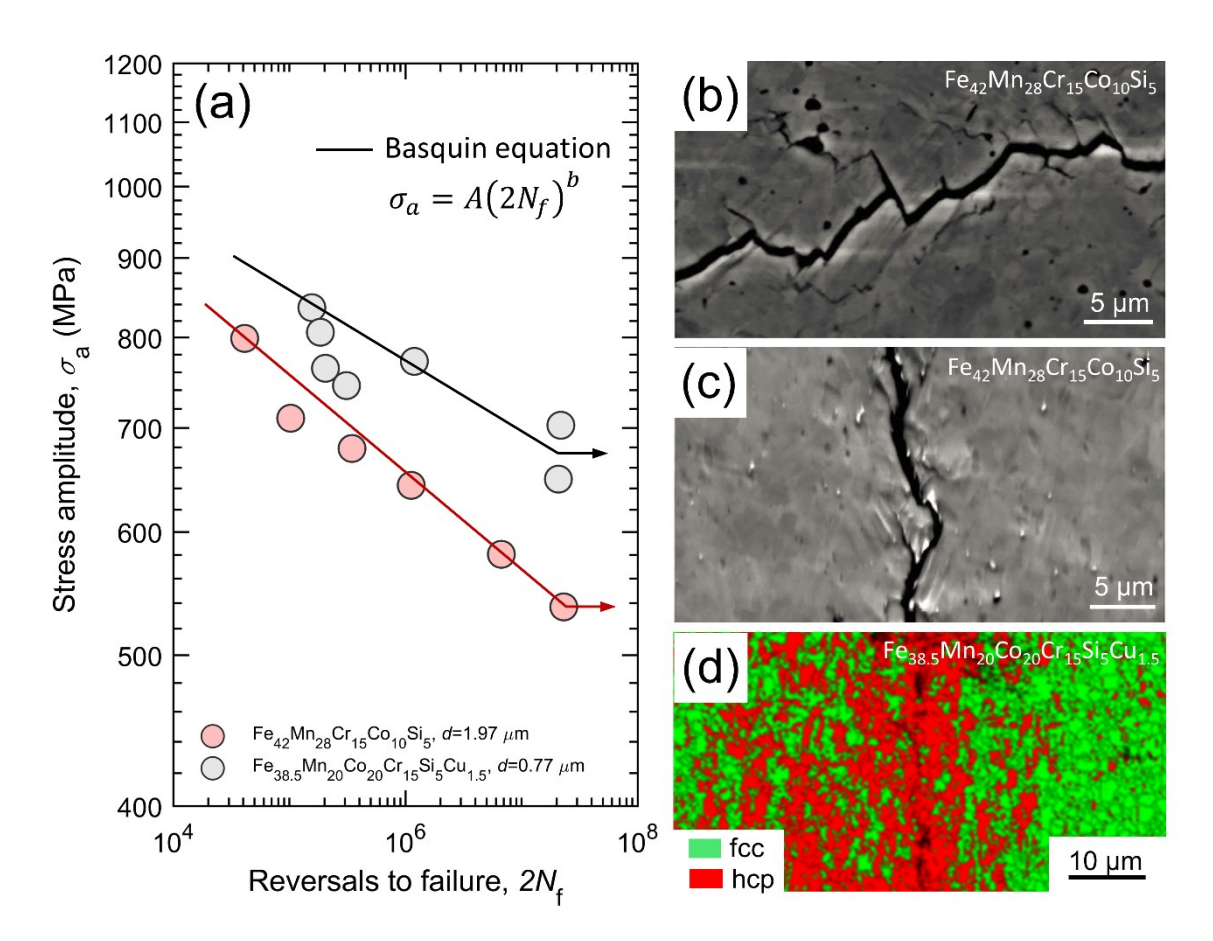


Figure 6.8 High-cycle fatigue behaviors of the metastable Fe<sub>42</sub>Mn<sub>28</sub>Cr<sub>15</sub>Co<sub>10</sub>Si<sub>5</sub> with a mean grain size of 1.97 µm [91] and Fe<sub>38.5</sub>Mn<sub>20</sub>Co<sub>20</sub>Cr<sub>15</sub>Si<sub>5</sub>Cu<sub>1.5</sub> with a mean grain size of 0.77 µm [336]. (a) *S-N* data in terms of the stress amplitude  $\sigma_a$  against reversals to failure  $2N_f$ , the lines indicating the Basquin fits. Crack propagation trajectories in the Fe<sub>42</sub>Mn<sub>28</sub>Cr<sub>15</sub>Co<sub>10</sub>Si<sub>5</sub> HEA [91], revealing (b) crack deflection and branching and (c) crack branching along the twin boundaries. (d) EBSD phase map at the vicinity of the crack tip of the Fe<sub>38.5</sub>Mn<sub>20</sub>Co<sub>20</sub>Cr<sub>15</sub>Si<sub>5</sub>Cu<sub>1.5</sub> HEA [336].

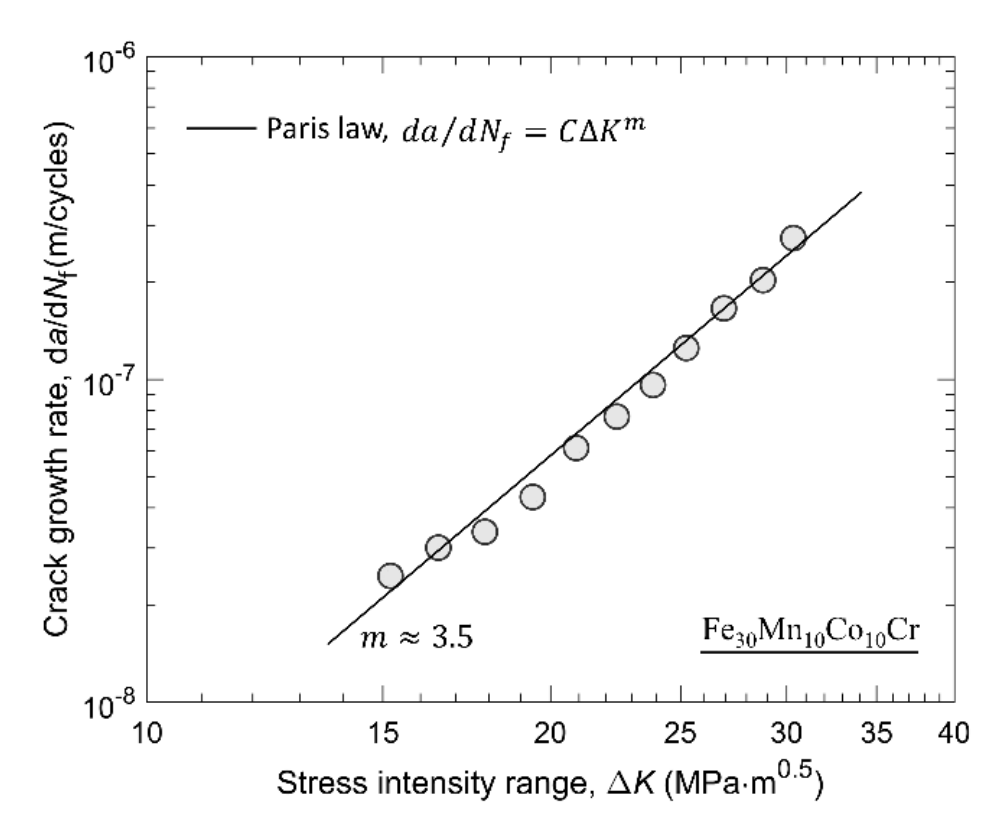


Figure 6.9 Fatigue crack growth rate along with the Paris law fit of the Fe<sub>30</sub>Mn<sub>10</sub>Co<sub>10</sub>Cr HEA, which is composed of a metastable fcc matrix and a hcp martensite phase [92].

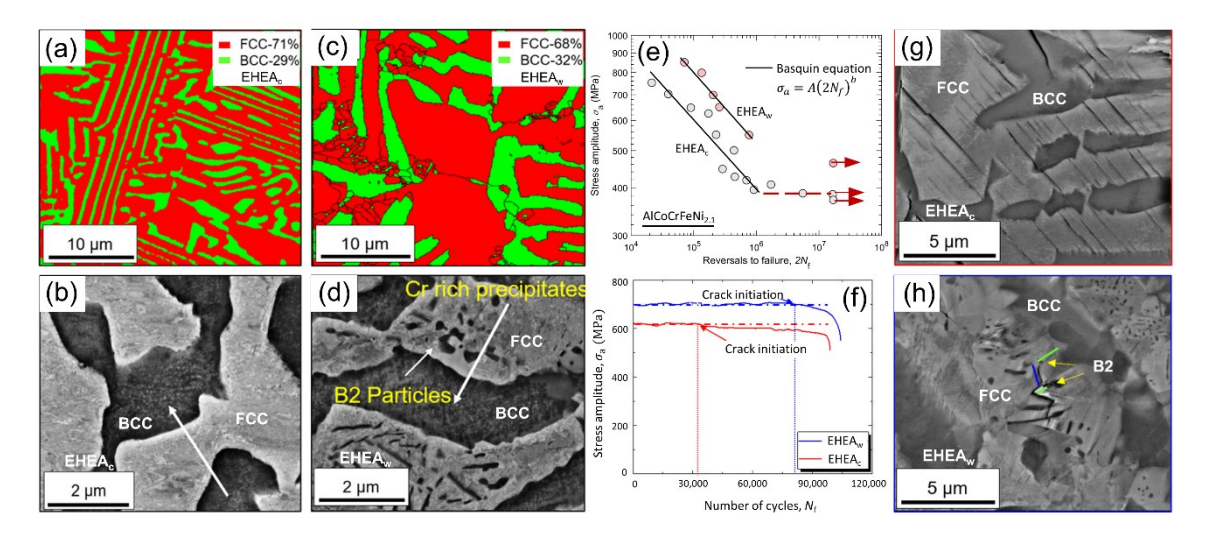


Figure 6.10 Microstructures and fatigue properties of the AlCoCrFeNi<sub>2.1</sub> eutectic HEA comprising ordered fcc (L1<sub>2</sub>) and bcc (B2) lamellae [338]. (a) EBSD phase map of the as-cast alloy, EHEA<sub>c</sub>. (b) BSE image of EHEA<sub>c</sub> with the arrow pointing to Cr-rich nanoprecipitates in the bcc phase. (c) EBSD phase map of the wrought alloy, EHEA<sub>w</sub>. (d) BSE image of EHEA<sub>w</sub> revealing Cr-rich nanoprecipitates in the bcc phase and B2 particles in the fcc phase. (e) *S-N* curves of EHEA<sub>c</sub> and EHEA<sub>w</sub> with the Basquin fits. (f) Full history of fatigue cycles at  $\sigma_a = 600 \, MPa$  for EHEA<sub>c</sub> and 700 MPa for EHEA<sub>w</sub>. (g) BSE image of the fatigued EHEA<sub>c</sub> showing the formation of straight PSBs in the fcc phase. (h) BSE image of the fatigued EHEA<sub>w</sub> showing the formation of curved PSBs by the deflection of B2 particles in the fcc phase.

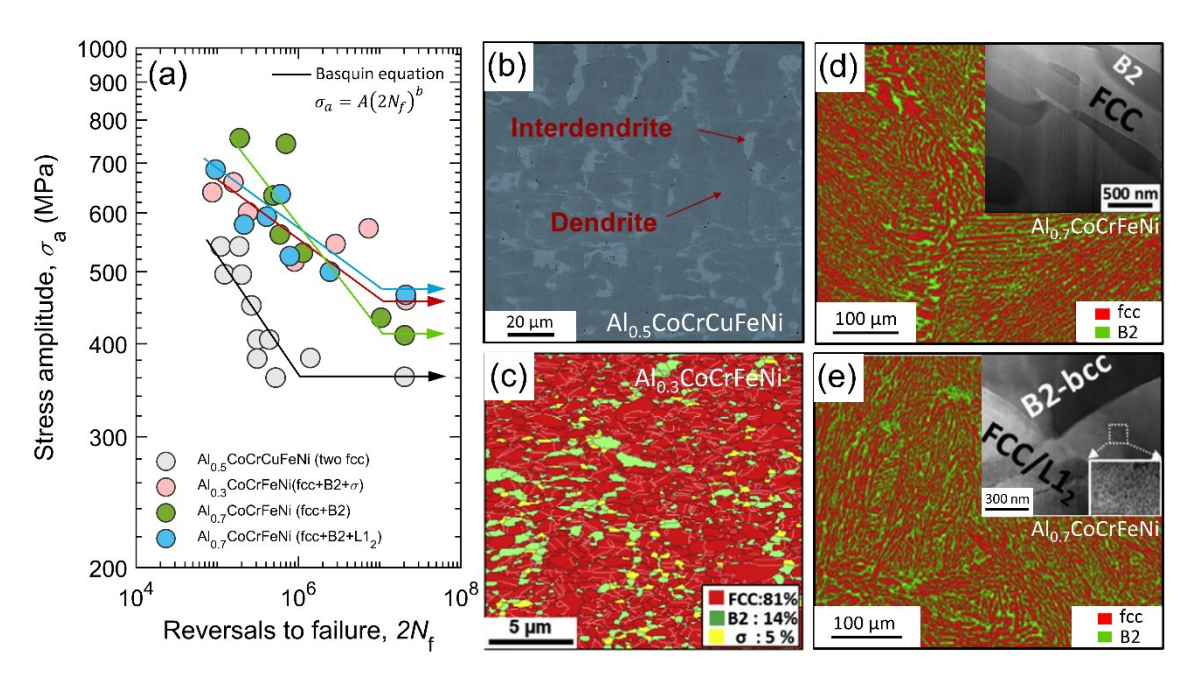


Figure 6.11 (a) *S-N* curves of the Al<sub>0.5</sub>CoCrCuFeNi [341], Al<sub>0.3</sub>CoCrFeNi [342], and Al<sub>0.7</sub>CoCrFeNi [343] HEAs along with the Basquin fits. (b) SEM micrograph showing that the Al<sub>0.5</sub>CoCrCuFeNi HEA has a duplex microstructure comprising of a dendritic fcc phase (dark color) and a Cu-rich interdendritic fcc phase (light color) [340]. (c) EBSD phase map of the Al<sub>0.3</sub>CoCrFeNi HEA showing a triplex microstructure containing the ultrafine-grained fcc matrix phase, and nano-sized B2 and tetragonal Fe-Cr-rich *σ* precipitates [342]. EBSD phase maps and SEM micrographs of the Al<sub>0.7</sub>CoCrFeNi HEA with two different lamellar microstructures, (d) fcc and B2 phases, (e) fcc, B2, and nano-sized L1<sub>2</sub> precipitates [343].

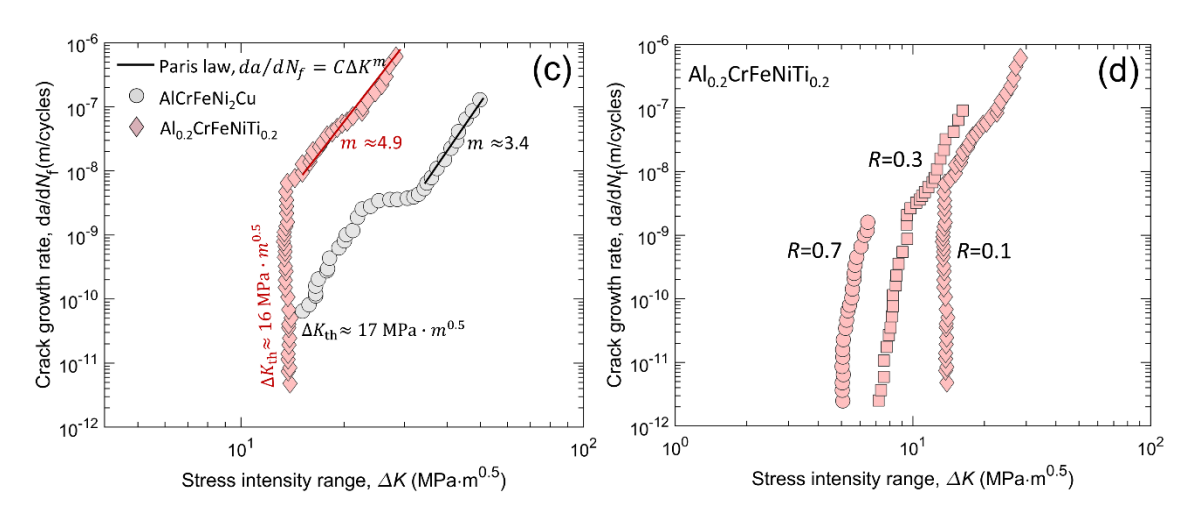


Figure 6.12 Fatigue crack growth behavior of the  $Al_{0.2}$ CrFeNiTi<sub>0.2</sub> and AlCrFeNi<sub>2</sub>Cu HEAs [303]. (a) Fatigue crack growth rate and Paris law fits of both HEAs at a stress ratio of R = 0.1. (b) Effect of the stress ratio R on the fatigue crack growth rate of the  $Al_{0.2}$ CrFeNiTi<sub>0.2</sub> HEA.

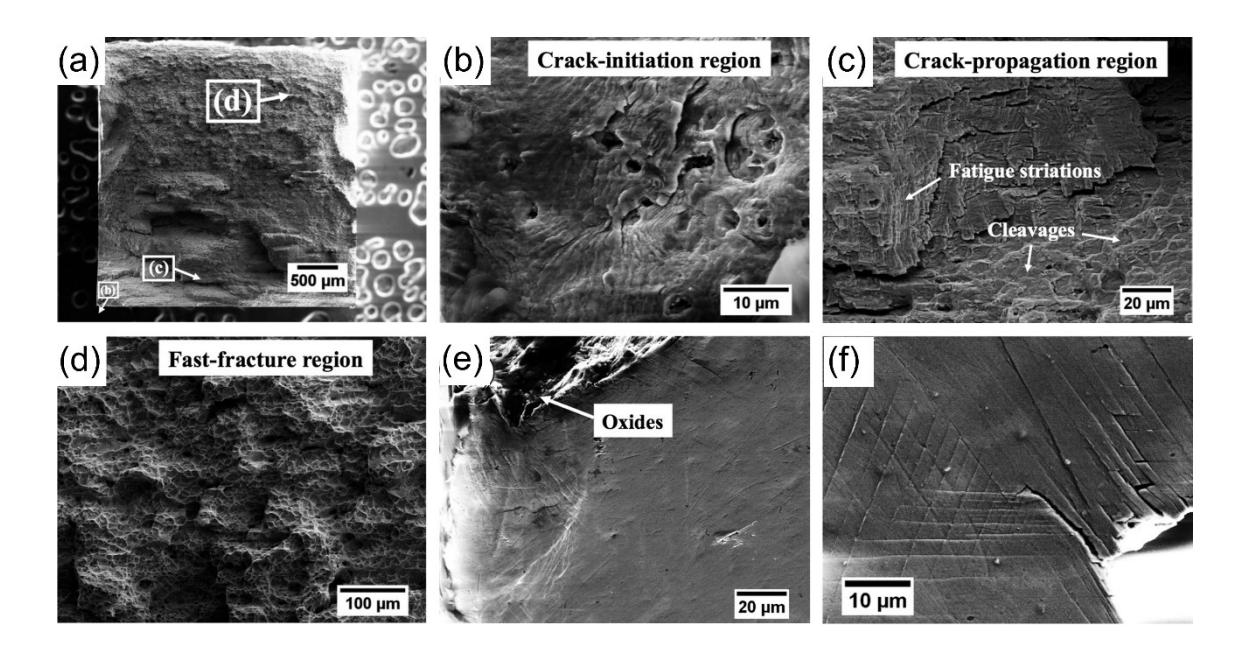


Figure 6.13 Fracture morphologies of the Al<sub>0.5</sub>CoCrCuFeNi HEA made from high purity raw materials (> 99.9%), failed at  $\sigma_a = 495 \, MPa$  [341]. (a) Overall view. (b) The crack initiation region. (c) The stable crack propagation region. (d) The fast fracture region. (e) Initiation of fatigue cracks from oxides. (f) Formation of cracks along slip bands.

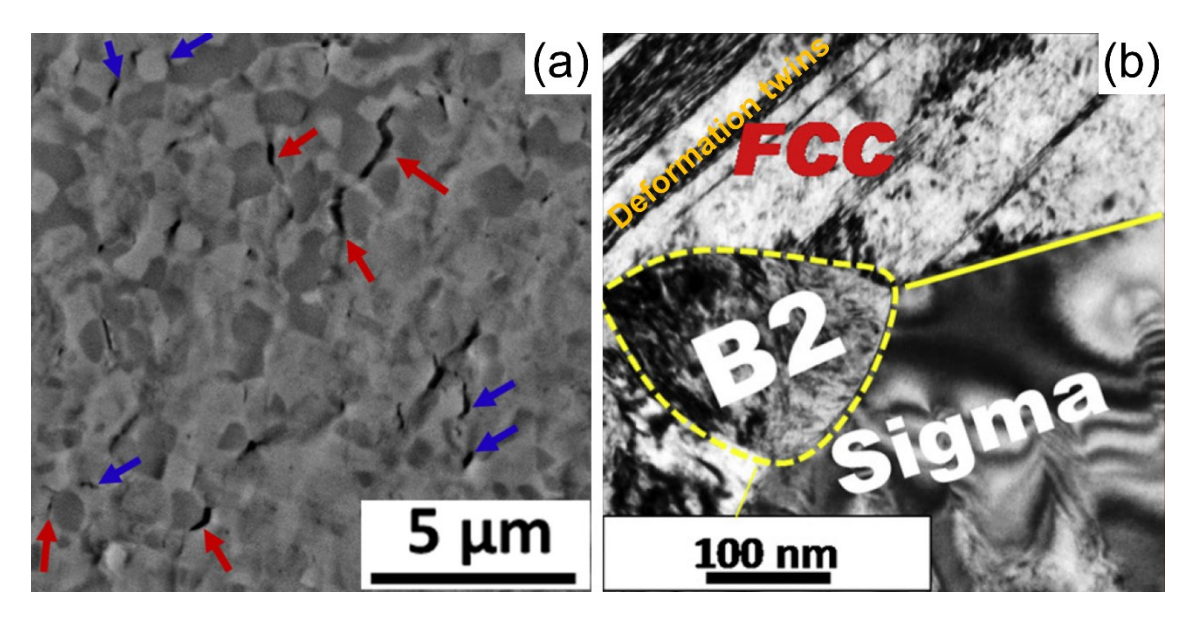


Figure 6.14 Fatigue mechanism in the  $Al_{0.3}$ CoCrFeNi HEA with fcc, B2 and  $\sigma$  phases [342]. (a) Formation of fatigue cracks along the interface between the fcc matrix and hard second phase particles (B2 and  $\sigma$ ). (b) Extensive micro- and nano-sized deformation twins in the fcc matrix to intensify working hardening and thus fatigue resistance.

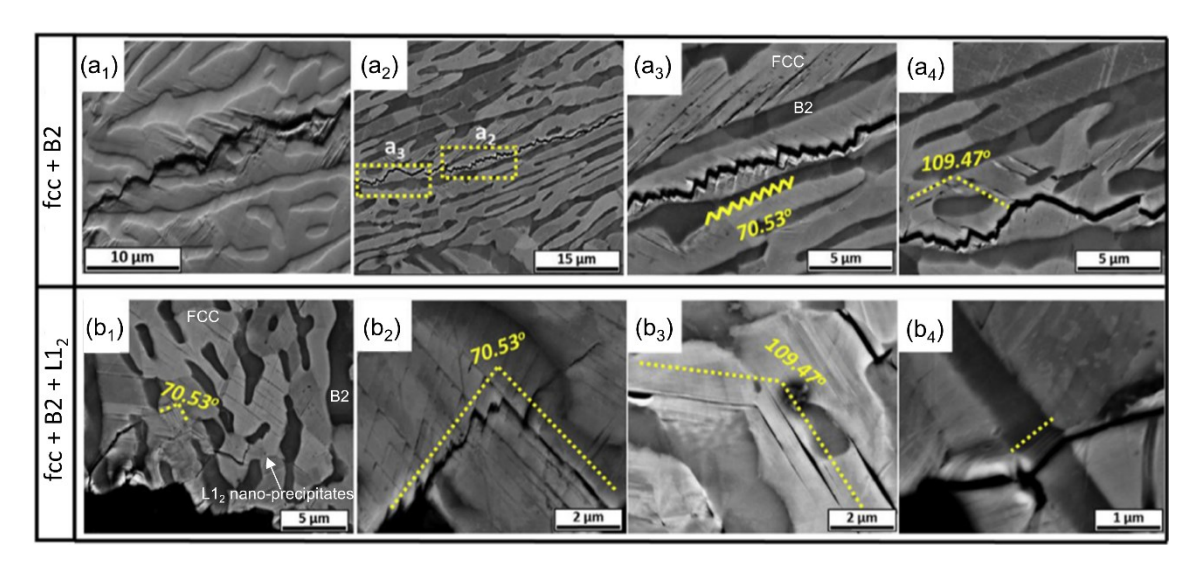


Figure 6.15 The crack trajectories of the Al<sub>0.7</sub>CoCrFeNi HEA with two different microstructures [343]. (a) fcc and B2 phases. (b) fcc, B2, and L1<sub>2</sub> nano-sized particles.

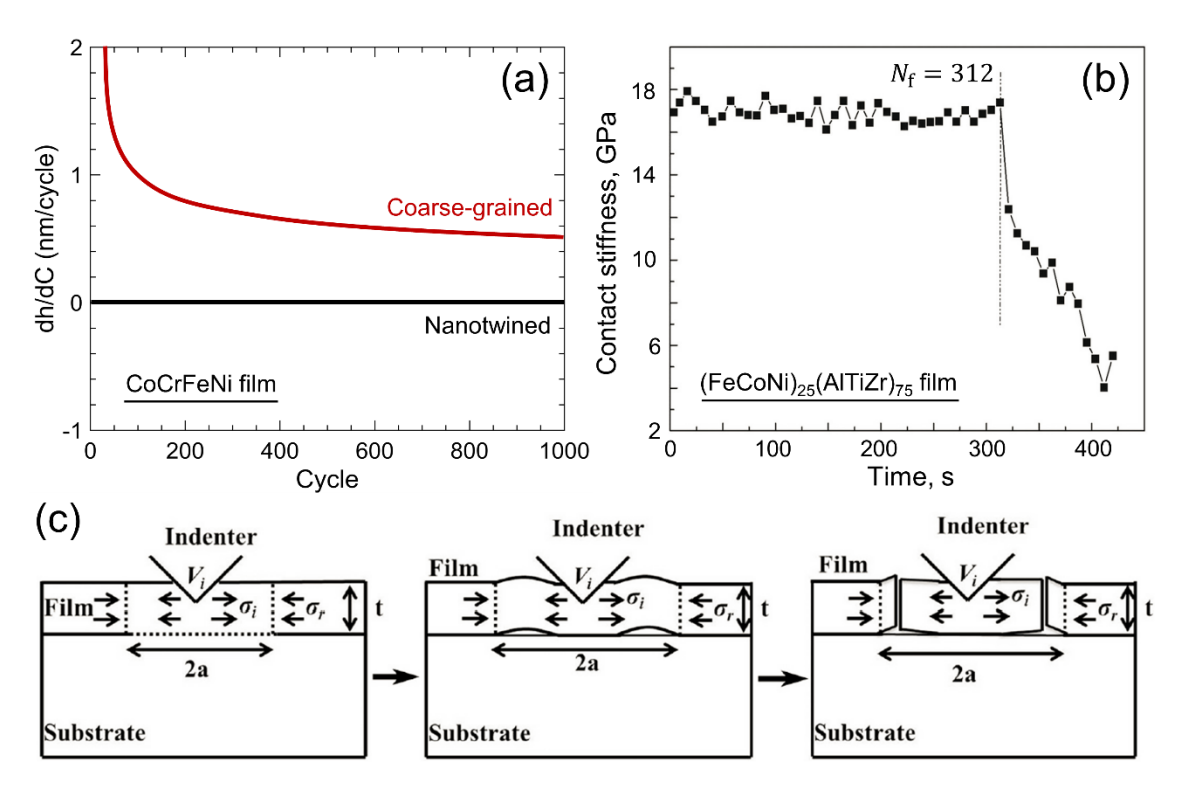


Figure 6.16 Nanoindentation fatigue of HEA thin films. (a) The changing rate of the nanoindentation penetration depth with respect to the fatigue cycle,  $\frac{dh}{dc}$ , against the fatigue cycle for the coarse-grained and nanotwined CoCrFeNi films at different impact energies [347]. (b) Variation of the contact stiffness over time for the (FeCoNi)<sub>25</sub>(AlTiZr)<sub>75</sub> film, on which the sudden drop in the contact stiffness marks the initiation of fatigue [348]. (c) Three stages of nanoindentation fatigue mechanics of thin films: compressional deformation stage, the buckling and layering stage, and the crack and delamination stag [348].

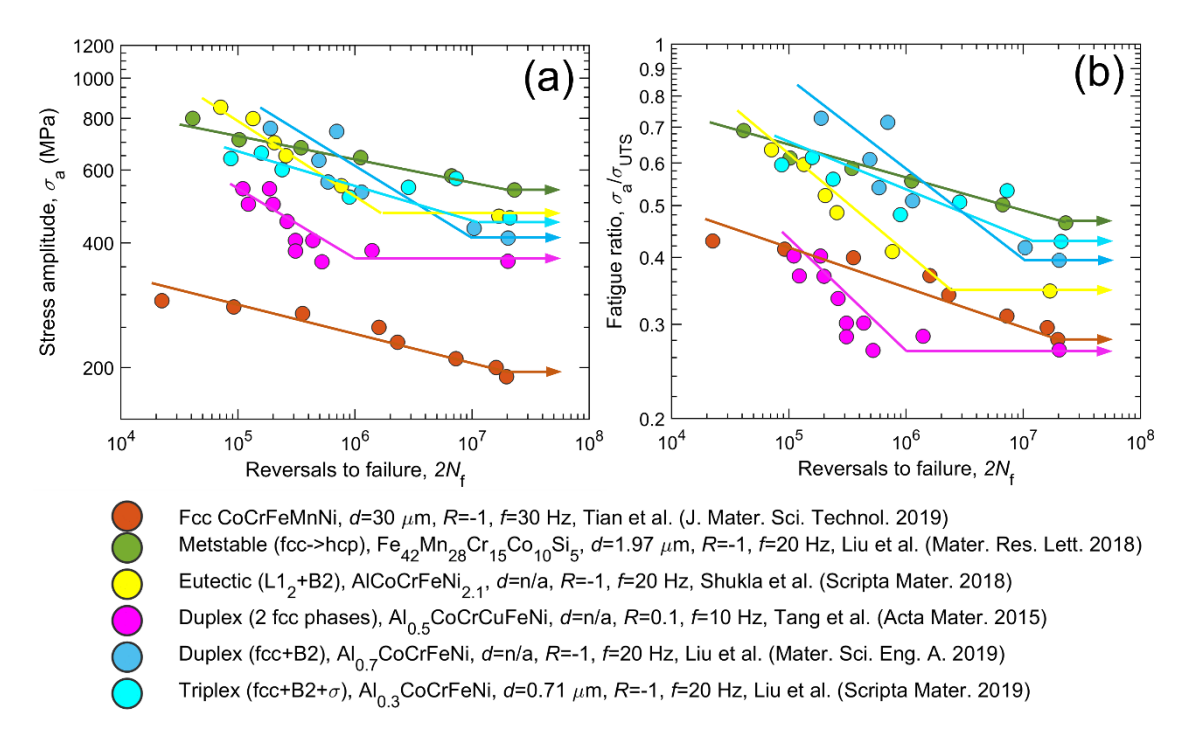


Figure 6.17 Comparison of the high-cycle fatigue responses of different categories of HEAs classified by phase constitution. (a) S-N data in terms of stress amplitude  $\sigma_a$  versus reversals to failure  $2N_f$ . (b) Fatigue ratio  $\frac{\sigma_a}{\sigma_{UTS}}$  versus  $2N_f$ . For clarity, the data points in (a) and (b) are overlaid with trend lines.

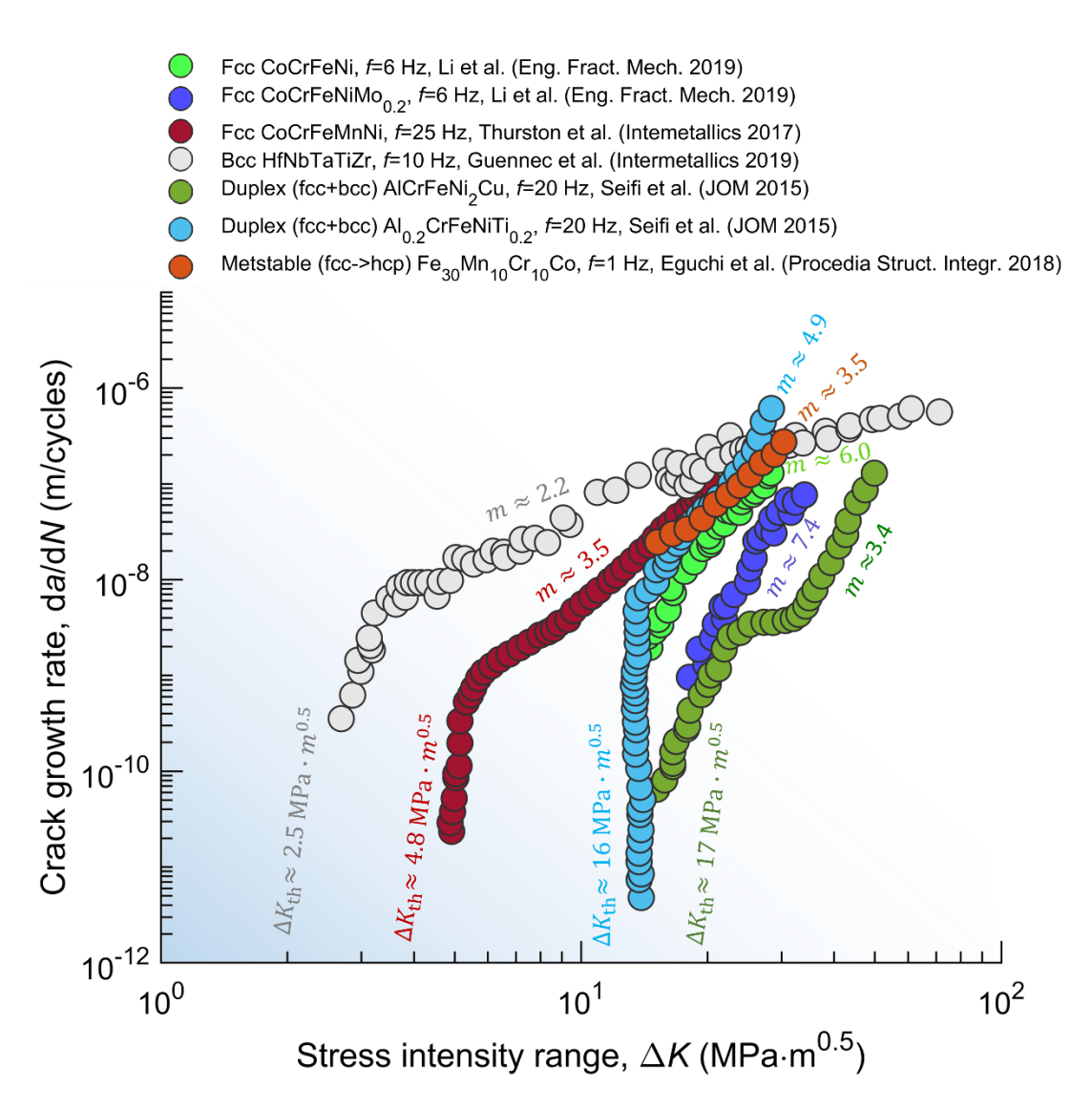


Figure 6.18 Comparison of fatigue crack growth rates of HEAs tested at similar conditions, i.e., room temperature and a stress ratio of R = 1.

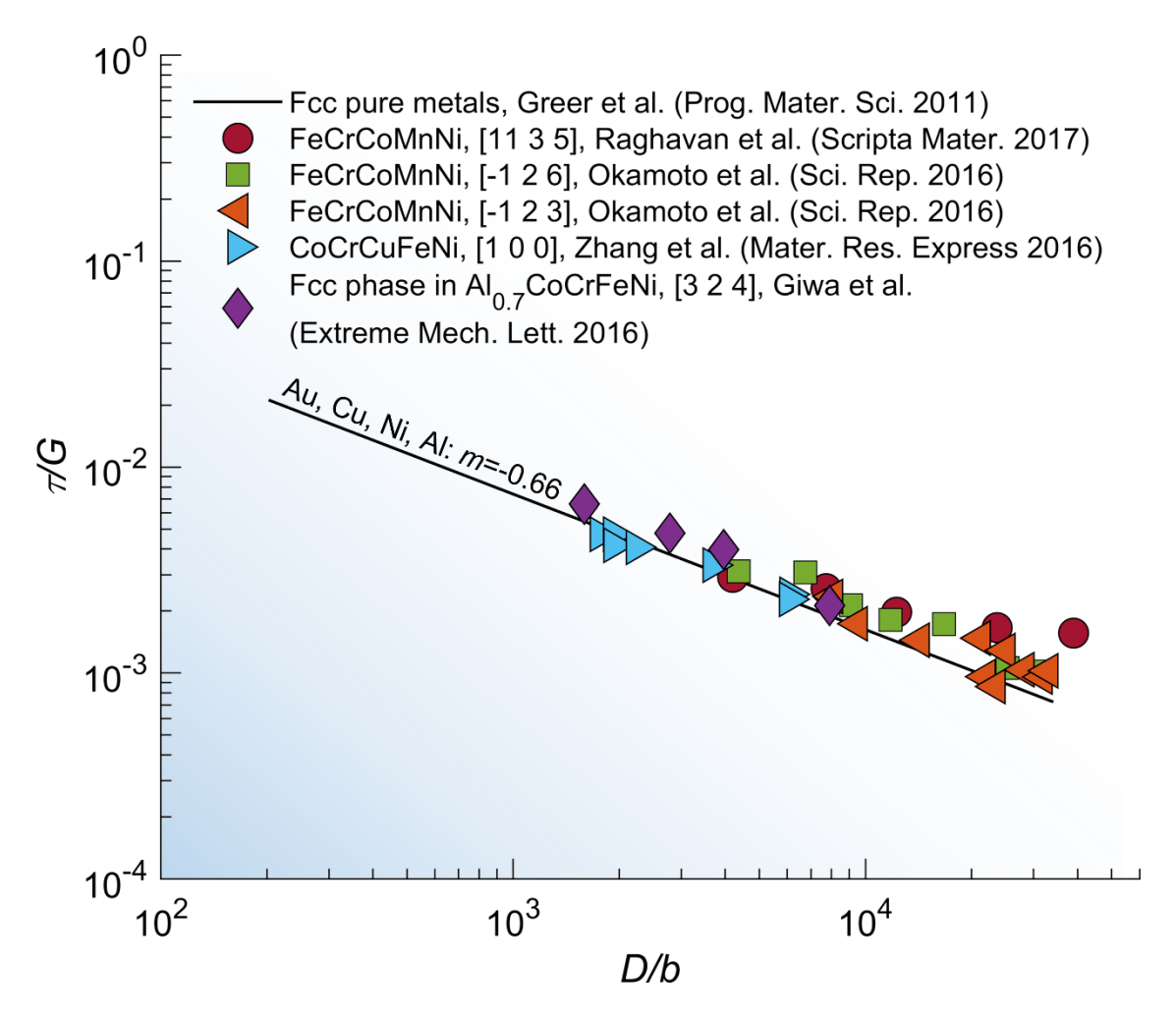


Figure 7.1 The power-law dependence of the resolved shear stress normalized by shear modulus,  $\frac{\tau}{G}$ , on the pillar dimeter divided by the magnitude of Burger's vector,  $\frac{D}{b}$ , for single crystalline fcc pure metals and HEA pillars. The numbers enclosed by square brackets in the legend are loading crystallographic direction. Corresponding data for HEAs are found in Table 7.1.

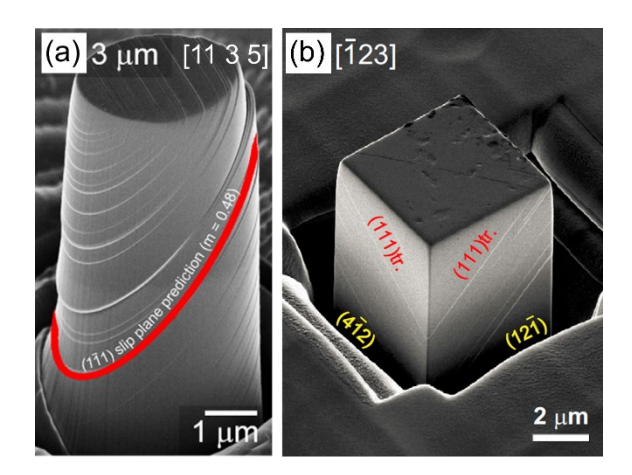


Figure 7.2 Planar slip traces on the {111}(110) slip system in the single crystalline fcc FeNiCrCoMn micropillars. (a) Cylindrical pillar compressed in the [11 3 5] crystallographic orientation [354]. (b) Square pillar compressed in the [123] orientation [379]. Both imaged by scanning electron microscopes (SEM).

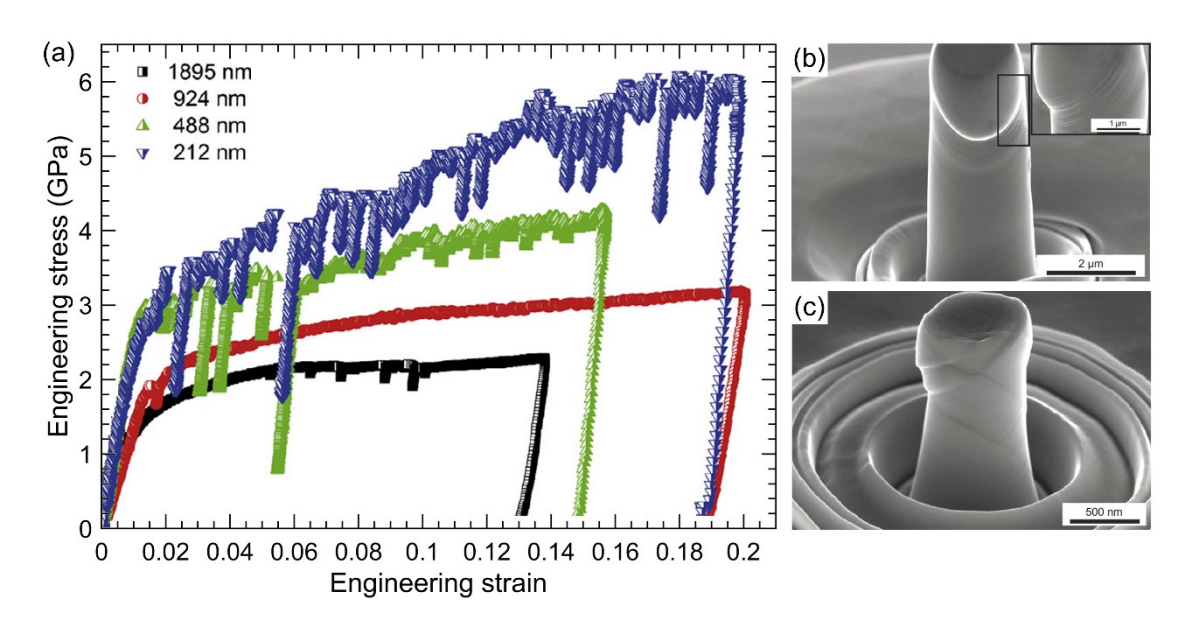


Figure 7.3 Compression of the single crystalline bcc NbMoTaW micropillars along the [316] crystallographic orientation [57]. (a) Engineering stress-strain curves of the 0.2-2  $\mu$ m dimeter pillars. Scanning electron microscopy images of the deformed pillars with approximate diameters of (b) 2  $\mu$ m and (c) 0.25  $\mu$ m.

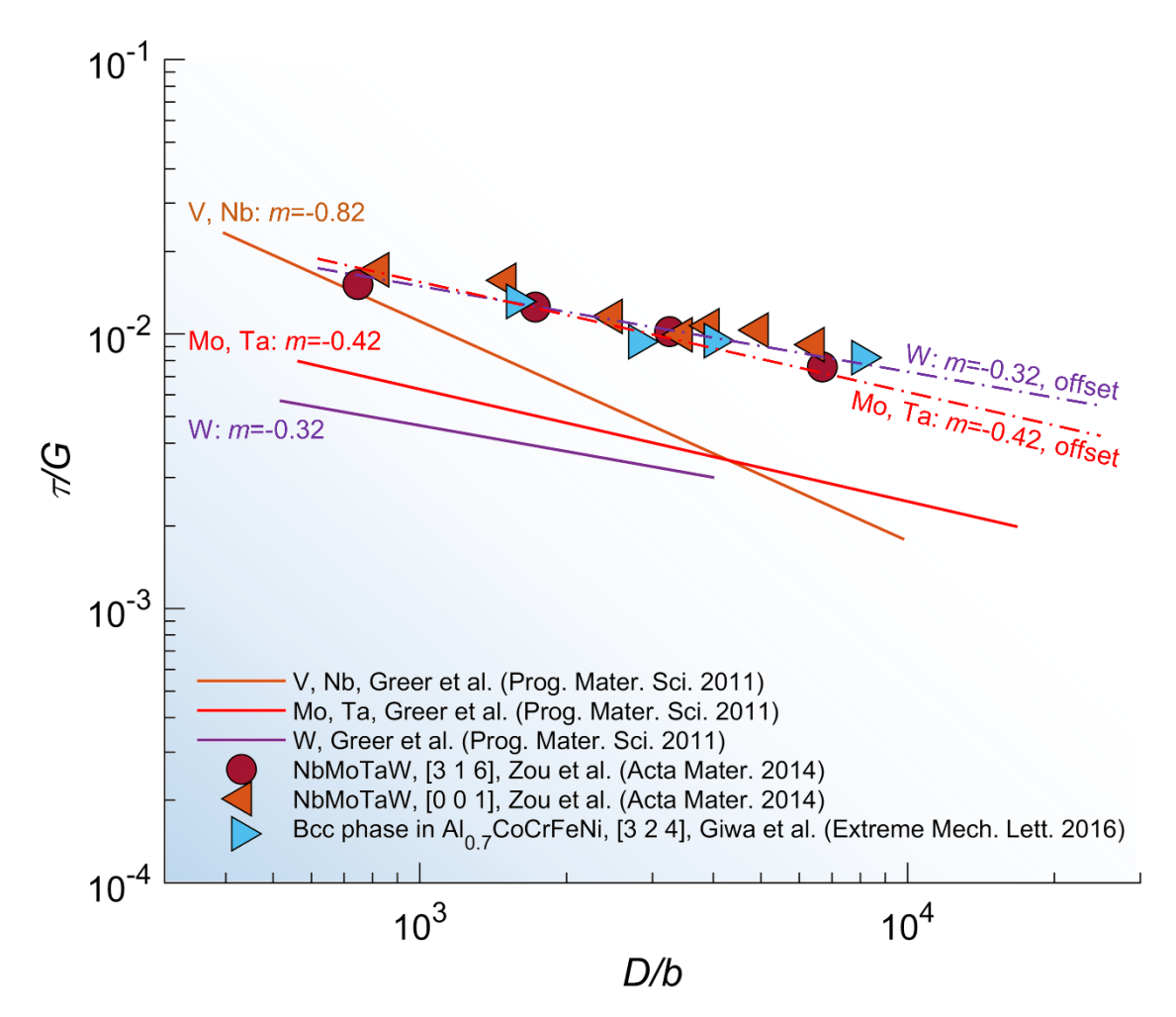


Figure 7.4 The power-law dependence of the resolved shear stress normalized by shear modulus,  $\frac{\tau}{G}$ , on the pillar dimeter divided by the magnitude of Burger's vector,  $\frac{D}{b}$ , for the single crystalline bcc pure metal and HEA pillars. The numbers enclosed by square brackets in the legend are loading crystallographic direction. Corresponding data for HEAs are found in Table 7.1.

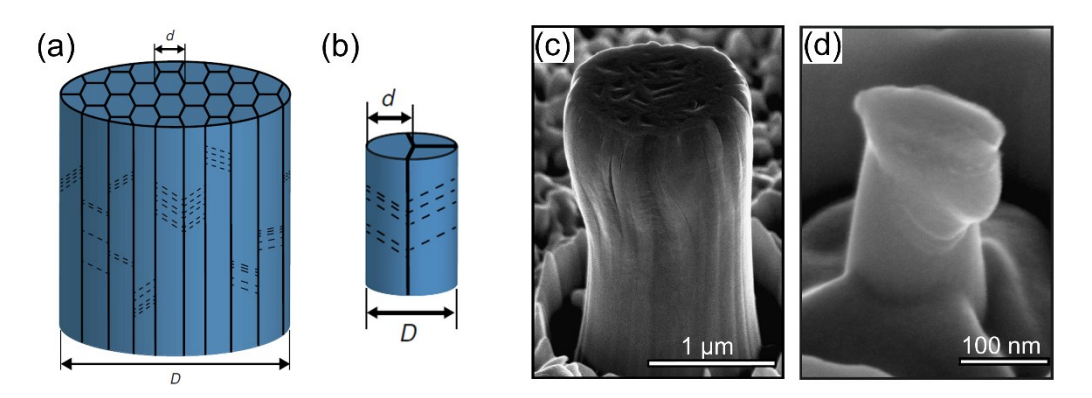


Figure 7.5 Nanocrystalline bcc NbMoTaW nanopillars [356]. Schematics of (a) a larger pillar and (b) a small pillar containing textured, nanosize, columnar grains. Scanning electron microscopy images of the post-compressed (c) 1 µm and (d) 100 nm pillars.

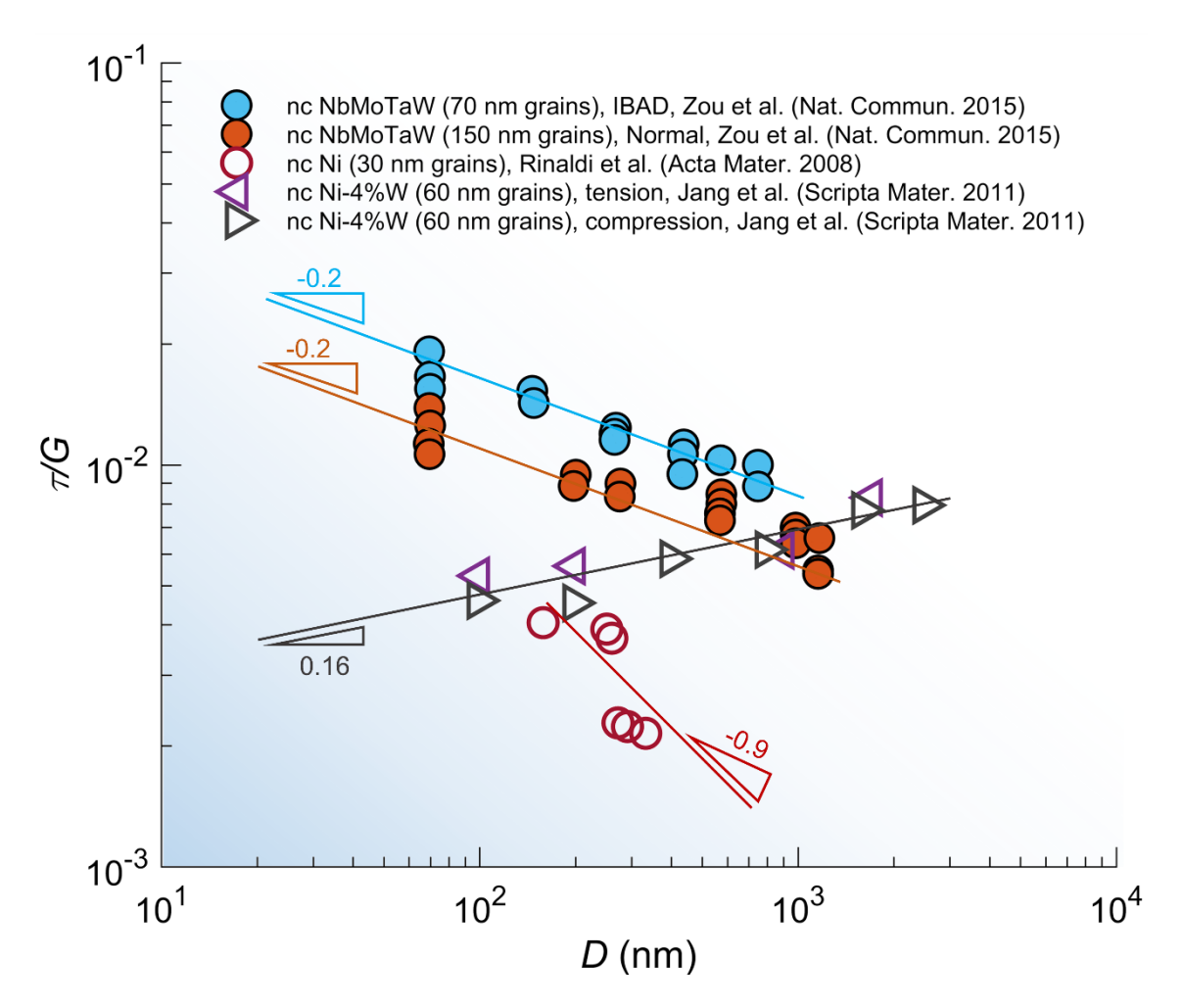


Figure 7.6 The power-law dependence of the resolved shear stress normalized by shear modulus,  $\frac{\tau}{G}$ , on the pillar dimeter, D, for the nanocrystalline Ni, Ni-4%W, and NbMoTaW HEA pillars. Normal and IBAD denote pillars produced from the normal direct current magnetron cosputtering technique and the ion beam-assisted film deposition, respectively [357].

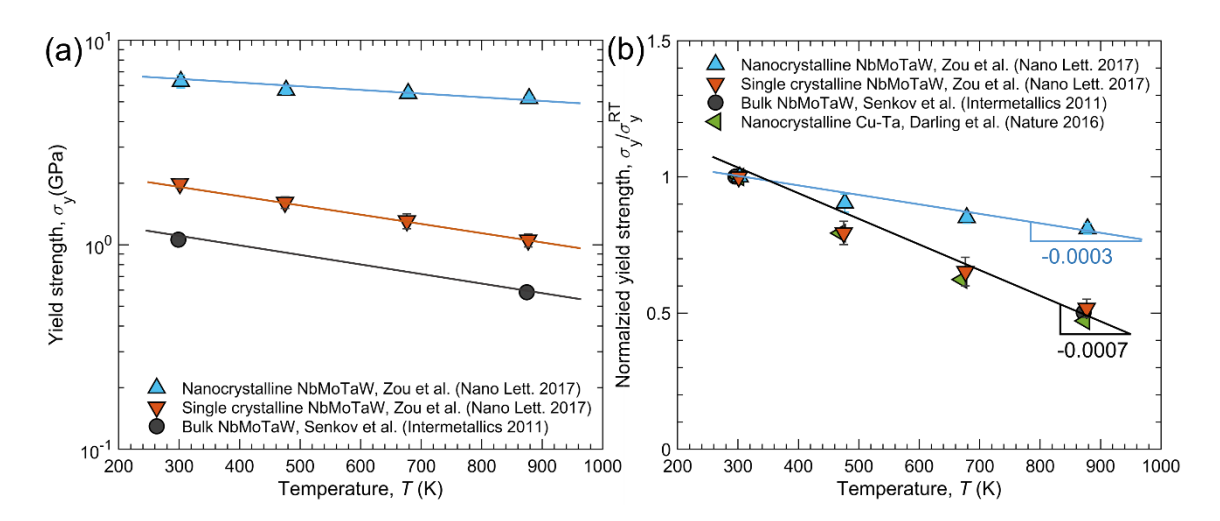


Figure 7.7 (a) The temperature-dependent yield strengths of the single crystalline and nanocrystalline NbMoTaW HEA micropillars of  $\sim 1~\mu m$  in dimeter [357] as well as the coarse-grained bulk polycrystalline NbMoTaW [16]. (b) Temperature-induced strength reduction for the nanocrystalline and single crystalline NbMoTaW pillars [357], bulk polycrystalline NbMoTaW [16], and nanocrystalline Cu-Ta alloy [392].

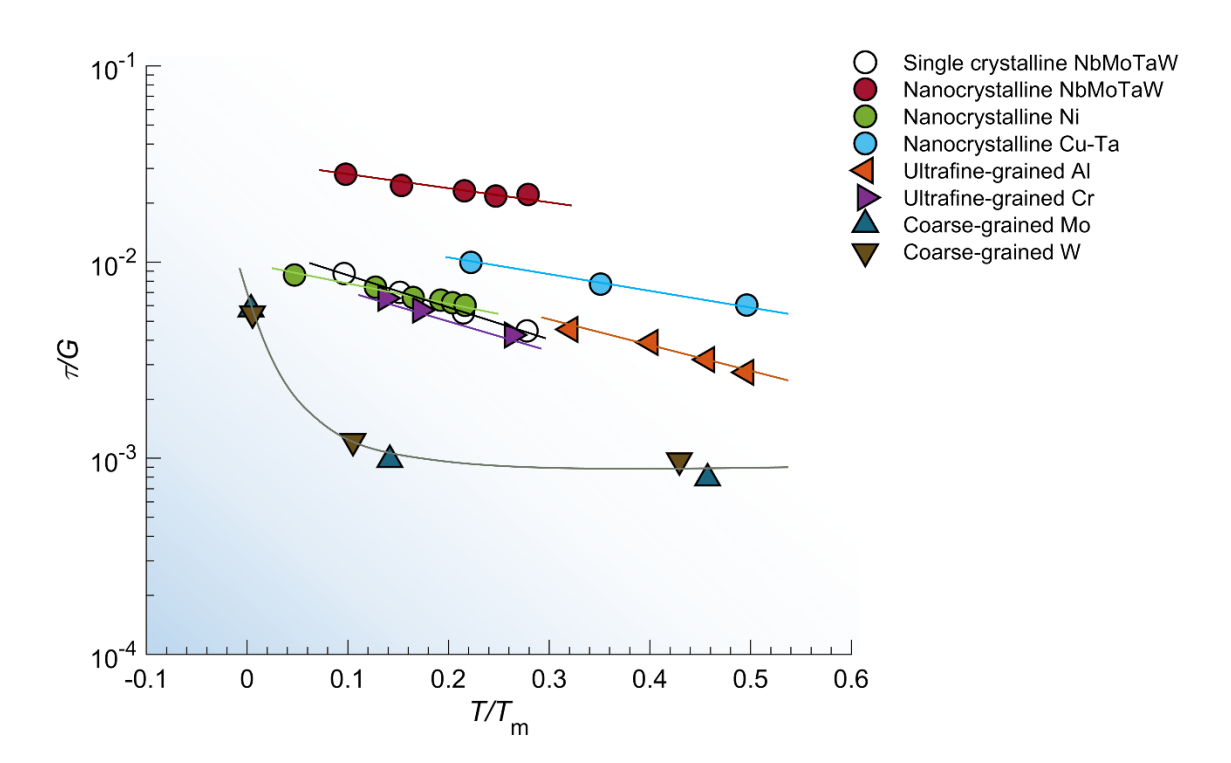


Figure 7.8 The critical resolved shear stress normalized by the shear modulus,  $\frac{\tau}{G}$ , as a function of the homologous temperature,  $\frac{T}{T_m}$ , for the single crystalline (sc) and nanocrystalline (nc) NbMoTaW HEA micropillars [357], nc Ni [396], and nc Cu-Ta alloy [392], ultrafine-grained (ufg) Al [395], ufg Cr [397], coarse-grained (cg) Mo and W [393]. All tested at a strain rate of  $\sim 10^{-3}$  s<sup>-1</sup>.

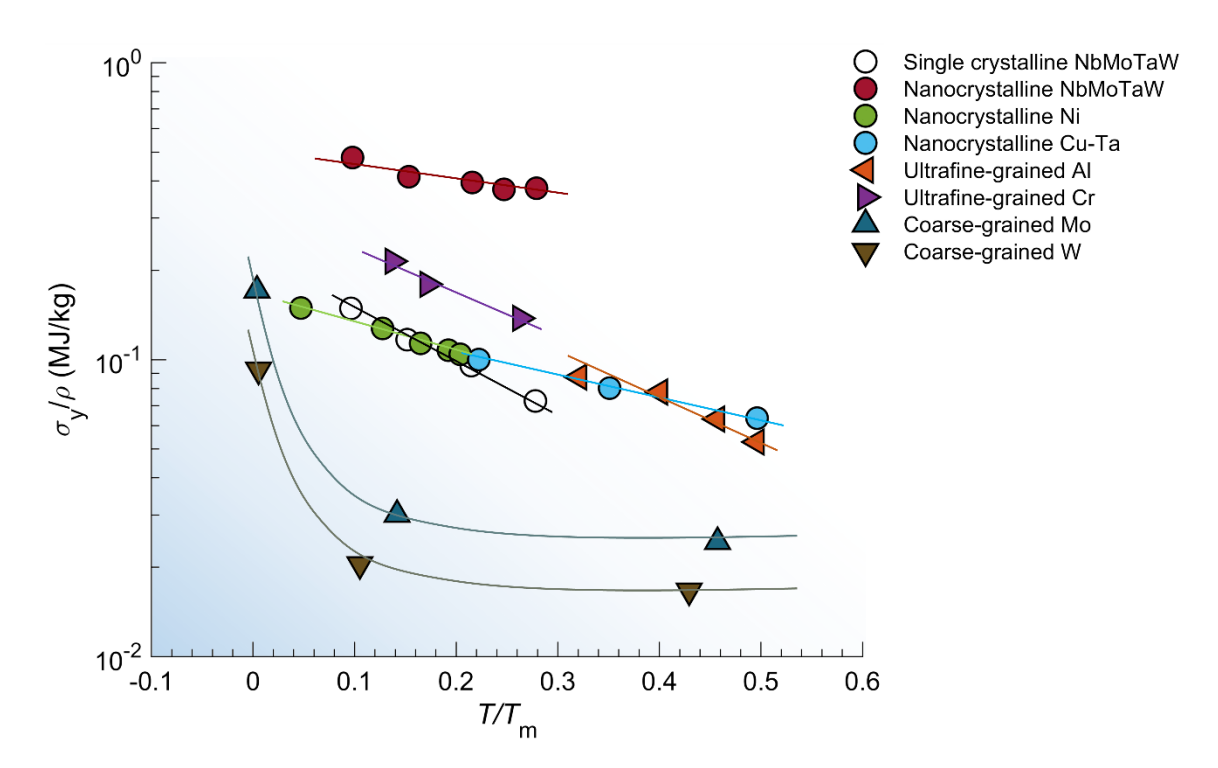


Figure 7.9 The specific strength,  $\frac{\sigma_y}{\rho}$ , as a function of the temperature, T, for the single crystalline (sc) and nanocrystalline (nc) NbMoTaW HEA micropillars [357], nc Ni [396], and nc Cu-Ta alloy [392], ultrafine-grained (ufg) Al [395], ufg Cr [397], coarse-grained (cg) Mo and W [393]. All tested at a strain rate of  $\sim 10^{-3}$  s<sup>-1</sup>.

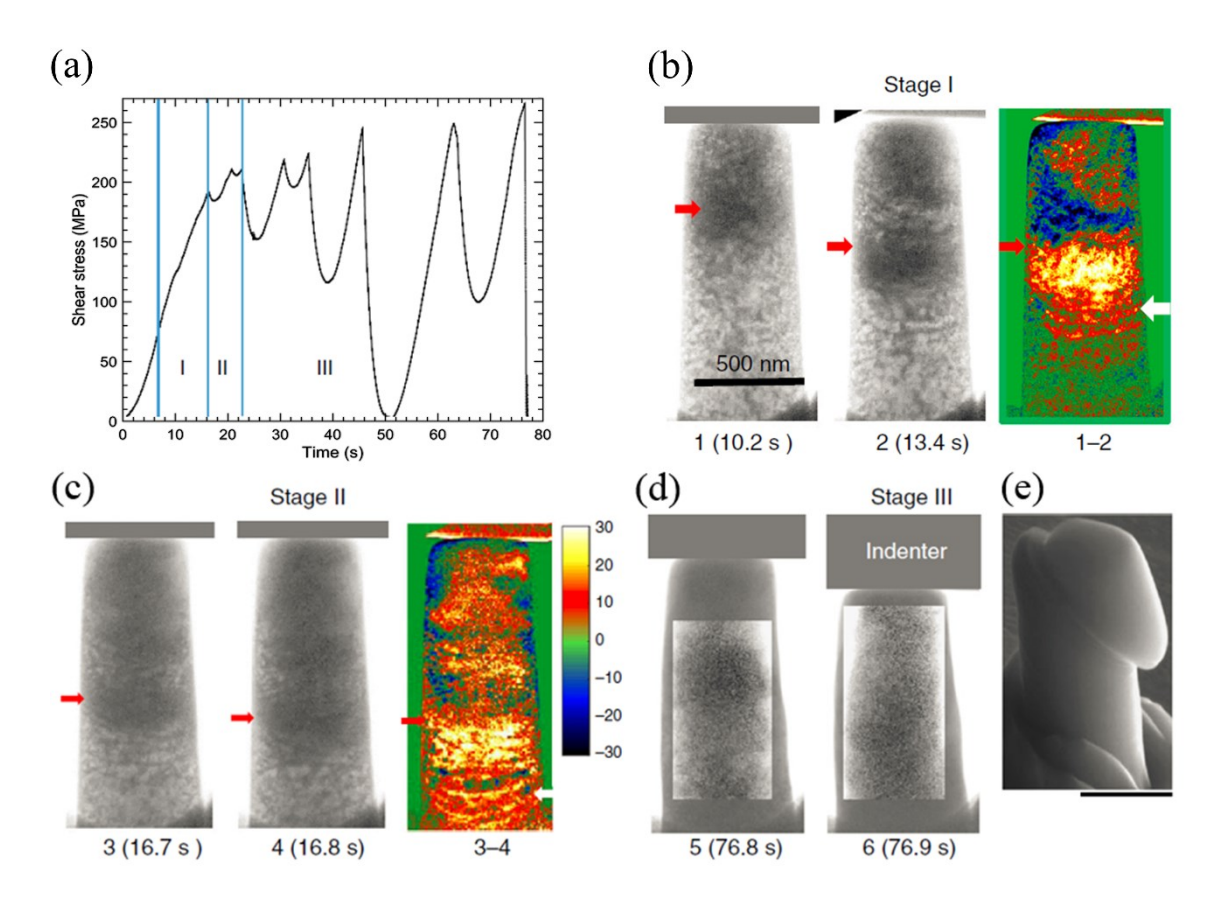


Figure 7.10 In situ compression of a Al<sub>0.1</sub>CoCrFeNi pillar and the observation of dislocation avalanches by the transmission electron microscope (TEM) [359]. (a) Measured shear stress-time curve, on which three deformation stages (I, II, and II) are delimited. (b-d) TEM-observed deformation process at each stage. 1-2 and 3-4 are the differences of two consecutive TEM images (i.e., 1 and 2, 3 and 4), in which the positive and negative intensities are indicative of the creation and annihilation of dislocations, respectively. (e) Scanning electron microscopy (SEM) image showing a large slip step in the deformed nanopillar.

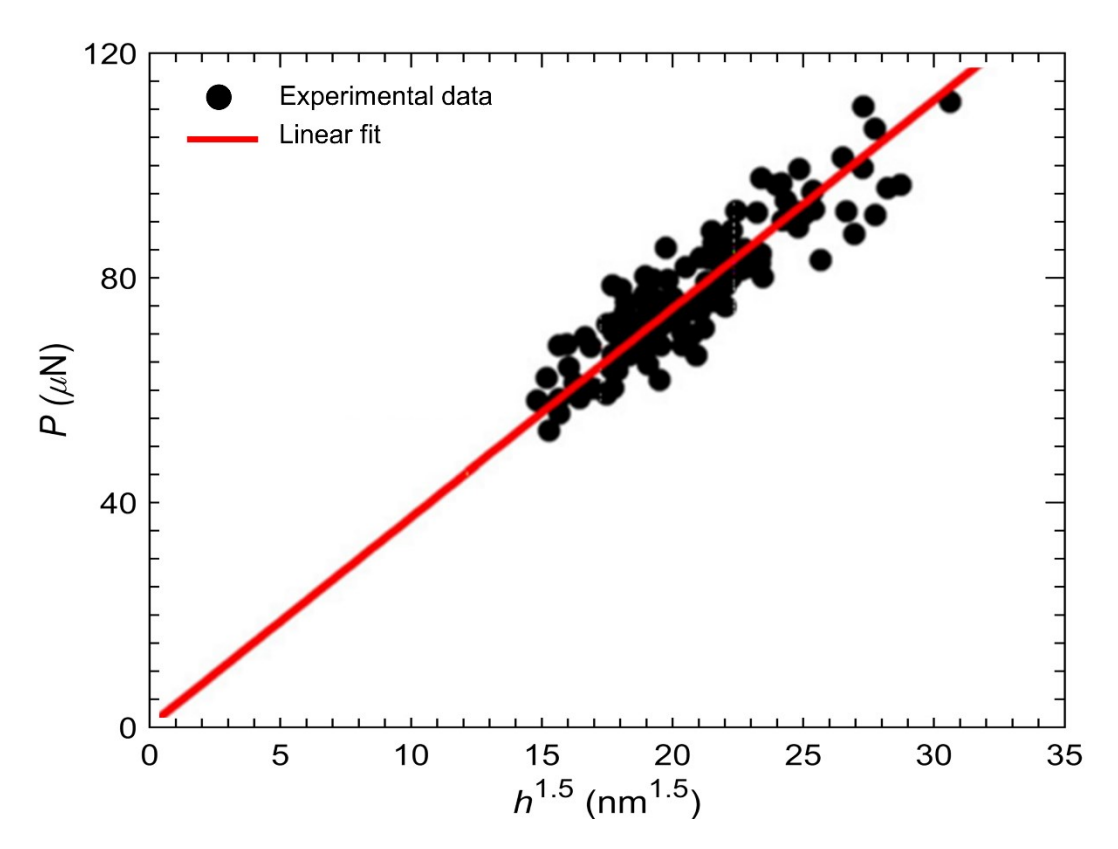


Figure 7.11 An example linear fit to a collection of  $P - h^{3/2}$  data at nanoindentation pop-ins for extracting the Young's modulus from the slope constant according to the Hertzian theory in Equation (7.3). The example is demonstrated by  $\sim 120$  nanoindentation tests on the fcc FeCoCrNiMn HEA [355].

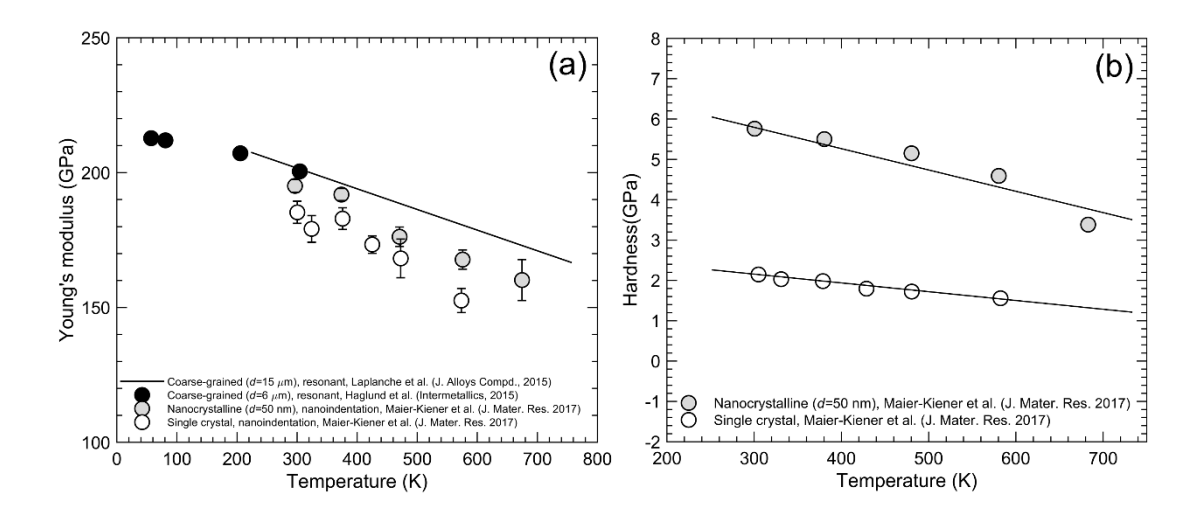


Figure 7.12 Young's modulus and hardness of the fcc FeCoCrNiMn HEA measured by nanoindentation [415]. (a) Temperature dependence of Young's modulus and (b) hardness of the nanocrystalline and the coarse-grained (measured on the elastically softest <110> grains) samples [415]. Alongside compared are the resonance spectroscopic measurements on the same alloy with grains  $\sim 4 \mu m$  [419] and  $\sim 15 \mu m$  [148] in size.

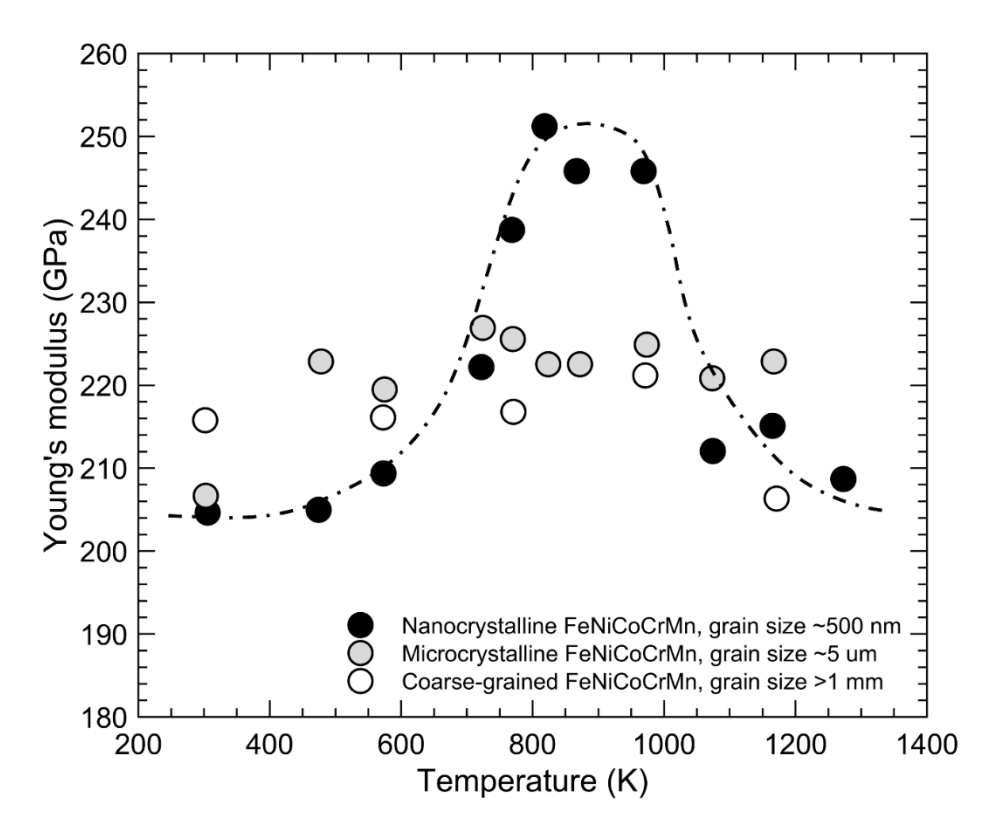


Figure 7.13 Temperature dependence of the Young's moduli of the nanocrystalline, microcrystalline, and coarse-grained alloys [412], with the hump indicative of certain phase transformation in the nanocrystalline alloy.

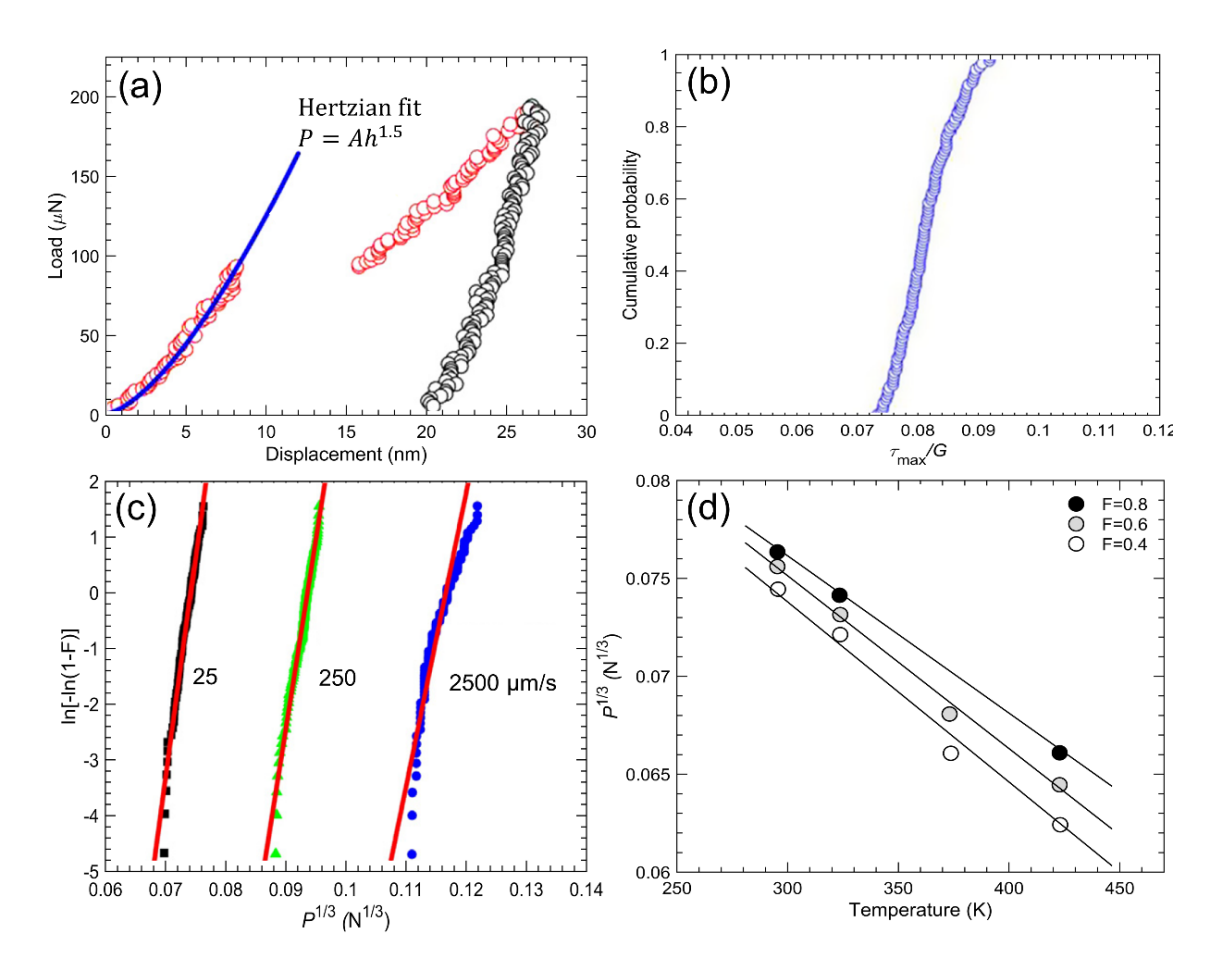


Figure 7.14 Incipient plasticity in the fcc FeCoCrNiMn HEA studied by nanoindentation [355]. (a) A typical load-displacement curve showing a pop-in event marking the onset of plasticity. The elastic portion prior to the pop-in is well fitted by the Hertzian theory [418]. (b) Representative cumulative probability of the normalized maximum shear stress by the shear modulus,  $\tau_{max}/G$ , at pop-ins of  $\sim 120$  indentations. (c) Linear fits to the ln[-ln(1-F)] versus  $P^{1/3}$  data at three different loading rates according to Equation (7.6), from which the pop-in activation volumes can be determined from the slopes. (d) Linear fits to the  $P^{1/3}$  versus T according to Equation (7.8), from which the pop-in activation energies can be retrieved from the intercepts. Note that the fits at three cumulative probability (F) levels converge to a single intercept, thus a single activation energy.

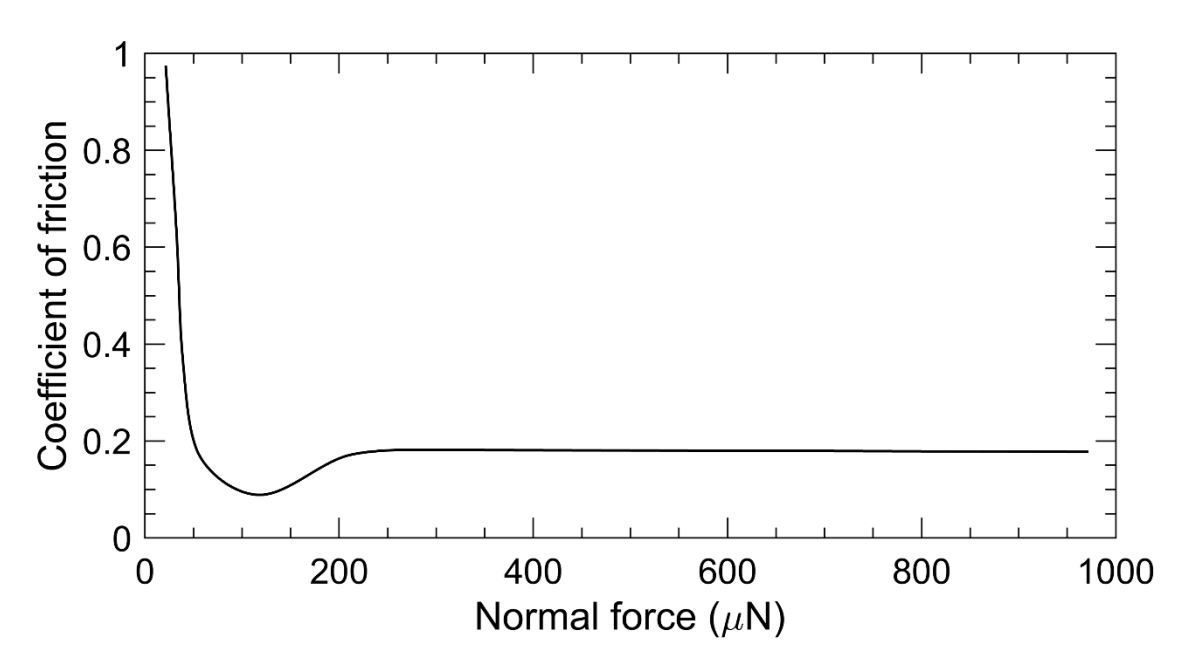


Figure 7.15 Friction behavior of the bcc TiZrHfNb HEA studied by nanoscratch tests [414]. (a) Coefficient of friction (COF) of the high entropy (HE), Nb, and C103 alloys under a ramping load linearly increasing from 0 to 1000  $\mu$ N. (b) COF of the HEA under constant loads from 10 to 1000  $\mu$ N, with each point being the average COF under an individual constant load. In both loading modes, an elastic deformation dominated region (Region I) is followed by a plastic deformation dominated region (Region II).

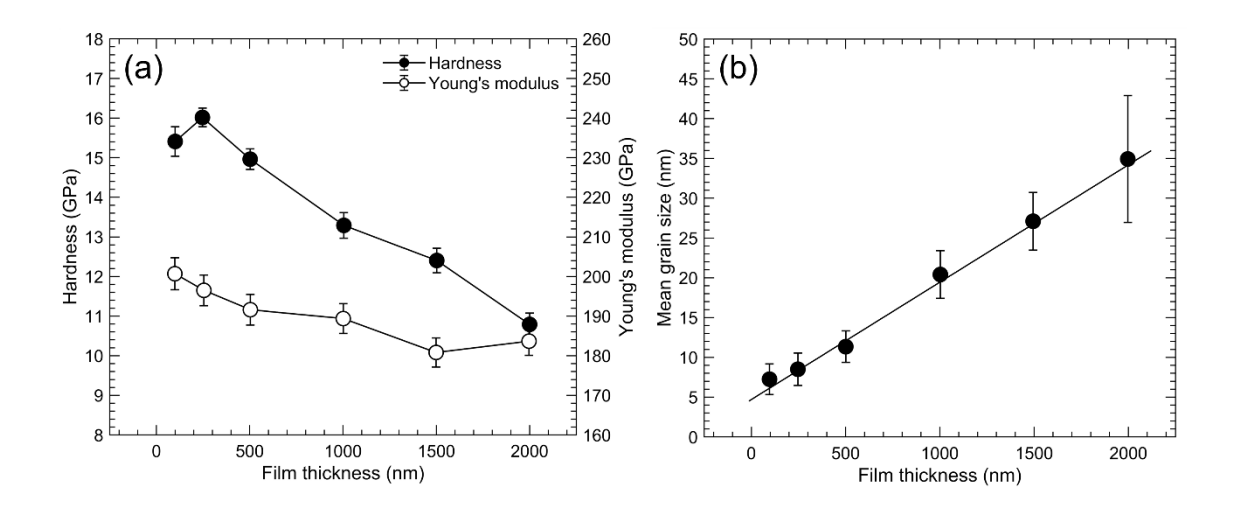


Figure 7.16 The size effect in the naoncrystalline NbMoTaW thin films [436]. (a) The variation of the hardness and Young's modulus (measured at a strain rate of 0.1 s<sup>-1</sup>) with the film thickness. (b) The linear correlation between the film thickness and the grain size.

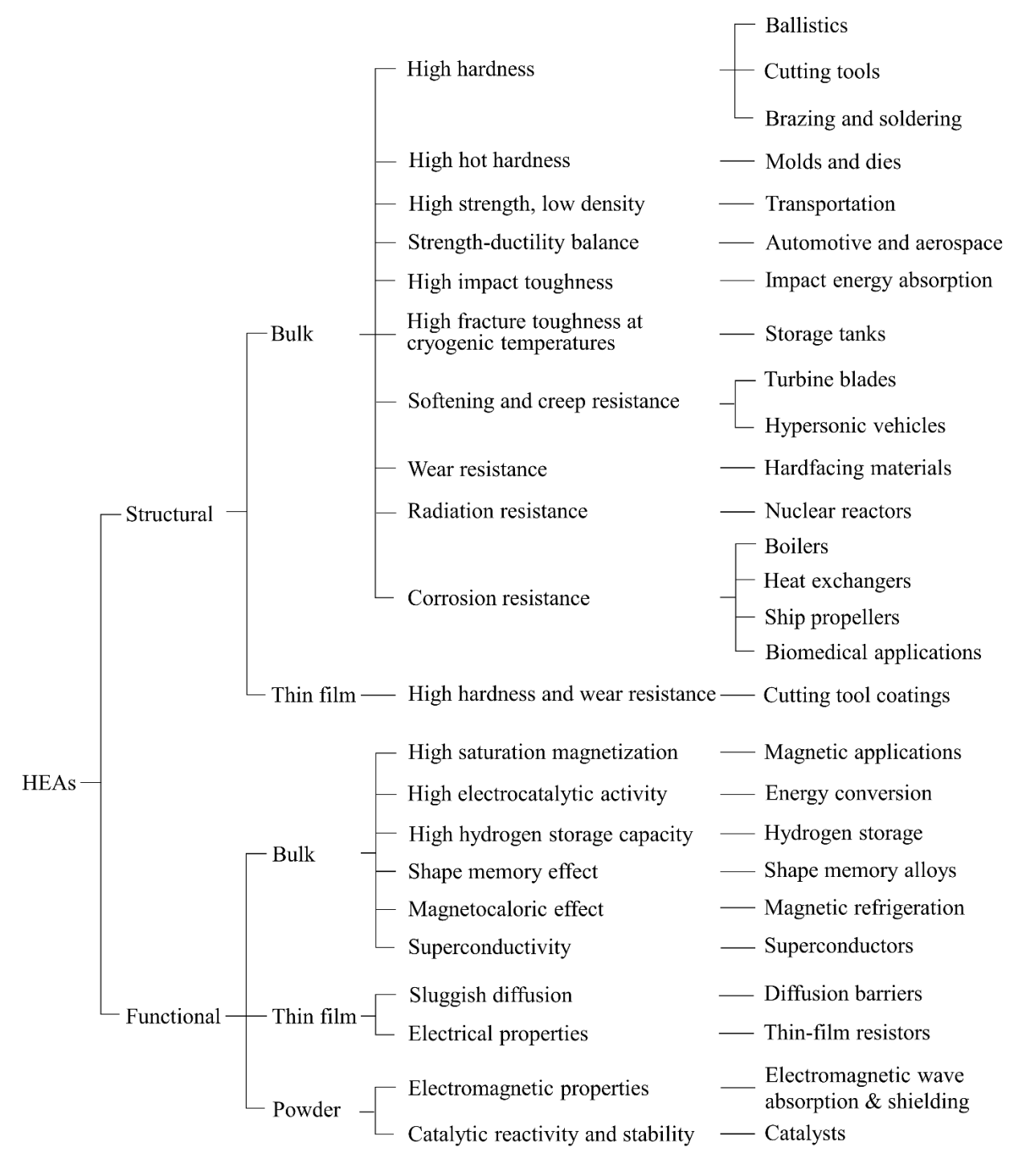


Figure 8.1 Tree map of structural and functional applications along with determining properties for various forms of high entropy alloys.